CHARACTERISTICS OF HADRONIC STATES OBSERVED IN HIGH ENERGY DIFFRACTIVE PHOTOPRODUCTION IN HYDROGEN

by

Alan Lee Duncan

B.A., University of Oklahoma, 1976

A thesis submitted to the

Faculty of the Graduate School of the

University of Colorado in partial fulfillment

of the requirements for the degree of

Doctor of Philosophy

Department of Physics

1982

This thesis for the Doctor of Philosophy degree by

Alan Lee Duncan

has been approved for the

Department of

Physics

by

Uriel Nauenberg

Uriel Nauenberg

James Glanda

DATE _____

Duncan, Alan Lee (Ph.D., Physics)

Characteristics of Hadronic States Observed in High Energy Diffractive Photoproduction in Hydrogen

Thesis directed by Professor Uriel Nauenberg

A large multi-particle spectrometer was constructed at the Fermi National Accelerator Laboratory to study the interaction of high energy photons with protons in a fixed liquid hydrogen target. The energy of the incident photons was measured for each event ranging from 40 to 160 GeV. Data was accumulated for events characterized by the presence of hadronic particles in the spectrometer. An on-line trigger processor identified protons in the recoil spectrometer surrounding the target and calculated the missing mass, selecting only those events with a missing mass between 2 and 11 GeV. The data sample thus consists of high mass diffractive events containing hadronic particles in the final state.

A drift chamber system consisting of four separate modules containing a total of 29 active planes was used to reconstruct the momentum components of all charged particles present within the acceptance of the spectrometer. Two large volumn gas Cerenkov counters were used to identify electrons. The recoil spectrometer provided sufficient information to reconstruct the 4-momentum of all charged particles within its acceptance. Using this information events were selected which contained a single charged particle in the recoil spectrometer identified as a proton. A minimum of three charged particles was required in the forward spectrometer.

(Electrons were not counted.) Only charged particles were used in the analysis.

A jet-like structure is observed in the center of mass. This structure is characterized by a decrease in the sphericity and a limiting value for the transverse momentum as the missing mass increases. Comparisons are made with other hadronic and e+e- annihilation experiments. The Feynman X, rapidity, and P_t inclusive distributions are studied as a function of the missing mass in the central and photon fragmentation regions. Fits are made to functional forms motivated by QCD counting rules. The results are in good agreement with the theory in the large Feynman X region. Scaling is observed in this region. In the central region scaling violations are observed and measured as a function of the center of mass energy.

The form and content of this abstract are approved.
I recommend its publication.

Signed Uriel Nauenberg
Faculty member in charge of thesis

ACKNOWLEDGMENTS

The history of this experiment extends back many years and involves the ideas and efforts of many people. I would like to thank all of my collaborators for their support and encouragement, and for their assistance in preparing this thesis.

THE FERMILAB TAGGED PHOTON SPECTROMETER COLLABORATION

J. Appel[4], D. Bartlett[2], S. Bhadra[2], V. Bharadwaj[1], J. Biel[4], D.Bintinger[4], D. Blodgett[6], S. Bracker[6], J. Bronstein[4], L. Chen[4], B.Denby[1], A. Duncan[2], A. Eisner[1], J. Elliott[2], P. Estabrooks[3], G.Hartner[6], G. Kalbfleisch[5], R. Kennett[1], R. Kumar[6], M. Losty[3], A.Lu[1], G. Luste[6], P. Mantsch[4], J. Martin[6], R. Morrison[1], T. Nash[3], U. Nauenberg[2], J. Pinfold[3], M. Robertson[5], K. Shahbazian[6], C. Sliwa[4], J. Spalding[6], M. Sokoloff[4], K. Stanfield[4], M. Streetman[4], D. Summers[1], S. Willis[4], M. Witherell[1], C. Zorn[6]. W. Schmidke[4].

[1]University of California at Santa Barbara; [2]University of Colorado at Boulder; [3]Carleton University and National Research Council of Canada; [4]Fermi National Accelerator Laboratory; [5]University of Oklahoma; [6]University of Toronto, Canada.

I would like to thank my advisor, Uriel Nauenberg, for his efforts over the last few years which have made this final moment of success possible. His constant encouragement, personal attention, and concern made it possible to continue when times were

hard. I consider myself fortunate to have had this opportunity to benefit from his knowledge and experience. I would also like to express a special thanks for the personal interest that Uriel has shown in my career and in the success of this effort.

I would like to thank Jim Elliott and Sampa Bhadra for their assistance in all aspects of this effort, and in particular for their contributions to the analysis proceedures. I have benefited immensely from their suggestions and stimulating discussions.

I would like to thank the members of the Proton Department at Fermilab for the technical support that made this experiment possible. It was a monumental effort over several years to maintain the complex apparatus necessary to make this experiment a success.

I would like to thank the members of the collaboration for the opportunity to work with them and benefit from their knowledge and experience. It has been a rewarding experience in many ways. I value the friendships and professional relationships that have developed as a result of our mutual efforts. I would like to express a special thanks to those who helped prepare this thesis by taking the time and effort to provide many helpful suggestions and comments.

I would like to thank Tom Nash for his advice and for his personal interest in my efforts.

I would like to thank my fellow graduate students for their encouragement and companionship, especially during the years at Fermilab.

I would like to thank James Randa and Tom DeGrand for their assistance in preparing the theoretical ideas presented in this thesis. They were always available to answer questions and make suggestions which proved to be invaluable.

I would like to thank Debra Taylor for her assistance in preparing the manuscript.

Finally, I would like to express a very special thanks to my wife Kim who has stood beside me through some difficult years. I am deeply grateful for her willingness to make the sacrificies that have been necessary to bring this effort to a close. Her strength and encouragement have shielded me against the frustrations that have threatened to overwhelm me.

FIGURES

FIGURES

TABLES

TABLE

CONTENTS

CHAPTER 1

THEORY

Brief History

Many experiments have demonstrated for low beam energies the striking similarities between the production of hadronic states by photon induced and hadron induced processes.[1] These similarities were not anticipated prior to the experimental observations, due to the abscence of any obvious connection between the strong interactions of hadrons and the considerably weaker interactions of photons. The photon undergoes predominantly electromagnetic interactions. At high energies the principal component of the total cross section of the photon is the process of electromagnetic pair production. The experiments clearly demonstrated, however, a strong motivation for some connection between the structure of a hadron and a photon. For example, the total hadronic and photon cross sections for producing hadrons in the final state show large resonance structure at low energies and above 2 - 3 GeV become structureless, slowly declining then rising gradually as the energy increases. They differ only in normalization, the photon total cross section being suppressed approximately by a factor of α, the fine structure constant that characterizes electromagnetic interactions. Many additional similarities have been observed at lower energies, including such things as inclusive P_t distributions,

longitudinal momentum distributions, diffractive momentum transfer distributions and nuclear shadowing.[2] It is apparent, therefore, that a photon whose properties are described by quantum electrodynamics can initiate processes whose characteristics may be described by a theory of the strong interactions.

An early candidate for a model to explain the apparently intimate connection between the characteristics of photon induced and hadron induced interactions was Vector Meson Dominance (VMD). The copious production of vector mesons, particles containing the same quantum numbers as the photon (ρ,ω,ϕ), observed in photoproduction experiments indicated that these vector meson states might contribute significantly to the formation of the photon wave function.[1] VMD assumes that the physical photon state is composed of a bare photon state undergoing point-like electromagnetic interactions and a hadronic state undergoing strong interactions with hadrons.[2]

$$|\gamma\rangle \approx \sqrt{Z_3}|\gamma_b\rangle + \sqrt{\alpha}|h\rangle \qquad (1.1)$$

Z_3 - provides proper normalization

$|\gamma_b\rangle$ - bare photon state

$|h\rangle$ - hadronic photon state

VMD then assumes that the hadronic part of the photon wave function is simply a superposition of vector meson states. VMD developed into a quantitatively useful model for long range interactions such

as diffractive photoproduction. Diffractive photoproduction could be expressed in terms of vector meson scattering requiring only knowledge of the initial superposition which constituted the hadronic part of the photon wave function.

The limitations of VMD involve processes characterized by short range interactions which probe the constituent structure of the target nucleons. Within this kinematic domain, a model which describes the dynamics of the individual constituents is more appropriate. The parton model[3,4] portrays a hadron as a composite, constructed from elementary constituents called partons. The partons undergo point-like interactions and are assumed to behave like ordinary free particles during short range interactions. The parton model does not, however, explain how the constituent partons form a bound state hadron. To complete the picture, the photon must be viewed in the light of a more comprehensive theory.

Quantum Chromodynamics (QCD) is such a comprehensive theory of the strong interactions of hadrons[5]. QCD is, in principle, a simple theory which describes the interactions of elementary fermions called quarks, mediated by the SU(3) gauge field of bosons called gluons. The simplicity of the basic theory becomes somewhat obscure when confronted with the task of describing the physically realizable composite hadrons. Viable perturbation schemes have, however, been developed which are capable of making a quantitative assesment of varous processes in certain kinematic domains[6,7]. Solutions of the theory within certain limited frameworks have also

produced valuable information regarding the character of the physical hadron states.

Perturbative QCD is most successful in making quantitative predictions when confined to the kinematic domain previously occupied by the parton model, (short range "hard" scattering processes[6]). Non-perturbative effects, however, are not well understood, and their affect on the perturbative expansion are uncertain, in some cases. In spite of this uncertainty, people have attempted to use these techniques to examine low P_t or long range interactions[8]. In this domain, non-perturbative effects are expected to contribute significantly to any conclusions drawn from the perturbative approach. QCD has, however been used to study such topics as total cross sections, central region multiplicity, and fragmentation distributions.[8]

Kinematics

Figure 1a describes the basic process being investigated by this thesis.

$$(\gamma p \to pX) \qquad \text{4-vector equation} \qquad \gamma + P_0 = P + X \qquad (1.2)$$

γ ≡ incident photon 4-vector

P_0 ≡ target proton at rest 4-vector

P ≡ recoil proton 4-vector

$q \equiv P_0 - P$ 4-vector of exchanged particle

M_X ≡ invariant mass of the multiparticle state X

$$(M_X = (\gamma + P_0 - P)^2)$$

$s \equiv (\gamma + P_0)^2$; $\sqrt{s} \equiv$ center of mass energy

This process is described in three different reference frames.

LAB	(target proton at rest)
INITIAL CENTER OF MASS	(center of mass of $\gamma + P_0$)
FORWARD CENTER OF MASS	(center of mass of $\gamma + P_0 - P$)

The photoproduction process being studied in this thesis involves the dissociation of a real photon via an exchange of a state with a 4-vector q which leaves the target proton intact. Such a process is referred to as a diffractive dissociation process since it involves an exchange which carries the quantum numbers of the vacuum (usually called a pomeron exchange). Diffractive processes are usually characterized by the following features.[9,10]

1.) $d\sigma/dt$ ($t = q^2$) has a large peak at low t.

2.) The total cross section varies slowly with the energy of the incident projectile (typically a logarithmic dependence).

3.) Scattering from hadrons and their anti-particles are very similar.

4.) The energy of the incident particle must be sufficiently

large to satisfy coherence criteria over the dimensions of the target hadron.

For this experiment an event is considered to be diffractive if a recoiling proton is cleanly identified and well separated in rapidity from the system X.

Global "Jet-like" Properties

Figure 1b illustrates the simplest diagram that describes the diffractive dissociation of a photon based on perturbative QCD. In the QCD model proposed by Low and Nussinov[11], the pomeron is represented by multiple gluon exchange with the gluons contained in a SU(3) color singlet state[12]. The simplest interpretation of the pomeron in this model is, therefore, a two gluon system. Since the gluons carry no quantum numbers other than SU(3) color, the color singlet two gluon exchange involves no exchange of quantum numbers, thereby satisfying the diffractive criteria. The diagram shown is actually one of many with the same order in the perturbation expansion involving permutations of the two gluons connected to different quark lines. It should be noted that the actual pomeron exchange should contain significant contributions from higher order color singlet multiple gluon exchanges.

In a QCD model proposed by Randa and De Grand[13], the diffractive photon-pomeron cross section is expected to contain two components. The dominant component involves a soft hadronization process which produces a two jet topology. Fast particles in the

forward jet (defined by the photon direction) result from the fragmentation of the photon, and particles in the backward jet result from the fragmentation of the pomeron. The axis of these "soft" jets should be nearly parallel to the photon-pomeron axis due to the small momentum transfer in the soft hadronization process. The second component involves a large momentum transfer process to produce a quark anti-quark pair back to back in the center of mass. In this case the resulting two jet topology would involve quark jets, with calculable properties based on perturbative QCD[14,15]. These two possible sources of jet structure in the diffractive process being investigated are indistinguishable in terms of the results presented in this thesis.

Hadronic interactions are, in general, limited in P_t relative to the beam direction. If the average momentum in the center of mass increases faster than the average P_t, as the center of mass energy increases, then the global character of the event begins to reflect a jet-like structure. Standard analysis of this type of dynamical behavior based on certain jet variables (sphericity, thrust, spherocity, and acoplanarity as defined in equations 7.15, 7.19, 7.20, 7.21) are used to quantify this phenomenon. They do not, however, provide a clear distinction between possible sources of the jet structure of the events. In the context of this thesis, a "jet" refers to the P_t limited character of the photon - pomeron fragmentation whose dominant contribution is not expected to have the same origin as e^+ e^- quark jets, or high P_t quark jets induced by hadronic interactions.

Photon Fragmentation

Near $X_{\parallel}=1$, perturbative QCD calculations are possible. The fragmentation of the photon at large Feynman X ($X_{\parallel}$)

$$X_{\parallel} = 2P_{\parallel}/\sqrt{s} \qquad (1.3)$$

$P_{\parallel} \equiv$ component of the hadron momentum in the center of mass along the beam direction

$\sqrt{s} \equiv$ center of mass energy

can be described in terms of point-like QCD fragmentation diagrams such as those shown in figure 1c. The $X_{\parallel}$ dependence of the fragmentation process can be computed from the following counting rule.[16]

$$X_{\parallel}dN/dX_{\parallel} \propto (1-X_{\parallel})^{2n_h+n_{pl}-1} \qquad (1.4)$$

$n_h \equiv$ number of "hadronic" spectators

$n_{pl} \equiv$ number of "point-like" spectators

A "hadronic" spectator refers to a quark that is connected by a gluon to a quark contained within the initial bound state or a quark contained within the emitted hadron produced in the fragmentation process. A "point-like" spectator refers to quarks generated by a gluon bremsstrahlung from an incoming quark. Applying this counting rule to the di-quark fragmentation process illustrated by figure 1c gives the following results.

I) $(u\bar{u}) \rightarrow \pi^+$ (1.5)

$n_h = 0$

$n_{pl} = 2$

$X_\parallel dN/dX_\parallel \propto (1-X_\parallel)$

II) $(u\bar{u}) \rightarrow \pi^+$ (1.6)

$n_h = 2$

$n_{pl} = 0$

$X_\parallel dN/dX_\parallel \propto (1-X_\parallel)^3$

III) $(u\bar{u}) \rightarrow \pi^+$ (1.7)

$n_h = 0$

$n_{pl} = 4$

$X_\parallel dN/dX_\parallel \propto (1-X_\parallel)^3$

Similar diagrams lead to the production of π^- and $K^{\mp}$ with the same $X_\parallel$ dependence. Process II and III should be suppressed relative to process I leading to a $1-X_\parallel$ dependence at large $X_\parallel$ for the photon fragmentation[8]. In addition to the di-quark fragmentation diagrams, the photon fragmentation might proceed through a single quark fragmentation identical to the fragmentation observed in e+e- annihilation. In the forward center of mass the photon absorbs the pomeron and converts into a quark, anti-quark pair moving in opposite directions. Figure 1d illustrates this process for uu production leading to a fast π^+.

$$(u) \rightarrow \pi^{+} \tag{1.8}$$

$$n_h = 1$$

$$n_{pl} = 0$$

$$X_{\parallel} dN/dX_{\parallel} \propto (1-X_{\parallel})$$

$\pi^{\mp}$ and $K^{\mp}$ would be produced with the same $X_{\parallel}$ dependence at large $X_{\parallel}$. The single quark fragmentation would thus give the same $X_{\parallel}$ dependence as the di-quark fragmentation, so the two processes would be indistinguishable.

Scaling

The concept of scaling states that the inclusive cross section for hadrons should depend only on the scaling variable (Feynman $X=X_{\parallel}$)[4,17]. The $X_{\parallel}$ distributions should, therefore, be independent of center of mass energy. For large center of mass energies such that parton mass effects are negligible, scaling in the parton model is exact. In particular, for the process ($e^+e^- \rightarrow hX$), the inclusive cross section has the following form.

$$\frac{d\sigma}{dX_{\parallel}} \propto \frac{1}{q^2} \cdot f(X_{\parallel}) \tag{1.9}$$

$q \equiv$ 4-momentum of the virtual photon

For the diffractive photoproduction process being investigated, the inclusive cross section is assumed to be of the following general form.

$$\frac{d\sigma}{dX_{\parallel}} \propto f(M_X) \cdot g(X_{\parallel}) \qquad \text{(forward center of mass)} \qquad (1.10)$$

The inclusive distributions can then be plotted for different mass bins to determine to what extent the inclusive cross section can be factorized, and whether or not the function $g(X_{\parallel})$ is uniquely determined. The Feynman X distributions can also be studied in the initial center of mass,

$$\frac{d\sigma}{dX_{\parallel}} \propto f(s) \cdot g(X_{\parallel}) \qquad \text{(initial center of mass)} \qquad (1.11)$$

plotted for different photon energy bins.

The concept of scaling, based on the parton model, requires that the partons interact as pointlike and structureless constituents of the composite hadron. In QCD, this assumption is valid only for large momentum transfer processes subject to higher order corrections. It is expected, therefore, that scaling violations should occur. These scaling violations reflect the energy dependence of the strong coupling constant, which gives an energy dependence to the gluon radiation processes that soften the pointlike interactions. To provide a quantitative measure of the deviation of the photoproduction data from scaling, the inclusive cross section is written in the following form.

$$\frac{d\sigma}{dX_{\parallel}} \propto f(ECM) \cdot h(ECM, X_{\parallel}) \qquad (1.12)$$

$ECM \equiv M_X$ (forward center of mass)

s (initial center of mass)

The function f(ECM) is determined in the large $X_{\parallel}$ region where scaling is observed. Dividing out the explicit center of mass energy dependence, the scaling violation can then be measured in terms of the ratio $h(ECM_1,X_{\parallel})/h(ECM_0,X_{\parallel})$ as discussed in more detail in chapter 9. The dependence of this ratio on the center of mass energy can thus be studied for different regions in $X_{\parallel}$. In particular, other experiments have observed that at $X_{\parallel}$ = 0 the inclusive cross section increases as the center of mass energy increases.

To summarize the physics objectives of this thesis, high energy diffractive photoproduction of hadronic states provides a unique probe of the dynamics governing the strong interactions. The qualitative features of this process can be described in terms of a model based on QCD. These features include such things as jet structure in the center of mass, leading particle fragmentation distributions, and scaling violations. The non-perturbative, low momentum transfer domain of this process does not, however, permit quantitative comparisons with theory, except for leading particle distributions near $X_{\parallel}$=1. The characteristics of the data will be described in terms of what theoretical information is available and in terms of experimental results from other types of experiments in order to determine the validity of the present theoretical picture of high energy diffractive photoproduction.

CHAPTER 2

TAGGED PHOTON BEAM

Description of Beam Characteristics

The data for the experiment described in this thesis was taken at Fermilab's tagged photon laboratory. Fermilab is a 400 GeV accelerator located near Batavia, Illinois. Figure 2 contains a schematic description of the accelerator's experimental beam lines. The primary proton beam is accelerated to its final energy in the main ring. It is then extracted and split horizontally in the switchyard area to form three components which are separated to form the three experimental beam lines leading to the meson, neutrino, and proton experimental areas. Each individual beam is then split further to support multiple experiments in each area. In particular, in the proton area, the beam is split horizontally to form three beam lines; P west, P center, and P east. The tagged photon laboratory is located at the end of the P east beam line.

The P east beam line contains a transport system capable of producing an electron beam of known energy. The 400 GeV protons entering the beam line are targeted on a 30 cm long beryllium target contained in the proton east target box. Charged particles are then bent by a magnet into a dump, allowing neutral particles only to exit the target box. This neutral beam consists primarily of neutrons, kaons, and photons produced in the target. Twelve

meters downstream of the target, the neutral beam passes through a lead converter .32 cm. thick (1/2 radiation length), which converts the photons to electron - positron pairs, and a small fraction (approximately 1.5 %) of the neutrons and neutral kaons to charged pions. The pion contamination in the beam is reduced to a negligible level by the electron transport system, which selects electrons of the desired energy. This transport system consists of a two stage beam line. Each stage consists of a set of quadrupole magnets to focus the charged beam and a set of dipole magnets to bend the beam, thus allowing momentum selection. In addition there are horizontal and vertical collimators which define the momentum interval of the electron beam and remove the dispersed pion contamination. The electron transport system, therefore, delivers an electron beam well defined in momentum, and relatively free of any hadronic contamination. A detailed schematic of the primary proton beam targeting area and the electron transport system is provided in figures 3 and 4. Table 1 identifies the function of the principal components of the beam line referenced in figure 3.

The electron beam thus produced can be tuned to any desired energy within the range 10 - 300 GeV. The data for this experiment was taken at an electron beam energy of 170 GeV. The momentum resolution of the electron beam has a typical sigma of $\mp 2.5\%$. The choice of electron beam energy was determined by a trade off between energy and intensity. The intensity, or electron yield per incident proton, decreases as a function of electron beam energy and is shown in figure 5.

After the electron beam is tuned to the desired energy, it passes through a Cu radiator .2 radiation lengths long. In the presence of the coulomb field of the massive nuclei in the radiator, some of the electrons bremsstrahl producing photons along the beam direction. The beam then passes through a set of dipole magnets which deflect the electrons, leaving a neutral photon beam which enters the tagged photon spectrometer. The deflected electrons enter the tagging system which consists of a hodoscope array to measure the position of the electrons and a set of lead glass total absorption counters to measure the energy. From this information a measurement is made of the photon energy, which is the difference between the electron beam energy and the energy of the recoiling electron. Non-interacting electrons are deflected into a dump. The electron beam is thus converted into a spectrum of high energy photons with known energy. The electron beam energy determines the high energy cut-off of the spectrum. The bremsstrahlung spectrum, which falls as $(1/E\gamma)$, has a low energy cut-off determined by the tagging system described below.

Tagging System

Figure 6 shows the basic components of the tagging system. After passing through the radiator, the recoiling electrons are deflected through a vacuum vessel of rectangular cross section into the tagging system counters. The dimensions of the total absorption shower counters are given in table 2. L1 and L2 are made of 20 layers of lead and lucite to avoid radiation damage incurred by

the high rate in these counters. L1 was used as a veto counter to exclude the high rate from low energy photons. The other counters (L3 - L13) are made of lead glass and were cleaned of radiation induced discoloration once a week. The blocks were cleaned by radiating them with a high intensity light source for a period of about 24 hours. L13 was orientied perpendicular to the beam, (note figure 6), and, therefore, due to its shallow depth, included a 1/2 inch strip of lead placed in front of it to initiate the shower. All of the shower counters are optically connected to RCA 6342 A photomultiplier tubes whose anode signals are digitized by 10 bit Le Croy 2249 ADCs.

The scintillation counter hodoscope is composed of thirteen elements (H1 - H13), a pair of which overlap at the center of each of the shower counters (except L13). Thus, an electron entering the central region of a shower counter is defined as a coincidence between two adjacent hodoscope elements. For this restrictive sample of events all of the light generated in a particular lead glass block by the recoiling electron is confined to that single channel. Events requiring such a double hodoscope coincidence were used to calibrate the tagging system channels. An acceptable tagged photon event required only a single hodoscope in coincidence with a shower counter channel $((H_i+H_{i+1})\cdot L_i)$. The hodoscope can, therefore, be used to exclude events containing two electrons simultaneously entering the tagging system, and other contamination where more than two adjacent hodoscope elements fire. In addition, there is a set of anti counters (A1 - A10) to identify electrons

and positrons produced by electron - electron scattering and trident production. The anti counters also identify electromagnetic pairs produced in the radiator by the photons.

There is a set of muon counters (M1 - M8) which are located between the shielding blocks just upstream of the experimental target. These scintillation counters were used to identify some of the muons entering the experimental area and to define muon calibration events in conjunction with the muon counters at the downstream end of the spectrometer. Finally, there are two dump counters (D1 and D2) located between the photon beam and the first shower counter (L1), which identify electrons entering that area.

Sufficient information is available from the tagging system to determine a valid tag of known energy. Thus the tagging system serves three functions: it determines the energy of the interacting photon for each event, removes contamination from the data sample, and provides a component of the basic experimental trigger.

CHAPTER 3

TAGGED PHOTON SPECTROMETER

Overview

A collaboration of physicists from the University of California at Santa Barbara, Carleton University, the University of Colorado, Fermilab, the University of Oklahoma, and the University of Toronto participated in the design and construction of the tagged photon spectrometer facility at Fermilab. The purpose of the facility was to provide the capability for a wide range of experiments requiring knowledge of multi - particle exclusive final states of interactions initiated by a photon of known energy. To achieve this purpose the spectrometer was designed to provide the information necessary to fully reconstruct all charged and neutral particles present within the acceptance of the spectrometer. A wide variety of physics objectives could then be reached by providing an appropriate experimental trigger. Figure 7 shows the basic layout of the spectrometer. The spectrometer is divided into a recoil spectrometer and a forward (downstream) spectrometer. Table 3 contains the basic parameters which define the spectrometer. A description of each major component of the spectrometer is provided in the remainder of this chapter.

Recoil Spectrometer

The recoil system is designed to measure the 4-vectors of particles recoiling off the hydrogen in the target. Identifying recoil protons and calculating their energy and momentum components then permits a determination of the missing mass present in the forward spectrometer, as described in chapter 5. In this manner the diffractive missing mass triggers are generated. The recoil system is composed of a set of 3 cylindrical proportional wire chambers and a calorimeter dE/dx detector. The proportional wire chambers provide a measurement of the track parameters (vertex, θ, ϕ), and the calorimeter provides a measurement of the energy and mass of each track within the recoil calorimeter acceptance (as discussed in chapter 7).

Recoil Calorimeter

The calorimeter is composed of 15 sectors, each covering an azimuthal angle of 22.1 degrees (see figure 8). This constitutes a total coverage of about 90% of the full 360 degrees leaving a dead region at the bottom (24.5 degrees) used for structural supports, and an upper right and left support (about 1 degree) to strengthen the liquid scintillator cavity. Each of the 15 sectors is then divided into four layers to provide as many as four dE/dx samples, depending upon the depth of penetration of the track. Altogether there are 60 compartments (channels), each containing multiple phototubes to collect the light produced by recoiling charged particles. Table 4 provides a description of the channels contained

in each of the four layers. The signals from the phototubes of each channel are summed to form a single input to a Le Croy 2280 system (anode signals), and a fast ADC system (dynode signals) used as input to the recoil trigger processor.

An additional Z measurement is made to provide a link between sectors of the calorimeter and PWC cathode tracks in the trigger processor. It also helps resolve ambiguities due to the fact that there are only 2 orthogonal views in the PWCs. This measurement is made in the A layer by using one phototube on each end of the scintillator to provide end to end timing (EET). The Z position of the track in the A layer measured by the EET method can, therefore, be compared to the Z measurement projected to the A layer from the cathode track and a correlation made between cathode tracks and calorimeter sectors. In addition to the EET, a time of flight (TOF) measurement is made to resolve ambiguities in particle identification for tracks that stop in the A layer.

When a particle penetrates the A layer it generates light which is collected at both ends of the plastic scintillator by phototubes. The phototube anode signals are then routed to the counting room where they are digitized. To provide the time of flight and end to end timing information the signals are first processed by constant fraction discriminators (CFD). The discriminator splits the input signal, inverts and delays half of the signal by a set delay time, then recombines the two parts of the signal. The resulting signal has the following shape.

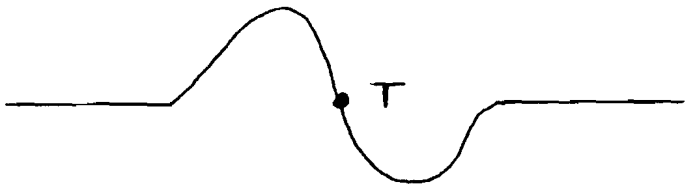

The point T is almost independent of the amplitude of the original signal, which reduces the effects of amplitude variations on the relative timing of the start and stop signals. The time T can then be used as a start or stop signal for a TDC. For the end to end timing measurement, the CFD processed signals from the downstream end of the A - layer counters provides the start signals, and the CFD processed signals from the upstream end of the A - layer provides the stop signals. The difference between these times as measured by the TDC provides a measurement of the location of the particle within the A-layer. This information can then be correlated with the location of the particle within the A-layer as determined by the tracking through the PWC cathodes. Sectors in the calorimeter can then be associated with particular PWC cathode tracks.

The start signal for the time of flight measurement is provided by a tag indicating the presence of a photon in the target. The stop signal is determined by averaging the upstream end time and the downstream end time. An octal meantimer inputs the CFD processed signal from the downstream end of the A-layer (T1) and the CFD processed signal from the upstream end of the A-layer (T2) and outputs the average (T1+T2)/2. This signal then becomes the stop signal for the TOF TDC. The time measured by the TDC is proportional to the velocity of the particle, thus providing

additional information to assist in distinguishing between pions and protons, whose identification would otherwise be impossible for particles that stop in the A-layer.

Proportional Wire Chambers (PWC)

The recoil spectrometer contains a set of cylindrical proportional wire chambers to provide tracking information for recoiling charged particles. There are three chambers in the recoil system whose specifications are listed below.

CHAMBER	NUMBER OF CATHODE WIRES	NUMBER OF ANODE WIRES	RADIUS
INNER	1312	268	18 cm
MIDDLE	1312	536	36 cm
OUTER	1312	804	54 cm

Each chamber is composed of three layers, an inner cathode made of aluminized mylar, the anode with wires stretched longitudinally along a frame parallel to the beam axis, and the outer cathode with flattened copper wires glued along the circumference of a cylindrical frame. Figure 9 contains a cutaway view of one of the PWC chambers. The anode is held at approximately 2500 volts, sandwiched between the inner and outer cathodes with a spacing of 6 mm. The cathodes are held at ground.

The anode wires are stretched horizontally along the

surface of a cylindrical frame consisting of two endpieces and three equal spaced inner support rings. These rings were necessary to provide electrostatic stability for the anode wires. The wires were spaced 4 mm. apart and combined into groups of 2 for the inner chamber, 4 for the middle chamber, and 6 for the outer chamber resulting in a channel spacing that is constant in the azimuthal angle phi. Signals are taken from the upstream end of the anode wires and passed to the readout electronics, thereby providing a measurement of the azimuthal angle of the track. The readout electronics for the anodes consists of a set of anode boards. Each board processes sixteen channels. A shift register containing one bit per channel is set by the input signals after each signal passes through a preamp and discriminator. The signals must be in time with the TAGH trigger (described in chapter 5).These shift registers are then read out by a clock, one bit per clock pulse, and written to tape.

The cathode wires of the outer cathode are glued to a mylar cylinder, spaced 1.5 mm along the active length of the chamber. There are locally inefficient regions (efficiency $\approx$ 60%) about 2 cm. wide at the anode support rings. Two consecutive wires are connected to form a single channel, thus giving a total of 656 channels per chamber. These channels are read out at the bottom of each chamber, overlapping the dead region of the calorimeter. The cathode track projection has no azimuthal orientation but provides a measurement of recoil angle relative to the beam line.

The readout electronics for the cathode channels is

identical to the anode channels in the initial stage. A cathode board contains 16 inputs which set a shift register. The readout of the shift register is, however, very different. The cathode data must be available sooner to be analyzed by the trigger processor. The center finder, started by a low level trigger, reads out all boards containing data and calculates the centroid and width of each cluster (for each track the induced pulse on the cathode is typically 6 channels wide). The values of these quantities are then sent to the trigger processor. The readout processtakes about 150ns/cluster with all three chambers being processed simultaneously. Figure 10 contains a side view of one section of a chamber.

(A,B)	CHANNEL NUMBERS DEFINING LIMITS OF A CLUSTER
(A+B)/2	CENTROID
B-A	WIDTH

The region between the cathodes is filled with a gas mixture composed of 15% isobutane, 2.5% methylal, 82.5% argon. The methylal is used to quench the avalanche.

Analyzing Magnets

There are two analyzing magnets in the spectrometer whose function is to bend the charged particles' trajectories sufficiently to provide a momentum measurement using the drift chamber tracking information with the desired resolution. The upstream magnet (M1), containing a single coil, provides an average

integrated field of about 5 kg-m. The downstream magnet (M2), containing two coils, can provide an average integrated field of about 14 kg-m, limited in the experiment by acceptance inefficiencies for large angle tracks in the Cerenkov counters. M2 was run with an average integrated field of 5 kg-m. The two magnet system allows reconstruction of wide angle tracks using only the two most upstream drift chambers (D1 and D2 shown in figure 7), even though the tracks are outside of the aperture of M2. The integrated fields mentioned above were obtained with a magnet current of 1800 amps for M1 and 900 amps for M2. A field map of the point field amps was obtained using a computer controlled magnet mapping machine which measured the three components of the field at spatial points. Points were measured for M1 at magnet currents 1800 and 2500 amps, and for M2 at magnet currents 900, 1800, and 2500 amps. The measured field increased linearly with the current, demonstrating that the magnets were not saturated.

Cerenkov Counters

Particle identification in the forward spectrometer is provided by two segmented Cerenkov counters, an upstream counter (C1) and a downstream counter (C2). The basic characteristics of the counters are described in table 5. C1 (figure 11) is composed of two distinct sections. The downstream main body is made of 1/4 inch sheet aluminum. It contains an access opening sealed with an aluminum door and 28 circular openings along the transverse perimeter, 20 of which are currently being used as Winston cone

portals. The main body is reinforced with aluminum I-beams to increase its rigidity and to serve as a location to clamp the Winston cone mounting assemblies. The aluminum main body is bolted to the fiberglass upstream section which is inserted into the downstream magnet (M2). This section is made of 3/8 inch fiberglass to eliminate eddy currents produced by sudden changes in the magnetic field which could cause a metallic structure to collapse. Each end of the counter is sealed with a flexible window to provide a gas tight volume. The window material is a laminate, black vinyl on the inside, aluminum foil covered by mylar on the outside. The material is about 20 mils thick.

C2 (figure 12) is also composed of two sections. The division was made solely to make the counter more readily transportable. Each section is made of 1/4 inch sheet aluminum reinforced with aluminum I-beams. The counter contains an access door and 32 circular openings along the transverse perimeter, 20 of which are presently used as Winston cone portals[18]. Note that the surface containing these portals faces the opposite direction than in C1. This is due to the different optics in C1 and C2, described later. The ends of C2 are sealed with the same window material as C1. Both counters are mounted on a set of four wheels. These wheels allow the counters to be rolled transverse to the beam line along a set of rails. The wheel support structure is also used for leveling and to provide some limited motion along the beam line.

Figure 13 contains a diagram of the optics for C1 and C2. Each counter contains a primary focusing mirror plane and a set of

Winston cones, one for each cell, to collect the light and transmit it to the phototube. C1 contains an additional non-focusing secondary mirror plane. This allows the light to be collected from the downstream end of the counter. It is not possible to collect the light in the same manner as in C2 due to the prescence of the magnet (M2). It is also important to place the phototubes as far away from the magnetic fields as possible.

The primary focusing mirror plane for C1 and C2 is segmented into 20 cells. This plane has quadrant symmetry, each quadrant containing 5 cells. (The outer two cells in each quadrant are composed of two mirrors since a single mirror would be too cumbersome to support properly.) The cell sizes of a quadrant are contained in table 6. (see figure 14 for location of mirrors in mirror plane) The mirrors were cut from sheet plexiglass and slump molded in a large spherical polished aluminum mold. They were then aluminized at the Berkeley laboratory. The mirrors have a focal length of 6 1/2 feet. There is a 3 cm. gap between the upper and lower halves of the mirror plane to avoid collecting light from the large flux of electromagnetic pairs produced in the midplane. This reduces the background counting rate which could leak into the ADC gate used to read out the triggered event.

Each mirror is held in place with 7 strings (18 lb. test dacron line in C1 and 35 lb. test dacron line in C2) whose orientations are illustrated in figure 14. The string support system provides a method for positioning the mirrors without placing any high mass structures in the active beam region of the counters.

The three strings fastened to the upstream face of the mirror are adjustable, permitting alignment of the mirror by vertical and horizontal rotations about an axis defined by the downstream strings.

The Winston cones were formed, at the Argonne National Laboratory, by spinning epoxy on a polished steel mandrel. The inside surface was then aluminized. The curvature of the reflecting surface is defined as a rotation of an off axis ellipse. It was designed to focus light into the phototube with at most a single reflection off the Winston cone surface[18]. The large opening of the Winston cone measures 15 inches, the small opening 5 inches. The light is then transmitted through an aluminized lucite collar into a 5 inch RCA 8854 phototube. The Winston cone - phototube assembly is shown in figure 15. Magnetic shielding is provided by a cast steel outercasing and, surrounding the phototube, a netic and a conetic magnetic shield. The phototube anode signals are digitized by a Le Croy 2249 ADC system and written to tape. The dynode signals are used for a variety of triggers which are discussed in chapter 5.

C1 contains dry nitrogen gas. C2 contains a mixture of nitrogen and helium. The mixture is maintained by a gas cart which regulates the flow of the helium and nitrogen, and provides the ability to remove traces of oxygen and water vapor from the gas mixture. The gas composition is monitored with a gas chromatograph. There is also a nitrogen purge line to the Winston cone - phototube assemblies of both C1 and C2 which maintains a circu-

lation to remove water vapor and helium from the phototube environment. Helium will eventually contaminate a phototube and produce after pulsing[19].

Drift Chambers

A set of four drift chamber modules is used to track and determine the momentum of charged particles in the forward detector system. Labeled D1 - D4, a schematic of the active planes in the drift chamber system is shown in figure 16. There are a total of two measurement points in D1, each point consisting of four views (U,V,X,X'), and seven measurement points in D2-D4, each point consisting of three views (U,X,V). The X and X' wires are stretched vertically, while the U and V wires are rotated $\mp$ 20.5 degrees relative to the X, X' wires. This information helps to resolve some of the left - right ambiguities resulting from the fact that it is impossible to discern in any given view on which side of the sense wire the track had penetrated the cell. There are a total of 29 sense planes, 9 X views, 9 U views, 9 V views, and 2 X' views. The basic cell structure of each chamber is shown in figure 17.

D1 is the smallest chamber located inside the pole piece of the upstream analyzing magnet (M1). Each of the two assemblies within the chamber is composed of alternating sense wire planes and field wire high voltage planes. A sense wire plane contains alternating sense wires (25 micron gold plated tungsten) and field wires (127 micron hard copper). The sense wires (anode) are held at

ground while the field wires are held at negative high voltage (listed in table 7). On either side of a sense wire plane there is a high voltage field wire plane containing only field wires (spaced about 3 mm) which are stretched horizontally across a G-10 frame. The wires in the high voltage plane are held at a negative high voltage slightly different than the voltage of the field wires in the sense wire plane. Table 7 contains the relevant parameters for D1. The field wires determine the shape of the field across a cell, which defines the appropriate drift velocity characteristics. Thus, the negative voltages were chosen to give nearly cylindrical equipotential patterns around each sense wire. The sizes of the U and V cells are smaller than the X cells by a factor of cosine 20.5 degrees.

D2 and D3 are identical in design, consisting of three assemblies each containing three views (U,X,V). (see figure 16). All of the drift planes for these chambers are enclosed in a single gas tight container. In contrast to D1, the high voltage field planes are composed of field wires stretched vertically. The field wire negative voltages and other relevant parameters are listed in table 8. The D2 and D3 assemblies are enclosed in a gas tight aluminum container with a flexible window (2 mil Aclar and 5 mil Mylar) that covers the active area. The chambers are mounted on wheels to allow transverse movement, relative to the beam line, constrained by a set of rails. A ball socket was placed in the floor to allow exact repositioning of the drift chamber.

D4 contains a single assembly with three views (U,X,V).

The analog of the high voltage field planes in the other chambers are the ground planes in D4, composed of an aluminum sheet bonded to a hexcell backing to provide rigidity. The field planes and field wires in the sense planes are thus held at ground and the sense wires (in this case anodes) are held at positive high voltage. (The field wires in the sense planes may be held at a small positive voltage to adjust the field shape in the cells.) The basic specifications are listed in table 9. The complete chamber, including its gas tight outer aluminum shell, is hung from the ceiling on a trolley which allows transverse motion along a rail, thus providing access for repairs.

All chambers are filled with a gas mixture consisting of 50% argon and 50% ethane at a pressure of about 0.1 inches of water. Signals produced by charged particles proceed through a set of signal cards each of which processes 6 cells. A signal card consists of an amplifier and a discriminator which results in an ECL signal which is carried to the counting room on a twisted pair cable. This signal then provides a start signal to a channel of a Le Croy 2770 TDC. (The stop signal is provided by a low level trigger.) The times are thus digitized and written to tape.

SLIC (Segmented Liquid Scintillator Shower Counter)

The SLIC is a multilayered and segmented calorimeter used to detect electromagnetic showers produced by photons from pi-zeros, electrons, positrons, and photons. It is also used in conjunction with the hadrometer, which follows it, to detect

hadronic showers produced by neutral hadrons. Measurements are made of the energy, position, and angle of the electromagnetic particles entering the SLIC. These quantities allow us to reconstruct neutral tracks in the forward spectrometer.

There is a total of 60 lead-liquid scintillator layers that comprise the full depth of the SLIC, a total of 20 radiation lengths (2 nuclear interaction lengths for hadronic showers). Each layer contains a sheet of lead 1/8 inches thick laminated between 2 sheets of aluminum .04 inches thick, followed by a layer of liquid scintillator 1/2 inch thick. The liquid scintillator layer is segmented with Teflon coated light tight channels to obtain the X and Y coordinates of a track and remove ambiguities. The Teflon coating gives the channels the property of total internal reflection. There are three views (Y,U,V). A Y view contains strips with a horizontal orientation that directly measures Y. Each Y strip reaches to the center of the counter. The U and V views contain strips that are oriented $\mp$20.5 degrees relative to avertical line. Every third layer, progressing through the detector along the beam line contains the same view. The illustration in figure 18 shows the basic structure of the detector. Strips in the outer regions of the detector far from the beam line are coupled in pairs, creating double width channels which are viewed by a single phototube. The strips are coupled by the wave shifter bars described below. The position resolution is thus better in the central region of the detector where the tracks are most dense.

The 20 layers that comprise a single view are coupled with

a wave shifter bar located along the periphery of the detector. The bars are oriented longitudinally along the top and sides of the SLIC, one bar for each segment (channel) of each view. The wave shifter bar acts as a light guide and shifts the wavelength of the scintillation light to green. (The purpose of the waveshifter is to reduce reabsorbtion of the scintillation light by regenerating the light isotropically in the waveshifter bar.) Each wave bar is optically coupled to a phototube. The phototube is mated to the wave bar at a 45 degree angle to maximize the transmission efficiency. 2 inch RCA 4900s are used for the single width channels and 3 inch RCA 4902s are used for the double width channels.

The total number of channels is 334, 156 single width channels and 178 double width channels.

Y VIEW - 116 CHANNELS TOTAL
80 SINGLE WIDTH CHANNELS
36 DOUBLE WIDTH CHANNELS

U VIEW - 109 CHANNELS TOTAL
38 SINGLE WIDTH CHANNELS
71 DOUBLE WIDTH CHANNELS

V VIEW - 109 CHANNELS TOTAL
38 SINGLE WIDTH CHANNELS
71 DOUBLE WIDTH CHANNELS

The single width channels are 1 1/4 inches wide, while the double width channels are 2 1/2 inches wide. However, the distribution of the pulse heights from neighboring channels allows the position to be determined much more accurately than a channel width.

The phototube anode signals are digitized by a Le Croy 2285 ADC system and written to tape. The phototube dynode signals are summed to form the SLIC component of the hadronic trigger, described in chapter 5.

Outriggers (Upstream SLIC)

The outriggers constitute an extension of the effective active area of the SLIC. They are located upstream of the second analyzing magnet (M2) before the aperture of the magnet limits the geometric acceptance of all downstream tracks. (Their angular acceptances are compiled in table 3.) Its function is to increase the range of neutral track reconstruction to include photons with higher transverse momentum.

The outrigger assembly includes an upper and lower module mounted on two posts which are bolted to the floor of the TPL. The two modules are separated by an empty area to exclude any overlap with the effective active area of the SLIC. Therefore, it does not substantially reduce the acceptance of charged particles determined by the aperture of M2. A diagram of the outrigger assembly is shown in figure 19. The active area of each module measures 18 3/4 inches by 57 1/2 inches, with a depth of 11 1/2 inches (a total of 18 radiation lengths).

Progressing along the beam line there are 16 lead-plastic scintillator layers in each module. Each layer of lead is 1/4 inches thick. The layers are segmented to obtain a position measurement, 8 Y layers and 8 X layers as shown below.

UPPER MODULE	15 Y STRIPS	1 1/4 INCHES WIDE
	23 X STRIPS	2 1/2 INCHES WIDE
LOWER MODULE	15 Y STRIPS	1 1/4 INCHES WIDE
	23 X STRIPS	2 1/2 INCHES WIDE

Each view is skewed 3 degrees relative to the beam line so that the scintillator channels are perpendicular to tracks entering the detector.

The 8 layers comprising a Y view channel are coupled and optically connected to a 2 inch RCA 4900 phototube. A somewhat more complex system of waveshifter bars and mirrors couple the 8 layers of X view channels to 2 inch RCA 4900 phototubes. This is due to space restrictions longitudinally. The details of the module characteristics are illustrated in figure 19. Due to the close proximity of M2, the phototubes must be protected from the magnetic field. This is accomplished by enclosing the phototubes in steel casings and an inner layer composed of 14 mil conetic shielding.

The phototube anode signals are routed to the counting room and then digitized with a system of Le Croy 2280 ADCs, then written to tape. The phototube dynode signals are summed to form a com-

ponent of the hadronic trigger, and are also used to form a special high perpendicular momentum trigger.

Hadrometer

Hadronic showers are usually initiated in the SLIC and completed in the hadrometer, providing sufficient information to reconstruct the energy and angle of hadronic tracks. The hadrometer provides the only capability for observing any neutral hadrons and, therefore, serves an important function in total event reconstruction.

The hadrometer consists of multiple layers of steel and acrylic scintillator. There are 36 layers in the detector, each layer consisting of 1 inch steel and 3/8 inch scintillator. The hadrometer is separated into an upstream and a downstream module, each containing 18 layers, between which there is a 2 inch gap. The basic design is shown in figure 20. Each layer is segmented into alternating X and Y strips to obtain a position measurement with a resolution of about 2 inches. The total segmentation into counter channels is shown below.

MODULE 1	33 X STRIPS	5.7 INCHES WIDE
	38 Y STRIPS	5.7 INCHES WIDE
MODULE 2	33 X STRIPS	5.7 INCHES WIDE
	38 Y STRIPS	5.7 INCHES WIDE

The Y strips reach to the center of the detector, 19 channels on the east side and 19 channels on the west side for each module.

Each channel, composed of 9 layers in depth along the beam line, consists of acrylic scintillator segments wrapped in aluminum foil and a protective layer of plastic film. The 9 segments comprising a channel are optically connected by a lucite light guide to a 5 inch ~~RCA 6342A~~ EMI 9791 KB phototube. Each of these channels was constructed in an external environment, then inserted into the framework of steel sheets that provide the structural stability of the detector. The steel sheets also provided the material needed to obtain a sufficient interaction length to contain the hadronic showers.

The phototube anode signals are digitized by a Le Croy ~~2280~~ 2285 ADC system and written to tape. The dynode signals are discriminated and summed to form a principal component of the hadronic trigger.

C - Counter

The C-counter is a small calorimeter centered on the beam line directly upstream of the SLIC. Its function is to measure the energy of non-interacting gammas by producing electromagnetic showers. The determination of the energy is critical for monitoring the photon spectrum, and is also used to calibrate the tagging system lead glass blocks.

The active area of the C-counter is determined by the requirements that the photon generated showers be contained within

the counter to avoid contamination of the SLIC. The central section of the C-counter measures 4 1/2 inches high and 2 1/2 inches wide. The two side counters on either side of the central section measure 3 1/2 inches high and 2 5/8 inches wide. The counter contains 60 layers of alternating 1/16 inch tungsten and 1/16 inch lucite planes. Two groups of 30 layers each are optically coupled to a pair of phototubes, one for each group. This allows a separate measurement of the developing and terminating shower. The total depth constitutes 20 radiation lengths, which is sufficient to contain showers initiated by photons within the tagged photon spectrum.

The anode signal is digitized by a Le Croy 2249 ADC and written to tape. The C-counter signals are also used in the gamma trigger and as a veto in the hadronic trigger.

CHAPTER 4

CALIBRATION PROCEDURES

Overview

This chapter contains a description of the procedures used to maintain the calibration of the detectors. The data analysis described in chapter 6 requires only knowledge of the 4-vector of the recoil proton and the 4-vectors of the charged tracks in the forward spectrometer. This chapter, therefore, contains only a description of the calibration of the recoil spectrometer, the drift chamber system, and the Cerenkov counters.

RECOIL SPECTROMETER

Recoil Calorimeter

The primary task of the calibration procedure is to convert raw ADC counts to a measurement of the energy deposited in a particular channel of the calorimeter. This requires knowledge of the overall gain constant and the attenuation coefficients for each channel. To obtain these constants, data is fit to an equation of the form:

$$F(X) = EDEP \cdot A_1 \cdot (1 + A_2 \cdot EXP(-A_3 X)) \qquad (4.1)$$

X - SPATIAL COORDINATE (HORIZONTAL DISTANCE FROM THE TRACK TO THE PHOTOTUBE

EDEP - ENERGY DEPOSITED IN THE CHANNEL

A_1 - GAIN

A_2, A_3 ATTENUATION COEFFICIENTS

The constants (A_1, A_2, A_3) are determined by minimizing the chi-square with respect to each of these three variables. The chi-square has the following form:

$$\chi^2 = \sum\left([F(X)-(ADC-PED)]/\Delta(ADC-PED)\right) \qquad (4.2)$$

ADC - ADC COUNTS

PED - ADC PEDESTAL COUNTS

In addition to the normal calorimeter calibration constants the A layer of the recoil calorimeter is connected to TDCs to provide time of flight and end to end timing information. For end to end timing information, a fit is made to a straight line of the form:

$$Z = A + B \cdot TDC(EET) \qquad (EET \equiv \text{end to end timing}) \quad (4.3)$$

A measurement of Z is provided by the PWC cathodes, and the fit then determines the parameters A and B. The time of flight constants are also found by fitting to a straight line of similar form. The overall gains for all of the recoil system phototubes were made as uniform as possible so that the same constants could

be used for each sector in the trigger processor to calculate the missing mass for the diffractive trigger. The end to end timing resolution has a sigma of 10 cm. and the time of flight resolution has a sigma of 0.9 nanoseconds.

Drift Chamber Calibration

The objective of the drift chamber calibration procedure is to determine the relationship between the raw TDC count for a drift cell and the distance between the point of penetration of the cell by a charged track and the sense wire which defines the center of the cell. There are three distinct steps which comprise this procedure. The first step determines the relative timing of drift cells which constitute a single plane, and measures the gain for each cell which converts the TDC counts to time (nanoseconds). This is achieved with special data generated by the drift chamber pulser system described below. The second step of the procedure defines the absolute time intercept and measures the drift velocity. This information is obtained from special muon data and photoproduction data. The final step determines the relative spatial orientation of the drift chamber planes, matched to the overall spectrometer coordinate system. The data used for this alignment consists of muons distributed across the active area of the chambers with the analyzing magnets turned off. The last two steps of the calibration procedure are not independent but highly interconnected.

Step 1 (Relative Timing And Gains)

The relationship between TDC counts and time is of the following form:

$$TIME_i = TZERO_i + GAIN_i \cdot (TDC_i) \qquad (4.4)$$

(THE SUBSCRIPT DESIGNATES THE DRIFT CELL)

To measure the gains, data is generated at fixed time intervals (ΔTIME) such that:

$$GAIN_i = \Delta TIME_i / \Delta TDC_i \qquad \text{NANOSECONDS/COUNT} \qquad (4.5)$$

To measure the relative TZEROS ($RTZERO_i$), data is generated at a fixed time and compared to different cells in the same plane.

$$RTZERO_i = CONSTANT - GAIN_i \cdot (TDC_i) \qquad (4.6)$$

The choice of a reference point is arbitrary at this point in the calibration procedure.

A drift chamber pulser system was designed and implemented to generate the data described above. Figure 21 illustrates the basic design of this system. The pulser system was controlled by the on-line monitor task. Four separate delay times were selected for each drift chamber assembly to cover the full range of the TDC. (The TDC has a full range of 256 nanoseconds. The times selected were 60, 120, 180, and 240 nanoseconds.) In the "splitter

pulsing" mode a signal was induced at the amplifier-discriminator cards which provided the start signals at the TDCs. The stop signal was delayed by the appropriate predetermined amount. Since the difference in delay times for each setting is known, the data is then fit to obtain the gains of each channel. Appropriate delay times were selected for each of the drift chamber assemblies. Two events were generated every beam spill allowing a complete cycle through the entire drift chamber system in about two hours. In the "high voltage pulsing" mode, a signal was induced in the high voltage planes of a drift chamber assembly. The signals thus induced on the sense wires produced the start signals at the TDCs. A single setting delayed pulse provided the stop signal. The delay time was set to produce a high TDC count near the top of the range where the pulsing response was most uniform. This single time pulsing was then used to determine the relative timing for each plane (relative TZEROS as described above).

Step 2 (Absolute TZEROS and Drift Velocity)

After the data has been corrected for relative timing differences (for a complete plane), a histogram is made of the raw time distribution for the plane. Figure 22 shows a typical histogram. The full range of the TDC is 255 counts. Each module has a gain and offset adjustment allowing modification of the centering and width of the time distribution. The points T1 - T5 are determined by an off-line semiautomated calibration program. The background under the time distribution is produced mostly by out of

time tracks not associated with the trigger and is dependent upon the beam intensity. The region T1-T2 indicates the magnitude of this background. T2 was chosen to be the initial estimate of the absolute TZERO due to its stability over long periods of time. It was determined by finding the intersection point between a line drawn to fit the rise between T2 and T3 and the plateau region between T1 and T2. The results of this calculation were averaged over several runs. An estimate of the drift velocity is made from the width of the time distribution and the physical cell size.

$$\text{VDRIFT} = (\text{CELL SIZE}) \; / \; [(T4+T5)/2-(T2+T3)/2] \qquad (4.7)$$

Corrections are then made by a more sophisticated technique described below.

To obtain the corrections to these initial estimates, tracks are reconstructed and fit to the data points. Histograms are then filled which contain the fitted minus measured coordinates. The mean is then calculated and plotted as a function of the position of the track in the drift cell. The plots in figure 23 represent such histograms. Plot A shows a plane with good constants. Plot B is uniformly shifted due to an overall alignment error relative to the other planes. Plot C has a bad absolute TZERO causing the data to be shifted in opposite directions on opposite sides of the sense wire. Plot D has a bad drift velocity causing the error to increase as a function of the distance from the sense wire. The errors represented by these plots may, of

course, all appear in one plane and must be disentangled by an iterative process. In addition to the corrections to the basic constants, non-linearities near the sense wire and field wires are parametrized and included as a correction to the calibration procedure.

Step 3 (Alignment)

A muon trigger requiring a coincidence between the upstream muon counters near the tagging system and the muon wall downstream of the hadrometer provided single muon events used to align the drift chambers. Plots of the type shown in figure 23 are produced for the muon data. These single track events are easily reconstructed and fit to a straight line through all four drift chambers. An iterative procedure is then carried out to obtain the correct calibration constants and relative alignment. The absolute alignment to the spectrometer coordinate system was taken from an on-site optical survey of the physical apparatus. Tolerances on the wire-laying process were carefully maintained within acceptable limits so that the external survey reflected the actual positions of the drift cells.

Once the calibration procedure was completed for appropriate intervals of data (approximately once per week) the resolution of each plane could be determined. After track reconstruction, histograms were made of the residuals summed over all momentum. Typical plots for the four chambers are shown in figure 24. The efficiency of each plane was also measured with single track muon

events. The results are shown in table 10. The resolutions contained in the table are for photoproduction events. The resolutions calculated for single track muon events are significantly better (approximately 30%).

Cerenkov Calibration (C1 - C2)

The calibration of the two gas Cerenkov counters used for particle identification involves several complementary procedures. These procedures include methods for determining the index of refraction of the gas mixtures, the location of the mirror boundaries, the alignment and focusing properties of the mirror-winston cone combinations, measurements of efficiencies, and threshold properties of each counter. The goal of the calibration procedure is to associate with each reconstructed charged track a prediction for each mass hypothesis of the mean number of photoelectrons that should be observed in each cell of the Cerenkov counters. The procedures described in this section provide the parameters needed to achieve this objective.

Gas System

The nominal values for the index of refraction of the gas in each counter was determined by separating each gas component with a gas chromatograph and measuring the relative abundance of each component.

COUNTER	COMPOSITION
C1	100% N_2
C2	20% N_2 80% He

The composition measurements made by the chromotograph were used during the experimental run to maintain a constant gas mixture in C2 and to monitor the prescence of any contaminants. The index of refraction of the gas in C2 depended strongly upon the percentage of nitrogen in the gas mixture. Due to limitations in the ability to measure this relative abundance with the gas chromatograph, this method for measuring the index of refraction of the gas in C2 was not accurate enough for the reconstruction program. Therefore, another procedure was employed. After charged tracks had been reconstructed through the drift chamber system, histograms were made of the number of photoelectrons observed in each counter as a function of the track momentum. The threshold for Cerenkov light radiation by pions could then be used to determine the index of refraction.

$$N = 1/\beta \tag{4.8}$$

N - INDEX OF REFRACTION

PTHRSH - THRESHOLD MOMENTUM

M_π - MASS OF PION

ETHRSH - $(PTHRSH^2 + M_\pi^2)^{1/2}$

β - PTHRSH/ETHRSH

The threshold curves for both C1 and C2 are shown in figure 25. The value of the threshold momentum was determined by a fit of the form:

$$\bar{N}(P) = A(B + (1 - B)\cdot(1 - (PTHRSH/P)^2)) \qquad (4.9)$$

$\bar{N}$ - AVERAGE NUMBER OF PHOTOELECTRONS

P - TRACK MOMENTUM

A,B,PTHRSH - FIT PARAMETERS

The results of the fit give the following values:

COUNTER	PTHRSH (GEV)	INDEX OF REFRACTION
C1	5.97 ∓.04	1.00027
C2	9.14 ∓.05	1.00012

Mirror Boundary Survey

The physical mirror boundaries which define a cell in a Cerenkov counter are necessary as input to the Cerenkov reconstruction program. Before the counters were sealed and filled with

gas, an optical survey was made to determine these quantities.From a fixed distance in front of the mirror plane, the horizontal and vertical angles of all four corners of each mirror were measured using an optical survey instrument. These measurements were made from two survey points separated by a known distance parallel to the mirror plane. (see figure 26). The distance from the center line to the x and y cordinate of the mirror corners was then calculated and written to a file for use in the reconstruction process.

The effective mirror boundaries which define the region of the mirror which reflects light into the phototube were determined from the data. Thus any mirror movement or other misalignment problems could be monitored and the constants updated as necessary. Initially these cell boundaries were determined using the 5 and 10 GeV electron calibration runs taken prior to the experimental run. These are the same runs used in the inital calibration of the SLIC using a rotating magnet to sweep the beam across the entire active area. After reconstructing the tracks using the drift chamber reconstruction program, the positions of the tracks at the Cerenkov mirror planes were plotted against the number of photoelectrons seen in the Cerenkov cells. Tracks hitting near a boundary injected light into adjacent mirrors. The plots were then used to determine the boundary positions based on the drift chamber tracking information. A similar procedure was used to maintain the calibration using photoproduction data collected during the experimental run.

Mirror And Winston Cone Alignment

The optical alignment of the mirror-Winston cone combinations was designed to maximize the efficiency for collecting light from charged particles in the spectrometer. Before sealing the Cerenkov counters, a model of the extended target was set up using incandenscent light sources. The sources were placed at the extreme points defined by the tracks of threshold (5 GeV) momentum pions (both positive and negative). The mirrors were then rotated until all the light from these sources entered the appropriate Winston cone. Figure 27 illustrates the optics of the alignment procedure. In addition to mirror alignment, the Winston cones were moved closer to or further from the mirror to achieve the proper focal length.

In addition to the need to optimize the light collection efficiencies, it was necessary to determine if the light collected actually reached the phototube. A laser was set up at the light source points described in figure 27 and scanned across each of the mirrors. An observation was then made at the phototube end of the Winston cone to see if the rays defined by the laser beam would enter the phototube or be reflected back out of the Winston cone. The number of reflections inside the Winston cone were also counted for different regions of each mirror. The central axis of the Winston cones was aligned along a laser beam generated at the center of the target and striking the center of the mirror.

The mirrors and Winston cones were aligned in an iterative process involving the two procedures described above, in an attempt

to optimize the final efficiencies measured with the data. C1, being closer to the target, was limited by the dispersion of the light in the focal plane due to the different track trajectories and the additional reflection to reverse the orientation of the Winston cones. C2, due to the larger angles involved, was limited by the ability of the Winston cone to collect large angle off-axis rays (maximum 15 - 20 degrees).

Efficiencies And Gains

The raw ADC counts must be converted into the number of photoelectrons seen by the phototube. A pulsed laser system was used to inject light into the phototubes. Figure 28 contains a diagram of the laser system. A pulse of light is generated from a nitrogen laser and injected into the light distribution system. A photodiode measures the intensity before and after the pulse passes through a transmission filter wheel containing various neutral density filters. The transmission coefficient of the filter can be changed by rotating the filter wheel. The light is then distributed via a fiber optics network to the phototubes contained in the various detectors. To determine the gains, the filter wheel was set to a low transmission filter so that the single photoelectron peak could be observed on the raw ADC plot (see figure 29). This provided the information needed to calculate the gains.

$$\text{GAIN} = \text{ADC} - \text{PED} \quad (\text{COUNTS/PE}) \tag{4.10}$$

ADC - ADC VALUE AT SINGLE PHOTOELECTRON PEAK

PED - ADC PEDESTAL

The laser system was also used to periodically check the linearity of the ADCs.

A comparison of the number of photoelectrons observed by the phototube and the prediction given by a particular mass hypothesis requires a calculation of the efficiency of each cell in the Cerenkov counters. This efficiency includes the effect of multiple reflections off the mirrors and Winston cones, absorption by contaminates (especially O_2) in the gas, misalignment of the mirrors or Winston cones, phototube efficiency, as well as other unknown effects. The initial calculation of these efficiencies was made using the electron scan made prior to the experimental run. The energy of the single electron events was known so that a prediction of the number of photoelectrons that should be generated in each phototube could be made and compared to the observations. (Sufficient statistics were available to accurately determine the mean of the poisson distributions.)

$$\bar{N} = \epsilon \cdot \bar{N}PRED \qquad (4.11)$$

$\bar{N}$ = OBSERVED NUMBER OF PHOTOELECTRONS

$\bar{N}PRED$ = PREDICTED NUMBER OF PHOTOELECTRONS

ϵ = EFFICIENCY

During the run, these efficiencies were calculated from the data using reconstructed muons and electrons identified by the muon detectors and calorimeters. Table 11 contains the results of the Cerenkov calibration.

CHAPTER 5

EXPERIMENTAL TRIGGERS

ON-LINE SOFTWARE AND HARDWARE

Triggers

A successful experiment requires a careful selection of those processes containing interesting physics from the much larger non-interesting background. In this experiment the quantity of data that the on-line software can write to tape is a small fraction of the total interactions in the spectrometer so that the selection must be made with the on-line triggers. Figure 30 depicts the evolution of the experimental triggers from the high level stage to the computer interrupt stage as defined below.

At the high level stage, the trigger signals are passed through prescalers so that only a specified fraction of the events from each trigger interrupt the computer. The low level triggers result from the coincidences of various discriminated fast analog signals obtained from the spectrometer. The low level triggers start the digitization process which is either stopped and cleared if the trigger is rejected at the high level stage or read out by the computer if the trigger is accepted at the high level stage and a computer interrupt generated. During the read out of an event a busy signal is raised which vetoes all triggers at the low level

stage, thus protecting the data stored in the CAMAC modules until the read out is complete.

The detailed logic diagrams describing the generation of these triggers can be found in appendix A. The following text contains a brief description of each of these trigger signals.

PHOTON - The photon trigger is produced by a large signal in the C-counter indicating the presence of a non-interacting photon. These events are used to calibrate the tagging system.

PAIR - To generate the pair trigger, a sum is made of the signals from the central pair strips in the SLIC in coincidence with a tag. The trigger is vetoed if there is sufficient hadronic energy in the hadrometer. This trigger is used to provide events containing electromagnetic pairs to be used in maintaining the SLIC calibration.

DIMUON - The dimuon trigger selects events containing two muons as determined by the muon counters. These events are used to study psi production.

TAG - A tag indicates the prescence of an electron in the tagging system whose energy is measured by the lead glass blocks. Various vetoes attempt to select a clean sample of single bremsstrahlung events as described in chapter 2.

TAG-H - The H component of TAGH determines that the event contained a hadronic interaction. This component is produced by a balanced sum (equation 5.5) of the analog signals from the hadrometer, SLIC, (excluding the pair plane), and the outriggers (UPSTREAM SLIC). This signal in coincidence with a TAG provides the basic experimental trigger, discussed in detail in the next section. (see figure 31).

CALIBRATION - Special events for calibration and monitoring purposes are generated by the computer to fire the laser and pulser systems. These triggers, generated outside of the beam pulse, are discussed in more detail later in this chapter.

Hadronic Trigger

The principal experimental trigger (TAGH, described briefly above) requires that the hadronic energy deposited in the downstream calorimeters exceed a certain fraction of the interacting photon's energy.

$$E_h > x \cdot E\gamma \qquad (5.1)$$

E_h - hadronic energy

$E\gamma$ - photon energy

The photon energy is determined from the initial electron beam energy and the energy deposited in the tagging system lead glass

blocks.

$$E\gamma = E_e - E_e' \qquad (5.2)$$

E_e - initial electron beam energy

E_e' - recoiling electron energy after bremsstrahlung

This leads to the following relationship;

$$E_h > x(E_e - E_e') \qquad (5.3)$$

which can be rewritten in the following form:

$$E_h + x(E_{LG}) > THRSH \qquad (5.4)$$

where, $E_{LG} = E_e'$

$THRSH = xE_e$

The logic diagram which decides whether or not this condition is satisfied is shown in figure 31. E_h represents a balanced sum of analog signals from the downstream calorimeters, excluding the pair strips in the SLIC. After balancing the SLIC and hadrometer sums, an additional compensation is made to emphasize the hadrometer, which is a better discriminator between hadronic and electromagnetic events.

$$E_h(\text{SLIC + HADR}) = E_h(\text{SLIC}) + 1.25E_h(\text{HADR}) \qquad (5.5)$$

E_{LG} represents an analog sum of the energy deposited in the 12 lead glass blocks in the tagging system. Deterioration in this signal due to yellowing of the lead glass blocks was compensated by appropriate adjustments of the high voltage to the lead glass block phototubes. These adjustments were made once per day and thereby assured that each channel made the proper contribution to E_{LG}. E_{LG} was also digitized by an ADC and written to tape on each event. (The contributions to E_h were also digitized and written to tape.) An attenuator (representing x in the equation) scales down the E_{LG} signal before it is summed with E_h. The resultant signal then becomes an input to a discriminator whose threshold represents THRSH. The discriminator will generate an output signal only if the input signal ($xE_{LG} + E_h$) is larger than THRSH.

All analog signals are attenuated or amplified such that a millivolt signal represents about 1/2 GeV energy deposit. Since THRSH is actually xEe, there is a relationship between the threshold setting and the attenuator value on E_{LG}. Table 12 defines this relationship. Scalers were set up to count the TAG and TAGH rate. The value of x and its corresponding threshold setting was varied and a plot made of the rate TAGH/TAG as a function of x. For small values of x, electromagnetic as well as hadronic interactions generate a TAGH, so the rate is very high. As x increases, this rate decreases rapidly until all electromagnetic interactions are

excluded, at which point a plateau develops. As x continues to increase, hadronic interactions begin to be excluded and the rate drops to zero. To achieve a hadronic trigger with maximum efficiency, x was chosen to be .3, at the beginning of the plateau region, such that the trigger rate was about twice the expected total cross section. Most electromagnetic interactions of the primary tagged photon are thereby excluded and the efficiency for hadronic interactions has not been degraded.

A study was made to determine the efficiency of the TAGH trigger for hadronic events. Two data tapes were filled with events selected by a TAG•(C) trigger (tagged photon with no significant energy deposited in the C-counter). The status of the TAGH trigger bit was written on the tape for each event. The data was analyzed by the charged track reconstruction program to eliminate events containing less than 3 charged tracks, which might be produced by the electromagnetic pair production process. Electromagnetic events should deposit most of the total event energy in the SLIC. The ratio of the total energy deposited in the SLIC to the photon energy measured by the tagging system was plotted, revealing a bump at a ratio of 1. To further reduce the electromagnetic contamination, only those events with a ratio less than 0.8 were accepted. At least one good recoil track identified by the recoil spectrometer was also required. All of the remaining events were assumed to be hadronic events. For these events, the number of times the TAGH bit was off was counted and the efficiency was calculated to be 97 $\mp$2%.

Recoil Triggers

An additional class of high level triggers is produced by the recoil processor[20]. These triggers are designated RECOIL 1,2,3,4. The recoil processor is started by a TAGH trigger at the high level stage. The purpose of the recoil processor is twofold. First, it identifies those events that contain a clean recoil proton in the recoil system. Second, it calculates the missing mass which decays into the forward spectrometer and partitions the events into mass bins. These triggers form the heart of the experiment, providing an enhanced sample of diffractive high mass states, and, therefore, dominate the data finally written to tape.

A simplified flow chart describing how the recoil processor functions is provided in figure 32. As stated previously, the recoil processor is started by a TAGH signal. The recoil processor begins then, by analyzing a presumed hadronic event. Each basic area of the processor is described in the following text.

Data Input

Each data word read into the processor from the PWC cathodes contains the centroid and width of a cluster found by the PWC center finder. The recoil calorimeter data is digitized by fast ADCs and TDCs providing the processor with the time of flight, end to end timing, and calorimeter pulse heights for each sector of the calorimeter. This, then, provides the data base for the processor's analysis. The total data input time is about 1.5 microseconds.

Track Finder

The track finder begins executing after receipt of a cluster from each chamber. From this information the Z position at the middle PWC chamber is calculated by averaging the Z position as measured by the inner and outer PWC chambers. This predicted Z-position can then be used to search for a match with a hit in the middle chamber. When a match is found, the track parameters are stored in the track stack. (The track parameters are equivalent to the angle with respect to the beam axis and the Z-position at the center of the target, thus defining a cathode track. No azimuthal angle is measured by the PWC cathodes). The grand loop begins executing after the first track is found and stored. In parallel, the track finder continues filling the track stack with any additional tracks found. The fast ADC/TDC read in also proceeds in parallel with the track finder.

Sector Finder

The purpose of the sector finder is to match the cathode tracks with a sector in the recoil calorimeter, thus providing information to be used in particle identification. The cathode track is projected into the A-layer (inner) of the recoil calorimeter and the Z-position at that point is calculated. A search is then made for a match using the Z-positions calculated from the end to end timing information available in the A-layer. If a match is found, the number of the calorimeter sector associated with the cathode track is stored.

Particle-Energy Combinations

The combination of a calorimeter sector ADC data and a cathode track provides sufficient information to calculate the energy deposited in each layer of the recoil calorimeter. The data is first passed through a calibration MLU (memory lookup unit) which contains all of the overall attenuation coefficients to convert the raw ADC data to energy measurements.

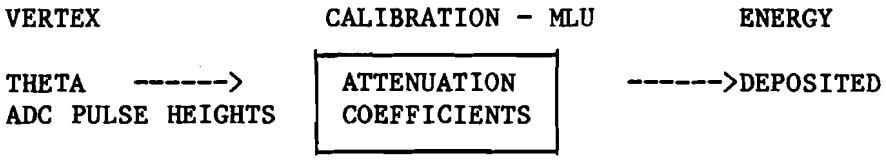

The output of the calibration MLU is then fed into the E(energy) MLU which calculates E1 (particle energy using A and B calorimeter layers only) and E2 (particle energy using C and D calorimeter layers only). These energies are calculated for both the proton and pion mass hypothesis.

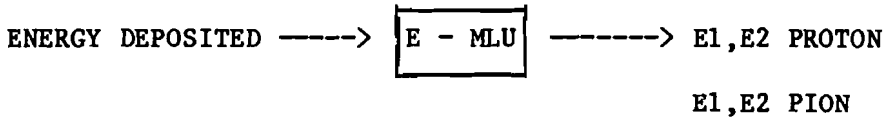

The output of the E-MLU then becomes the input to the PROTON MLU, which classifies the track, placing it into one of the following categories:

1. - INCONSISTENT

2. - POSSIBLY A PROTON (PROTON OR PION)

3. - NON-HADRON

4. - PROTON DEFINITE

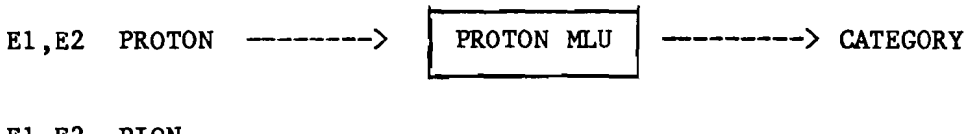

There is a TOF MLU (not shown) which predicts whether the particle is a proton or non-hadron based on E1, theta, Z-vertex as compared to the time of flight prediction measured in the A layer.

If the track is classified as containing inconsistent data, or it is best fit as a non-hadron, control returns to the sector finder and a search is made for another match. The vertex information is stored before returning control to the sector finder for tracks occupying the "possibly a proton" category (pion or proton consistent with data). If the track is classified as a "proton definite", the angle, energy, and vertex information is stored before searching for additional matches. This "grand loop" continues until the track stack is exhausted. If the track recoils backwards (theta greater than 90 degrees) it is automatically classified as a non-hadron and the grand loop sector match search is aborted.

On subsequent passes through the grand loop, additional tracks are classified. If the later track is downstream of the initial track, appropriate scalers are incremented. Tracks originating from the same vertex are also counted. If the later

track is upstream of the initial track and is classified as a hadron, the new vertex, angle, and energy are stored.

After all of the tracks have been reconstructed and classified, the missing mass is calculated using the missing mass MLU.

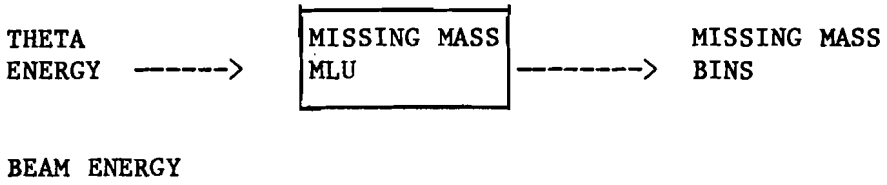

The missing mass is calculated using the energy and angle of the most upstream recoiling proton. The missing mass bins can be changed using a MLU loading program, thus changing the physics contents of the recoil triggers. Once the missing mass has been calculated the trigger type can be calculated, or the event rejected.

Four recoil trigger types were generated. Recoil 1 contains a recoil proton with no missing mass cut. This trigger was prescaled to reduce the rate at which this data type was written to tape. Recoil 2 contains a recoil proton with a missing mass in the range 2.0 - 5.5 GeV. All triggers of this type were accepted.

Recoil 3 contains a recoil proton with a missing mass in the range 5.5 - 11.0 GeV. All triggers of this type were accepted. Recoil 4 contains multiple tracks in the recoil detector. This trigger type was prescaled.

On Line Computer Configuration

Figure 33 outlines the basic on-line configuration. The on-line system serves two primary functions. Prompted by a computer interrupt generated by the high level trigger logic, the computer reads out the CAMAC modules using three branches controlled by Jorway 411 branch drivers. The data is formatted by the data acquisition task and written into the bulk memory to be transcribed to tape during the inter-spill period. Each event is identified by a trigger word and a logical record number. The trigger word consists of individual bits set on or off by the high level trigger logic and transmitted to the data acquisition task through an interface device (Bison Box) which allows the computer to transfer information to and from the high level trigger logic. The Bison Box also provides the event interrupt signals, timing signals to define the start and end of aspill (beam spill plus special calibration triggers outside of the beam spill), and transmits the computer busy to block data input during the readout.

The second primary function of the on-line system is to monitor the data and hardware to insure the integrity of the data being written to tape. This was accomplished using various independent tasks which communicated through shared common areas with

the standard on-line analysis package (MULTI). Controlled by an independent monitor scheduling task, MULTI sampled the data available in the bulk memory, always selecting the non-data calibration events first.

A separate processor in MULTI was written to analyze this data and make comparisons with standard values read in from the disk. A complete summary of the monitor results was then written to the disk and later copied to the data tape. Warning messages appeared immediately on the main terminal screen, accompanied by additional details which were automatically printed on the line printer.

The monitor scheduling task communicated through a 24 bit CAMAC output register with a special module designed to generate special calibration and monitor events (called the Black Box). These events were always generated outside of the beam gate so as not to interfere with the data resulting from beam triggers. The Black Box generated the gate strobes for the ADCs and TDCs, fired the lasers and pulsers, and set the bits for the trigger word. No more than four special events were selected for any given spill, always outside of the beam burst. Events produced in this manner were of the following types.

DOWNSTREAM LASER

UPSTREAM LASER

PEDESTAL

DRIFT CHAMBER PULSER

(HIGH VOLTAGE PULSING)

(SPLITTER PULSING)

The scheduling task could also rotate the laser filter wheels to change the transmission factor to the fiber optics system, and change the delay time of the drift chambers pulser systems.

In addition to the primary monitoring system, an independent voltage monitoring task periodically checked the high voltages on the calorimeter phototubes, and a series of low voltage readouts set up to check various devices such as drift chamber voltages, etc. Other checks of the data and hardware were made less frequently by an off-line monitor program which included some sample reconstruction, and the maintenance of various calibration files.

These primary functions of the on-line system consumed a large part of the resources of the PDP 11/55. MULTI was, however, able to access a small portion of the data stream and provide the experimenter with some simple interactive data analysis. Histograms of the various data sets could be defined and viewed on the graphics terminals as the experiment accumulated data. This provided the necessary flexibility in locating and correcting various failures quickly.

The following list details the procedures used to monitor all relevant quantities.

MONITOR LIST

PHOTOTUBES -- (CERENKOV AND CALORIMETERS)

SLIC,RECOIL,HADROMETER

OUTRIGGERS,C1,C2

Each phototube was illuminated with a laser pulse, routed through a transmission filter in an optical fiber. A mean and sigma was determined for about 50 events and compared to a milestone value, thus maintaining the proper gain. All channels deviating from their milestone values by more than three sigma produced immediate error messages.

DRIFT CHAMBERS — D1-D4

A CAMAC command issued by the scheduling task changed the delay of the pulser system. This allowed a direct measure of the gain of the TDC channel, measured at four different delay times (10 events for each time). Data was accumulated for two sets of delay times and the gain calculated. Milestones were then read in from the disk and a comparison made. Any channels deviating from the milestones by more than three sigma produced an error message on the main console. Also, zeros and overflows were counted and the number of hits per plane was monitored.

RECOIL SPECTROMETER

PROPORTIONAL WIRE CHAMBERS--CATHODES 1-3

The continuity of the hits in the cathodes was checked to see if there were gaps due to dead or inefficient wires. (TAGH + RECOIL triggers). This continuity test required that a particular channel respond at nearly the same rate as its two nearest neighbors. Large gaps involving multiple wires were also detected and

reported as errors. In addition to the continuity checks, the number of clusters was averaged over 100 events and compared to a milestone value (for each chamber), providing a faster test for any catastrophic failure.

PEDESTALS

Empty gates were generated outside of the beam spill and read out as an event. This provided a measurement of the ADC pedestals for which means and sigmas were accumulated and compared to milestone values. If noise levels or ADC failures were corrupting the data, immediate error messages were generated.

TAGGING SYSTEM — LEAD GLASS BLOCKS, HODOSCOPES
C-COUNTER

2000 events (TAGH + RECOIL) were filtered to select events containing single recoiling electrons in the center of a lead glass block. The filter required a coincidence between a lead glass block and the two hodoscopes overlapping it. The means and sigmas thus obtained were compared to standard values. The average number of hits in each of the hodoscopes was also monitored.

SCALERS

A large number of scalers were monitored to guard against trigger failures, beam steering and rate problems, and software errors. Table 14 contains a list of the scalers being monitored and the potential failure modes avoided.

HIGH VOLAGE -- LE CROY, HV 4030S

All phototubes powered by the 4032 modules were directly monitored by the computer to detect drifts and failures.

LOW VOLTAGE

Constant low voltage ADCs checked a variety of quantities including drift chamber and PWC high voltage settings, threshold and low voltage settings, magnet currents, and cerenkov and tagging system power supplies.

DATA INTEGRITY

MULTI performed some simple tests on the data sets including such things as number of words for each type of data, checking for start and stop bits in the PWC data, and proper formatting of the drift chamber data.

CHAPTER 6

DATA REDUCTION

Overview

An initial data sample of about 500,000 events was reconstructed to provide the data base for the analysis described in this thesis. This data sample constitutes about 5% of the total data sample written to tapes during the experimental run. The off-line reconstruction package provided the following information; momentum components of charged tracks in the recoil system including mass hypothesis, vertices in the recoil system, photon energy with a status flag indicating error conditions, momentum components and charge of tracks in the forward spectrometer, vertices of tracks reconstructed in the forward spectrometer correlated with recoil tracks if possible, mass hypothesis based on Cerenkov data, and associated errors on all relevant quantities. The reconstruction program used to generate this data base did not include any reconstruction of the neutral particles in the forward system from data provided by the SLIC and the hadrometer. These 500,000 events include the following trigger types:

RECOIL 1	44,290 EVENTS
RECOIL 2	144,327 EVENTS
RECOIL 3	219,207 EVENTS

RECOIL 4	155,135 EVENTS
DI-MUONS	83,619 EVENTS

The large number of recoil triggers biased the data towards diffractive events.

This chapter contains a description of the reconstruction algorithms and the data analysis procedures. The data was first reconstructed, then all events which survived the diffractive filter were processed by the analysis routines.

RECONSTRUCTION ALGORITHMS

Charged Track Reconstruction

There are a total of 29 drift chamber planes measuring U,X,V coordinates. D1 contained 2 X' planes which were used to help resolve ambiguities. Figure 16 shows the basic layout of these planes relative to the magnetic field regions. A charged particle may be tracked through both magnets or only the most upstream magnet. Particles which penetrate only the upstream magnet are tracked through D1 and D2 only, containing a maximum of 17 drift chamber planes.

After converting the TDC data to spatial coordinates, a tracking algorithm formulates track hypothesis which associates drift chamber hits with tracks. Each track hypothesis is fit through the magnetic field regions using a five parameter iterative fit procedure.

FIT PARAMETERS

dx/dz	measured in the field free region between the magnets
dy/dz	measured in the field free region between the magnets
X_0	intercept extrapolated from dx/dz
Y_0	intercept extrapolated from dy/dz
1/p	inverse momentum

Using these five fit parameters equations governing the particle trajectory are defined.

$$X=X_0+(dx/dz)\cdot((Z-Z_0)+(1/p)\cdot(p_0\cdot Fx(Z)) \quad (6.1)$$

$$Y=Y_0+(dy/dz)\cdot((Z-Z_0)+(1/p)\cdot(p_0\cdot Fy(Z)) \quad (6.2)$$

Fx(Z) and Fy(Z) are approximations to the particle trajectory within the magnetic field regions. The initial estimate of the momentum (p_0) is calulated from the initial track parameters. These functions are helices with boundary conditions matched at segment boundaries throughout the field. Monte Carlo tracks were used to determine the number of segments and boundary positions necessary to achieve the optimum momentum resolution. Since the helix functions contain the fit parameters, it is necessary to iterate the fit to obtain the desired accuracy. After two iterations any changes due to additional iterations are so small that they do not improve the resolution of the measurement. Figure 34 contains the

chi-square and degrees of freedom distributions obtained using this fit. Note the double peaks in the degrees of freedom plot. The lower peak is due to tracks which only make it through the upstream magnet.

Monte Carlo tracks were generated, smeared to simulate real data conditions, and reconstructed by the charged track reconstruction program. The overall charged track efficiency was determined to be about 85% (slightly lower - about 80% for tracks only penetrating the upstream magnet). The efficiency is shown in figure 43 and described in more detail in chapter 7.

Vertex Reconstruction

All charged tracks are verticized by minimizing the distance of closest approach among sets of tracks. The track furthest from the common vertex is then removed and the minimization procedure repeated. Tracks are removed until the distance of closest approach of each track used in the calculation of the vertex is acceptable. All tracks used in the vertex are marked as vertex associated. The downstream tracks vertex is associated with the recoil tracks vertex and a common vertex calculated, if possible. Figure 35 contains the X,Y,Z distributions of the vertices. Most vertices lie within the limits of the hydrogen target with one exception; electromagnetic pairs tend to verticize near the beginning of the first magnetic field region, since they are produced with a very small initial opening angle. Note that the center of the Y vertex distribution is below the center of the target.

Photon Energy Reconstruction

The energy deposited in the lead glass blocks of the tagging system in conjunction with the position information provided by the hodoscopes determines the number of recoiling electrons and their energy. The initial electron beam energy is known so the photon energy can be calculated.

$$E(PHOT) = E(BEAM) - E(TAG\ ELECTRON) - E(C\ CNTR) \qquad (6.3)$$

E(BEAM)	ELECTRON BEAM ENERGY
E(PHOT)	PHOTON ENERGY
E(TAG ELECTRON)	ENERGY DUMPED INTO LEAD GLASS BLOCKS
E(C CNTR)	ENERGY DUMPED INTO C COUNTER

Removing the C-counter energy reduces miscalculations of the interacting photon's energy due to the presence of non-interacting photons from multiple bremsstrahlungs. An error-status word is set for each event. It contains information including the number of electrons reconstructed in the tagging system, mismatches between overlapping hodoscopes and lead glass blocks, error conditions if calculation of the photon energy is impossible, and the status of the anti-counters. An error for the photon energy is also calculated.

DATA ANALYSIS

Diffractive Filter

From this data base, a set of cuts were used to select a sample of clean diffractive events. The following discussion provides a brief description of each cut, its purpose and its effects.

Recoil trigger cut - Only those events identified by the on-line recoil processor as events containing a recoil proton were selected. Of these recoil triggers only those classified as a Recoil 2 or 3 were analyzed, defining an on-line missing mass range of 2 - 12 GeV.

Recoil proton cut - The recoil system was required to contain only one charged particle, whose mass was reconstructed by the off-line reconstruction program to be consistent with that of a proton. No cuts were made on possible neutrals in the recoil system. The intent of this cut was to eliminate events containing secondary interactions in the hydrogen target and producing particles which entered the recoil spectrometer downstream of the primary interaction. It also reduced the amount of non-diffractive contamination of the data sample by requiring a cleanly identified proton in the recoil system. This cut reduced the data sample by 32%.

Tagging system - Events containing multiple electrons in the

tagging system were removed from the data sample by requiring that there be only 1 electron reconstructed in the tagging system. Multiple bremsstrahlung events were removed by cutting on excessive energy in the C-counter. The energy measured by the tagging system could, therefore, be associated with the interacting photon. This cut reduced the data sample by 10%.

Total charged energy cut - The magnitudes of the momenta of the charged tracks were summed and required to be less than 1.25 times the interacting photon energy. This cut reduced the data sample by 5%.

Multiplicity cut - A minimum of 3 charged tracks was required. This cut insured a sufficient number of tracks to calculate the jet variables. This cut reduced the data sample by 23%.

Electron cut - Particles identified as electrons or positrons by the cerenkov counters were removed from the data sample. Most of these electrons or positrons resulted from e+ e- pair production from photons produced in π^0 decays. This cut reduced the data sample by 6%.

The primary purpose of these cuts was to obtain a data sample composed mainly of diffractively photoproduced events, for which, the energy of the interacting photon was known. Using the knowledge of the momentum components of the recoiling proton and the

photon energy, the data could then be analyzed in the center of mass reference frame for the forward system. The other cuts (multiplicity, charged energy) served to make the data more amenable to analysis based solely on charged track reconstruction.

The following plots characterize the final data sample, after cuts, used for the physics analysis.

photon spectrum - figure 36

mass spectrum - figure 37

To summarize the important features of the data, the total sample contains 56,374 events with an average photon energy of 100 GeV ranging from 0 to 170 GeV, with an average forward missing mass of 6 GeV ranging from 2 to 12 GeV. The data was subdivided into twenty photon energy - missing mass classes.

class 1	-	(0-75 GeV)	(2-4 GeV)	3,097 events
class 2	-	(0-75 GeV)	(4-6 GeV)	3,247 events
class 3	-	(0-75 GeV)	(6-8 GeV)	1,485 events
class 4	-	(0-75 GeV)	(8-10 GeV)	84 events
class 5	-	(0-75 GeV)	(10-12 GeV)	0 events
class 6	-	(75-100 GeV)	(2-4 GeV)	5,225 events
class 7	-	(75-100 GeV)	(4-6 GeV)	6,812 events
class 8	-	(75-100 GeV)	(6-8 GeV)	5,735 events
class 9	-	(75-100 GeV)	(8-10 GeV)	1,769 events
class 10	-	(75-100 GeV)	(10-12 GeV)	12 events

class 11	-	(100-125 GeV)	(2-4 GeV)	3,499 events
class 12	-	(100-125 GeV)	(4-6 GeV)	4,314 events
class 13	-	(100-125 GeV)	(6-8 GeV)	4,582 events
class 14	-	(100-125 GeV)	(8-10 GeV)	2,649 events
class 15	-	(100-125 GeV)	(10-12 GeV)	415 events
class 16	-	(125-170 GeV)	(2-4 GeV)	2,608 events
class 17	-	(125-170 GeV)	(4-6 GeV)	3,185 events
class 18	-	(125-170 GeV)	(6-8 GeV)	3,740 events
class 19	-	(125-170 GeV)	(8-10 GeV)	2,916 events
class 20	-	(125-170 GeV)	(10-12 GeV)	1,000 events

Inclusive Distributions

After passing through the diffractive filter, the data was analyzed and various inclusive distributions were generated for each of the data classes. All variables are defined in terms of a right handed coordinate system in which the positive z axis defines the beam direction and the positive y axis is directed upwards. Theta (θ) is defined as the angle relative to the positive z axis, and phi (ϕ) is the angle of a projection of a vector in the x,y plane relative to the positive x axis.

The data classes are defined in terms of the interacting photon energy ($E\gamma$) and the missing mass (M_X). The following four vectors are produced by the reconstruction routines described previously.

$$E = (0,0,E\gamma,E\gamma) \qquad (6.4)$$

$$P = (Px, Py, Pz, E_p) \qquad (6.5)$$

$$P_0 = (0, 0, 0, M_p) \qquad (6.6)$$

M_p = proton mass

E_p = energy of the recoiling proton

These vectors refer to the process described in figure 1a. The missing mass is then defined as the invariant mass of the 4-vector sum $(E + P_0 - P)$. The calculation of this mass requires no information from the forward spectrometer.

In addition to the lab. reference frame, there are two center of mass reference frames in which the data is presented. The first of these two is the initial center of mass, denoted as CMI in subscripts. The initial center of mass refers to the reference frame in which the momentum vector part of the 4-vector sum $(E + P_0)$ is zero. In other words it is the center of mass of the incoming photon and the target proton at rest in the lab. In this reference frame, the center of mass energy E_{CMI} can be easily calculated.

$$E_{CMI} = (2 \cdot M_p \cdot E\gamma + M_p \cdot M_p)^{1/2} \qquad (6.7)$$

$$E_{CMI} \approx (2 \cdot M_p \cdot E\gamma)^{1/2} \qquad E\gamma >> M_p$$

The second center of mass reference frame is the forward center of mass, denoted as CMF in subscripts. The forward center of mass refers to the reference frame in which the momentum vector part of the 4-vector sum $(E + P_0 - P)$ is zero. In other words, it is the

center of mass of everything going forward produced by the fragmenting photon with the recoil proton subtracted out. In this reference frame, the center of mass energy E_{CMF} is simply the missing mass M_X.

The following equations define the inclusive variables used to present the data.

$$X_{\parallel}=2P_{\parallel}/E_{CM} \quad E_{CM} = (E_{CMI},E_{CMF}) \tag{6.8}$$

($P_{\parallel}$ is the momentum projected to the photon axis)

$$X=2P/E_{CM} \tag{6.9}$$

$$y=1/2\cdot\ln[(E+P_{\parallel}/(E-P_{\parallel})] \tag{6.10}$$

$$t=2M_p^2-2M_pE_p = 2M_pKE \tag{6.11}$$

KE ≡ kinetic energy

$$s=(E_{CMI})^2 \tag{6.12}$$

$X_{\parallel}$ refers to Feynman x, y refers to the rapidity, and t refers to the invariant momentum transfer between the initial target proton and the recoiling proton. In addition to these variables, the inclusive distributions are presented as functions of the transverse momentum (P_t), P_t squared, the magnitude of the momentum (P_{lab},P_{cmf}), and $P_{\parallel}$.

The final presentation of the data includes various forms of the normalized invariant cross section.

$$\frac{2Ed^3\sigma}{\sigma\, dp^3} = F(p,s) \tag{6.13}$$

P and E are the momentum and energy of the inclusive final state hadron and s is the initial center of mass energy squared. The function F is covariant so there is no specified reference frame in which p and E must be measured. There is a relationship between various forms of the invariant cross section involving different sets of variables, determined by the Jacobians of the coordinate transformations. The relevant forms are contained in the following equations.

$$2E\frac{d^3\sigma}{dp^3} = \frac{2E}{\pi}\frac{d^2\sigma}{dP_{\parallel}dP_t{}^2} \qquad (6.14)$$

$$= \frac{2E}{\pi P_{max}}\frac{d^2\sigma}{dX_{\parallel}dP_t{}^2}$$

$$= \frac{2}{\pi}\frac{d^2\sigma}{dydP_t{}^2}$$

P_{max} is approximately $E_{CM}/2$, where E_{CM} can be either the initial or forward center of mass energy depending upon which reference frame is used to calculate the other variables.

"Jet" Analysis

The jet analysis performed on the photoproduction data sample described previously is identical to the analysis performed on e+ e- data to describe the production of quark jets. The word "jet", in our case, is used to describe any phenomenom resulting in a limited P_t relative to some axis, regardless of the origin of the jet-like phenomenon. The following definitions define the

global variables used in the analysis to describe the global jet properties.

The first such variable to be extensively used by experimentalists is the sphericity of an event[21].

$$S = 3/2 \min(\sum|P_t{}^i|^2/\sum|P^i|^2) \qquad (6.15)$$

The sum runs over all observed particles. P_t is the component of the momentum perpendicular to a selected "jet" axis. The coefficients that define this axis are then allowed to vary until the quantity reaches a minimum. The algorithm actually used to calculate the sphericity first generates the momentum tensor.

$$T^{\alpha\beta}=\sum(\delta^{\alpha\beta}p_i{}^2-p_i{}^\alpha p_j{}^\beta) \qquad (6.16)$$

The indices i and j refer to the spatial components of the momentum vector. Eigenvalues (A1,A2,A3) are obtained by diagonalizing T. The sphericity can then be written in terms of the eigenvalues.

$$S = (3*A1)/(A1+A2+A3) \qquad (6.17)$$

The eigenvector corresponding to A1 defines the jet axis. This variable has the advantage that it can be quickly calculated analytically since the momentum components are individually squared. The sphericity approaches zero for perfectly jet-like events and 1 for large multiplicity isotropic events.

There are theoretical objections to the use of sphericity as a viable variable. In QCD, calculations of the differential cross section ($d\sigma/dS$) are not believed to be reliable due to infra-red singularities that arise in the perturbation theory.[22] These singularities result from the fact that the sphericity contains sums of squares of the momentum components. It is therefore very unlikely that there would be any cancellation due to the interference of various diagrams.

Additional variables have been defined which are not believed to lead to infra-red singularities. Initially proposed to study hadronic collisions[23], the principal momentum (later renamed thrust) maximizes the longitudinal components of the momenta relative to a jet axis. This original definition is somewhat impractical for calculational reasons. The actual algorithm used in the analysis uses the following definition[24], where the sums run over all observed particles.

$$T = \text{MAX}\left(\sum\left|P_{\parallel}^{i}\right| / \sum\left|p^{i}\right|\right) \qquad (6.19)$$

Since the sums contain only linear momentum components there is no simple analytic solution for the thrust as there was for the sphericity. To find the thrust all possible groupings of the observed tracks for an event are generated and the thrust and thrust axis calculated. The grouping that maximizes the thrust then defines the hypothetical jet. The thrust approaches 1/2 for large multiplicity isotropic events and 1 for jet-like events. The thrust is

believed to be a "safe" variable leading to a singularity free cross section.

Another QCD safe variable which is strongly correlated with the thrust though independent is the spherocity.[22]

$$S = \left(\frac{4}{\pi}\right)^2 \left(\sum \left|P_t^i\right| / \sum \left|p^i\right|\right)^2 \qquad (6.20)$$

As in the thrust the sums contain only linear momentum components, so the calculational techniques are the same. For isotropic distributions the spherocity approaches 1 and for jet-like events the spherocity approaches zero. Since the variables S and T are independent, the thrust and spherocity axis do not necessarily coincide. It is expected that there is a strong correlation with deviations in second order perturbative QCD (non-perturbative effects might also cause deviations).

To determine the extent to which an event is planar, the acoplanarity of each event is calculated.[22]

$$A = 4 \cdot \min \left(\sum \left|Pout^i\right| / \sum \left|p^i\right|\right)^2 \qquad (6.21)$$

$Pout^i$ is the momentum component perpendicular to a plane allowed to vary in order to minimize A. The sums run over all observed particles. The procedure used to calculate the acoplanarity is identical to that used to calculate the thrust and spherocity.

CHAPTER 7

DETECTOR ACCEPTANCE AND EFFICIENCY

Overview

To obtain accurate results the data must be corrected to account for geometrical constraints which reflect the physical size of the detectors and reconstruction inefficiencies. The magnitude of these corrections and their dependence on the relevant kinematical variables are calculated using Monte Carlo techniques and available redundancies in the detectors. The following discussion describes these corrections for the recoil spectrometer and the forward charged track spectrometer

Recoil Spectrometer Acceptance

The recoil spectrometer acceptance function was determined using a simple Monte Carlo to fold together the measured detector efficiencies and the known spatial limits of the detector. The detector efficiencies were calculated using data provided by a hadronic trigger (TAGH). These triggers required no input from the recoil calorimeter and, therefore, provided an unbiased data sample. The data was submitted to a series of cleanliness cuts to reduce the level of accidentals and thus make the systematic error due to background subtraction negligible.

To obtain the efficiency of a given detector component, use was made of the available redundancies (listed in table 15) in the

detectors. A collection of clean events was accumulated, in which the redundant components suggested a particular value for the component being studied. The number of agreements between the redundant components and the component under study was then counted and the efficiency calculated.

$$\text{EFFICIENCY} = \frac{(\text{NUMBER OF AGREEMENTS})}{(\text{NUMBER OF EVENTS} - \text{BACKGROUND})} \qquad (7.1)$$

Table 15 contains a compilation of these efficiencies for the various recoil detector components. For tracks reaching the outer layers of the calorimeter, corrections were made for nuclear absorption. This correction is path length dependent and, therefore, depends on the angle θ.

The final acceptance is a combination of these detector component efficiencies and the geometrical constraints of the spectrometer. The acceptance function can be written as follows:

$$P(\theta,KE) = P_{az} \cdot P_{fid}(\theta) \cdot P_{edge} \cdot P_{pwc} \cdot P_{tp} \cdot P_{e2e} \cdot P_{recon}(\theta,KE) \qquad (7.2)$$

P_{az} is a measure of the azimuthal acceptance of the 15 calorimeter sectors. It has a value of .921, due primarily to the dead region at the bottom of the calorimeter (as shown in figure 8).

$P_{fid}(\theta)$ defines the acceptance within a fiducial region of the PWCS and the A and B layers of the calorimeter. This acceptance determines the probability that a recoil track generated

uniformly along the axis of the target with an angle θ relative to the target will enter the active region of the recoil spectrometer. Figure 38 contains a plot of $P_{fid}(\theta)$. The region defined by $45^{\circ}<\theta<65^{\circ}$ has an acceptance of 1. Figure 39 shows the fiducial acceptance as a function of the missing mass for different ranges of photon energies. The most important effect is the geometrical limitation (defined as the function $P_{fid}(\theta)$). Particles with a value of $\cos(\theta)$ close to 1 may exit the end of the cylindrical volume of the spectrometer before penetrating any of the calorimeter layers. A Monte Carlo was written to measure this contribution to the acceptance. Events were generated using the following distributions.

t (invariant momentum transfer) - $\exp(-bt)$ (7.3)

$b = .5+5/M_X$

M_X (missing mass) - flat distribution $2<M_X<12$ GeV

$E\gamma$ (photon energy) - flat distribution $50<E\gamma<150$ Gev

Z (recoil vertex in target) - flat distribution $0<Z<140$ cm

The acceptance was then calculated by taking the ratio of the number of events entering the active region and the total number of events generated. This leads to the sharp cut-off in the acceptance for high missing mass events. As the photon energy increases, the point at which this cut-off begins to dominate the acceptance migrates to higher missing mass.

A particle must also have sufficient kinetic energy to

deposit 5 MeV in the A layer before it is considered detectable. For protons, this minimum kinetic energy increases from 30 MeV to 50 MeV as cosec(θ) increases from 1 to 3. This minimmum kinetic energy requirement is included in the fiducial acceptance shown in figure 39, resulting in the tapering off of the acceptance for low missing mass events. The low mass inefficiency is not a function of the photon energy. It is equivalent to the statement that a recoiling proton must have a minimum t (approximately .06 GeV**2) to be detectable in the recoil spectrometer.

P_{edge} is the probability that light deposited in the A f despite edge effects. These edge effects can distort the signal seen by the phototubes. These effects include such things as; boundary non-uniformity between scintillator blocks, mis-alignment of scintillator blocks, θ dependence of the path length through the scintillator block (due to the fact that the block is not curved but flat) , UV absorption by the scintillator wrapping, and straggling during the last few millimeters of range. It was determined that such effects were serious only if the track passed within 2 mm of a boundary, leading to a value for P_{edge} of .98.

P_{pwc} and P_{e2e} are the PWC - cathode and end to end timing efficiencies described previously and found in table 15. Precon(θ,KE) refers to the proton kinetic energy reconstruction efficiency. This efficiency depends upon the depth that the track penetrates the calorimeter and involves the calorimeter ADC information. For tracks stopping in the A layer, it depends upon a

combination of the ADC information for the A layer and the time of flight information. The efficiencies are calculated from the redundancies as described previously. P_{tp} refers to the trigger processor efficiency, estimated to be about .7. The final product $P(\theta,KE)$ is shown in figure 40. The acceptance function is shown for the two extreme cases, the solid line representing the acceptance for protons whch have just enough kinetic energy to deposit 5 MeV in the A layer before stopping in the A layer, and the dashed line representing the acceptance for protons that have sufficient kinetic energy to penetrate the C layer.

Event Generation Techniques

Data corrections to account for inefficiencies and acceptance limitations in the forward spectrometer were calculated using Monte Carlo techniques. In high energy reactions, the data is characterized by large multiplicities and limited transverse momenta. To simulate this data, events were generated using a phase space distribution with limited transverse momentum. Several Monte Carlos have been written and used which contain these characteristics. The Monte Carlo used in the data corrections described in this thesis is based on an event generation algorithm written by Carey and Drijard[25].

The phase space integral K decomposes into a transverse and a longitudinal part with amplitudes FL and FT as described in the following equations.

$$K = \int F dv \tag{7.4}$$

$$F(p_{\parallel}, p_t) = FL(p_{\parallel}, p_t) \cdot FT(p_t)$$

The transverse amplitude can then be factorized into a product of amplitudes for each particle (equation 7.5). Assuming a particular form for the transverse amplitudes, the transverse momenta are generated. Removing the p_t dependence from the longitudinal amplitude, the longitudinal momenta are then generated.

The transverse momentum components can be generated according to any integrable distribution function that can be decomposed into individual particle distribution functions.

$$FT(p_t) = \Pi f(p_t) \tag{7.5}$$

From these individual particle distribution functions, a complete set of transverse momenta are generated then transformed to a new set of momenta which satisfy momentum conservation. This transformation contributes a weight factor to the total event weight which gives the probability that the event is generated according to the appropriate distribution. To determine the geometrical acceptance of the downstream spectrometer, events were generated with a gaussian p_t distribution.

$$f(p_t) = \exp(-p_t^2/R^2) \tag{7.6}$$

$$R = .45$$

For such a gaussian distribution, the contribution to the event weight is unity.

The longitudinal momentum components are generated through a series of quasi-two-body decays. The method attempts to maximize the generation efficiency by producing weight contributions that vary slowly within the kinematic range. A particular longitudinal distribution function can be incorporated into the generation procedure. The events generated to study the acceptance used a normal longitudinal phase space distribution.

Geometrical Acceptance

A data simulation algorithm was written to provide a measure of the forward spectrometer acceptance. An event was generated in the forward center of mass defined by an incident photon, a target proton at rest in the lab., and a recoiling proton.

To provide the recoil proton 4-vector and incident photon energy values, 10,000 real data events were analyzed and the appropriate distributions generated. Random selection from these distributions defined, on an event by event basis, the center of mass in which a particular event was generated. The missing mass, photon, and recoil proton spectrum from the Monte Carlo generated events, therefore, exactly matched the real data distributions.

In addition to the center of mass energy (defined as the missing mass in the forward center of mass), the Monte Carlo event generator requires a multiplicity and individual mass assignments

for the particles being generated. The multiplicity was generated randomly from a KNO probability distribution[26,27]. The particular function used was of the following form.

$$P(x) = (EXP(a + bx + cx^2 + dx^3))/\langle n\rangle \qquad (7.7)$$

$x = n/\langle n\rangle$

$a = -3.31$

$b = 8.76$

$c = -5.3$

$d = 0.6$

This function was obtained from a fit to proton, anti-proton interaction experiments[28]. The probability distribution function was normalized to 1 in the region x=0 to x=4, where the function was cut off before it begins its rise to infinity. A typical shape for $\langle n\rangle$=4 is shown in figure 41. The mean charged multiplicity input into the KNO distribution function has the following center of mass energy dependence.

$$\langle n\rangle = a + b\cdot\exp(c\cdot(\log(M_x^2/d))^{1/2}) \qquad (7.8)$$

$a = 2.38$

$b = 0.04$

$c = 1.92$

$d = 0.25 \quad (GeV)^2$

This functional form was fit to e+ e- annihilation data with good results[29]. To get the total multiplicity, the neutral multiplicity was generated independently according to the same distribution and scaled to account for about 45% of the total energy, as observed in our photoproduction data.

Assuming about 10% of the particles were kaons, events were generated in the center of mass. The particles to be designated as neutrals were then randomly selected from the particle list so as not to induce any systematic error in the charged particle distributions. The neutrals were thereafter ignored. All particle momentum components were then transformed to the lab. reference frame using the knowledge of the recoil proton 4-vector and the incident photon energy.

In the lab. reference frame, each particle was subjected to the geometrical acceptance criteria. These criteria where defined by the geometrical limits of the forward spectrometer. Table 16 contains a description of these criteria. Each particle was assigned a positive or negative charge (alternating signs such that the total charge of the event was zero). The particles trajectory was projected through the fields of the analyzing magnets and tested against the acceptance criteria. If it failed one of the criteria in the x or y dimension, the particle was removed from the particle list.

For any given event, the final particle list included only those charged particles whose trajectories remained within the boundaries of the charged particle tracking system. This list was

then passed to the same analysis program used to analyze the real data, and a complete set of histograms were generated. An acceptance plot was generated for each data plot by submitting a Monte Carlo simulated data sample to the standard data analysis program twice; once without subjecting the individual particles to the acceptance criteria, and once with the reduced particle list subject to the acceptance criteria. For every data plot, the corresponding acceptance plot was then calculated.

$$A_i = DWA_i/DNA_i \qquad (7.9)$$

A_i = acceptance - ith bin

DWA_i = Monte Carlo data with acceptance cuts ith - bin

DNA_i = Monte Carlo data no acceptance cuts ith - bin

Before calculating the acceptance, the Monte Carlo parameters were adjusted to match the real data in the momentum, multiplicity, and transverse momentum distributions, though the final results were relatively insensitive to small changes in the Monte Carlo event generator.

Efficiency Studies

In addition to acceptance losses due to purely geometrical constraints, there were losses due to hardware and reconstruction inefficiencies. To obtain a measure of these inefficiencies, the Monte Carlo generator described previously was used in conjunction

with a simulated hardware configuration to produce a simulated raw data tape. The simulated data tape was then reconstructed with the standard charged track reconstruction program and compared with the Monte Carlo tracks to determine the efficiency as a function of various track parameters.

The input to the Monte Carlo event generator was slightly different than that used in the geometrical acceptance studies. The photon energy was generated randomly from a single bremsstrahlung spectrum with a high energy cut-off at 170 GeV. The low energy cut-off was set to 80 GeV. The diagram in figure 42 defines the production parameters generated randomly from the following distributions.

$$t: \quad \exp(-bt) \qquad b = 2 \tag{7.10}$$

$$M_x: \quad (dN/dM_x)^2 = \text{flat distribution}$$

The multiplicity was generated from the KNO scaling distribution function, also used in the geometrical acceptance studies.

Each particle was transformed to the lab. reference frame, then projected through the forward spectrometer. The magnetic field map was used to determine the particles trajectory through the analyzing magnets and the track parameters in the field free regions. The intersection points of the particle's trajectory at each drift chamber plane was calculated to determine the tracks position in a particular drift chamber cell.

Before simulating the drift time digitization, the data was

subjected to various smearing effects due to resolution and hardware inefficiencies. These effects included such things as cumulative errors in wire positions across a drift chamber plane, drift time errors due to drift statistics and 2770 TDC resolution, time corrections due to signal transit time along the drift chamber sense wires, and cross talk among neighboring drift cells fired by a single track. Additional muons and e+ e- pairs were generated out of time in different RF buckets and tracked through the drift chamber system. K-shorts and lambdas were allowed to decay downstream of the primary interactions, and primary decay products were allowed to undergo secondary interactions in the target.

The simulated data was cast into the form of a standard raw data tape format. An additional file was formed containing the uncorrupted tracks as generated by the Monte Carlo event generator. The standard charged track reconstruction program was used to reconstruct tracks from the simulated data tape. A comparison was made between the original Monte Carlo tracks and the tracks reconstructed by the charged track reconstruction program. If a Monte Carlo and a reconstructed track satisfy a sufficient similarity criteria, it is considered to be successfully reconstructed. The efficiency is defined as the number of successfully reconstructed tracks divided by the number ofgenerated tracks. This efficiency includes only tracks that are reconstructable; that is, they lie within the geometrical limits of the forward spectrometer. The efficiency measurements are, therefore, complementary to the geometrical acceptance studies. The geometrical acceptance was not

calculated using the full simulated data tape due to the sparsity of simulated data. The detailed projection through the magnetic fields and data smearing was extremely slow compared to the event generation.

The charged track reconstruction efficiency is shown in figure 43 for tracks that are reconstructed in all four drift chamber modules (D1-D4) and for tracks that are only reconstructed in the first two drift chamber modules (D1-D2). The efficiency is plotted as a function of the lab. momentum. The two dominant effects leading to reconstruction inefficiencies are the inefficiency in the reconstruction of low momentum, wide angle tracks and the inefficiency in the reconstruction of tracks in the central, high flux, region of the chambers (dominantly high momentum tracks). Figure 44 contains the final acceptance of the forward spectrometer plotted as a function of $X_{\parallel}$ in the initial center of mass. Figure 45 contains the final acceptance plotted as a function of $X_{\parallel}$ in the forward center of mass. These plots include the geometrical acceptance and the charged track reconstruction efficiency. The acceptance is plotted for different missing mass bins in the forward center of mass and different photon energy bins in the initial center of mass.

CHAPTER 8

SYSTEMATIC ERRORS

Nucleon Resonance Decays

In addition to the diffractive process that leaves the target proton intact, there are diffractive dissociation processes that involve the production of a nucleon resonance and its subsequent decay. Figure 46 illustrates this N* diffractive process and the resonance decay modes that contribute to the background in the single proton diffractive process. Decay modes containing charged pions are eliminated by the diffractive filter which removes events containing additional charged tracks in the recoil detector. The following two processes, therefore, were studied to determine their contributions to the systematic errors.

$$\gamma\ p \rightarrow (p\ \pi^0)\ X \qquad (8.1)$$
$$\gamma\ p \rightarrow (p\ \pi^0\ \pi^0)\ X$$

Table 17 contains a list of the nucleon resonance decay modes, the quantum numbers of the decay particles, and the relative coefficients for each decay mode calculated from the isospin coupling.

Proton-proton interaction experiments at the CERN ISR have measured the 3-body decay $N \rightarrow p\pi^+\pi^-$ for both the inclusive process[28] $pp \rightarrow (p\pi^+\pi^-)+X$ and the exclusive process[29] $pp \rightarrow$

$(p\pi^+\pi^-)+p$. The measurements were made at center of mass energies of $\sqrt{s}$ = 35,45,53 GeV. The mass spectrum of the $p\pi^+\pi^-$ system is dominated by the N(1520) and N(1688) resonances. Analysis of the $p\pi^+$ mass spectrum shows that the spectrum is dominated by the $\Delta^{++}(1236)$. The dominant decay of the N^* is thus $N^* \rightarrow \Delta^{++}\pi^- \rightarrow (p\pi^+)\pi^-$. The cross section was measured for the 3-body charged decay mode.

$$\sigma(pp\rightarrow(p\pi^+\pi^-)+X) = 0.2 \mp 0.04 \text{ mb} \qquad (8.2)$$

Studies of the inclusive reaction $pp\rightarrow pX$ at CERN[30] have determined the total single diffractive cross section for $1<M_X<10$ GeV. The cross section is approximately 5 mb, and shows only a very weak energy dependence at ISR energies. With this information, an estimate can be made of the fraction of the total diffractive cross section that produces an N^* with a subsequent charged 3-body decay.

$$\frac{\sigma(pp\rightarrow(p\pi^+\pi^-)+X)}{\sigma(pp\rightarrow p+X)} \simeq 0.04 \qquad (8.3)$$

This value is in reasonable agreement with lower energy results from πp, γp, and pp diffractive production[9] which yield a ratio of approximately .05-.06.

Table 17 can then be used to relate the charged 3-body decay mode $(p\pi^+\pi^-)$ to the neutral 3-body decay mode $(p\pi^0\pi^0)$. Considering only the isospin coupling gives the following

relationship.

$$\frac{\sigma(N^* \to p\pi^0\pi^0)}{\sigma(N^* \to p\pi^+\pi^-)} \approx 0.5 \qquad (8.4)$$

A reasonable upper limit can then be set on the diffractive photoproduction process leading to unobserved 3-body N^* decays.

$$\frac{\sigma(\gamma p \to (p\pi^0\pi^0)+X)}{\sigma(\gamma p \to (p+X))} \approx .03 \qquad (8.5)$$

Two body N^* decays have also been extensively studied. At low energies ($\sqrt{s} \approx$ 4-7 GeV), the diffractive process[9] $\pi^{\mp}$, K^-, $pp \to (N\pi)X$ measured by different experiments gives the following ratio.

$$\frac{\sigma(ap \to a(N\pi))}{\sigma(ap \to ap)} \approx 0.11 \mp .02 \qquad (8.6)$$

$a \equiv \pi^{\mp}, K^-, p$

The results are independent of the beam particle type. At ISR energies for pp interactions, the following result was obtained.[31]

$$\frac{\sigma(n \to p\pi^-)}{\sigma(p \to p\pi^+\pi^-)} \approx 1.20 \mp .12 \qquad (8.7)$$

Using equation 8.3 gives:

$$\frac{\sigma(pn\rightarrow(p\pi^-)+X)}{\sigma(pp\rightarrow p+X)} \approx .05 \qquad (8.8)$$

From the isospin coupling of the 2-body states to the dissociating nucleon, the relative amplitude of $n\rightarrow p\pi^-$ and $n\rightarrow N\pi$ can be calculated (a factor of 3). Using equation 8.8 gives;

$$\frac{\sigma(pn\rightarrow(N\pi)+X)}{\sigma(pp\rightarrow p+X)} \approx .15 \qquad (8.9)$$

which is in reasonable agreement with equation 8.6. Finally, table 17 can be used to estimate the relative contributions of ($N^* \rightarrow p\pi^0$) and $N^{*+} \rightarrow n\pi^+$.

$$\frac{\sigma(N^{*+}\rightarrow p\pi^0)}{\sigma(N^{*+}\rightarrow n\pi^+)} \approx 1/2 \qquad (8.10)$$

Combining equations 8.10 and 8.9 gives the following upper limit on the unobserved 2-body N^* decays.

$$\frac{\sigma(\gamma p\rightarrow(p\pi^0)+X)}{\sigma(\gamma p\rightarrow p+X)} \approx .08 \qquad (8.11)$$

A reasonable estimate of the undetectable N^* decays would, therefore, not exceed about 10%.

The amount of N^*s present in the data was also estimated by two additional methods. The first method involved a direct

comparison between the Monte Carlo described in chapter 7 and the data. To make this comparison the following quantity was defined.

$$Rm = M_f/M_x \tag{8.12}$$

$M_f \equiv$ forward mass of all charged tracks

$M_x \equiv$ missing mass calculated by the recoil spectrometer

The forward mass was calculated by summing the 4-vectors of all charged tracks entering the downstream spectrometer and completing the resultant invariant mass. Before calculating the forward mass for the Monte Carlo generated events, the tracks were subjected to the geometrical acceptance criteria and weighted by the reconstruction efficiency, described in chapter 7. The results are shown in table 18 for the missing mass bins used in the data analysis. The value of Rm, calculated from the data, deviates from the value predicted by the Monte Carlo in the large missing mass region. As expected for N^* decays, the actual forward mass is less than the missing mass calculated using the proton that is produced in the N^* decay. To quantify the amount of N^*s necessary to account for the high missing mass deviations in the quantity Rm, N^* events were generated in the Monte Carlo and allowed to decay through 2 and 3 body decay modes. The missing mass M_x, used in the calculation of Rm, was calculated using the proton 4-vector resulting from the N^* decay. The results are shown in table 18, for a Monte Carlo data sample containing 10% N^*s. The amount of

N^*s was allowed to vary and the resulting distributions fit to the data distributions. The final N^* contribution was estimated to be 10 $\mp$5%.

In the second method for estimating the N^* contamination in the final data sample, the cuts used to select the final data sample were varied to study the effect on the quantity Rm. In addition to the "diffractive filter" discussed in chapter 6, a set of looser cuts and a set of tighter cuts were studied.

"Loose Cuts" - A proton was required to be identified in the recoil spectrometer, though additional charged tracks were allowed at the same vertex. No cuts were made on possible neutral tracks.

"Diffractive Filter" - A proton was required to be identified in the recoil spectrometer. No additional charged tracks were allowed anywhere in the detector. No cuts were made on possible neutral tracks.

"tight cuts" - A proton was required to be identified in the recoil spectrometer with no additional charged tracks in the detector. The event was rejected if there were any possible neutral tracks depositing more than 20 MeV in the calorimeter.

The results of the analysis for the three different data samples are shown in table 18. The quantity Rm for a given high

missing mass bin shows a net increase as the cuts are tightened, as expected if the number of N^*s are being reduced. The "diffractive filter" cuts account for about 60% of the total effect. If the initial data sample contained about 30% N^*s, the reduction of 60% by the diffractive filter would lead to an estimate of 12 $\mp$5% for the remaining N^* contamination in the data selected by the diffractive filter. This is consistent with the result obtained from the Monte Carlo study, and the prediction based on results from other experiments.

In the data analysis, the missing mass is calculated using the proton identified by the recoil spectrometer. If there are pi-zeroes associated with a nucleon resonance decay, the mass calculated from the recoil proton will differ from the actual forward mass of the system X (γ p -> (p π^0 ,p π^0 π^0) X). The difference between the forward mass and the missing mass calculated from the proton was calculated for the 2-body N^* diffractive process. N^*s were generated assuming the same t, missing mass, and photon energy distributions used in the acceptance Monte Carlo. In the center of mass of the N^*, the p,π^0 decay products were generated isotropically then Lorentz transformed back to the lab. reference frame. Finally, the missing mass was calculated using the proton and compared to the missing mass associated with the original N^*. Figure 47 shows this mass difference as a function of the missing mass calculated from the proton for an N* mass of 1.5 GeV (and a width of 200 MeV).

Secondary Interactions

After an incident photon interacts with a proton in the liquid hydrogen target, there is a possibilty that the particles produced in the primary interaction will themselves interact with a proton before exiting the target, thereby producing a secondary interaction. The probability for such an interaction can be expressed in the following form.

$$p = 1 - \exp(-L/\langle L\rangle) \tag{8.13}$$

L - path length from primary vertex to point where track leaves the target

$\langle L\rangle$ - mean free path

The mean free path is determined by the number of scattering centers per length and the cross section for an interaction.

$$\langle L\rangle = 1/(\rho \cdot N_0 \cdot \sigma \cdot A) \tag{8.14}$$

ρ - density of the liquid hydrogen

N_0 - Avagadro's number

σ - cross section

A - atomic number (for hydrogen A=1)

A typical hadronic cross section on protons has a value of about 20 millibarns. This leads to a mean free path in liquid hydrogen of

about 700 cm.

Particles were generated at the primary vertex according to a transverse momentum limited phase space model as described previously. The path length (L) was calculated for each generated particle and the probability for a secondary interaction determined. If the probability exceeded a random number generated between zero and one, a secondary interaction was generated randomly along the particle trajectory within the target. The following results were obtained from the Monte Carlo studies.

NUMBER OF EVENTS	4239
NUMBER OF EVENTS CONTAINING	
NO SECONDARY INTERACTIONS	3248
NUMBER OF EVENTS CONTAINING	
1 SECONDARY INTERACTION	858
NUMBER OF EVENTS CONTAINING	
2 SECONDARY INTERACTONS	121
NUMBER OF EVENTS CONTAINING	
MORE THAN 2 SECONDARY INTERACTIONS	12

In the total event sample 22% of the events contained at least one secondary interation.

Events were removed from the data base if there were additional charged tracks in the recoil spectrometer other than the recoiling proton from the primary interaction. This cut removed most of the events containing secondary interactions from the final

data analysis. The Monte Carlo was used to determine the number of events containing secondary interactions in which all tracks produced at the secondary interaction vertex would not enter the recoil spectrometer. These events would pass the recoil cut and contaminate the data used for the analysis.

In the Monte Carlo, tracks were generated at the secondary interaction vertex according to the P_t limited phase space model. The tracks were generated in the center of mass reference frame of the interacting particle and the proton at rest in the lab., then Lorentz transformed back to the lab. Each particle was then projected through the region upstream of the first analyzing magnet to determine if it entered the active region of the recoil spectrometer. The following results were obtained from the Monte Carlo studies.

NUMBER OF EVENTS CONTAINING	
SECONDARY INTERACTIONS	3525
NUMBER OF EVENTS WITH	
0 ADDITIONAL TRACKS IN RECOIL SPECTROMETER	658
1 ADDITIONAL TRACK IN RECOIL SPECTROMETER	1374
2 ADDITIONAL TRACKS IN RECOIL SPECTROMETER	1004
> 3 ADDITIONAL TRACKS IN RECOIL SPECTROMETER	489

From this information the percentage of interacting photons containing secondary interactions and passing the diffractive filter can be calculated.

$$N \approx (.22 \cdot .19) \cdot 100 = 4\% \qquad (8.15)$$

Missing Mass Resolution

The missing mass is defined in terms of the photon, target proton, and recoil proton 4-vectors.

$$M_x^2 = (E\gamma + P_0 - P) \cdot (E\gamma + P_0 - P) \qquad (8.16)$$

$E\gamma$ - photon 4-vector

P_0 - target proton 4-vector

P - recoil proton 4-vector

This expression can be written in terms of the recoil proton momentum, the photon energy, and the angle of the recoil proton relative to the photon direction.

$$M_x^2 = 2Mp^2 + 2(Mp \cdot E\gamma - Mp \cdot \sqrt{(p^2 + Mp^2)} + E\gamma \cdot p \cdot \cos\theta) \qquad (8.17)$$

Mp - mass of the proton

$E\gamma$ - photon energy

p - recoil proton momentum

θ - recoil proton angle

The error in the measured missing mass can then be expressed in terms of the contributions due to the errors in the three variables $(E\gamma, p, \cos\theta)$.

$$\delta M_x^2 = [(\frac{\partial M_x^2}{\partial E\gamma} \cdot \delta E\gamma)^2 + (\frac{\partial M_x^2}{\partial p} \cdot \delta p)^2 + (\frac{\partial M_x^2}{\partial \cos\theta} \cdot \delta\cos\theta)^2]^{1/2} \quad (8.18)$$

The partial derivatives can be evaluated from the above expression for Mx^2.

$$\frac{\partial M_x^2}{\partial E\gamma} = 2Mp + 2p \cdot \cos\theta \quad (8.19)$$

$$\frac{\partial N_x^2}{\partial p} = 2E\gamma \cdot \cos\theta - 2Mp \cdot p/\sqrt{(p^2+Mp^2)}$$

$$\frac{\partial M_x^2}{\partial \cos\theta} = 2E\gamma \cdot p$$

Errors were accumulated for the photon energy, proton momentum, and the recoil angle (θ) for those events used in the final data analysis. These errors were calculated by the photon energy and recoil track reconstruction programs for each event. Distributions of the errors for each of the three variables contributing to the missing mass error were generated and plotted as a function of the calculated missing mass. The error on the missing mass was then calculated for each event using the formula described previously. The missing mass error was then plotted as a function of missing mass for the events used in the final data analysis. Figure 48 contains plots of the missing mass resolution. The average resolution as a function of missing mass is also shown in figure 48.

Momentum Resolution

The momentum resolution was determined using events generated by the same Monte Carlo used to measure the reconstruction efficiency. Further details concerning the event generation and data smearing techniques can be found in chapter 7. The momentum determined by the fitting algorithm in the charged track reconstruction program for a Monte Carlo generated track was compared to the original momentum with which it was generated.

$$\frac{\delta P}{P} = \frac{P_{mc} - P_r}{P_{mc}} \qquad (8.20)$$

P_{mc} ≡ Monte Carlo generated momentum

P_r ≡ momentum determined by a fit to the reconstructed track

The momentum resolution distributions were complied for different P_r bins to determine the momentum dependence of the resolution. The results are summarized in table 19. The resolution is worse for tracks that can be tracked through D1 and D2 only, due to the limited aperture of the second analyzing magnet (M2). Since these are low momentum tracks, the overall resolution improves as the momentum increases until a minimum in $\delta p/p$ is reached at about 7.5 GeV/c, at which point the resolution gets worse as the momentum continues to increase.

Systematic Errors on Fit Parameters

In order to obtain an estimate of the systematic errors on the fit parameters for various distributions described in chapter 9, the acceptance Monte Carlo was used to study the affect of the error sources and resolutions described in this chapter. Distributions were generated by the Monte Carlo which contained the appropriate amount of N^* production and secondary interactions in the target. The resulting tracks which entered the forward spectrometer were smeared by the momentum resolution, and the missing mass calculated from the recoil proton was smeared by the missing mass resolution. These distributions were compared to clean Monte Carlo distributions which contained no resolution or systematic error effects. Both distributions were fit to determine the resulting errors on the fit parameters. These errors are contained in the fit tables described in chapter 9.

CHAPTER 9

DATA PRESENTATION

Jet Analysis

From a global perspective the most dominant feature of the data is its jet-like character in the forward center of mass. A jet-like topology has been observed in e+e- annihilation experiments[32,33,34,35,36], and in hadron and photon beam experiments [37,38,39]. As was pointed out in chapter 1, the presence of a jet-like topology does not imply the existence of quark jets. Jet-like structure can also be associated with soft hadronization processes.

The four jet variables discussed in chapter 6 are calculated and plotted against the missing mass. The data is plotted for each of the four different photon energy bins in figures 49 and 50. Table 20 contains a comparison between the results from this experiment and other experiments. The angle of the jet axis relative to the initial photon direction, determined by the sphericity method, is shown in figure 51 for the five different missing mass bins summed over photon energy. The data shows very clearly that the sphericity axis distribution becomes more sharply peaked at $\cos\theta=1$ as the missing mass increases. This is a reflection of the fact that as the missing mass increases the data deviates more and more from a uniform phase space distribution and

selects the photon direction as the relevant axis in the center of mass. To determine the orientation of the jet axis, two independent methods were used. Figure 52 [2 GeV<Mx<4 GeV], figure 53 [6 Gev <Mx< 8 GeV], and figure 54 [10 GeV<Mx<12 GeV] show the angular distribution of the jet axis as determined by the sphericity and thrust methods. The axis as determined by the two independent methods have very similar distributions.

This overall jet-like structure in the center of mass is also evident in figure 55, which shows the average P_t and $P_\parallel$ measured relative to the sphericity axis and plotted as a function of the missing mass. The average $P_\parallel$ fits well to a straight line which increases slowly as a function of mass. This rise is due to the fact that the average multiplicity does not increase as fast as the available energy. The multiplicity increases only as a logarithmic function of mass. We observe such a slow rise in the average multiplicity in our data. The average P_t, however, begins rising at low mass, then reaches a plateau and remains constant as the mass continues to rise. This behavior is also observed in e+e- and hadron initiated reactions. Figure 56 shows the distribution $dN/dP_\parallel$, normalized to unit area, for three different missing mass bins. $P_\parallel$ is again measured relative to the sphericity axis. The distributions differ primarily in the high $P_\parallel$ tail of the distributions. Figure 57 shows the distribution dN/dP_t (P_t measured relative to the sphericity axis), normalized to unit area, for three different missing mass bins. The two high mass distributions are nearly identical. The low mass distribution is, on the

other hand, significantly different, peaking at a lower P_t. The P_t and $P_\parallel$ distributions are consistent with the observation of a jet-like structure in the center of mass.

Inclusive Distributions

The rest of the data plots show inclusive distributions with all relevant variables measured relative to the photon beam direction. The recoil proton required by the diffractive filter appears in two sets of plots. The first set, figures 58-62, show the t distributions for the five different missing mass bins, summed over photon energy. Each distribution is fit to the following form.

$$\frac{dN}{dt} \propto e^{(At+Bt^2)} \qquad (9.1)$$

t_{min} effects begin to dominate the distributions for the high mass bins. The data is compiled in table 21 and the results of the fits are contained in table 22. The second set, figures 63 and 64, show the $X_\parallel$ distributions of the recoil proton as it appears in the initial center of mass. Figure 63 shows the distribution $dN/dX_\parallel$ for all observed tracks for three different missing mass bins. The recoil proton appears in the negative $X_\parallel$ region, well separated from the rest of the particles. Figure 64 shows only the recoil proton $X_\parallel$ distributions for all five missing mass bins. The curves in both figures 63 and 64 are not fits, only visual aids. The shift towards the central region in $X_\parallel$ as the mass

increases is a calculable kinematic effect which reflects the decreasing amount of energy available to the recoil proton.

The transverse momentum distributions of forward charged tracks shown in figures 65 and 66 reflect the P_t limiting character of the data. Table 23 shows some comparisons of the average transverse momentum with other experiments.[40,41] Figure 65 shows the distribution dN/dP_t, normalized to unit area, plotted for three different missing mass bins, summed over photon energy. The lowest mass bin P_t distribution deviates from the others in the high P_t tail of the distribution, being somewhat lower in magnitude resulting in a smaller average P_t. The two high mass P_t distributions are very similar throughout the range for which they are plotted. Figure 66 contains dN/dP_t^2 vs P_t^2, normalized to unit area, for the same missing mass bins, summed over the photon spectrum. The difference in the high P_t tails of the high and low mass distributions is more prominent. The P_t distribution for the different mass bins were fit to the following forms and summarized in the indicated tables.

$$\text{I)}\quad \frac{dN}{dP_t} \propto e^{(-A \cdot P_t)} \qquad \text{(table 24)} \qquad (9.2)$$

(fitted for different ranges of P_t)

$$\text{II)}\quad \frac{dN}{dP_t^2} \propto e^{(-A \cdot P_t^2)} + C \cdot e^{(-B \cdot P_t^2)} \qquad \text{(table 25)}$$

$[0.0 < P_t^2 < 1.0]$ $(GeV/c)^2$

Figures 67-71 show the P_t^2 distributions of forward charged tracks for each of the 5 missing mass bins. The solid line depicts

the results of fit II (the two component exponential in P_t^2). Table 25 contains some comparisons of these fit parameters to data from other experiments[41]. The data is compiled in table 26. The fits to the data show very clearly the presence of two components in the P_t distribution. Near $P_t = 0$, the slope is much steeper than for large P_t (near P_t=1 GeV/c). This feature of the data is also observed by other multi - hadron production experiments (table 25).

The rapidity distributions also reflect the jet-like character of the events in the forward center of mass. Figure 72 shows the distributions dN/dy for the five different missing mass bins summed over the photon spectrum. The different distributions are normalized in such a way that the central region plateaus overlap. The data is plotted in the forward center of mass for the forward hemisphere only (y>0). The most dominant feature of the rapidity distributions is the broadening of the central plateau, characteristic of events in which the average P_t remains constant while the average momentum increases. Figure 73 contains rapidity distributions for this experiment [2 GeV<M_X<4 GeV] and for the Mark I e+e- experiment[42,43] at SPEAR [Ecm=3.0 GeV], normalized to unit area. The two distributions are very similar. Figure 74 makes the same comparison for the missing mass bin [6 Gev<M_X<8 Gev] and e+e- [Ecm=7.4 GeV]. These distributions are also very similar, showing the same broadening of the central rapidity plateau.

There are several plots containing X and $X_{\parallel}$ distributions for both the initial and forward center of mass. All of these

inclusive distributions contain only data in the forward hemisphere ($X_{\parallel}>0$). The acceptance is quite good and slowly varying in this region, as shown in figures 44 and 45. In the initial center of mass, the forward hemisphere defines the photon fragmentation region and the distributions at large $X_{\parallel}$ ($X_{\parallel}\rightarrow 1$) should reflect the structure of the fragmentation process. The distributions are always plotted as a function of the center of mass energy (Ecm=$\sqrt{s}$ (photon energy) for the initial center of mass and Ecm=M_X (missing mass) for the forward center of mass). Various fits are made to provide a basis for comparisons with other experiments and with theoretical predictions. The fits also provide a quantitative measure of the center of mass energy dependence.

In the initial center of mass, the "normalized momentum" distributions dN/dX, normalized to unit area, are plotted in figure 75 for each of the four photon energy bins. All four distributions very nearly coincide, showing only a rather weak center of mass energy dependence. The data is compiled in table 27. Various fits were made to equations of the following form.

I) $$\frac{XdN}{dX} \propto (1-X)^{k1} + A(1-X)^{k2} \qquad (9.3)$$

II) $$\frac{XdN}{dX} \propto (1-X)^{k} \qquad (9.4)$$

3 regions
- $(0.3<X<1.0)$
- $(0.3<X<0.5)$
- $(0.5<X<1.0)$

III) $$\frac{XdN}{dX} \propto e^{(-A\cdot X)} \qquad (9.5)$$

3 regions
- $(0.3<X<1.0)$
- $(0.3<X<0.5)$
- $(0.5<X<1.0)$

These functional forms were motivated by the theoretical models discussed in chapter 1. The results of these fits are summarized in table 28. The fits show no significant dependence of the fit parameters on the center of mass energy.

The Feynman X distributions in the initial center of mass $dN/dX_{\parallel}$, normalized to unit area, are plotted in figure 76 for the four different photon energy bins. An additional plot, figure 77, contains the normalized invariant cross section $E^{*}d\sigma/(\sqrt{s})dX_{\parallel}$ for the four different photon energy bins. The data is compiled in table 29. Various fits were made to equations of the following form.

I) $$\frac{X_{\parallel}dN}{dX_{\parallel}} \propto (1-X_{\parallel})^{k1} + A(1-X_{\parallel})^{k2} \qquad (9.6)$$

II) $$\frac{X_{\parallel}dN}{dX_{\parallel}} \propto (1-X_{\parallel})^{k} \qquad (9.7)$$

3 regions
- $(0.2<X_{\parallel}<1.0)$
- $(0.2<X_{\parallel}<0.5)$
- $(0.5<X_{\parallel}<1.0)$

III) $$\frac{dN}{dX_{\parallel}} \propto e^{(-A\cdot X_{\parallel})} \qquad (9.8)$$

3 regions
- $(0.2<X_{\parallel}<1.0)$
- $(0.2<X_{\parallel}<0.5)$
- $(0.5<X_{\parallel}<1.0)$

A summary of the results of these fits is contained in table 30. In these fits there does seem to be a systematic increase in the slope at small $X_{\parallel}$ as the center of mass energy increases. The slope at

large $X_{\parallel}$, however, remains constant.

In the forward center of mass, the "normalized momentum" distributions dN/dX, normalized to unit area, are plotted in figure 78 for four of the missing mass bins. There is an obvious rise in the forward peak (X near zero) as the missing mass increases. The data is compiled in table 31. Identical fits were made in the forward center of mass as were made in the initial center of mass. The results of the fits are summarized in table 32. In this reference frame, there is a steady rise in the slope of the distribution for small X as the center of mass energy (missing mass) increases. The slope at large X shows no significant change.

The Feynman X distributions $dN/dX_{\parallel}$ in the forward center of mass, normalized to unit area, are plotted in figure 79 for three different missing mass bins. In addition, the invariant cross section $E^{*}d\sigma/(M_{X})dX_{\parallel}$, normalized to unit area, is plotted in figure 80 for the same missing mass plots. The data is compiled in table 33. Fits identical to those made in the initial center of mass determined the slopes for the different missing mass bins. The results are summarized in table 34. Once again there is a systematic rise in the slope for small $X_{\parallel}$ as the center of mass energy increases, while the slope for large $X_{\parallel}$ shows no significant change. In addition to the fits, some direct comparisons were made with some e+ e- data. Figure 81 shows the Feynman X distributions for data from this experiment [2 GeV$<M_{X}<$4 GeV] and e+e- data [Ecm=3.0 GeV][42,43]. The two distributions show very similar structure. Additional comparisons at different center of mass

energies are shown in figure 82 ([4 GeV<M_X<6 GeV] and e+e- [Ecm=4.8 GeV]) and figure 83 ([6 GeV<M_X<8 GeV] and e+e- [Ecm=7.4 GeV]). These distributions also show nearly identical structure.

The two component Feynman X fits (fit I as discussed previously) are drawn on plots of $\ln(X_{\parallel} dN/dX_{\parallel})$ versus $\ln(1-X_{\parallel})$ for the different missing mass bins in the forward center of mass and the different photon energy bins in the initial center of mass.

FIGURE 84	2<Mx<4 GeV	CMF
FIGURE 85	4<Mx<6 GeV	CMF
FIGURE 86	6<Mx<8 GeV	CMF
FIGURE 87	8<Mx<10 GeV	CMF
FIGURE 88	10<Mx<12 GeV	CMF
FIGURE 89	0<Eγ<75 GeV	CMI
FIGURE 90	75<Eγ<100 GeV	CMI
FIGURE 91	100<Eγ<125 GeV	CMI
FIGURE 92	125<Eγ<170 GeV	CMI

Table 35 lists some results of similar fits to $X_{\parallel}$ distributions made by other experiments.[8,44,45,46,47,48]

Scaling

As was noted in the previous discussion of the Feynman X distributions, for large $X_{\parallel}$ ($X_{\parallel}$>.5) the inclusive distributions have the same functional form. This implies that the inclusive

cross section can be factorized in the following manner.

$$\frac{d\sigma}{dX_\parallel} \propto f(ECM)\cdot g(X_\parallel) \qquad X_\parallel > .5 \qquad (9.9)$$

$$g(X_\parallel) = \frac{1-X_\parallel}{X_\parallel}$$

$ECM \equiv M_X$ forward center of mass

$\sqrt{s}$ initial center of mass

To make a quantitative measure of the rise in the inclusive cross section for $X_\parallel \simeq 0$, the unknown function f(ECM) is removed from consideration by dividing it out of the cross section.

$$h(ECM, X_\parallel) \propto \frac{d\sigma/dX_\parallel}{f(ECM)} \qquad (9.10)$$

The quantity R is defined as the ratio of the function h measured at different center of mass energies to the function h measured at some arbitrary point.

$$R_1(X_\parallel) = \frac{h(ECM_1, X_\parallel)}{h(ECM_0, X_\parallel)} \qquad (9.11)$$

$ECM_0 = 3.0$ GeV (M_X) CMF

11.1 GeV ($\sqrt{s}$) CMI

To determine R, the following procedure is used. The inclusive $X_\parallel$ distributions ($dN/dX_\parallel$) for each center of mass reference frame are normalized to each other in the region $X_\parallel > .5$. This is equivalent to setting the function f(ECM) equal to 1. The function R can then be determined from these normalized distributions.

$$R_1(X_\parallel) = \frac{(1/N_t^{\,i})\cdot(dN^i/dX_\parallel)}{(1/N_t^{\,0})\cdot(dN^0/dX_\parallel)} \qquad (9.12)$$

(i indexes the missing mass or photon energy bins)

$N_t^{\,i} \equiv$ number of tracks with $X_\parallel > .5$

The function R was calculated for different center of mass energy and $X_\parallel$ bins, for both center of mass reference frames. The results are contained in table 36. Figure 93 contains plots of R versus missing mass in the forward center of mass and R versus the photon energy in the initial center of mass for different $X_\parallel$ bins. The rise in the inclusive cross section as the center of mass energy increases is strongest at $X_\parallel = 0$. The rise gradually diminishes as $X_\parallel$ increases, disappearing completely at $X_\parallel \simeq .20-.25$.

Conclusions and Summary

Comparisons have been made between soft (or low P_t) hadronic, e+e- annihilation, and lepton-nucleon interactions which investigate multi-hadron production at high energies.[53] These studies have concluded that there is substantial agreement in the general characteristics of these different multiparticle production processes. These similarities have led some to conclude that there is a common underlying dynamical principle which describes all of these processes. It is important to note, however, that many of the characteristics of the data are consistent with different interpretations of the origins of the phenomena being investigated. One such interpretation describes the data in terms of soft hadronic

jets, as discussed in chapter 1.

We have observed that in high mass diffractive dissociation of photons, the global event topology reveals a jet-like structure with the jet axis closely associated with the initial photon direction. The mean sphericity, thrust, and spherocity which were plotted as a function of the missing mass clearly demonstrate that the jet-like structure of the events becomes more prominent as the center of mass energy increases. The dynamical behavior reflected by these variables is consistent with the limitation of the average P_t as the center of mass energy increases, while the average momentum increases linearly. This is a characteristic of all low P_t hadronic multiparticle production. These observations are consistent with the interpretation of the jets as the soft hadronization of the photon-pomeron interaction which was discussed in chapter 1. Other processes, such as e+e- annihilation results, also reveal a similar jet-like structure. The global jet variables cannot distinguish between quark jets and "soft" photon-pomeron jets.

We have made an extensive investigation of the inclusive rapidity, momentum, P_t, and Feynman x distributions over a broad range of center of mass energies. The rapidity distributions clearly show a central plateau which broadens as the center of mass energy increases. Comparisons with e+e- annihilation results show good agreement for different center of mass energies. Fits to the P_t^2 distributions reveal two exponential slopes. The exponential which fits the low P_t region has a slope which varies from 16 to

11 $(GeV/c)^{-2}$ in reasonable agreement with other hadron beam experiments. The high P_t region has a slope which varies from 3 to 4.5 $(GeV/c)^{-2}$ also in good agreement with other experiments. There is an indication that the slopes decrease as the center of mass energy increases.

The X and $X_\parallel$ distributions were fit to functional forms motivated by QCD counting rules believed to be valid near $X_\parallel \approx 1$. Our results give an exponent of 1 for fits above $X_\parallel = 0.5$, independent of the center of mass energy. This result is consistent with a calculation using the QCD counting rule for diquark fragmentation of a quark anti-quark system, as discussed in chapter 1.

$$X_\parallel \frac{dN}{dX_\parallel} \propto (1-X_\parallel)^n$$

$n \approx 1$ for $X_\parallel > 0.5$

In the central region ($X_\parallel \approx 0$), fits to these forms reveal a significant center of mass energy dependence. The value of the exponent n varies from 1.6 to 2.5 for $X_\parallel < 0.5$. This increase in the slope of the $X_\parallel$ distributions in the central region as the center of mass energy increases occurs in both the initial and forward center of mass. The same phenomena is observed in the X distributions.

The center of mass energy dependence of the $X_\parallel$ distributions in the central region leads to scaling violations. A quantitative measurement of this scaling violation is made relative to the large $X_\parallel$ ($X_\parallel > 0.5$) region where the inclusive cross section

is observed to scale with the center of mass energy. Scaling violations are observed from $X_{\parallel}=0$ to $X_{\parallel}=0.2$. The sharpest rise in the normalized cross section occurs at $X_{\parallel}=0$.

To summarize, high mass diffractive photoproduction provides an important tool for investigating soft hadronization processes. Serious attention has been focused on the significant similarities between the overall structure between such soft processes and hard collisions such as e+e- annihilation and deep inelastic lepton scattering. Various models proposed within the framework of QCD have attempted to address the dynamics of low P_t interactions, but the results are questionable due to the dominant non-perturbative nature of the process. Efforts to comprehend how these phenomena relate to QCD should provide a fruitful endeavor.

REFERENCES

1. J.J. Sakurai, Properties of the Fundamental Interactions Vol. 9 Part A ,243 (1973).

2. T. H. Bauer et al., Reviews of Modern Physics 50, 261 (1978).

3. J. D. Bjorken and E. A. Paschos, Physical Review 185,1975 (1969).

4. R. P. Feynman, Physical Review Letters 23, 1415 (1969).

5. C. Quigg, FERMILAB-CONF-80/64-THY, (1980).

6. J. Ellis, Th.2744 - CERN, (1979).

7. A. Rujula, Th.2739 - CERN, (1979).

8. J. F. Gunion, Partons in Soft-Hadronic Processes, 293 (1981); Proceedings of the Europhysics Study Conference, Erice, Italy.

9. U. Amaldi et al., Annual Review of Nuclear Science 26, 385 (1976).

10. U. Amaldi, Soviet Physics - USP 21, 328 (1978).

11. F.E. Low, Physical Review D12, 163 (1975);
S. Nussinov, Physical Review Letters 34, 1286 (1975);
Physical Review D14, 246 (1976).

12. A. R. White, CERN Th.3058, (1981).

13. T.A. DeGrand and J. Randa, Physics Letters 110B, 484 (1982).

14. J. Randa, Physical Review D23, 1662 (1981).

15. S. F. King et al., Nuclear Physics B167, 98 (1980).

16. J. F. Gunion, SLAC - PUB - 2607, (1980).

17. Tung-mon Yan, Annual Review of Nuclear Science 26, 199 (1976).

18. H. Hinterberger and R. Winston, Review of Scientific Instruments 37, 1094 (1966)

19. D. F. Bartlett, A. L. Duncan, and J. R. Elliott, Review of Scientific Instruments 52, 265 (1981).

20. E. Barsotti et al., IEEE Trans. Nucl. Sci. 26, 686 (1979).

21. G. Hanson et al., Physical Review Letters 35, 1609 (1975).

22. De Rujula et al., Nuclear Physics B138, 387 (1978).

23. S. Brandt et al., Physics Letters 12, 57 (1964).

24. R. Devenish, Surveys in High Energy Physics 1, 1 (1979).

25. D.C. Carey and d. Drijard, Journal of Computational Physics, 28, 327 (1978).

26. Z. Koba et al., Nuclear Physics B40, 317 (1972).

27. K. Goulianos, Rockefeller University Report No. DOE/ER/40033-20

28. Baksay et al., Physics Letters 53B, 485 (1975).

29. C. Berger et al., Physics Letters 95B, 313 (1980).

30. R. Webb et al., Physics Letters 55B, 331 (1975).

31. M. G. Albrow et al., Nuclear Physics B54, 6 (1973).

32. R. Webb et al., Physics Letters 55B, 336, (1975).

33. Berger et al., Physics Letters 78B, 176 (1978).

34. B. H. Wiik, DESY 80/129, (1980).

35. S. L. Wu, DESY 81/003, (1981)

36. P. Duinker, DESY 81/012, (1981)

37. P. Soding and G. Wolf, DESY 81/013, (1981).

38. D. Aston et al., Nuclear Physics B166, 1 (1980).

39. M. Basile et al., Physics Letters 92B, 367 (1980).

40. J. Wdowczyk and A. W. Wolfendale, Nuovo Cimento 54A, 433 (1979).

41. Eisenberg et al., Nuclear Physics B154, 239 (1979).

42. V. Luth, Proceedings of Summer Institute on Particle Physics (SLAC-204), 219 (1977).

43. K. C. Moffeit, Proceedings of Summer Institute on Particle Physics (SLAC-204), 181 (1977).

44. D. Cutts et al., Physical Review Letters 43, 319 (1979).

45. J. Laurent et al., Nuclear Physics B149, 189 (1979).

46. Crouch et al., Physical Review Letters 13, 640 (1964).

47. Brandelik et al., Nuclear Physics B148, 189 (1979).

48. D. Denegri et al., Physics Letters 95B, 127 (1981).

49. J. L. Seigrist et al., SLAC-PUB-2834, (1981).

50. V. Akimov et al., Physical Review Letters 39, 1432 (1977).

51. I. Yotsuyanagi et al., Physical Review D19, 19 (1979).

52. G. Feldman and M. Perl, SLAC-PUB-1972.

53. W. Kittel, Partons in Soft-Hadronic Processes, 1 (1981); Proceedings of the Europhysics Study Conference, Erice, Italy.

TABLE 1

PRINCIPAL BEAM COMPONENTS

QUADRAPOLE DOUBLETS	QH409, QV410 QH436, QV435
HORIZONTAL BENDS	BH415 BH425 BH438
VERTICAL BENDS	BV410 BV426 BV437
VERTICAL COLLIMATORS	CV409 CV423
HORIZONTAL COLLIMATORS	CH410 CH423
FIELD LENS	QH423
TAGGING MAGNET	AN440
SWICS (used to measure beam position)	SC404 SC405 SC425 SC435 SC440 SC441 SC442

TABLE 2

TAGGING SYSTEM LEAD GLASS BLOCKS

COUNTER	DESCRIPTION	DIMENSIONS (cm)
L1 - L2	Pb - Lucite	6.35 x 6.35 x 25.4
L3 - L8	Pb - Glass	6.35 x 6.35 x 58.4
L9 - L13	Pb - Glass	12.7 x 12.7 x 50.8

TABLE 3

TAGGED PHOTON SPECTROMETER SPECIFICATIONS

COMPONENT		X (cm)	Y (cm)	ANGULAR ACCEPTANCE (radians)	Z(FRONT) (cm)	Z(BACK) (cm)
RECOIL SPECTROMETER		cylindrical r=105.5			484.4	724.3
TARGET		cylindrical r=2.5			474.4	624.3
M1		91.4	40.4	θ_x<.259 θ_y<.114	917.7	902.6
D1		61.0	34.9	θ_x<.234 θ_y<.134	757.5	810.0
D2		137.2	68.6	θ_x<.301 θ_y<.151	917.7	1005.1
OUTRIGGERS	INNER	182.9	27.9	θ_x<.258	1020.9	1049.9
	OUTER	182.9	119.3	.039<θ_y<.168		
M2		91.4	40.6	θ_x<.129 θ_y<.057	1050.9	1259.0
C1		76.2	38.6	θ_x<.147 θ_y<.043	1066.4	1440.2
D3		152.4	68.6	θ_x<.152 θ_y<.068	1463.6	1551.2
C2		158.7	94.0	θ_x<.154 θ_y<.091	1583.2	2243.0
D4		243.8	121.9	θ_x<.142 θ_y<.071	2258.1	2269.5
SLIC		243.8	121.9	θ_x<.142 θ_y<.063	2367.0	2488.9
HADROMETER		243.8	137.2	θ_x<.110 θ_y<.062	2496.9	2771.2

TABLE 4

RECOIL CALORIMETER SEGMENTATION

LAYER	DESCRIPTION	PHOTOTUBES/SECTOR
A	Plastic Scintillator Depth - 5 cm Length - 215 cm	4 Phototubes Upstream (3 RCA 4902 - 2 inch) (1 RCA 6342 - 2 inch) 1 Phototube Downstream (1 RCA 5680 AVP - 2 inch)
B	Plastic Scintillator Depth - 5 cm Length - 240 cm	4 Phototubes (4 RCA 4902 - 2 inch)
C	Liquid Scintillator Depth - 16 cm Length - 240 cm Wall Thickness - .11 inches	2 Phototubes (2 RCA 6300 - 5 inch)
D	Liquid Scintillator Depth - 10 cm Length - 240 cm Wall Thickness - .11 inches	3 Phototubes (RCA 4900 - 3 inch)

Each layer has 15 sectors.

TABLE 5

CHARACTERISTICS OF THE CERENKOV COUNTERS

QUANTITY	C1	C2
GAS MIXTURE	100% N_2	80% He 20% N_2
LENGTH	3.7 meters	6.6 meters
INDEX OF REFRACTION	1.00027	1.00012
CERENKOV ANGLE	25 mrad	14 mrad
THRESHOLD FOR PIONS	6.0 GeV/c	9.1 GeV/c
THRESHOLD FOR KAONS	20 GeV/c	36 GeV/c
THESHOLD FOR PROTONS	38 GeV/c	69 GeV/c

TABLE 6

CERENKOV COUNTERS CELL DIMENSIONS

CELL	C1(WIDTH,HEIGHT) inches	C2(WIDTH,HEIGHT) inches
1-1	4.0 , 8.0	10.0 , 18.0
1-2	8.0 , 8.0	20.0 , 18.0
1-3	38.0 , 8.0	65.0 , 18.0
1-4	12.0 , 16.0	30.0 , 32.0
1-5	38.0 , 16.0	65.0 , 32.0

TABLE 7

D1 SPECIFICATIONS

PLANE	NUMBER OF WIRES	CELL SIZE (INCHES)	HIGH VOLTAGE (KV) (FIELD WIRES)
D1A - U (SENSE)	192	.169	1.72
V (SENSE)	192	.169	1.72
(HV)			2.28
D1A X'(SENSE)	32	.187	1.72
X (SENSE)	192	.187	1.72
(HV)			2.28
D1B - U (SENSE)	256	.169	1.67
V (SENSE)	256	.169	1.67
(HV)			2.28
D1B - X'(SENSE)	32	.187	1.8
X (SENSE)	256	.187	1.8
(HV)			2.3

TABLE 8

D2 AND D3 SPECIFICATIONS

PLANE	NUMBER OF WIRES	CELL SIZE (INCHES)	HIGH VOLTAGE (KV) (FIELD WIRES)
(D2A,D2B)			
U	176	.337	2.0
X	192	.375	2.05
V	176	.337	2.0
(HV)			2.3
(D2C)			
U	208	.337	2.0
X	224	.375	2.05
V	208	.337	2.0
(HV)			2.3
(D3A,D3B,D3C)			
U	160	.562	2.0
X	160	.625	2.05
V	160	.562	2.0
(HV)			2.3

TABLE 9

D4 SPECIFICATIONS

PLANE	NUMBER OF WIRES	CELL SIZE (INCHES)	HIGH VOLTAGE (KV) (SENSE WIRES)
(D4)			
U	128	1.125	2.7
X	160	1.25	2.7
V	128	1.125	2.7

TABLE 10

DRIFT CHAMBER RESOLUTIONS AND EFFICIENCIES

PLANE		RESOLUTION (microns)	EFFICIENCY %
D1A	U	380	92
	X	300	99
	V	425	98
	X'	340	99
D1B	U	360	96
	X	250	99
	V	380	96
	X'	230	99
D2A	U	310	98
	X	350	97
	V	300	96
D2B	U	310	99
	X	350	97
	V	290	99
D2C	U	320	99
	X	340	95
	V	310	97
D3A	U	300	99
	X	350	99
	V	310	99
D3B	U	280	99
	X	320	99
	V	270	99
D3C	U	290	99
	X	330	99
	V	290	99
D4A	U	700	99
	X	700	99
	V	700	99

TABLE 11

CERENKOV CALIBRATION CONSTANTS

C1 (CELL NUMBER)	NPE(MAX)	GAIN	C2 (CELL NUMBER)	NPE(MAX)	GAIN
1-1	8.3	15.0	1-1	5.2	14.0
1-2	8.9	15.5	1-2	5.2	14.0
1-3	5.8	16.0	1-3	7.1	16.5
1-4	13.2	16.5	1-4	7.1	14.5
1-5	6.3	18.0	1-5	3.5	13.0
2-1	8.6	14.0	2-1	6.7	13.5
2-2	6.5	16.0	2-2	6.9	13.5
2-3	2.1	19.0	2-3	4.5	15.0
2-4	10.1	16.5	2-4	5.5	15.5
2-5	3.5	18.0	2-5	2.1	15.0
3-1	6.9	12.5	3-1	4.4	15.0
3-2	5.2	16.5	3-2	1.8	12.5
3-3	4.1	19.0	3-3	4.4	14.5
3-4	7.1	16.5	3-4	5.3	14.5
3-5	5.1	16.0	3-5	5.1	13.5
4-1	5.5	16.0	4-1	2.1	14.0
4-2	6.2	16.0	4-2	6.2	15.5
4-3	4.4	19.0	4-3	6.1	16.0
4-4	5.7	15.5	4-4	4.3	14.0
4-5	7.2	16.0	4-5	6.7	16.5

TABLE 12

TAGH DISCRIMINATOR SETTINGS

X	ATTENUATOR	THRESHOLD(MILLIVOLTS)
.2	2.8 db	66.5
.3	4.2 db	99.7
.4	5.6 db	133.0
.5	7.0 db	166.0
.6	8.4 db	199.0
.7	9.8 db	232.0
.8	11.2 db	266.0

TABLE 13

ON LINE HARDWARE/SOFTWARE

HARDWARE

1	PDP 11/55
3	JORWAY 411 BRANCH DRIVERS
1	BISON BOX (COMMUNICATION LINK TO TRIGGER LOGIC)
2	STC 6250 TAPE DRIVES
	DISK STORAGE:
2	RL02
2	RK05
1	VERSATEC PRINTER/PLOTTER
4	INTERACTIVE TERMINALS
3	038 GRAPHICS TERMINALS

SOFTWARE

RSX 11M V3.2 OPERATING SYSTEM

DATA ACQUISITION

MONITOR:
- SCHEDULING (LINK TO MULTI)
- HIGH/LOW VOLTAGE MONITOR

MULTI (DATA ANALYSIS)

LINK TO BEAM LINE COMPUTER

TABLE 14

SCALER MONITOR LIST

1.) Tagging Channels

2.) Recoil Triggers

3.) TAGH (hadronic trigger)

4.) Number of events written to tape

5.) Beam Intensity

6.) Special Calibration Triggers

7.) Tagging Rate

8.) Magnet Currents

9.) Number of hits in drift chamber planes

10.) Number of hits in PWC chambers

11.) Clears (signals generated to clear ADCs if event aborted)

12.) Low Level Trigger Rates

TABLE 15

EFFICIENCIES OF RECOIL DETECTOR COMPONENTS

COMPONENT	REDUNDANT COMPONENTS	EFFICIENCY
PWC	PWC - MIDDLE, OUTER CATHODES	.83
INNER CATHODE	END TO END TIMING	∓ .02
	A,B,(C,D) LAYERS	
PWC	PWC - INNER, OUTER CATHODES	.85
MIDDEL CATHODE	END TO END TIMING	∓ .03
	A,B,(C,D) LAYERS	
PWC	PWC - INNER, MIDDLE CATHODES	.94
OUTER CATHODE	END TO END TIMING	∓ .03
	A,B,(C,D) LAYERS	
END TO END	ALL PWC CATHODES	.98
TIMING	A,B,(C,D) LAYERS	∓ .05
A - LAYER	ALL PWC CATHODES	.94
	END TO END TIMING	∓ .06
	B,C,(D) LAYERS	
	TIME OF FLIGHT	

TABLE 15 (CONTINUED)

B - LAYER	ALL PWC CATHODES	.98
	END TO END TIMING	∓ .07
	A,C LAYERS	
	TIME OF FLIGHT	
C - LAYER	ALL PWC CATHODES	.94
	END TO END TIMING	∓ .03
	A,B,D LAYERS	
	TIME OF FLIGHT	
PWC	PWC - MIDDLE, OUTER ANODES	.92
INNER ANODE	END TO END TIMING	∓ .02
	A,B,(C,D) LAYERS	
PWC	PWC - INNER, OUTER ANDODES	.95
MIDDLE ANODE	END TO END TIMING	∓ .03
	A,B,(C,D) LAYERS	
PWC	PWC - INNER, MIDDLE ANODES	.92
OUTER ANODE	END TO END TIMING	∓ .03
	A,B,(C,D) LAYERS	

TABLE 16

GEOMETRICAL ACCEPTANCE CRITERIA

DEVICE	ANGULAR ACCEPTANCE			
	FRONT OF TARGET		BACK OF TARGET	
	θ_x	θ_y	θ_x	θ_y
M1	.213	.094	.328	.145
M2	.116	.052	.144	.064
D1	.182	.104	.328	.188
D2	.258	.129	.360	.180
D3	.141	.064	.164	.109
D4	.136	.068	.148	.074

TABLE 17

NUCLEON RESONANCE DECAYS

2 - PARTICLE DECAYS DECAY MODE	ISOSPIN I_1, I_1^3	I_2, I_2^3	CLEBSCH-GORDAN COEFFICIENT
$p\ \pi^0$	(1/2,1/2)	(1,0)	$\sqrt{1/3}$
$n\ \pi^+$	(1/2,-1/2)	(1,1)	$\sqrt{2/3}$

3 - PARTICLE DECAYS DECAY MODE	ISOSPIN I_1, I_1^3	I_2, I_2^3	I_3, I_3^3	CLEBSCH-GORDAN COEFFICIENT
$\Delta^{++}\ \pi^- \rightarrow p\ \pi^+\ \pi^-$	(1/2,1/2)	(1,1)	(1,-1)	$\sqrt{1/2}$
$\Delta^+\ \pi^0 \rightarrow p\ \pi^0\ \pi^0$	(1/2,1/2)	(1,0)	(1,0)	$\sqrt{2/9}$
$\Delta^+\ \pi^0 \rightarrow n\ \pi^+\ \pi^0$	(1/2,-1/2)	(1,1)	(1,0)	$\sqrt{1/9}$
$\Delta^0\ \pi^+ \rightarrow p\ \pi^-\ \pi^+$	(1/2,1/2)	(1,-1)	(1,1)	$\sqrt{1/18}$
$\Delta^0\ \pi^+ \rightarrow n\ \pi^0\ \pi^+$	(1/2,-1/2)	(1,0)	(1,1)	$\sqrt{2/18}$
$p\ \pi^0\ \pi^0$	(1/2,1/2)	(1,0)	(1,0)	$\sqrt{1/3}$
$p\ \pi^+\ \pi^-$	(1/2,1/2)	(1,1)	(1,-1)	$\sqrt{2/3}$
$n\ \pi^+\ \pi^0$	(1/2,-1/2)	(1,1)	(1,0)	$\sqrt{2/3}$

TABLE 18

$Rm = M_f/M_x$

DATA STUDIES

M_x (GeV)	"Loose Cuts"	"Diffractive Filter"	"Tight cuts"
[2,4]	0.599 ∓.003	0.598 ∓.003	0.584 ∓.003
[4,6]	0.440 ∓.003	0.446 ∓.003	0.454 ∓.003
[6,8]	0.339 ∓.004	0.353 ∓.004	0.366 ∓.004
[8,10]	0.280 ∓.005	0.293 ∓.005	0.301 ∓.005
[10,12]	0.237 ∓.010	0.251 ∓.010	0.240 ∓.010

MONTE CARLO STUDIES

N_x (GeV)	$\Delta Rm/Rm$ % diffractive	$\Delta Rm/Rm$ % diffractive + 10% N^*
[2,4]	3.0 ∓1.	3.0 ∓1.
[4,6]	-3.0 ∓1.	-3.0 ∓1.
[6,8]	0.5 ∓1.	-.05 ∓1.
[8,10]	6.5 ∓1.5	.05 ∓1.5
[10,12]	12.0 ∓2.0	3.0 ∓2.0

TABLE 19

MOMENTUM RESOLUTION

MOMENTUM (GeV/c)	$\delta p/p$ %
[0,5]	4.5 ∓0.2
[5,10]	3.2 ∓0.2
[10,15]	2.6 ∓0.2
[15,20]	3.0 ∓0.2
[20,25]	3.4 ∓0.3
[25,30]	5.4 ∓0.7
[30,40]	5.8 ∓0.8
[40,50]	7.4 ∓1.0
[50,75]	9.2 ∓1.0
[75,100]	8.9 ∓1.5

TABLE 20

SPHERICITY

$\langle M_x \rangle$ (GeV)	$\langle S \rangle$ (this experiment)		$\langle S \rangle$ (PLUTO)		$.75W^{-1}/^2$ (PETRA fit)
3.08	.35	$\mp$.01 ($\mp$.01)	.38	$\mp$.01	.430
5.02	.347	$\mp$.004 ($\mp$.01)	.365	$\mp$.01	.335
6.96	.33	$\mp$.01 ($\mp$.01)	.32	$\mp$.01	.284
8.76	.30	$\mp$.02 ($^{-.02}_{+.01}$)	.28	$\mp$.02	.253
10.59	.26	$\mp$.02 ($^{-.03}_{+.01}$) *	.23	$\mp$.02	.231

THRUST

$\langle M_x \rangle$ (GeV)	$\langle 1-T \rangle$ (this experiment)		$\langle 1-T \rangle$ (PLUTO)	
3.08	.192	$\mp$.005 ($\mp$.01)	.23	$\mp$.01
5.02	.196	$\mp$.002 ($\mp$.01)	.22	$\mp$.01
6.96	.194	$\mp$.004 ($\mp$.01)	.195	$\mp$.01
8.76	.18	$\mp$.01 ($^{-.02}_{+.01}$)	.185	$\mp$.01
10.59	.17	$\mp$.01 ($^{-.03}_{+.01}$) *	.165	$\mp$.01

* extrapolated from lower energy data

TABLE 21

t RECOIL PROTON

t Gev^2	Mx [2,4]	Mx [4,6]	Mx [6,8]	Mx [8,10]	Mx [10,12]
0.-.1	21413	20011	7121	389	0
	(372)	(394)	(281)	(156)	(0)
.1 -.2	13958	16035	10036	1600	0
	(199)	(213)	(185)	(95)	(0)
.2 -.3	7596	9368	8643	3182	248
	(155)	(172)	(180)	(137)	(92)
.3 -.4	3869	6131	8109	4375	631
	(111)	(141)	(179)	(165)	(95)
.4 -.5	2805	3663	5335	4115	1354
	(94)	(110)	(145)	(162)	(136)
.5 -.6	1871	2638	4166	3749	980
	(77)	(93)	(129)	(159)	(106)
.6 -.7	1184	1905	3458	2949	988
	(61)	(79)	(113)	(130)	(100)
.7 -.8	595	1420	2768	2637	877
	(44)	(68)	(104)	(123)	(84)
.8 -.9	403	1072	2143	2467	876
	(36)	(60)	(88)	(118)	(84)
.9 -1.0	189	789	1804	2513	918
	(25)	(51)	(83)	(128)	(91)
1.0-1.1	148	497	1387	1790	920
	(22)	(41)	(76)	(103)	(88)
1.1-1.2	112	490	1023	1498	634
	(19)	(42)	(62)	(99)	(75)
1.2-1.3	161	382	879	1128	578
	(23)	(36)	(58)	(84)	(75)
1.3-1.4	129	274	717	1149	588
	(20)	(30)	(57)	(94)	(79)
1.4-1.5	87	299	529	772	366
	(17)	(32)	(45)	(74)	(58)
1.5-1.6	113	184	428	676	333
	(16)	(28)	(36)	(42)	(25)
1.6-1.7	65	159	316	554	241
	(15)	(24)	(35)	(61)	(46)
1.7-1.8	23	99	265	429	226
	(9)	(18)	(35)	(50)	(47)
1.8-1.9	39	90	202	350	140
	(11)	(17)	(31)	(51)	(34)
1.9-2.0	46	107	152	245	71
	(12)	(19)	(25)	(38)	(24)

TABLE 22

t - RECOIL PROTON (fits)

$dN/dt = C \cdot \exp(-(At+Bt^2))$

t RANGE (GeV^2)	Mx (GeV)	A		B		χ^2/DOF
0.1< t <1.0	[2,4]	6.15	∓.2	-1.1	∓.2	9.7
0.1< t <1.0	[4,6]	6.0	∓.2	-2.1	∓.2	1.2
0.3< t <1.2	[6,8]	3.4	∓.3	-.7	∓.2	3.6
0.5< t <1.5	[8,10]	0.07	∓.5	0.8	∓.2	3.0
0.5< t <1.5	[10,12]	-2.0	∓1.0	1.5	∓.5	1.0

TABLE 23

AVERAGE P_t AND P_t^2

	CENTER OF MASS ENERGY (GeV)	$\langle P_t \rangle$	$\langle P_t^2 \rangle$	
$K^+p \to h^{\mp}X$	11.5	.327 ∓.001	.160 ∓.001	total
		.332 ∓.001	.164 ∓.001	
		.294 ∓.002	.135 ∓.002	diffractive
$pn \to \pi^-X$	19.1	.336 ∓.003		backward hemishpere
		.350 ∓.005		forward hemisphere
$pn \to \pi^+X$	19.1	.341 ∓.004		backward hemisphere
		.361 ∓.004		forward hemisphere
$\pi^+n \to \pi^-X$	19.1	.336 ∓.006		backward hemisphere
		.340 ∓.006		forward hemishpere
$\pi^+n \to \pi^+X$	19.1	.327 ∓.005		backward hemisphere
		.388 ∓.006		forward hemisphere
$pn \to pX$	19.1	.454 ∓.010		backward hemisphere
		.472 ∓.0013		forward hemisphere
$\pi^+ \to pX$	19.1	.478 ∓.015		
$pp \to \pi^-X$	19.6	.336 ∓.003		
$pp \to \pi^+X$	19.6	.373 ∓.002		
$pn \to \pi^-X$	4.7	.299 ∓.006		

	MISSING MASS (Gev)	$\langle P_t \rangle$	$\langle P_t^2 \rangle$	
$\gamma p \to h^{\mp}X$	2-3	.296 ∓.001	.137 ∓.001	this
	3-4	.316 ∓.001	.155 ∓.001	experiment
	4-5	.325 ∓.001	.163 ∓.001	
	5-6	.331 ∓.001	.166 ∓.001	
	6-7	.332 ∓.001	.168 ∓.001	
	7-8	.336 ∓.001	.171 ∓.001	
	8-9	.336 ∓.001	.172 ∓.001	
	9-10	.333 ∓.002	.170 ∓.002	
	10-11	.335 ∓.003	.174 ∓.003	
	11-12	.325 ∓.006	.168 ∓.006	

TABLE 24

P_t - FITS

$$dN/dP_t = C \cdot \exp(-A \cdot P_t)$$

Mx (GeV)	A ($0.3<P_t<2.0$)	A ($0.3<P_t<1.0$)	A ($1.0<P_t<2.0$)
[2,4]	4.97 ∓.03 (∓.1)	4.49 ∓.03 (∓.1)	4.8 ∓.3 (∓.1)
χ^2/DOF	11.5	11.4	.87
[4,6]	4.36 ∓.03 (∓.1)	4.08 ∓.03 (∓.1)	4.3 ∓.2 (∓.1)
χ^2/DOF	11.5	11.8	1.9
[6,8]	4.21 ∓.03 (∓.1)	4.06 ∓.04 (∓.1)	4.0 ∓.1 (∓.1)
χ^2/DOF	7.1	9.0	2.8
[8,10]	4.09 ∓.04 (∓.1)	4.01 ∓.04 (∓.1)	3.7 ∓.2 (∓.1)
χ^2/DOF	4.3	8.2	1.3
[10,12]	4.04 ∓.06 (∓.1)	3.89 ∓.06 (∓.1)	4.3 ∓.5 (∓.1)
χ^2/DOF	.52	.53	.31

	A ($0.5<P_t<2.0$)	A ($0.5<P_t<1.0$)	A ($0.8<P_t<2.0$)
[2,4]	5.48 ∓.02 (∓.1)	5.29 ∓.09 (∓.1)	5.3 ∓.1 (∓.1)
χ^2/DOF	2.2	2.1	1.7
[4,6]	4.66 ∓.03 (∓.1)	4.49 ∓.05 (∓.1)	4.7 ∓.1 (∓.1)
χ^2/DOF	2.7	1.2	2.8
[6,8]	4.36 ∓.03 (∓.1)	4.37 ∓.06 (∓.1)	4.2 ∓.07 (∓.1)
χ^2/DOF	3.2	1.1	3.4
[8,10]	4.23 ∓.05 (∓.1)	4.44 ∓.08 (∓.1)	4.0 ∓.1 (∓.1)
χ^2/DOF	2.2	.85	1.5
[10,12]	4.11 ∓.1 (∓.1)	3.8 ∓.2 (∓.1)	4.4 ∓.2 (∓.1)
χ^2/DOF	.42	.41	.27

* systematic errors are shown in parenthesis

TABLE 25

P_t^2 - FITS

$$dN/dP_t^2 = A \cdot \exp(-B \cdot P_t^2) + C \cdot \exp(-D \cdot P_t^2)$$

$$(0 < P_t^2 < 1.0)$$

Mx (Gev)	C/A	B	D	χ^2/DOF
$\gamma p \to h^{\mp} X$ (this experiment)				
[2,4]	.34 ∓.03 (∓.01)	16.1 ∓.9 (∓.5)	4.6 ∓.15 (∓.1)	1.7
[4,6]	.26 ∓.02 (∓.01)	11.0 ∓.4 (∓.3)	3.5 ∓.35 (∓.1)	.48
[6,8]	.49 ∓.03 (∓.02)	13.3 ∓.6 (∓.5)	3.8 ∓.09 (∓.1)	12.7
[8,10]	.52 ∓.04 (∓.02)	12.6 ∓.9 (∓.5)	3.8 ∓.1 (∓.1)	3.5
[10,12]	.28 ∓.07 (∓.02)	10.7 ∓1.2 (∓.6)	3.1 ∓.4 (∓.1)	.75
BEAM MOMENTUM (GeV/c)				
$pn \to \pi^- X$ 195	.30 ∓.04	19.5 ∓1.6	4.6 ∓.3	1.6
$pp \to \pi^- X$ 205	.26 ∓.04	14.6 ∓.3	4.0 ∓.3	.89
$pn \to \pi^- X$ 11.6	.23 ∓.05	11.6 ∓1.1	4.0 ∓.3	2.2
$pn \to \pi^+ X$ 195	.29 ∓.03	20.2 ∓1.7	4.3 ∓.3	1.9
$pp \to \pi^+ X$ 205	.25 ∓.01	14.7 ∓.6	3.2 ∓.1	.32
$\pi^+ \to \pi^- X$ 195	.26 ∓.05	20.7 ∓2.6	4.6 ∓.5	2.0
$\pi^+ n \to \pi^+ X$ 195	.32 ∓.04	21.1 ∓2.1	4.4 ∓.3	1.1

TABLE 26

P_t

Pt (GeV/c)	Mx [2,4]	Mx [4,6]	Mx [6,8]	Mx [8,10]	Mx [10,12]
0.-.1	21872	27395	29295	19230	5428
	(650)	(440)	(444)	(437)	(284)
.1 -.2	42212	57808	62510	40361	10933
	(687)	(587)	(618)	(598)	(362)
.2 -.3	45012	61020	66392	42167	11004
	(626)	(565)	(612)	(588)	(340)
.3 -.4	35539	49695	53294	33229	8684
	(516)	(496)	(535)	(505)	(301)
.4 -.5	24449	35891	38290	24841	6248
	(410)	(420)	(451)	(439)	(265)
.5 -.6	16361	23805	25594	16692	4058
	(340)	(338)	(364)	(371)	(197)
.6 -.7	10164	15643	16376	10651	2596
	(278)	(281)	(291)	(272)	(158)
.7 -.8	6058	9989	11048	7214	1860
	(239)	(238)	(248)	(231)	(138)
.8 -.9	3257	6209	6918	4365	1338
	(182)	(204)	(198)	(177)	(117)
.9 -1.0	1816	3792	4318	2760	826
	(150)	(173)	(163)	(143)	(115)
1.0-1.1	924	2258	2748	1835	547
	(60)	(128)	(107)	(112)	(74)
1.1-1.2	581	1341	1711	1259	322
	(45)	(71)	(86)	(93)	(54)
1.2-1.3	346	849	1027	775	214
	(34)	(56)	(55)	(56)	(43)
1.3-1.4	189	476	715	539	135
	(26)	(42)	(45)	(56)	(34)
1.4-1.5	109	316	530	331	91
	(17)	(34)	(47)	(44)	(26)
1.5-1.6	73	211	448	305	69
	(16)	(28)	(36)	(42)	(25)
1.6-1.7	51	188	248	151	42
	(14)	(27)	(27)	(31)	(15)
1.7-1.8	24	133	117	200	42
	(10)	(22)	(22)	(39)	(20)
1.8-1.9	29	75	106	88	7
	(10)	(17)	(22)	(18)	(5)
1.9-2.0	21	59	85	61	7
	(8)	(15)	(19)	(17)	(5)

TABLE 27

X - CMI

X CMI	Eγ [0,75] GeV	Eγ [75,100]	Eγ [100,125]	Eγ [125,170]
0.0-.04	9326	31175	29416	28833
	(187)	(364)	(256)	(324)
.04-.08	20232	60977	54288	48211
	(284)	(499)	(458)	(420)
.08-.12	19174	49465	35772	29667
	(281)	(448)	(368)	(327)
.12-.16	13524	30855	22948	18476
	(224)	(350)	(296)	(260)
.16-.20	9677	21890	15852	12140
	(190)	(302)	(248)	(208)
.20-.24	6713	15275	10446	8095
	(159)	(252)	(198)	(170)
.24-.28	4881	10708	7344	6171
	(134)	(202)	(167)	(147)
.28-.32	3761	7941	5385	4626
	(124)	(186)	(141)	(128)
.32-.36	3106	6058	4155	3331
	(108)	(169)	(129)	(108)
.36-.40	2303	4631	3065	2484
	(93)	(137)	(114)	(94)
.40-.44	1893	3936	2690	2051
	(86)	(126)	(101)	(87)
.44-.48	1427	2896	2130	1499
	(73)	(103)	(91)	(74)
.48-.52	1090	2531	1620	1164
	(63)	(98)	(77)	(63)
.52-.56	735	1918	1425	1137
	(52)	(86)	(78)	(63)
.56-.60	669	1427	1036	734
	(50)	(79)	(64)	(50)
.60-.64	577	1181	793	603
	(47)	(74)	(59)	(47)
.64-.68	480	1012	661	580
	(43)	(60)	(48)	(46)
.68-.72	389	786	575	477
	(37)	(57)	(49)	(41)
.72-.76	316	630	404	295
	(38)	(51)	(36)	(31)
.76-.80	240	460	291	283
	(29)	(46)	(34)	(31)

TABLE 27 (CONT)

X - CMI

X CMI	E_γ [0,75] GeV	E_γ [75,100]	E_γ [100,125]	E_γ [125,170]
.80-.84	193	347	235	222
	(27)	(38)	(28)	(28)
.84-.88	101	308	187	136
	(20)	(35)	(25)	(21)
.88-.92	83	159	149	96
	(20)	(25)	(23)	(19)
.92-.96	75	90	79	97
	(20	(17)	(20)	(18)
.96-1.0	21	42	86	54
	(9)	(12)	(26)	(14)

TABLE 28

X - CMI (FITS)

(I) $XdN/dX = B_1(1-X)^{k1} + B_2(1-X)^{k2}$; $A=B_2/B_1$

$E\gamma$	k_1	k_2	A	χ^2/DOF
[0,75]	3.74 ∓.73 (∓.2)	0.89 ∓.16 (∓.04)	0.25 ∓.08 (∓.01)	1.3
[75,100]	3.31 ∓.60 (∓.2)	0.99 ∓.13 (∓.04)	0.36 ∓.10 (∓.01)	.86
[100,125]	2.19 ∓.22 (∓.2)	0.29 ∓.24 (∓.02)	0.07 ∓.04 (∓.01)	.83
[125,170]	3.94 ∓.59 (∓.2)	0.78 ∓.12 (∓.04)	0.19 ∓.05 (∓.02)	1.9

(II) $XdN/dX = A(1-X)^k$

$E\gamma$	k(0.3<X<1.0)	k(0.3<X<0.5)	k(0.5<X<1.0)
[0,75]	1.32 ∓.06 (∓.06)	2.1 ∓.3 (∓.1)	1.1 ∓.1 (∓.05)
χ^2/DOF	1.9	0.11	.63
[75,100]	1.35 ∓.04 (∓.06)	2.1 ∓.2 (∓.1)	1.19 ∓.07 (∓.05)
χ^2/DOF	2.2	.21	1.2
[100,125]	1.24 ∓.05 (∓.05)	1.9 ∓.2 (∓.1)	1.02 ∓.08 (∓.05)
χ^2/DOF	3.8	.24	2.8
[125,170]	1.15 ∓.06 (∓.05)	2.6 ∓.2 (∓.2)	0.92 ∓.09 (∓.05)
χ^2/DOF	4.3	.16	2.3

(III) $dN/dX = C \cdot \exp(-A \cdot X)$

$E\gamma$	A(0.3<X<1.0)	A(0.3<X<0.5)	A(0.5<X<1.0)
[0,75]	6.01 ∓.05 (∓.2)	6.1 ∓.2 (∓.2)	5.7 ∓.2 (∓.2)
χ^2/DOF	1.7	.64	2.1
[75,100]	5.96 ∓.03 (∓.1)	6.1 ∓.1 (∓.2)	6.4 ∓.1 (∓.2)
χ^2/DOF	3.0	1.4	3.3
[100,125]	5.88 ∓.05 (∓.1)	5.9 ∓.1 (∓.2)	6.1 ∓.1 (∓.3)
χ^2/DOF	.98	1.9	.74
[125,170]	5.98 ∓.04 (∓.2)	7.0 ∓.1 (∓.3)	5.8 ∓.2 (∓.3)
χ^2/DOF	2.5	1.3	2.2

* systematic errors in parenthesis

TABLE 29

$X_{\|}$ - CMI

$X_{\|}$ CMI	E_γ [0,75] GeV	E_γ [75,100]	E_γ [100,125]	E_γ [125,170]
0.0-.05	40689	95819	79492	71553
	(635)	(729)	(605)	(546)
.05-.10	26475	64467	48041	40693
	(430)	(575)	(462)	(419)
.10-.15	16709	37182	28510	23787
	(318)	(432)	(369)	(341)
.15-.20	11174	25587	19083	14911
	(274)	(371)	(319)	(265)
.20-.25	7641	17630	12263	9721
	(212)	(314)	(243)	(216)
.25-.30	5667	12048	8433	7399
	(177)	(254)	(199)	(205)
.30-.35	4249	8599	5912	4942
	(165)	(230)	(172)	(155)
.35-.40	3356	6438	4232	3349
	(143)	(184)	(143)	(118)
.40-.45	2554	5057	3452	2669
	(132)	(160)	(130)	(112)
.45-.50	1783	4017	2542	1767
	(103)	(148)	(107)	(87)
.50-.55	1246	2724	2193	1554
	(85)	(116)	(107)	(82)
.55-.60	1084	2065	1465	1116
	(85)	(107)	(86)	(69)
.60-.65	835	1759	1199	833
	(73)	(102)	(80)	(60)
.65-.70	653	1290	894	729
	(61)	(81)	(69)	(58)
.70-.75	549	1112	599	478
	(59)	(86)	(53)	(45)
.75-.80	351	820	460	432
	(46)	(84)	(52)	(48)
.80-.85	276	540	379	360
	(51)	(67)	(47)	(49)
.85-.90	230	437	292	157
	(67)	(58)	(42)	(29)
.90-.95	412	261	298	211
	(260)	(62)	(108)	(51)
.95-1.0	18	213	232	123
	(23)	(152)	(323)	(111)

TABLE 30

$X_{\parallel}$ - CMI (FITS)

(I) $X_{\parallel} dN/dX_{\parallel} = B_1(1-X_{\parallel})^{k1} + B_2(1-X_{\parallel})^{k2}$; $A=B_2/B_1$

$E\gamma$ (GeV)	k_1	k_2	A	χ^2/DOF
[0,75]	2.2 ∓.5 (∓.1)	0.8 ∓.5 (∓.05)	0.3 ∓.3 (∓.1)	1.1
[75,100]	2.3 ∓.2 (∓.1)	0.3 ∓.3 (∓.05)	0.3 ∓.06 (∓.1)	2.9
[100,125]	2.9 ∓.3 (∓.2)	0.6 ∓.3 (∓.08)	0.2 ∓.1 (∓.1)	2.2
[125,170]	3.1 ∓.3 (∓.2)	0.6 ∓.3 (∓.09)	0.2 ∓.08 (∓.1)	2.1

(II) $X_{\parallel} dN/dX_{\parallel} = A(1-X_{\parallel})^{k}$

$E\gamma$ (GeV)	$k(0.2<X_{\parallel}<1.0)$	$k(0.2<X_{\parallel}<.5)$	$k(0.5<X_{\parallel}<1.0)$
[0,75]	1.35 ∓.07 (∓.07)	1.7 ∓.2 (∓.09)	1.0 ∓.2 (∓.05)
χ^2/DOF	1.1	0.11	.63
[75,100]	1.32 ∓.05 (∓.06)	1.9 ∓.1 (∓.1)	1.0 ∓.1 (∓.05)
χ^2/DOF	2.6	.34	.51
[100,125]	1.38 ∓.06 (∓.07)	2.1 ∓.1 (∓.1)	1.1 ∓.1 (∓.06)
χ^2/DOF	2.3	.27	1.8
[125,170]	1.34 ∓.06 (∓.08)	2.5 ∓.2 (∓.1)	1.0 ∓.2 (∓.06)
χ^2/DOF	3.4	.28	1.6

(III) $dN/dX_{\parallel} = C \cdot \exp(-A \cdot X_{\parallel})$

$E\gamma$	$A(0.2<X_{\parallel}<1.0)$	$A(0.2<X_{\parallel}<0.5)$	$A(0.5<X_{\parallel}<1.0)$
[0,75]	5.53 ∓.03 (∓.09)	5.63 ∓.06 (∓.09)	4.8 ∓.2 (∓.1)
χ^2/DOF	.93	.46	.91
[75,100]	5.77 ∓.03 (∓.08)	6.13 ∓.05 (∓.09)	5.1 ∓.1 (∓.1)
χ^2/DOF	3.4	5.8	.85
[100,125]	5.85 ∓.03 (∓.1)	6.44 ∓.05 (∓.09)	5.1 ∓.2 (∓.1)
χ^2/DOF	3.1	3.8	.64
[125,170]	6.03 ∓.04 (∓.1)	6.83 ∓.06 (∓.1)	5.4 ∓.2 (∓.1)
χ^2/DOF	3.9	2.2	1.3

* systematic errors in parenthesis

TABLE 31

X - CMF

X CMF	Mx [2,4]	Mx [4,6]	Mx [6,8]	Mx [8,10]	Mx [10,12]
0.-.04	755	3029	7122	7557	2790
	(47)	(97)	(162)	(223)	(145)
.04-.08	3229	11921	23041	21246	7306
	(97)	(192)	(293)	(348)	(247)
.08-.12	5778	17913	26729	19959	5595
	(131)	(234)	(319)	(330)	(215)
.12-.16	7150	17062	21389	14352	4014
	(146)	(229)	(285)	(285)	(179)
.16-.20	7929	14684	16708	10546	2385
	(153)	(212)	(247)	(253)	(137)
.20-.24	7778	11534	11958	6956	1594
	(152)	(187)	(209)	(201)	(108)
.24-.28	7074	9484	8869	5077	1170
	(145)	(170)	(180)	(176)	(94)
.28-.32	6127	7157	6458	3717	960
	(135)	(148)	(156)	(152)	(80)
.32-.36	5257	5700	5033	2962	618
	(125)	(133)	(137)	(139)	(70)
.36-.40	4376	4437	3726	2212	530
	(115)	(117)	(117)	(122)	(73)
.40-.44	3463	3433	3118	1727	431
	(102)	(103)	(107)	(101)	(59)
.44-.48	3112	2716	2337	1337	359
	(95)	(91)	(95)	(84)	(50)
.48-.52	2326	2181	1787	977	196
	(83)	(82)	(81)	(72)	(38)
.52-.56	1888	1733	1502	927	205
	(76)	(72)	(75)	(72)	(37)
.56-.60	1572	1414	1233	589	154
	(69)	(66)	(67)	(59)	(42)
.60-.64	1225	917	1012	533	178
	(60)	(53)	(62)	(59)	(43)
.64-.68	1101	908	783	356	108
	(57)	(52)	(54)	(43)	(28)
.68-.72	797	788	635	386	108
	(49)	(49)	(48)	(47)	(27)
.72-.76	589	622	516	315	43
	(42)	(44)	(47)	(46)	(18)
.76-.80	555	485	391	237	52
	(41)	(40)	(38)	(43)	(19)

TABLE 31 (CONT.)

X - CMF

X CMF	Mx [2,4]	Mx [4,6]	Mx [6,8]	Mx [8,10]	Mx [10,12]
.80-.84	465	335	310	174	40
	(37)	(32)	(35)	(28)	(17)
.84-.88	315	262	237	110	30
	(30)	(28)	(30)	(24)	(21)
.88-.92	235	207	133	80	25
	(26)	(25)	(22)	(20)	(12)
.92-.96	143	186	149	66	22
	(20)	(27)	(26)	(18)	(12)
.96-1.0	109	110	32	53	17
	(18)	(18)	(11)	(53)	(17)

TABLE 32

X - CMF (FITS)

(I) $XdN/dX = B_1(1-X)^{k1} + B_2(1-X)^{k2}$; $A=B_2/B_1$

Mx (GeV)	k_1	k_2	A	χ^2/DOF
[2,4]	1.6 ∓.1 (∓.07)	0.2 ∓.2 (∓.05)	0.06 ∓.04 (∓.01)	1.9
[4,6]	2.6 ∓.2 (∓.1)	0.4 ∓.1 (∓.05)	0.11 ∓.03 (∓.02)	1.6
[6,8]	3.7 ∓.6 (∓.2)	0.9 ∓.1 (∓.06)	0.29 ∓.07 (∓.02)	.79
[8,10]	3.7 ∓.9 (∓.2)	0.8 ∓.2 (∓.06)	0.19 ∓.09 (∓.02)	.80
[10,12]	2.9 ∓.9 (∓.3)	0.3 ∓.5 (∓.05)	0.08 ∓.1 (∓.02)	.64

(II) $XdN/dX = A(1-X)^k$

Mx (GeV)	k(0.3<X<1.0)	k(0.3<X<0.5)	k(0.5<X<1.0)
[2,4]	1.06 ∓.05 (∓.05)	1.1 ∓.2 (∓.06)	0.92 ∓.07 (∓.04)
χ^2/DOF	4.0	.22	2.9
[4,6]	1.07 ∓.03 (∓.04)	2.1 ∓.2 (∓.1)	0.84 ∓.06 (∓.04)
χ^2/DOF	8.7	.03	4.5
[6,8]	1.27 ∓.04 (∓.05)	2.2 ∓.2 (∓.1)	1.03 ∓.08 (∓.05)
χ^2/DOF	3.2	.13	1.3
[8,10]	1.23 ∓.08 (∓.06)	2.3 ∓.3 (∓.1)	1.0 ∓.1 (∓.05)
χ^2/DOF	2.0	.02	1.1
[10,12]	1.0 ∓.2 (∓.08)	2.0 ∓.7 (∓.1)	0.7 ∓.3 (∓.06)
χ^2/DOF	0.74	.08	0.43

(III) $dN/dX = C \cdot \exp(-A \cdot X)$

Mx (GeV)	A(0.3<X<1.0)	A(0.3<X<0.5)	A(0.5<X<1.0)
[2,4]	5.22 ∓.03 (∓.08)	4.43 ∓.08 (∓.1)	5.6 ∓.1 (∓.1)
χ^2/DOF	3.2	1.3	2.2
[4,6]	5.81 ∓.03 (∓.08)	6.10 ∓.07 (∓.1)	5.7 ∓.1 (∓.1)
χ^2/DOF	1.5	1.3	2.0
[6,8]	5.89 ∓.03 (∓.09)	6.31 ∓.09 (∓.1)	5.7 ∓.1 (∓.1)
χ^2/DOF	1.2	.92	1.1
[8,10]	6.07 ∓.06 (∓.1)	6.4 ∓.1 (∓.1)	5.8 ∓.2 (∓.1)
χ^2/DOF	.90	.11	1.1
[10,12]	5.9 ∓.1 (∓.1)	6.2 ∓.1 (∓.1)	5.3 ∓.4 (∓.2)
χ^2/DOF	.56	.73	.51

* systematic errors in parenthesis

TABLE 33

$X_{\|}$ - CMF

$X_{\|}$ CMF	Mx [2,4]	Mx [4,6]	Mx [6,8]	Mx [8,10]	Mx [10,12]
0.-.05	18042	35880	49488	36125	10868
	(254)	(346)	(446)	(458)	(299)
.05-.10	14808	26223	32238	23055	6802
	(231)	(296)	(360)	(371)	(243)
.10-.15	11605	17313	20531	14786	4201
	(206)	(242)	(285)	(296)	(193)
.15-.20	8273	12340	14529	9451	2505
	(172)	(205)	(241)	(250)	(149)
.20-.25	6065	8581	9935	6266	1540
	(148)	(171)	(203)	(204)	(113)
.25-.30	4535	6295	6840	4732	1103
	(129)	(147)	(167)	(177)	(89)
.30-.35	3438	4565	4805	3445	892
	(109)	(125)	(142)	(169)	(94)
.35-.40	2519	3564	3905	2377	589
	(92)	(110)	(126)	(119)	(72)
.40-.45	1984	2747	3021	1837	500
	(84)	(97)	(114)	(110)	(65)
.45-.50	1533	2115	2127	1258	318
	(71)	(84)	(93)	(85)	(49)
.50-.55	1033	1584	1823	1103	288
	(57)	(74)	(86)	(82)	(51)
.55-.60	954	1136	1250	719	169
	(56)	(63)	(72)	(70)	(40)
.60-.65	633	993	1051	573	240
	(45)	(58)	(66)	(64)	(50)
.65-.70	501	681	748	513	136
	(40)	(48)	(55)	(52)	(33)
.70-.75	334	599	567	239	19
	(33)	(45)	(50)	(52)	(10)
.75-.80	269	405	441	256	73
	(30)	(37)	(42)	(45)	(26)
.80-.85	189	285	273	150	55
	(24)	(31)	(34)	(26)	(28)
.85-.90	129	185	205	133	26
	(20)	(24)	(28)	(28)	(12)
.90-.95	48	142	92	64	31
	(12)	(26)	(22)	(19)	(14)
.95-1.0	34	41	53	64	12
	(10)	(11)	(14)	(26)	(9)

TABLE 34

$X_{\parallel}$ - CMF (FITS)

(I) $X_{\parallel}dN/dX_{\parallel} = B_1(1-X_{\parallel})^{k1} + B_2(1-X_{\parallel})^{k2}$; $A=B_2/B_1$

Mx (GeV)	k_1	k_2	A	χ^2/DOF
[2,4]	1.7 ∓.1 (∓.1)	0.06 ∓.5 (∓.05)	0.02 ∓.03 (∓.02)	1.3
[4,6]	2.3 ∓.3 (∓.1)	0.8 ∓.2 (∓.05)	0.3 ∓.2 (∓.03)	0.6
[6,8]	2.1 ∓.2 (∓.1)	0.6 ∓.3 (∓.06)	0.1 ∓.1 (∓.05)	2.7
[8,10]	2.4 ∓.3 (∓.1)	0.5 ∓.3 (∓.07)	0.1 ∓.08 (∓.06)	0.8
[10,12]	3.0 ∓1.0 (∓.2)	0.6 ∓.4 (∓.08)	0.2 ∓.1 (∓.06)	0.4

(II) $X_{\parallel}dN/dX_{\parallel} = A(1-X_{\parallel})^{k}$

Mx (GeV)	$k(0.2<X_{\parallel}<1.0)$	$k(0.2<X_{\parallel}<0.5)$	$k(0.5<X_{\parallel}<1.0)$
[2,4]	1.35 ∓.05 (∓.06)	1.6 ∓.1 (∓.07)	1.1 ∓.1 (∓.05)
χ^2/DOF	1.8	0.1	1.2
[4,6]	1.27 ∓.04 (∓.06)	1.7 ∓.1 (∓.07)	1.1 ∓.09 (∓.07)
χ^2/DOF	1.7	.03	.74
[6,8]	1.32 ∓.05 (∓.07)	1.9 ∓.1 (∓.08)	1.1 ∓.1 (∓.07)
χ^2/DOF	1.9	.25	1.2
[8,10]	1.30 ∓.07 (∓.07)	2.2 ∓.2 (∓.09)	1.0 ∓.1 (∓.07)
χ^2/DOF	2.2	.08	1.6
[10,12]	1.2 ∓.1 (∓.08)	2.0 ∓.5 (∓.1)	1.0 ∓.3 (∓.07)
χ^2/DOF	0.8	.05	1.1

(III) $dN/dX_{\parallel} = C\cdot\exp(-A\cdot X_{\parallel})$

Mx (GeV)	$A(0.2<X_{\parallel}<1.0)$	$A(0.2<X_{\parallel}<0.5)$	$A(0.5<X_{\parallel}<1.0)$
[2,4]	5.74 ∓.03 (∓.09)	5.58 ∓.06 (∓.09)	6.3 ∓.2 (∓.1)
χ^2/DOF	2.4	.34	3.0
[4,6]	5.61 ∓.03 (∓.1)	5.67 ∓.05 (∓.09)	5.9 ∓.1 (∓.1)
χ^2/DOF	2.4	1.2	3.3
[6,8]	5.78 ∓.04 (∓.1)	6.08 ∓.05 (∓.1)	6.3 ∓.1 (∓.1)
χ^2/DOF	3.4	3.9	2.2
[8,10]	6.04 ∓.05 (∓.1)	6.37 ∓.07 (∓.1)	6.3 ∓.2 (∓.1)
χ^2/DOF	1.0	0.4	1.0
[10,12]	5.73 ∓.09 (∓.15)	6.0 ∓.1 (∓.1)	6.2 ∓.5 (∓.15)
χ^2/DOF	1.2	.31	1.8

* systematic errors in parenthesis

TABLE 35

FRAGMENTATION SPECTRA

$$X_{\parallel} dN/dX_{\parallel} \propto (1-X_{\parallel})^{k}$$

CHANNEL	k	COMMENTS
$\gamma \rightarrow h\mp$	$1.06 \mp(.08)$	$0.5<X_{\parallel}<1.0$
$\gamma \rightarrow h\mp$	$1.89 \mp(.25)$	$0.2<X_{\parallel}<0.5$
$\gamma \rightarrow h\mp$	$1.28 \mp(.08)$	$0.2<\times_{\parallel}<1.0$
$\pi^+ \rightarrow K^+$	$1.28 \mp(.05)$	$X_{\parallel}<0.7$ FNAL
$\pi^- \rightarrow K^-$	$1.40 \mp(.16)$	$X_{\parallel}<0.7$ FNAL
$K^+ \rightarrow \pi^+$	$2.28 \mp(.25)$	$X_{\parallel}<0.7$ FNAL
$K^- \rightarrow \pi^-$	$2.50 \mp(.09)$	$X_{\parallel}<0.7$ FNAL
$\pi^+ \rightarrow \pi^-$	$3.32 \mp(.23)$	$X_{\parallel}<0.7$ FNAL
$\pi^- \rightarrow \pi^+$	$2.94 \mp(.25)$	$X_{\parallel}<0.7$ FNAL
$\pi^+ \rightarrow K^-$	$2.30 \mp(.23)$	$X_{\parallel}<0.7$ FNAL
$\pi^- \rightarrow K^+$	$1.98 \mp(.21)$	$X_{\parallel}<0.7$ FNAL
$K^+ \rightarrow \pi^-$	$2.98 \mp(.39)$	$X_{\parallel}<0.7$ FNAL
$K^- \rightarrow \pi^+$	$2.51 \mp(.32)$	$X_{\parallel}<0.7$ FNAL
$K^+ \rightarrow K^-$	$3.40 \mp(1.37)$	$X_{\parallel}<0.7$ FNAL
$K^- \rightarrow K^+$	$3.20 \mp(1.76)$	$X_{\parallel}<0.7$ FNAL
$K^- \rightarrow \pi^-$	$1.2 \mp(.1)$	$X_{\parallel}>0.4$ MIR
	$2.45 \mp(.1)$	$0.2<X_{\parallel}<0.7$ MIR
$K^- \rightarrow \pi^+$	$3.0 \mp(.1)$	$0.2<X_{\parallel}<0.7$ MIR
$K^+ \rightarrow \pi^-$	$2.95 \mp(.1)$	$0.2<X_{\parallel}<0.7$ MIR

* FNAL[44] - 100,175 GeV/c beam momentum

* MIR[45] - 32 GeV/c beam momentum (MIRABELLE - SERPUKHOV)

TABLE 36

SCALING VIOLATION MEASUREMENTS

$\Delta X_{\parallel}$ CMF	VALUE OF THE RATIO R MISSING MASS BINS (GeV) [4,6]	[6,8]	[8,10]	[10,12]
0.0 - .05	1.35 ∓.017	1.74 ∓.017	2.16 ∓.019	2.37 ∓.031
.05 - .10	1.21 ∓.019	1.38 ∓.019	1.68 ∓.022	1.81 ∓.039
.10 - .15	1.02 ∓.023	1.12 ∓.023	1.38 ∓.027	1.42 ∓.049
.15 - .20	1.02 ∓.027	1.11 ∓.027	1.23 ∓.034	1.19 ∓.063
.20 - .25	0.96 ∓.032	1.04 ∓.032	1.12 ∓.041	1.00 ∓.077
.25 - .30	0.95 ∓.037	0.96 ∓.037	1.12 ∓.047	0.96 ∓.086
.30 - .35	0.90 ∓.042	0.89 ∓.049	1.08 ∓.058	1.02 ∓.11
.35 - .40	0.96 ∓.048	0.98 ∓.049	1.02 ∓.062	0.92 ∓.13

$\Delta X_{\parallel}$ CMI	PHOTON ENERGY BINS (GeV) [75,100]	[100,125]	[125,170]
0.0 - .05	1.14 ∓.017	1.36 ∓.017	1.62 ∓.017
.05 - .10	1.18 ∓.019	1.27 ∓.019	1.42 ∓.019
.10 - .15	1.08 ∓.022	1.19 ∓.023	1.31 ∓.024
.15 - .20	1.11 ∓.028	1.19 ∓.030	1.23 ∓.030
.20 - .25	1.12 ∓.033	1.12 ∓.034	1.17 ∓.036
.25 - .30	1.03 ∓.038	1.04 ∓.039	1.21 ∓.042
.30 - .35	0.98 ∓.047	0.97 ∓.048	1.07 ∓.050
.35 - .40	0.93 ∓.051	0.88 ∓.054	0.92 ∓.055

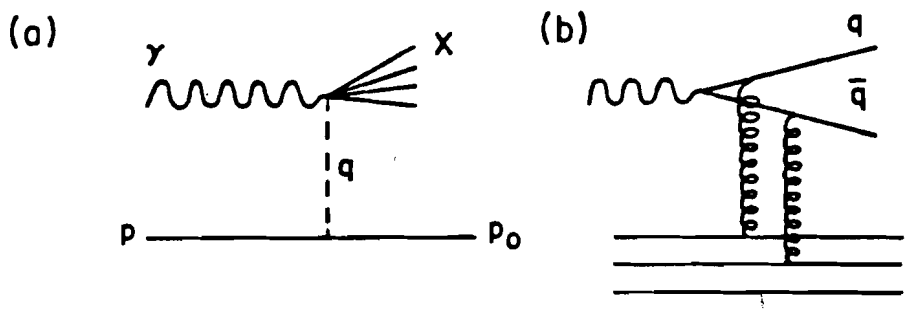

(c) DI-QUARK FRAGMENTATION DIAGRAMS

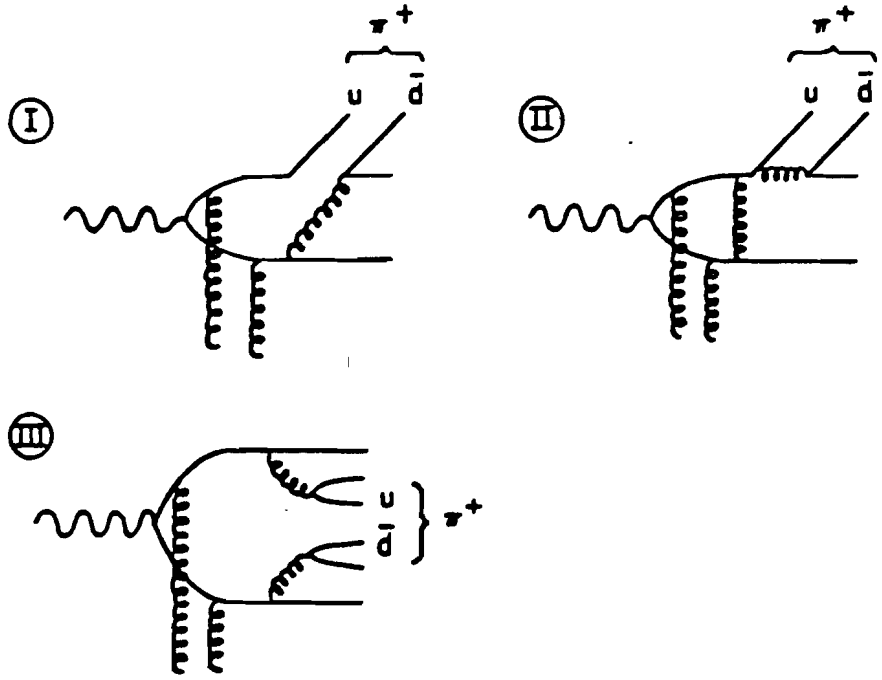

(d) SINGLE QUARK FRAGMENTATION DIAGRAM

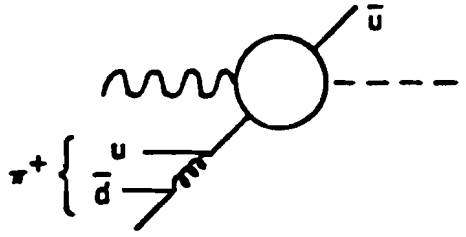

FIG. 1 Feynman diagrams.

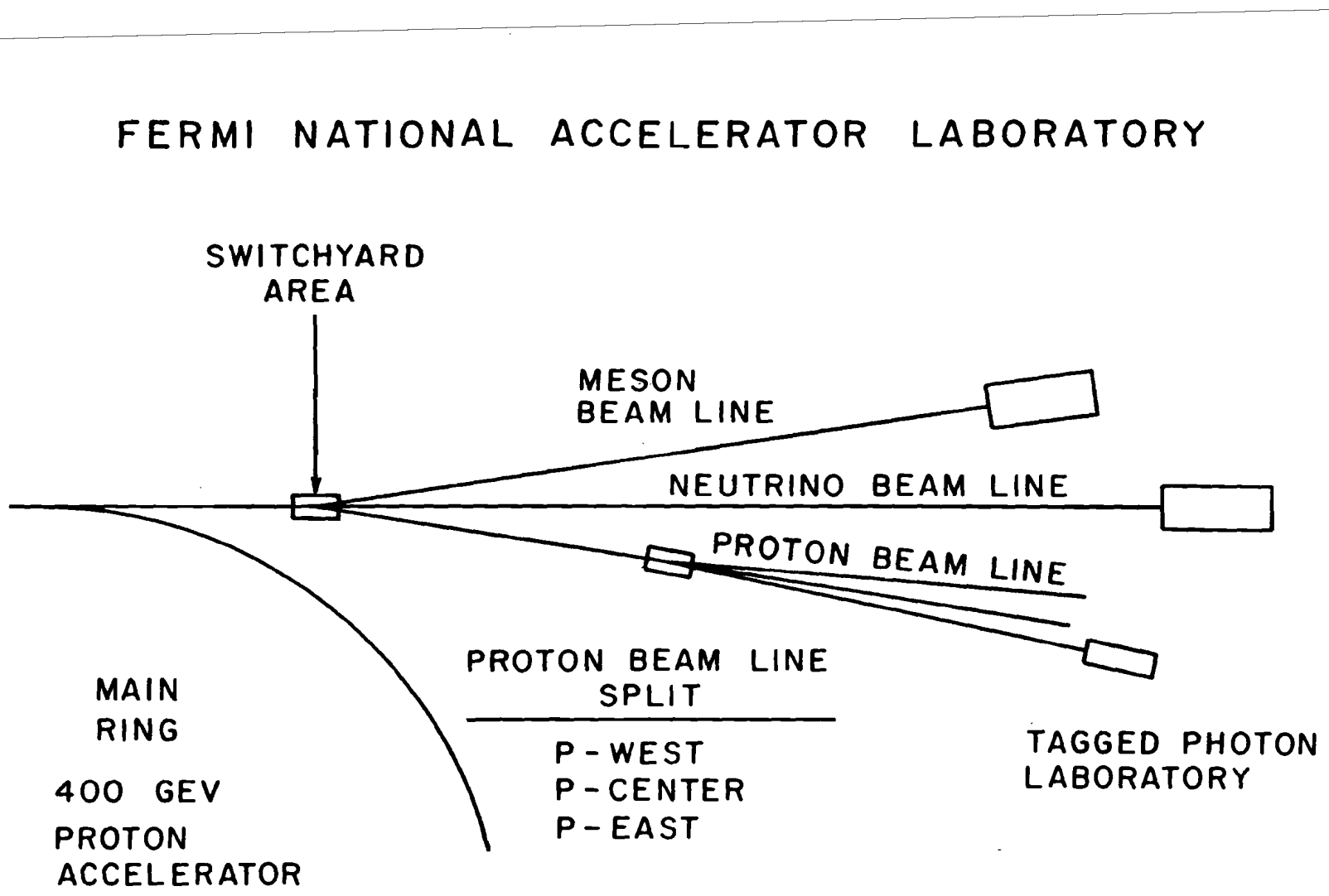

FIG. 2 Fermilab beam lines.

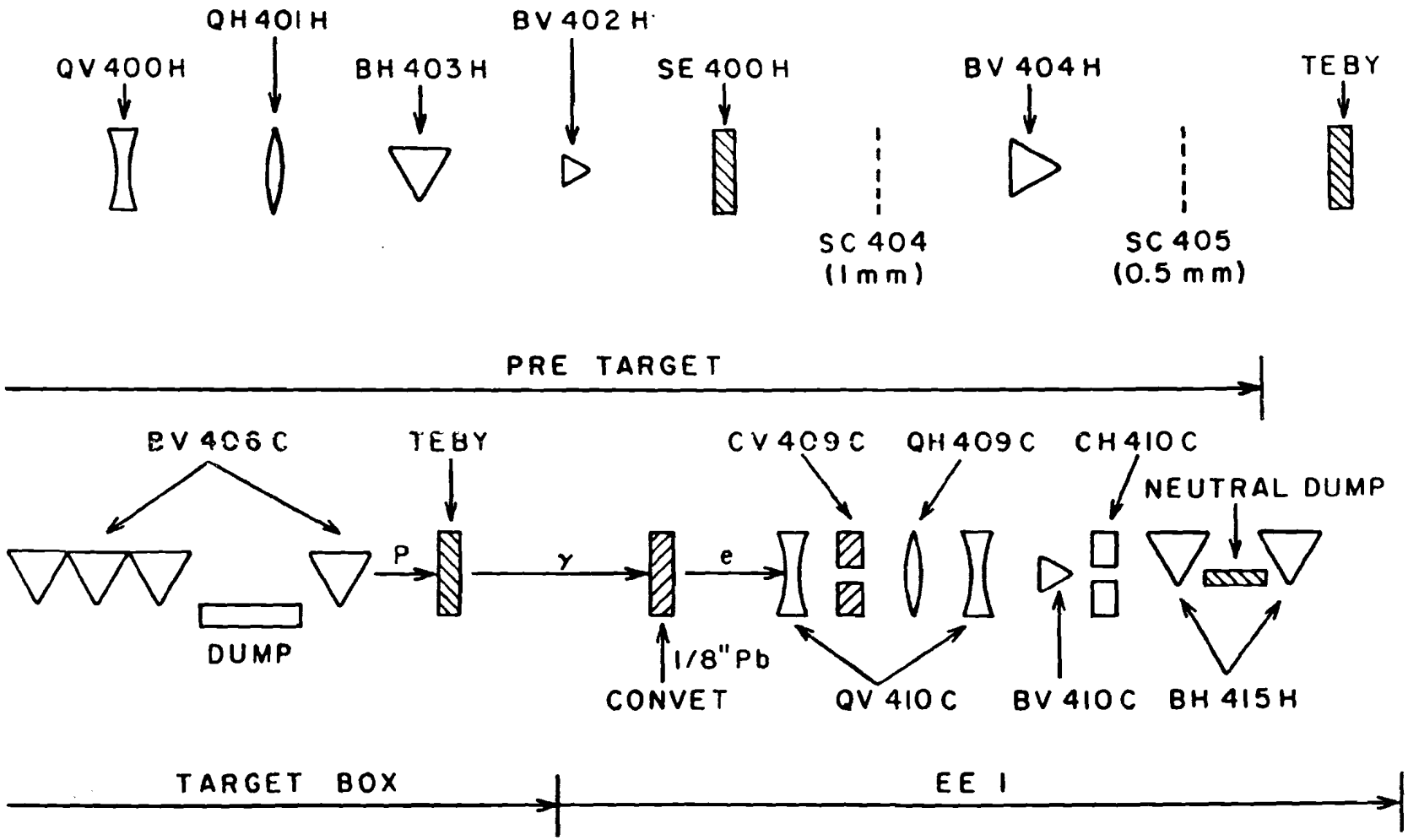

FIG. 3 P - East and tagged photon beam lines.

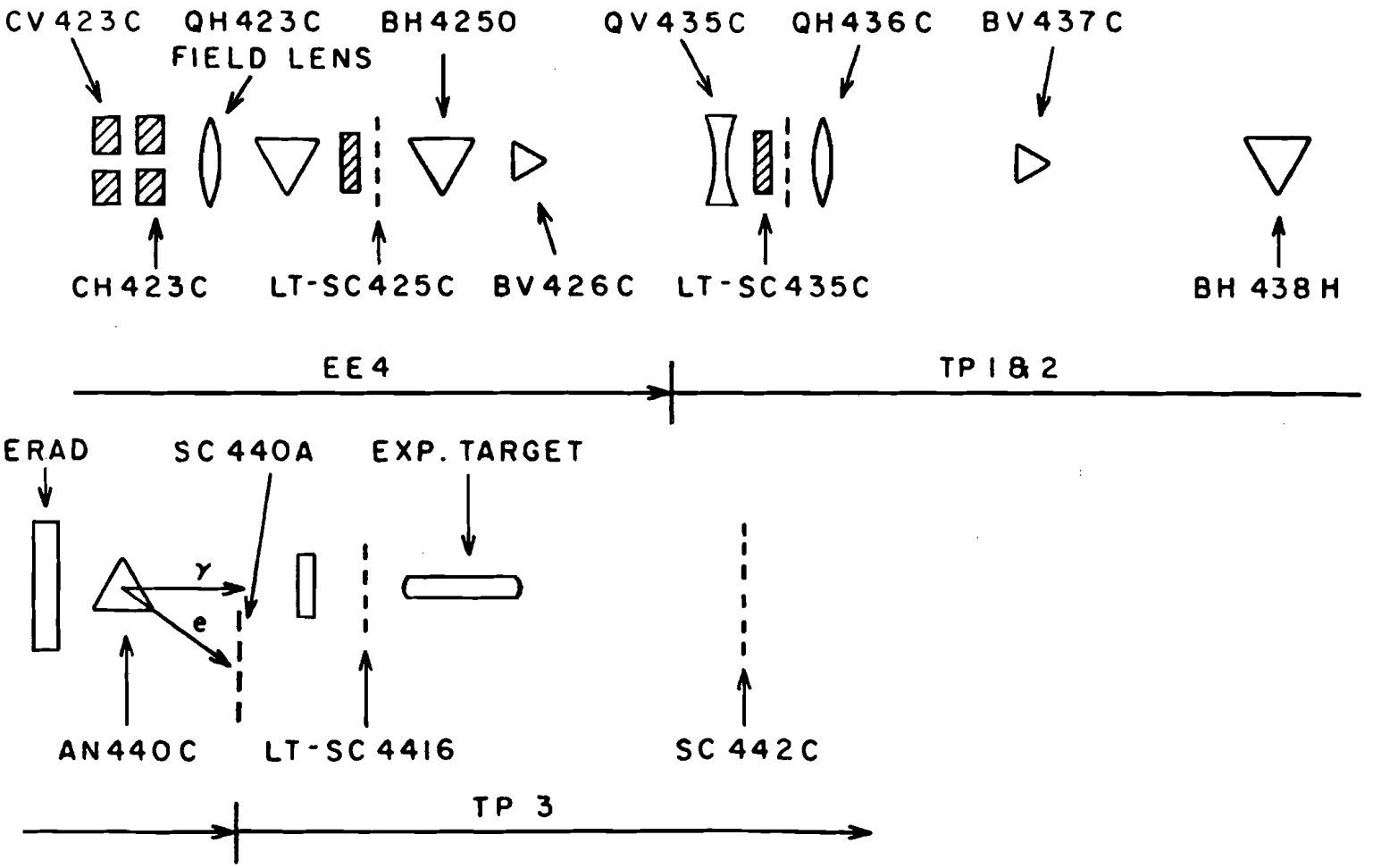
CV423C
QH423C
FIELD LENS
BH425O
QV435C
QH436C
BV437C
CH423C
LT-SC425C
BV426C
LT-SC435C
BH438H
EE4
TP1&2
ERAD
SC440A
EXP. TARGET
γ
e
AN440C
LT-SC4416
SC442C
TP 3

FIG. 3 (CONT.)

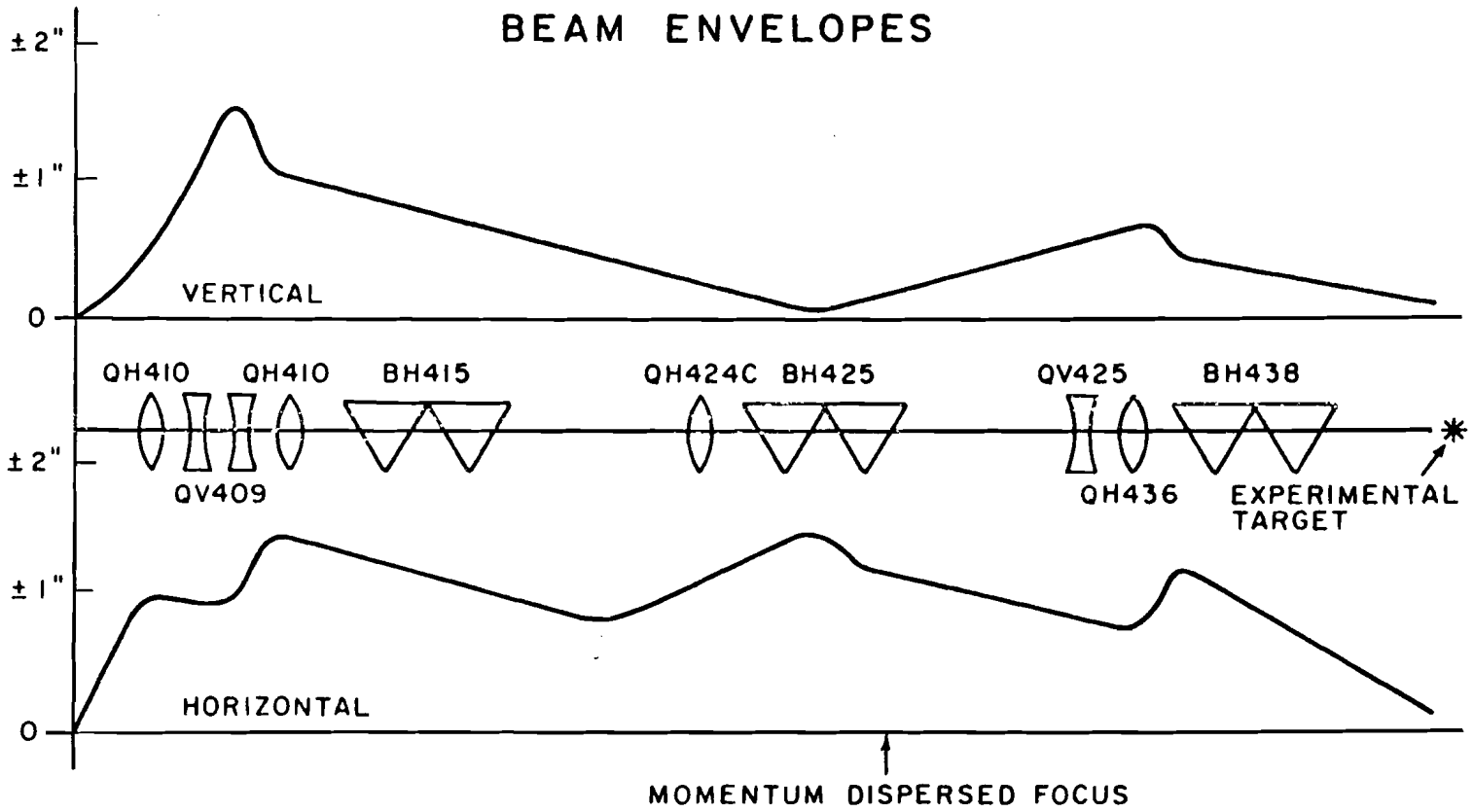

FIG. 4 Primary beam focussing components.

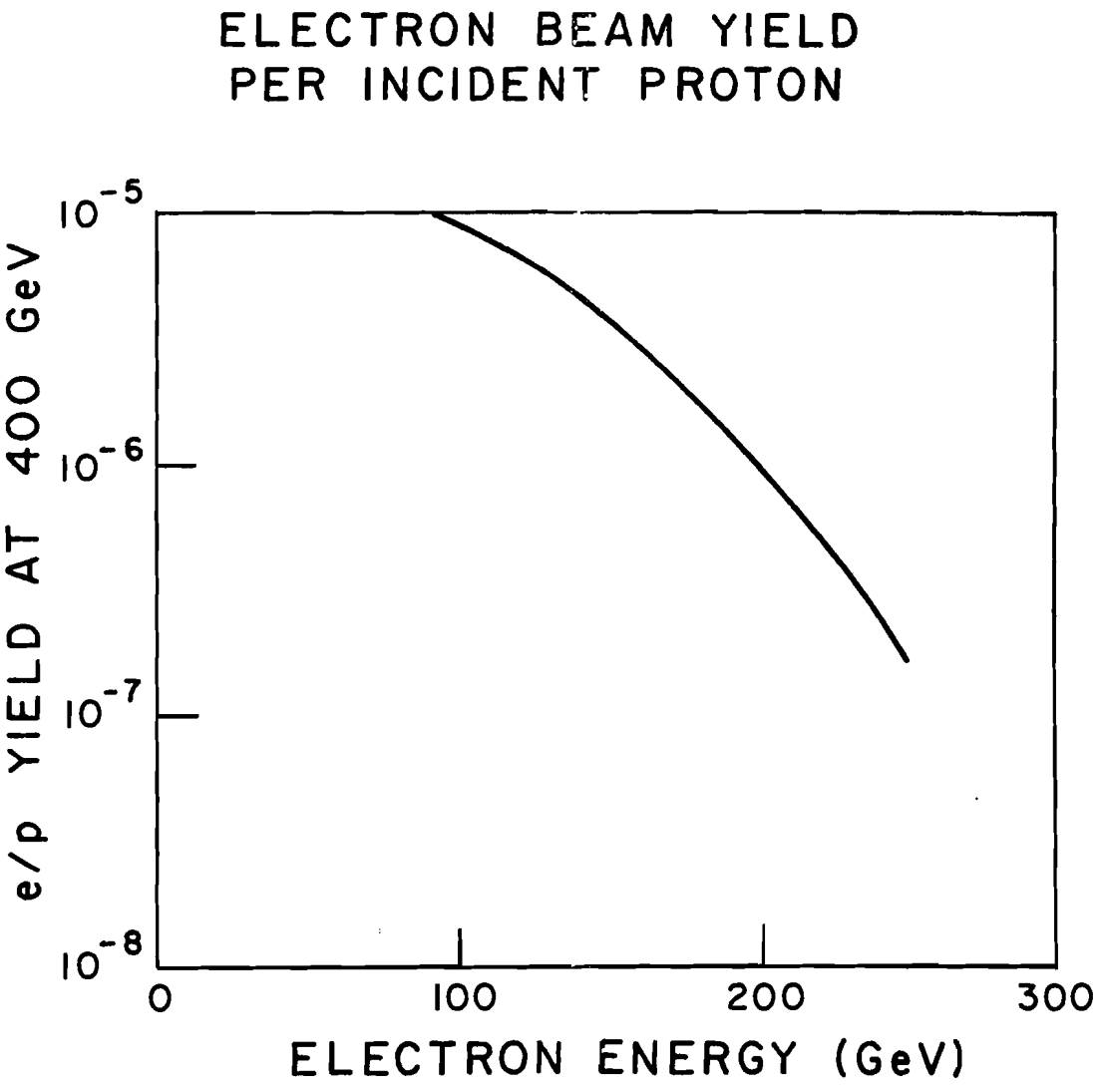

FIG. 5 Electron beam yield per incident proton as a function of the electron energy.

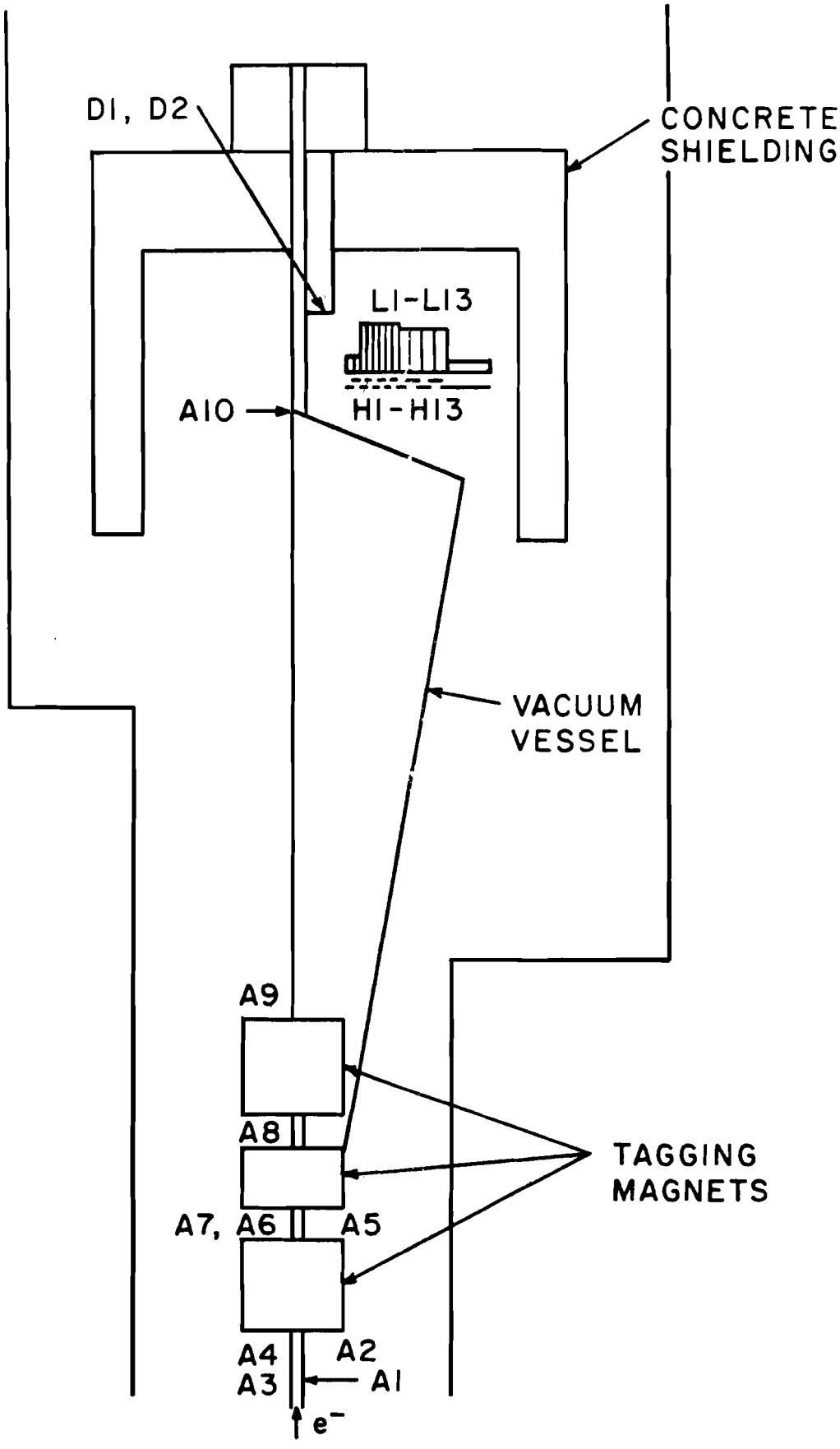

FIG. 6 Tagging system.

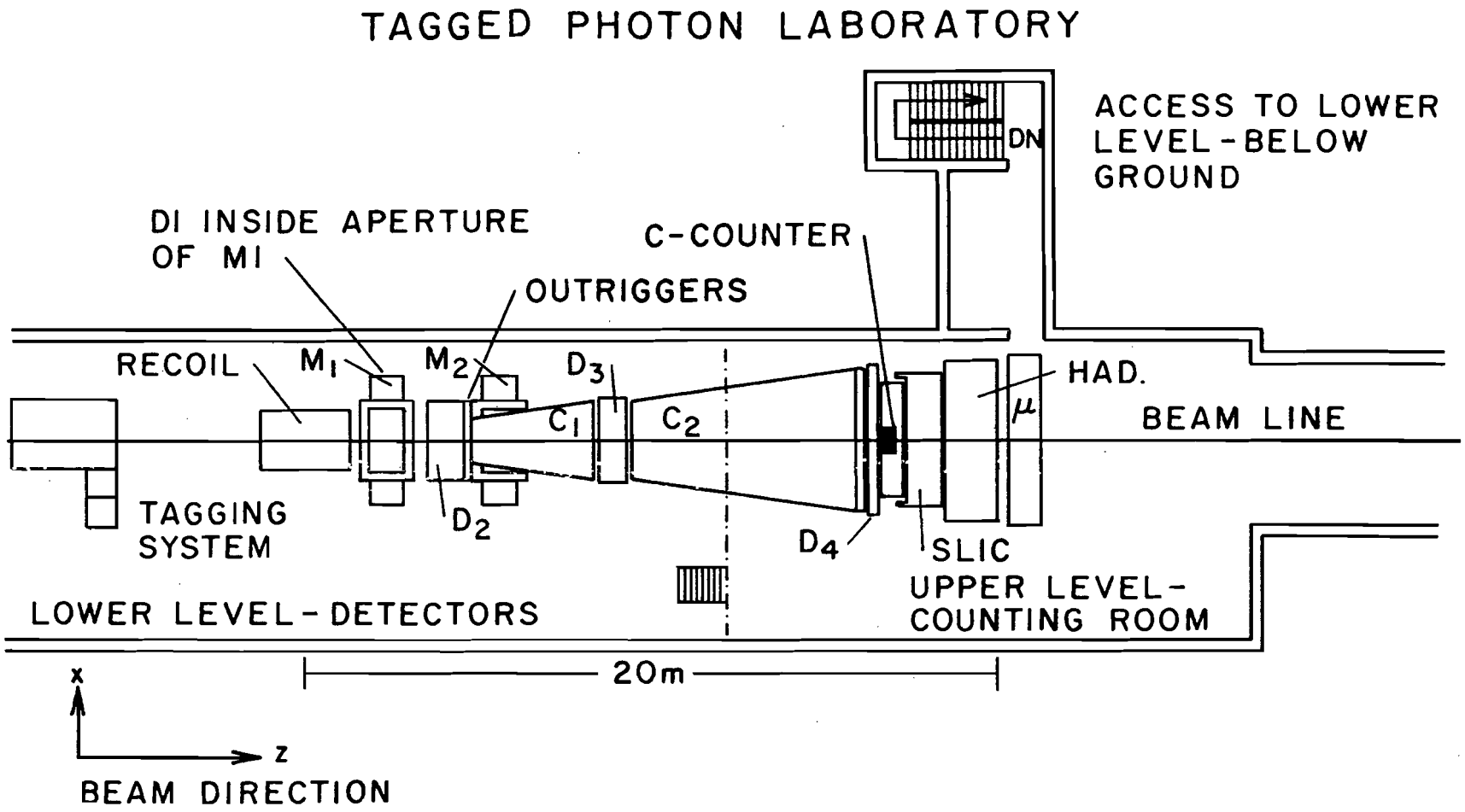
TAGGED PHOTON LABORATORY
ACCESS TO LOWER LEVEL - BELOW GROUND
DN
DI INSIDE APERTURE OF MI
C-COUNTER
OUTRIGGERS
RECOIL
M1
M2
D3
C1
C2
HAD.
μ
BEAM LINE
TAGGING SYSTEM
D2
D4
SLIC
LOWER LEVEL - DETECTORS
UPPER LEVEL - COUNTING ROOM
20m
x
z
BEAM DIRECTION

FIG. 7

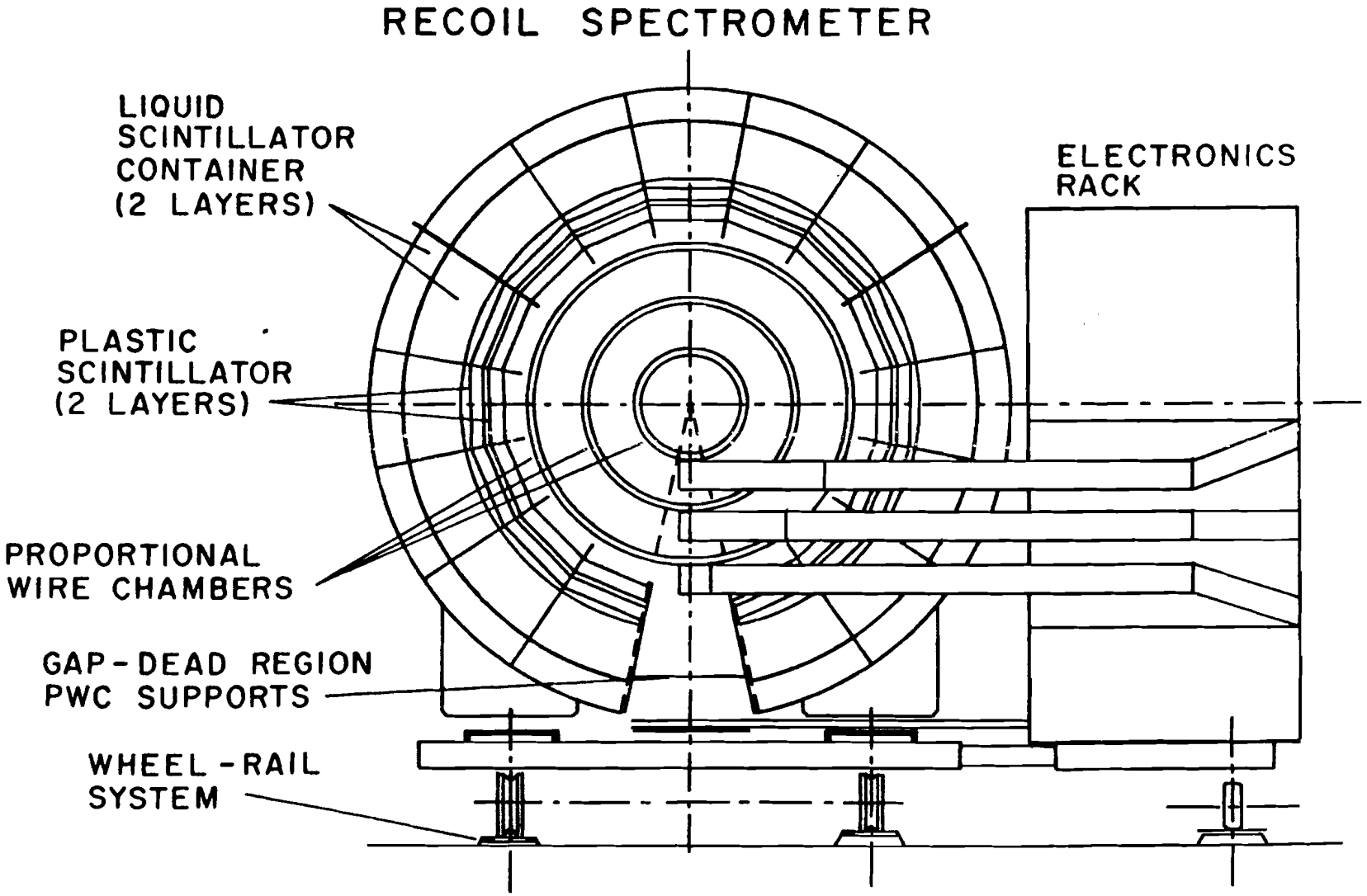
RECOIL SPECTROMETER
LIQUID SCINTILLATOR CONTAINER (2 LAYERS)
ELECTRONICS RACK
PLASTIC SCINTILLATOR (2 LAYERS)
PROPORTIONAL WIRE CHAMBERS
GAP - DEAD REGION PWC SUPPORTS
WHEEL - RAIL SYSTEM

FIG. 8

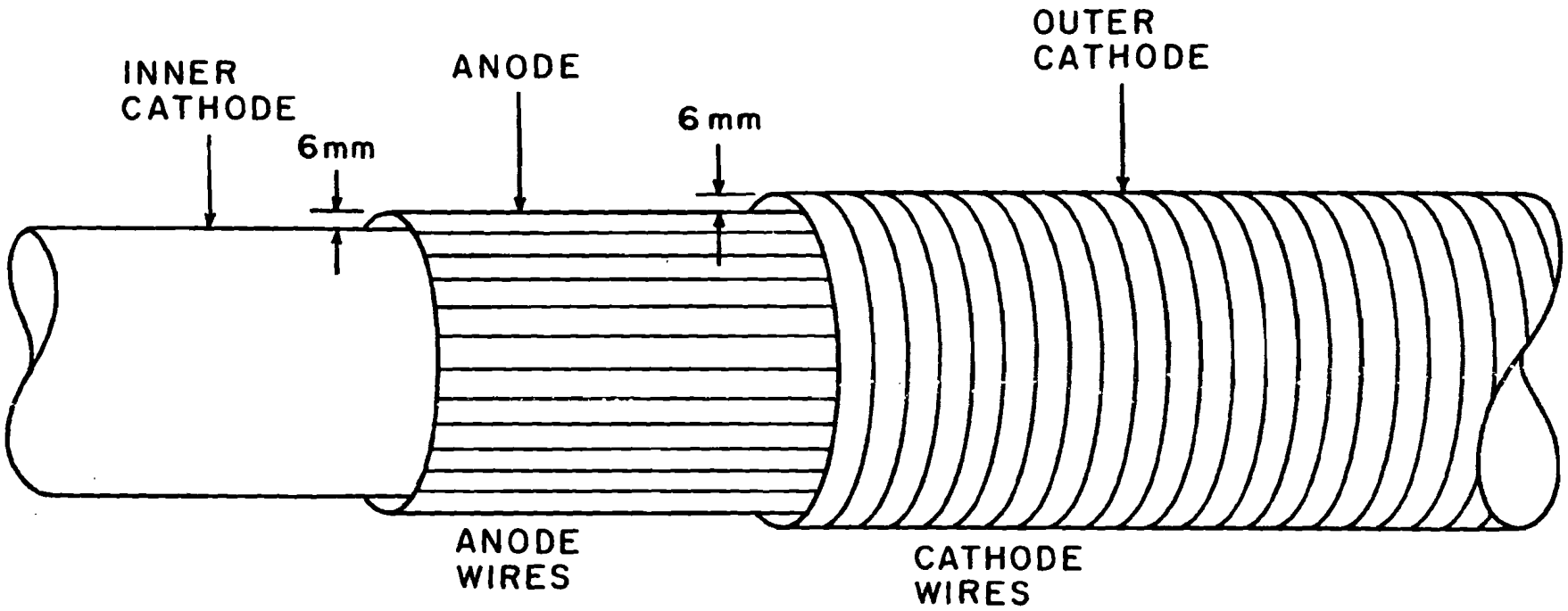

CUTAWAY VIEW OF PWC CHAMBER

FIG. 9

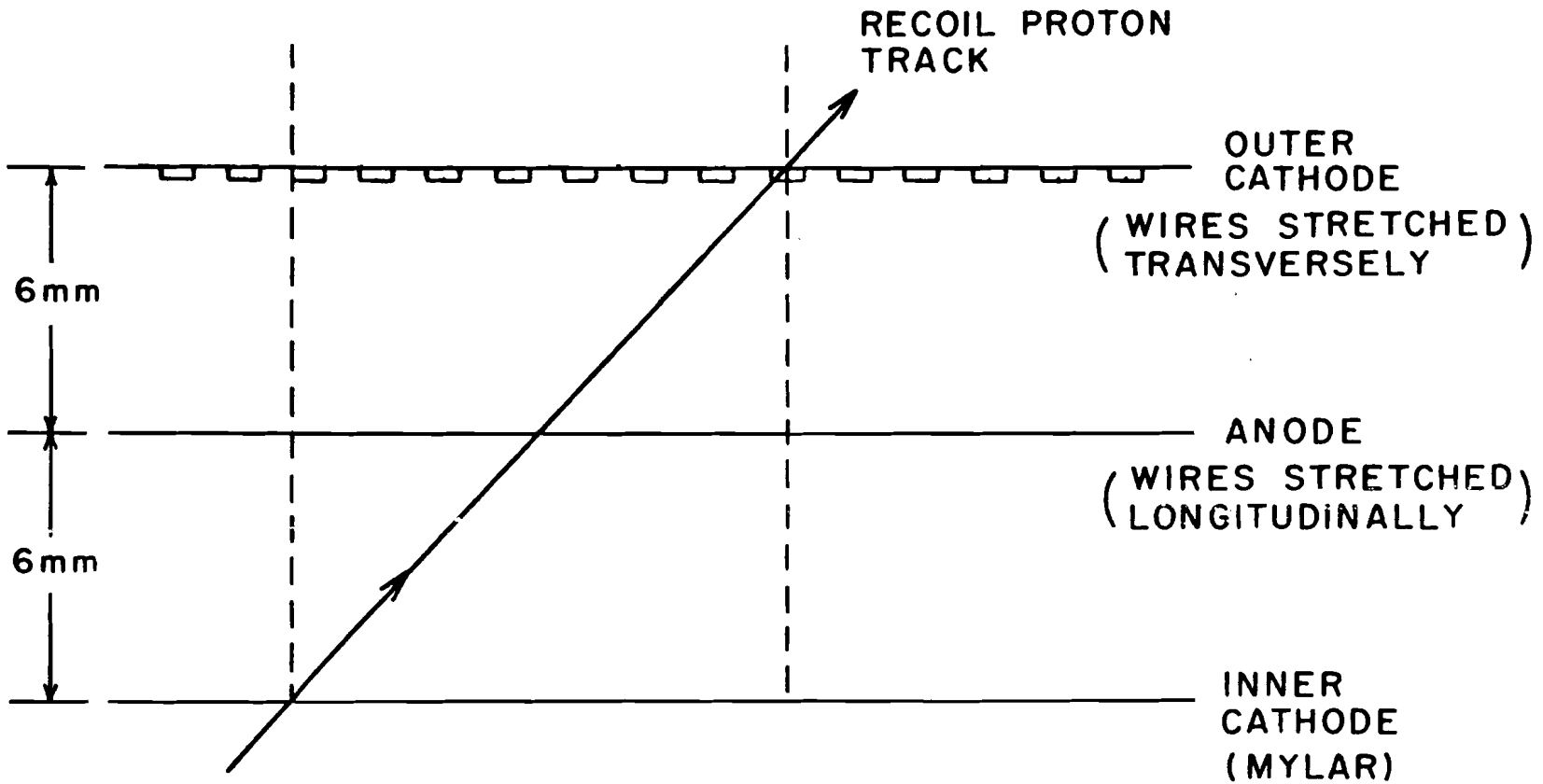

PWC CHAMBER
LONGITUDINAL CROSS SECTION

FIG. 10

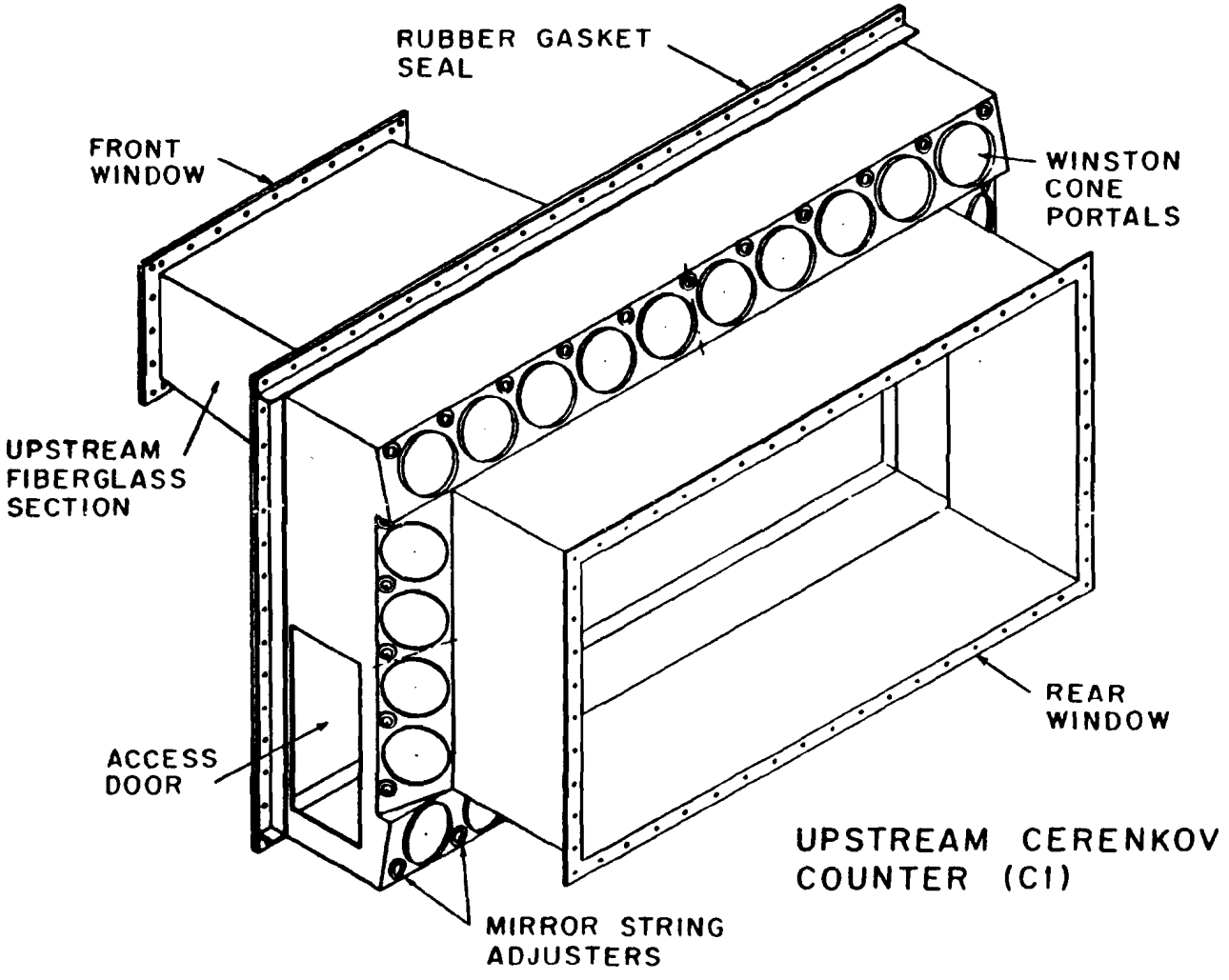
RUBBER GASKET SEAL
FRONT WINDOW
WINSTON CONE PORTALS
UPSTREAM FIBERGLASS SECTION
REAR WINDOW
ACCESS DOOR
MIRROR STRING ADJUSTERS
UPSTREAM CERENKOV COUNTER (C1)

FIG. 11

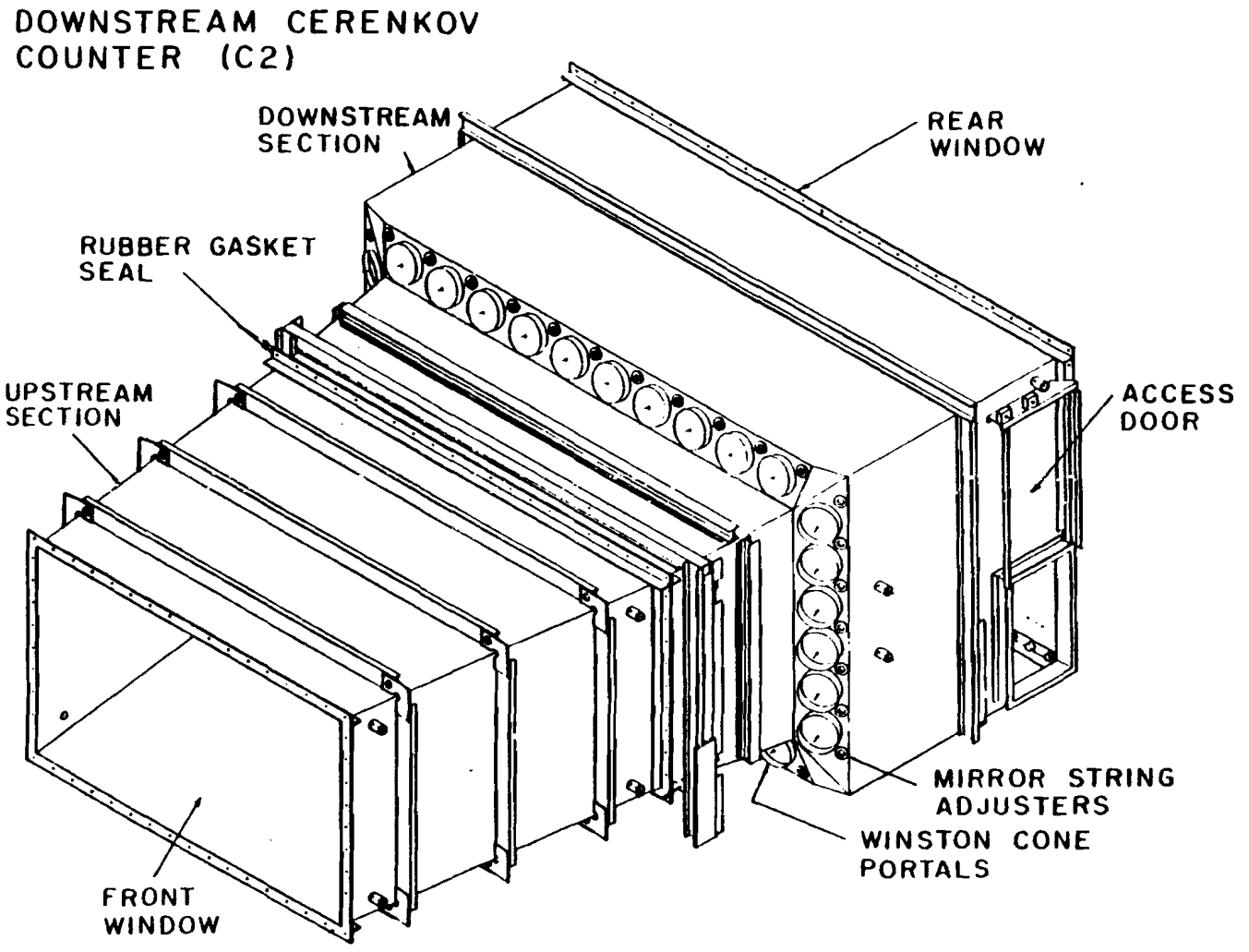
DOWNSTREAM CERENKOV
COUNTER (C2)
DOWNSTREAM
SECTION
REAR
WINDOW
RUBBER GASKET
SEAL
UPSTREAM
SECTION
ACCESS
DOOR
MIRROR STRING
ADJUSTERS
WINSTON CONE
PORTALS
FRONT
WINDOW

FIG. 12

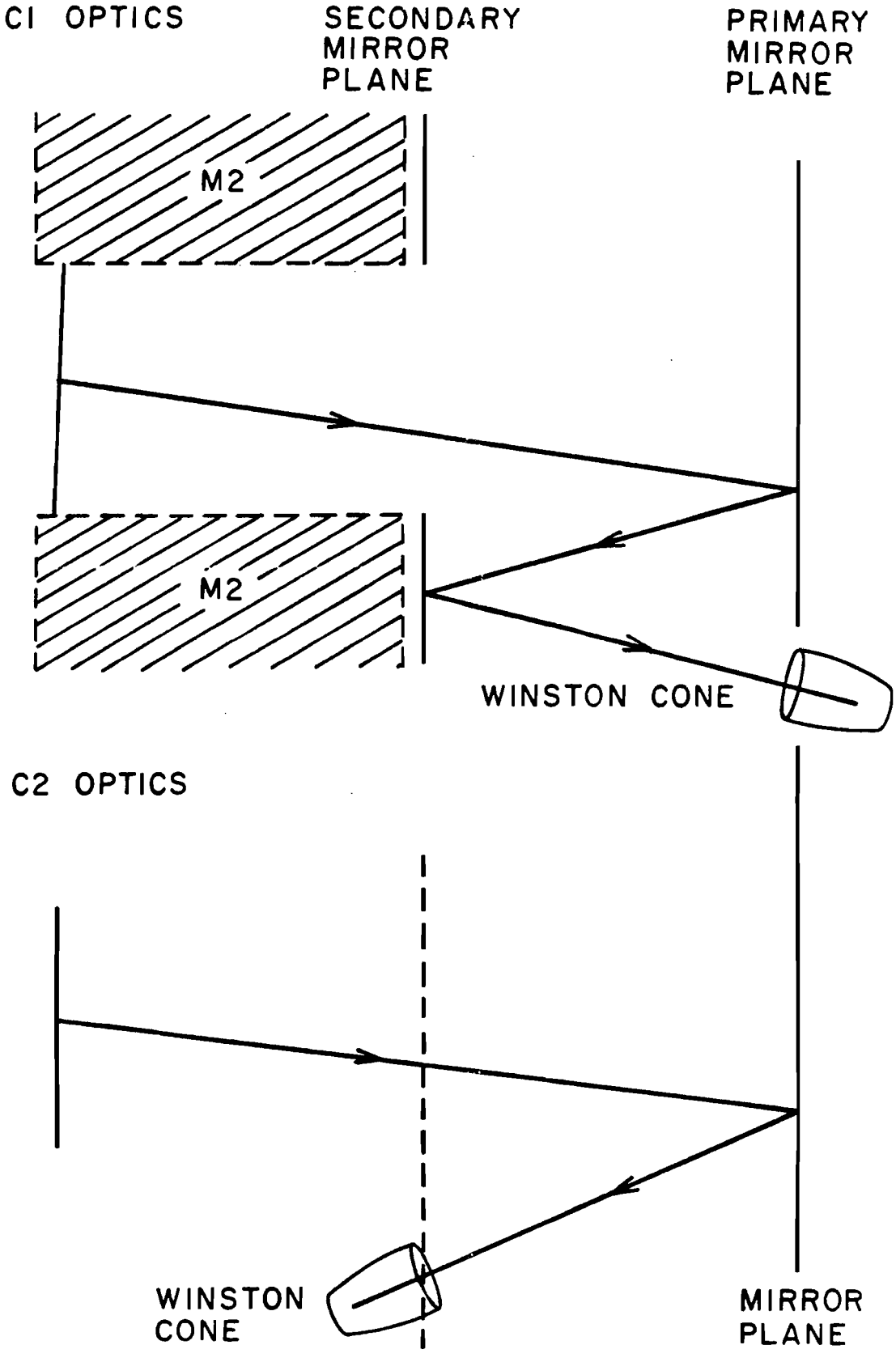

FIG. 13 Cerenkov counter optics.

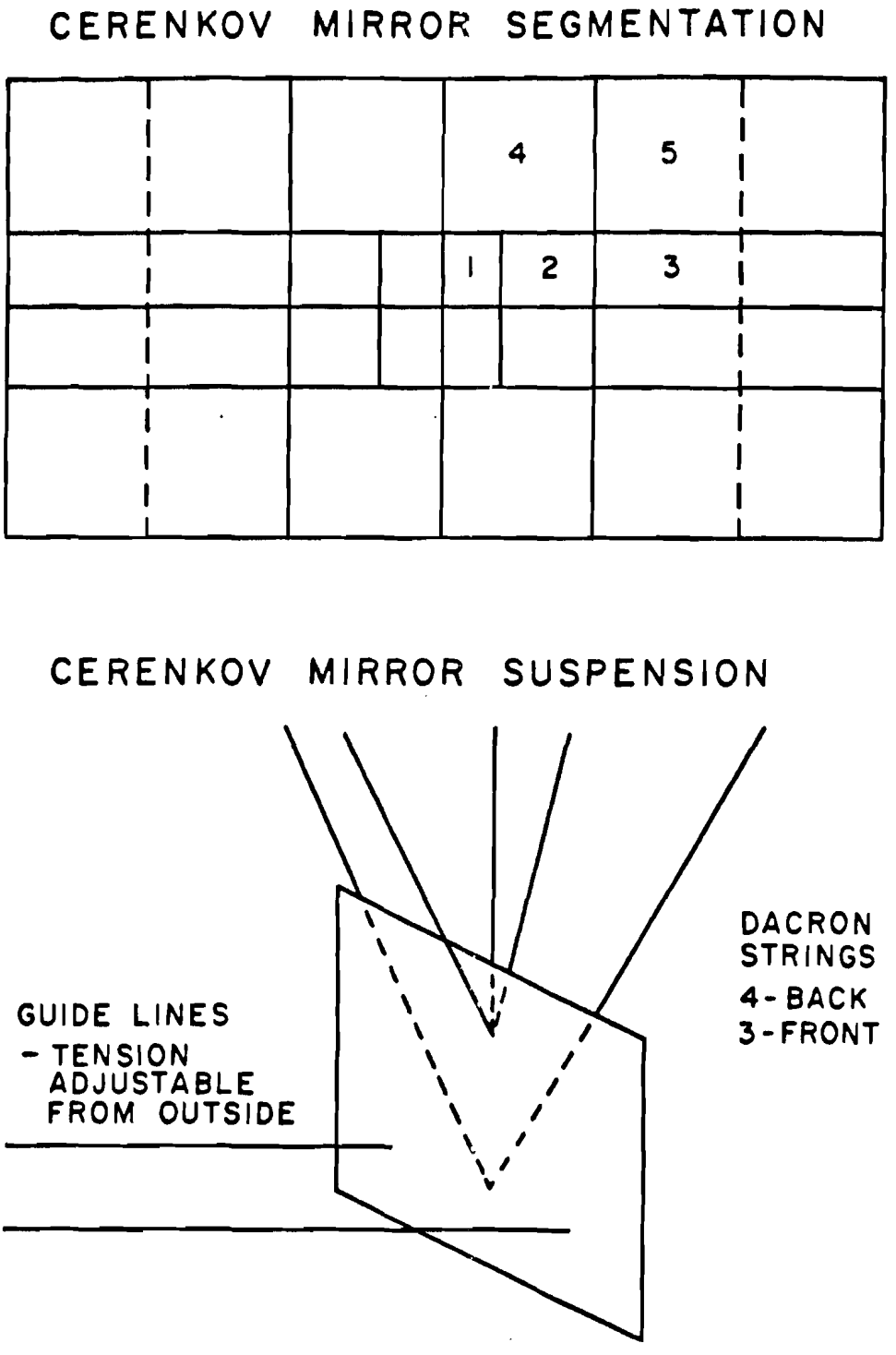

FIG. 14 Cerenkov counter mirror segmentation and support scheme.

WINSTON CONE - PHOTOTUBE ASSEMBLY

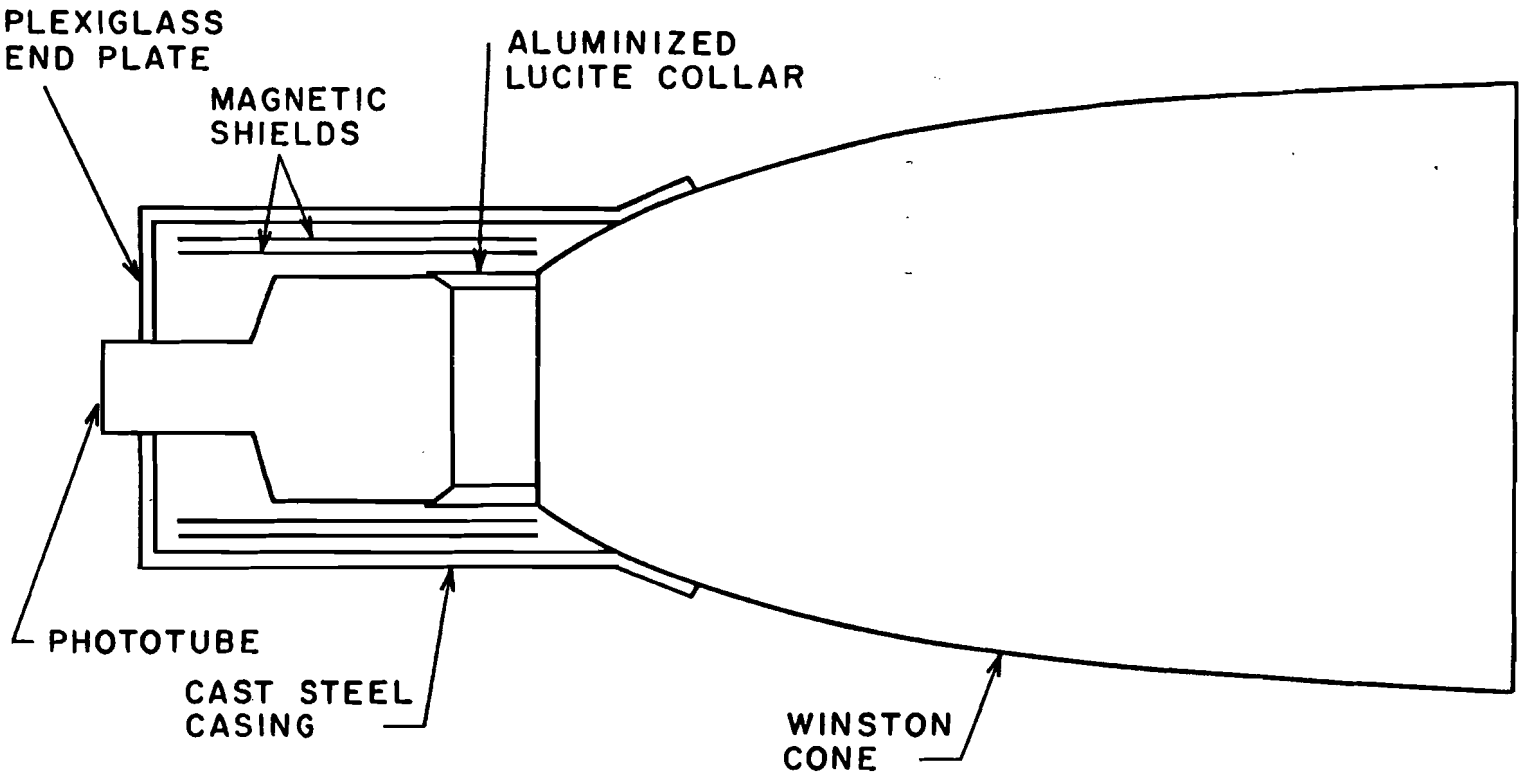

FIG. 15

DRIFT CHAMBER SYSTEM (TOP VIEW)
(TOTAL OF 29 PLANES)

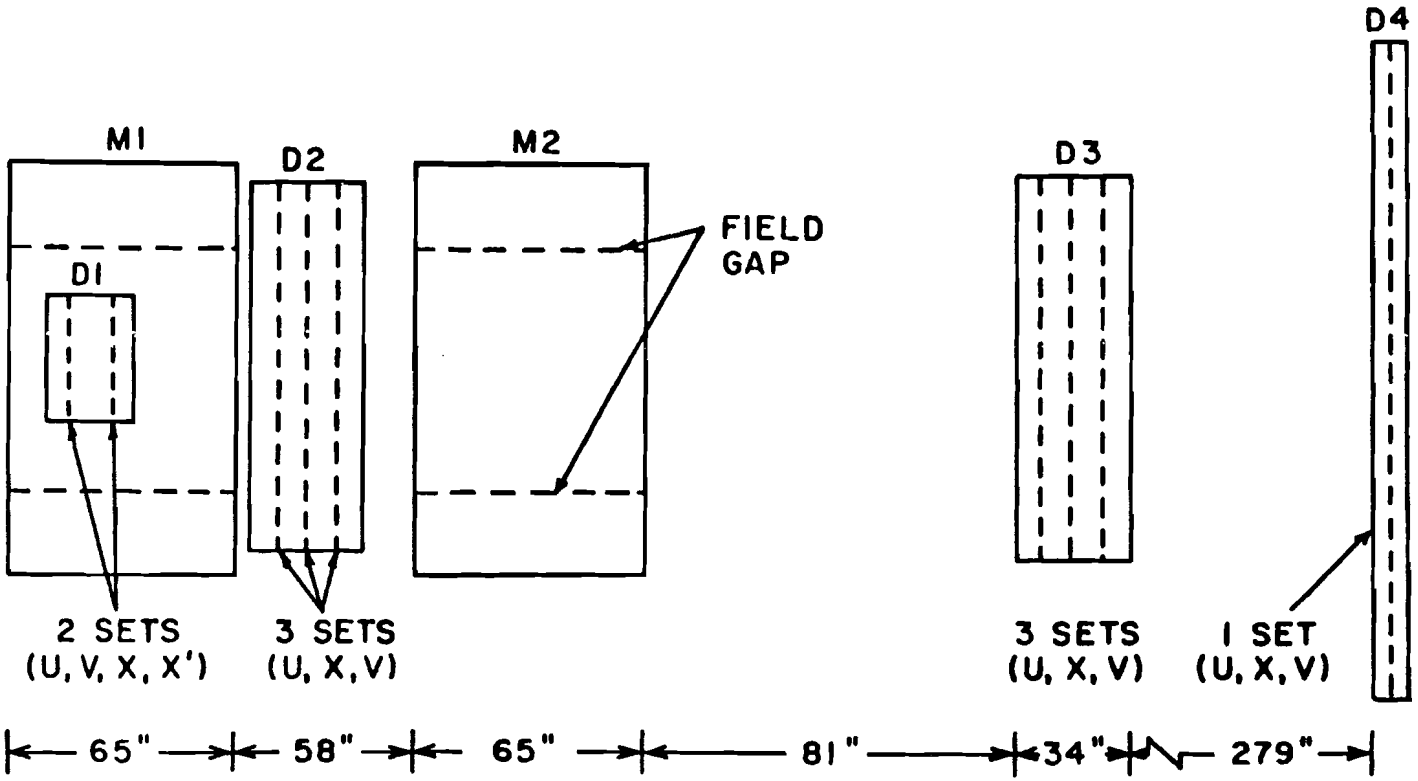

FIG. 16

D1 ASSEMBLY

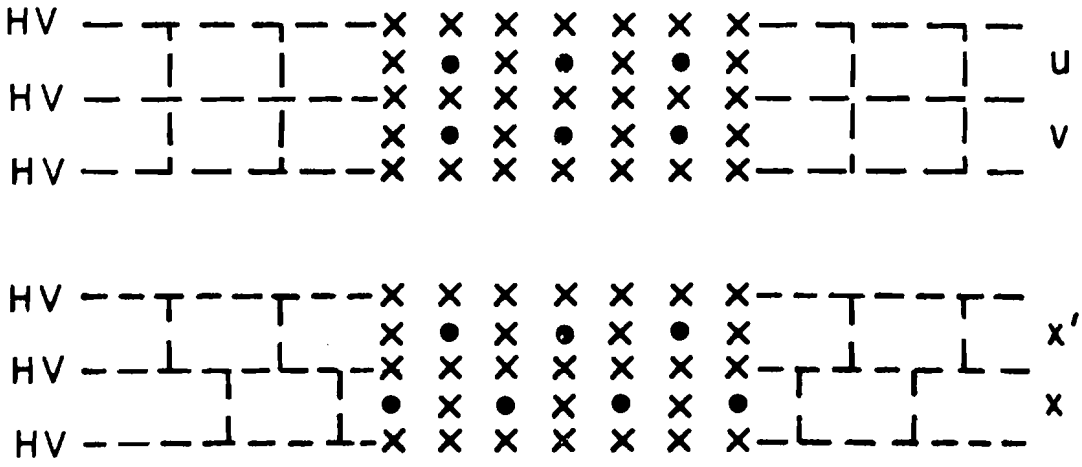

× - FIELD WIRES

• - SENSE WIRES

HV - HIGH VOLTAGE FIELD PLANES

D2-D4 ASSEMBLIES

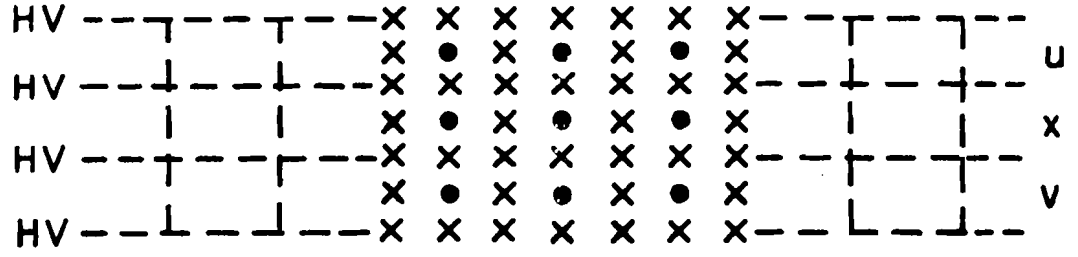

DRIFT CHAMBER CELL STRUCTURE

FIG. 17

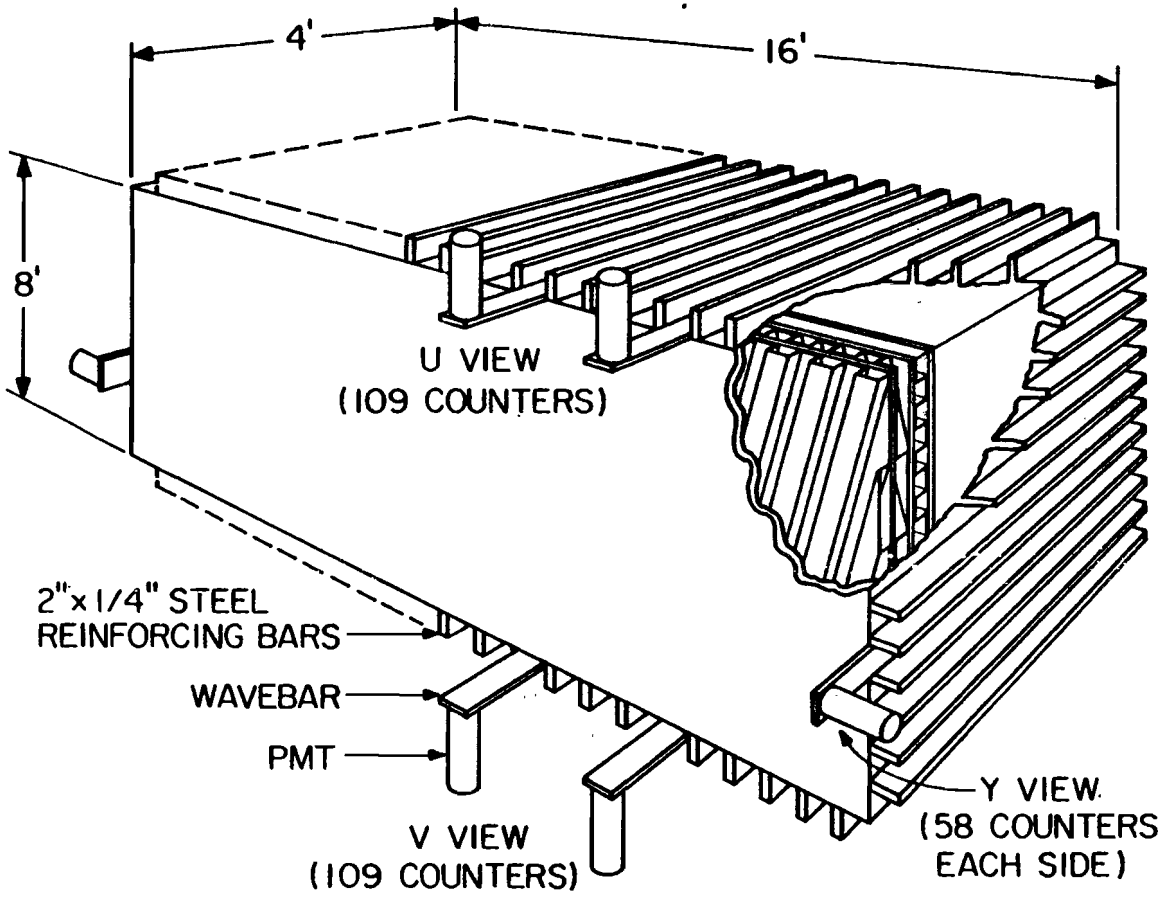

LEAD/LIQUID SCINTILLATOR SHOWER COUNTER (SLIC)
(SCHEMATIC)

FIG. 18

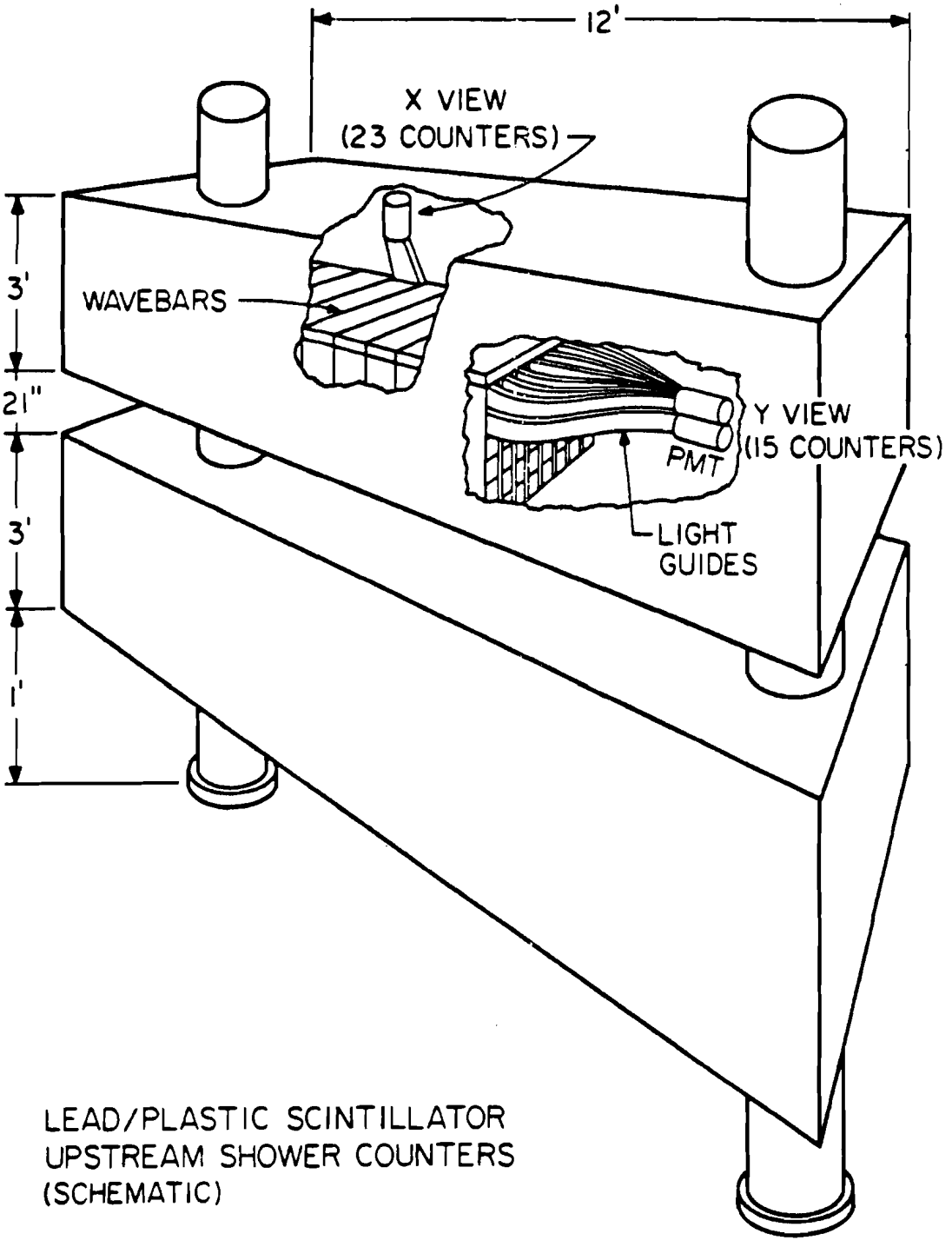

LEAD/PLASTIC SCINTILLATOR
UPSTREAM SHOWER COUNTERS
(SCHEMATIC)

FIG. 19

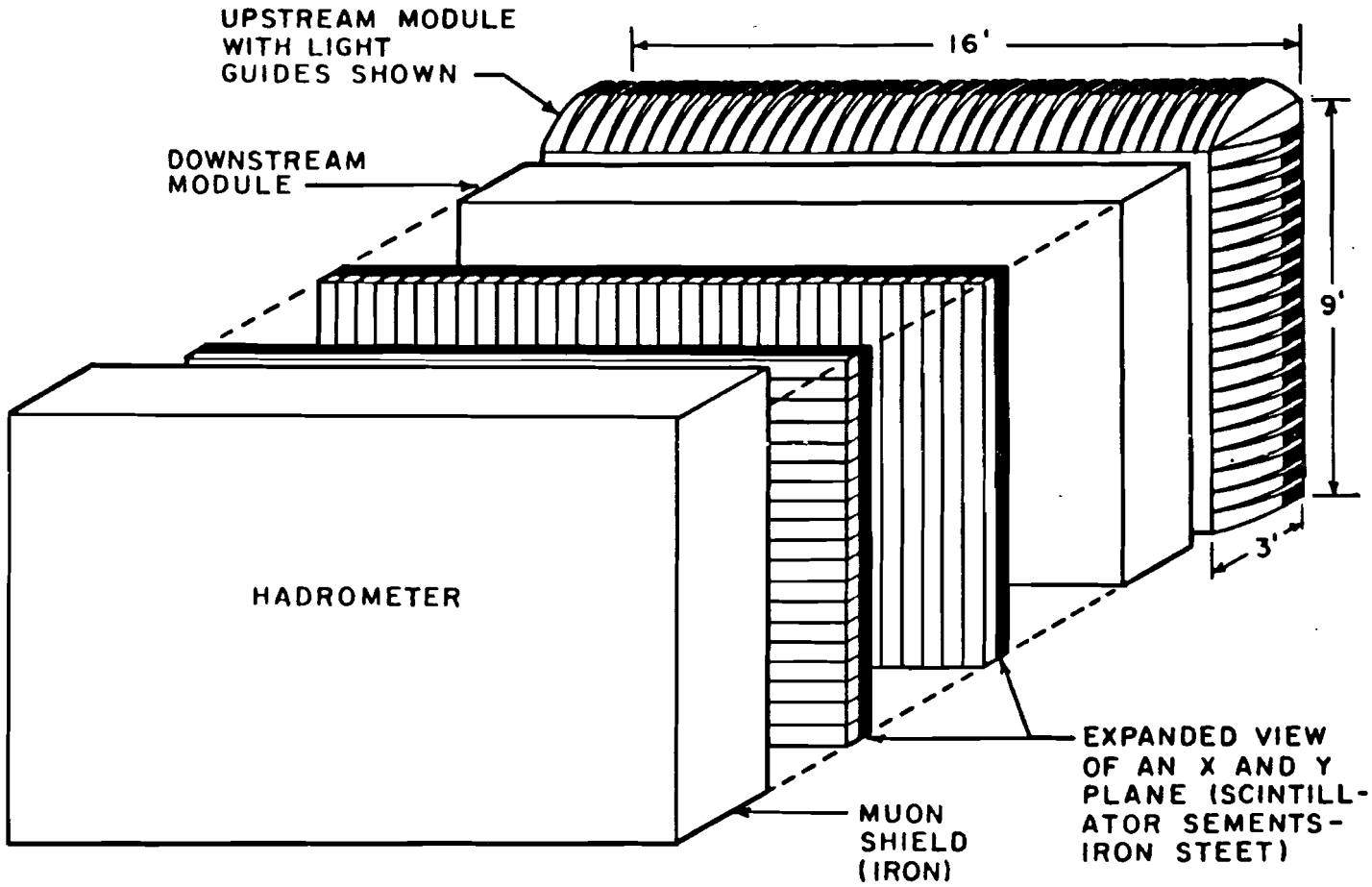
UPSTREAM MODULE
WITH LIGHT
GUIDES SHOWN
16'
DOWNSTREAM
MODULE
9'
3'
HADROMETER
EXPANDED VIEW
OF AN X AND Y
PLANE (SCINTILL-
ATOR SEMENTS-
IRON STEET)
MUON
SHIELD
(IRON)

FIG. 20

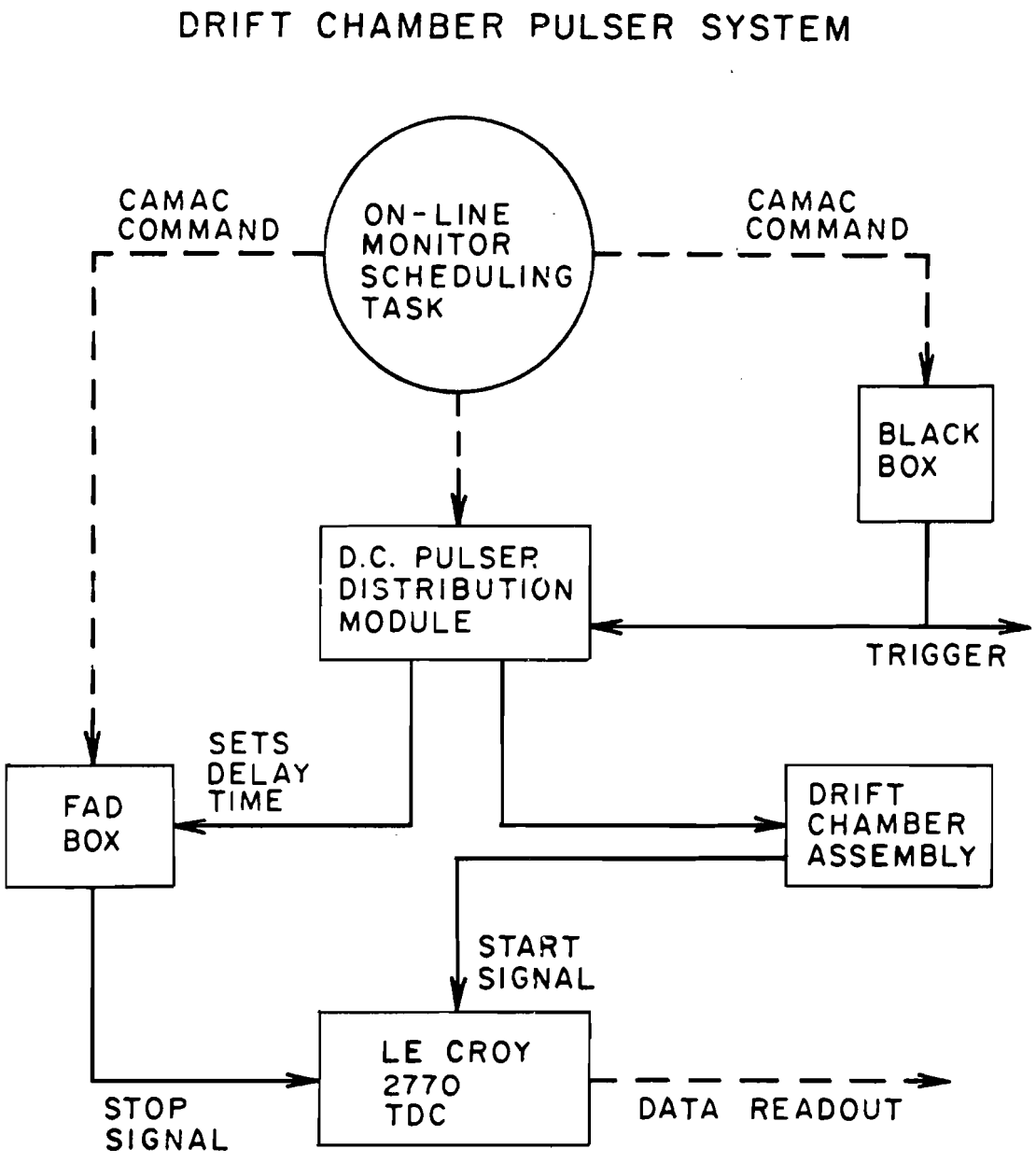

FIG. 21 Drift chamber pulser system logic diagram.

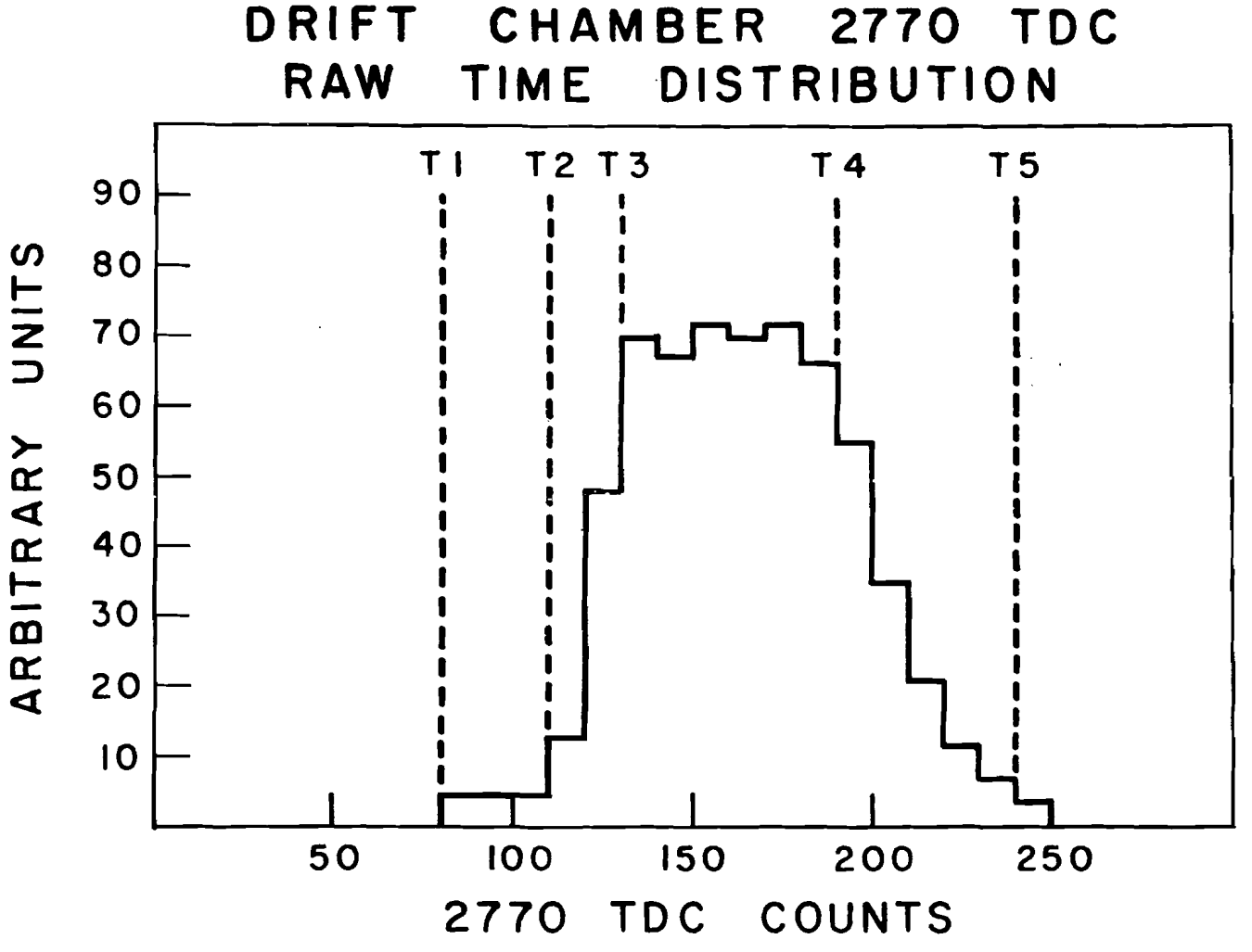
DRIFT CHAMBER 2770 TDC
RAW TIME DISTRIBUTION
T1
T2
T3
T4
T5
ARBITRARY UNITS
90
80
70
60
50
40
30
20
10
50
100
150
200
250
2770 TDC COUNTS

FIG. 22

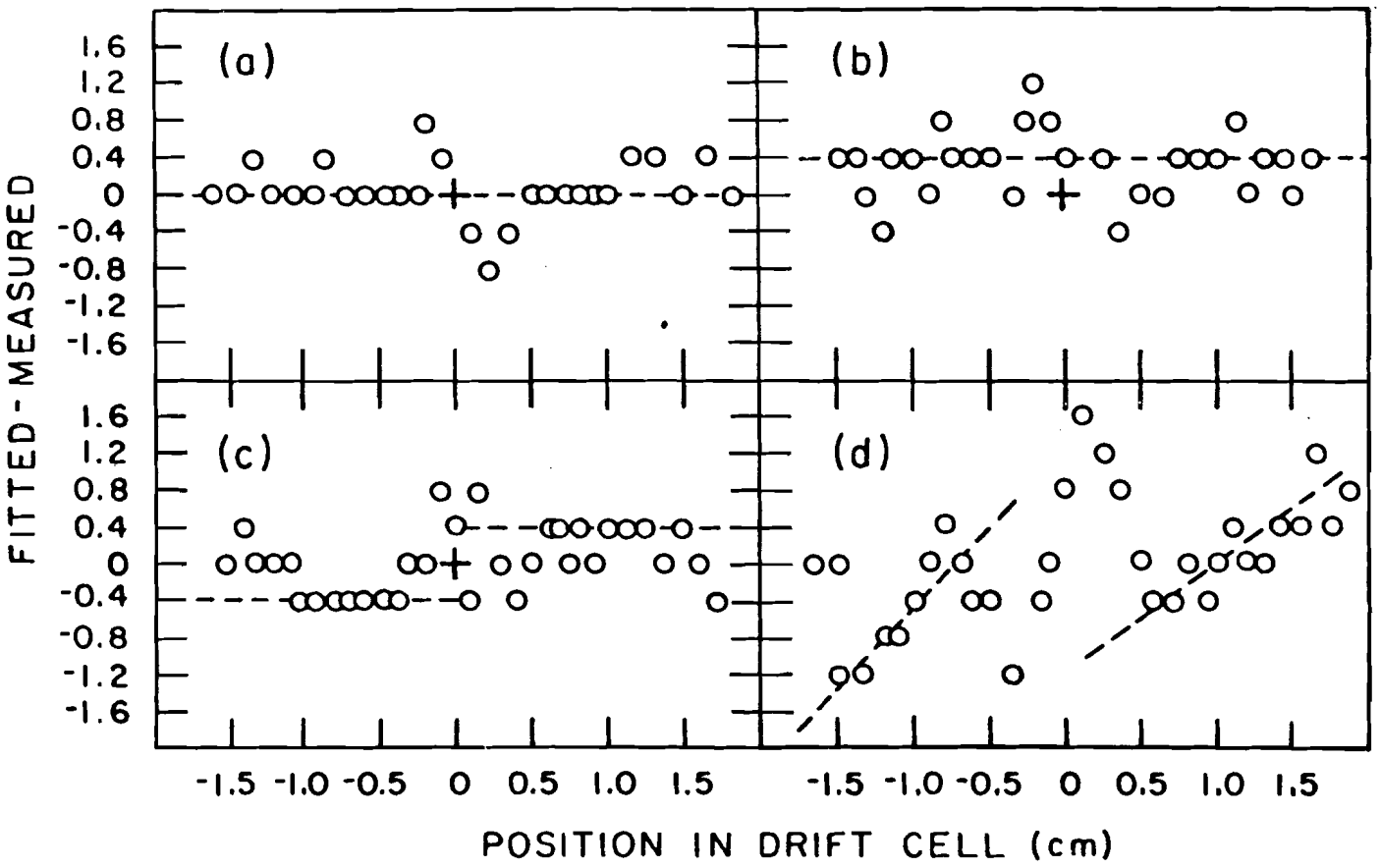

FIG. 23 Illustration of TØ and drift velocity corrections.

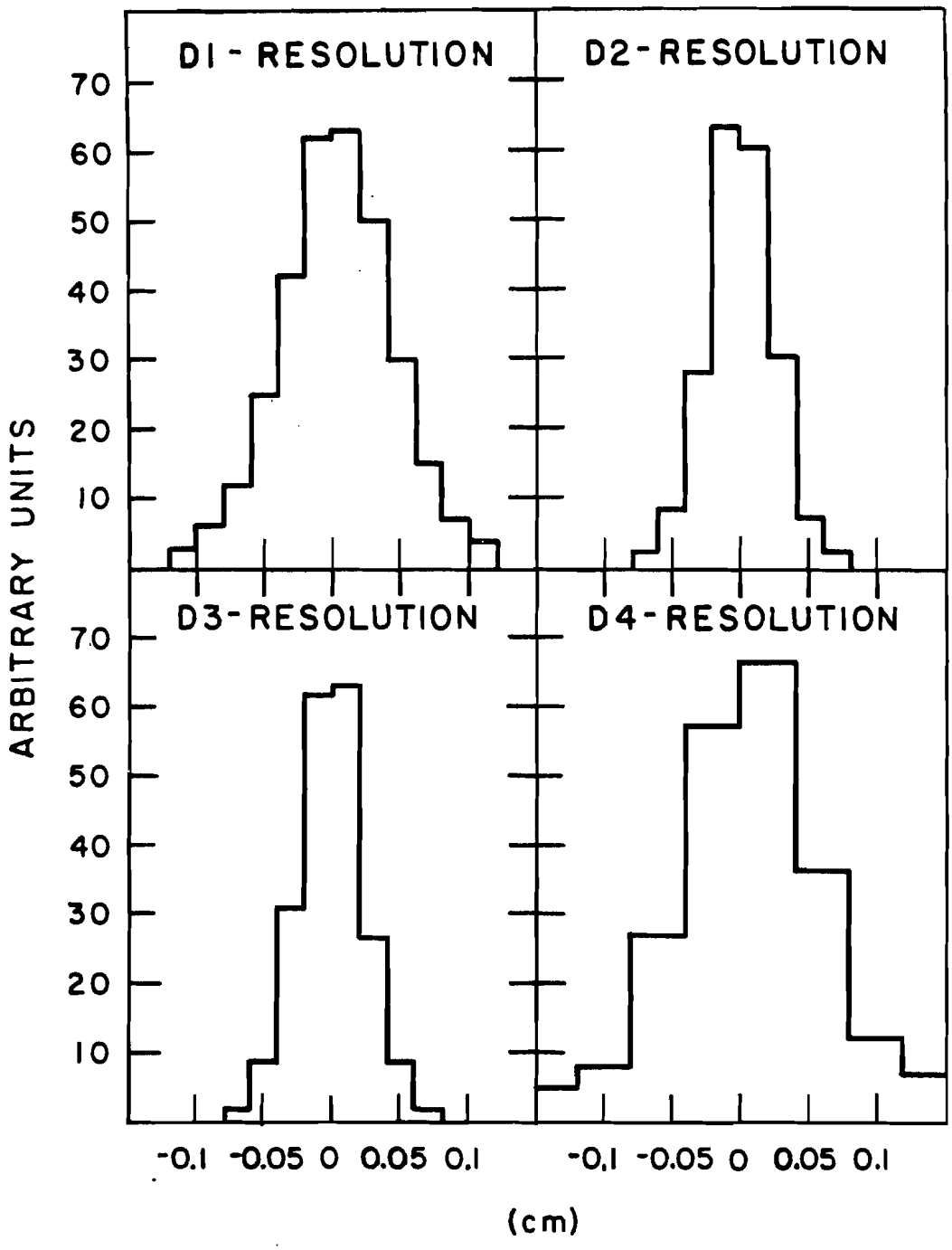

FIG. 24 Typical resolution plots for the four drift chambers.

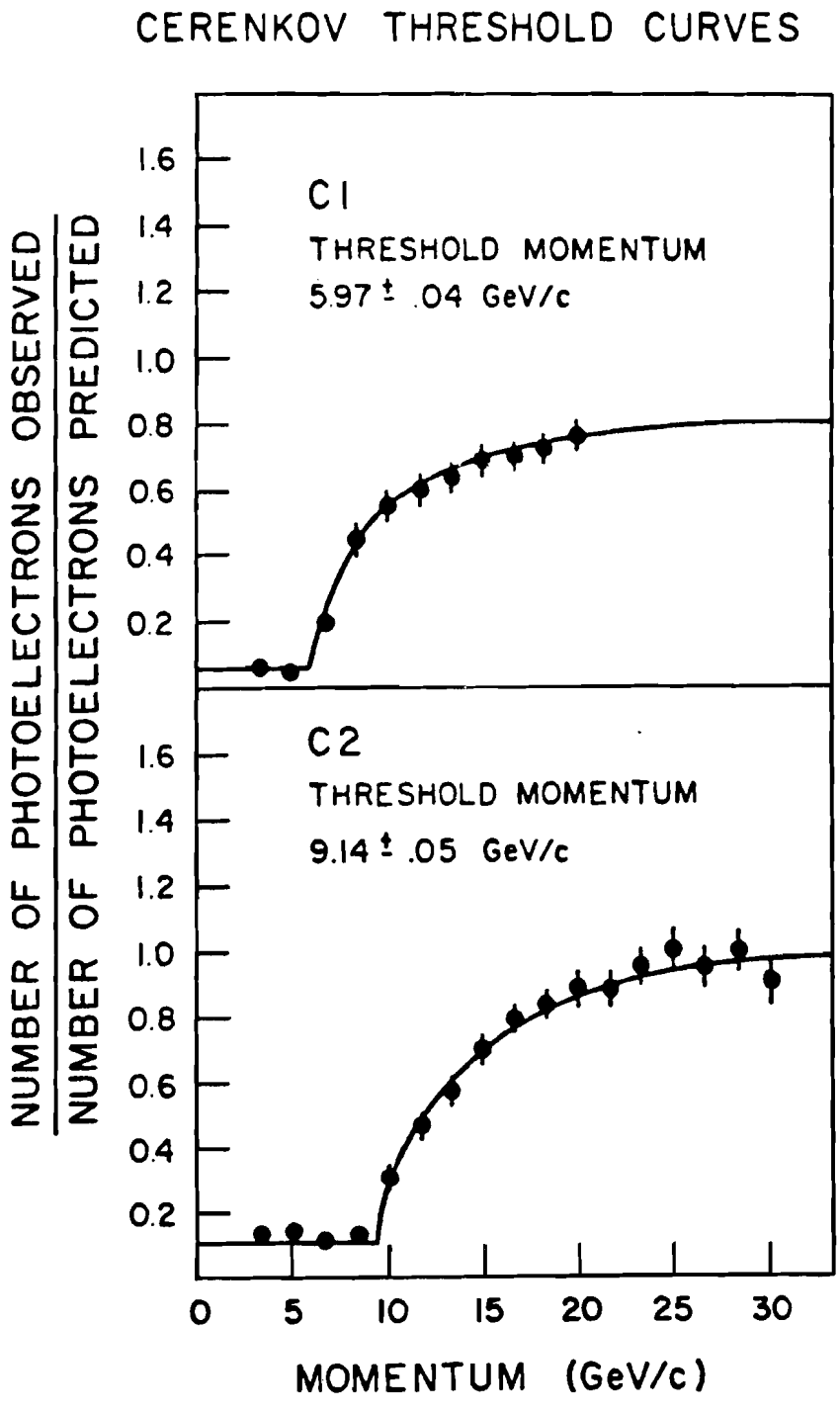

FIG. 25 Cerenkov threshold curves for pions.

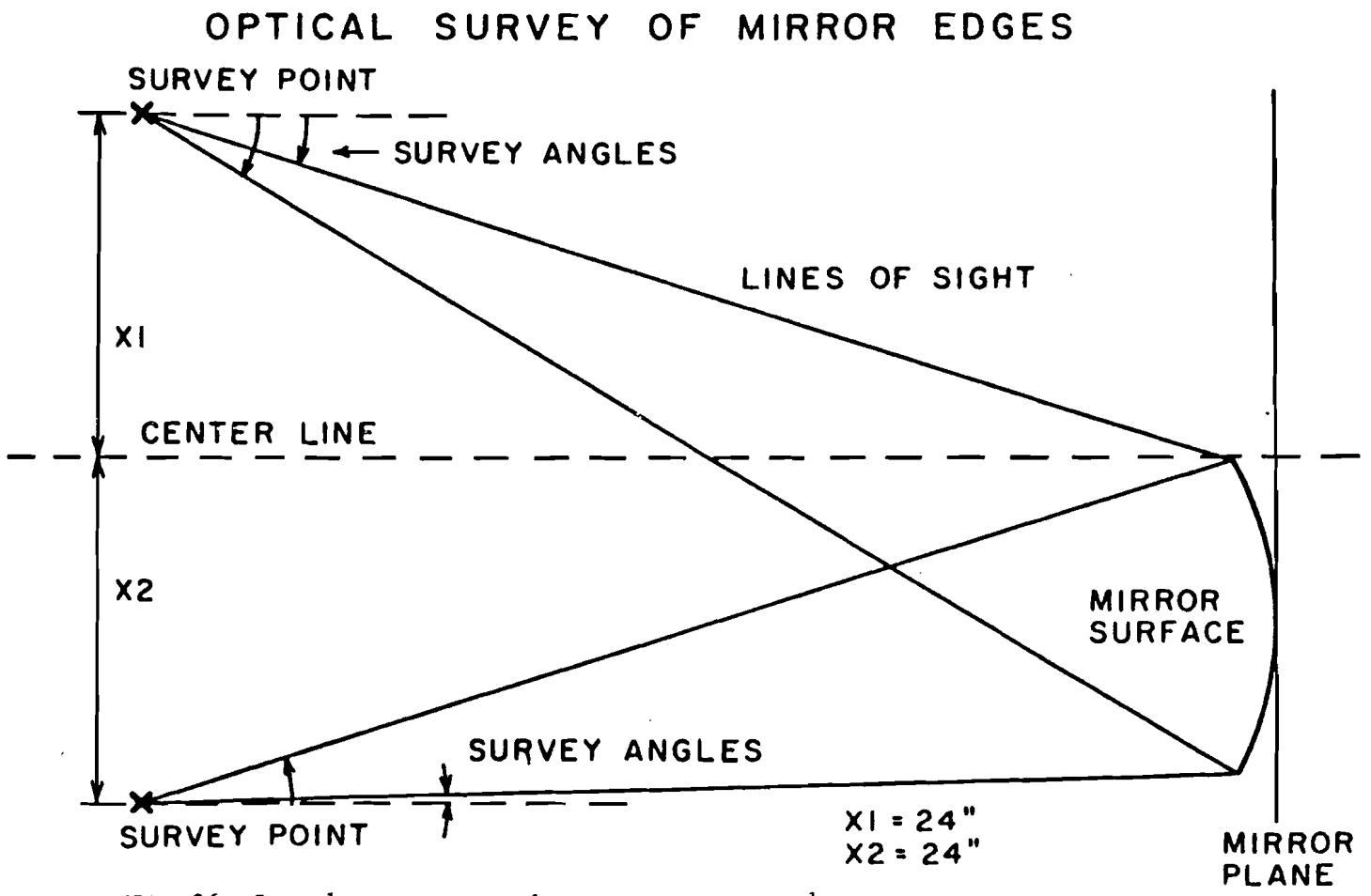

FIG. 26 Cerenkov counter mirror survey procedure.

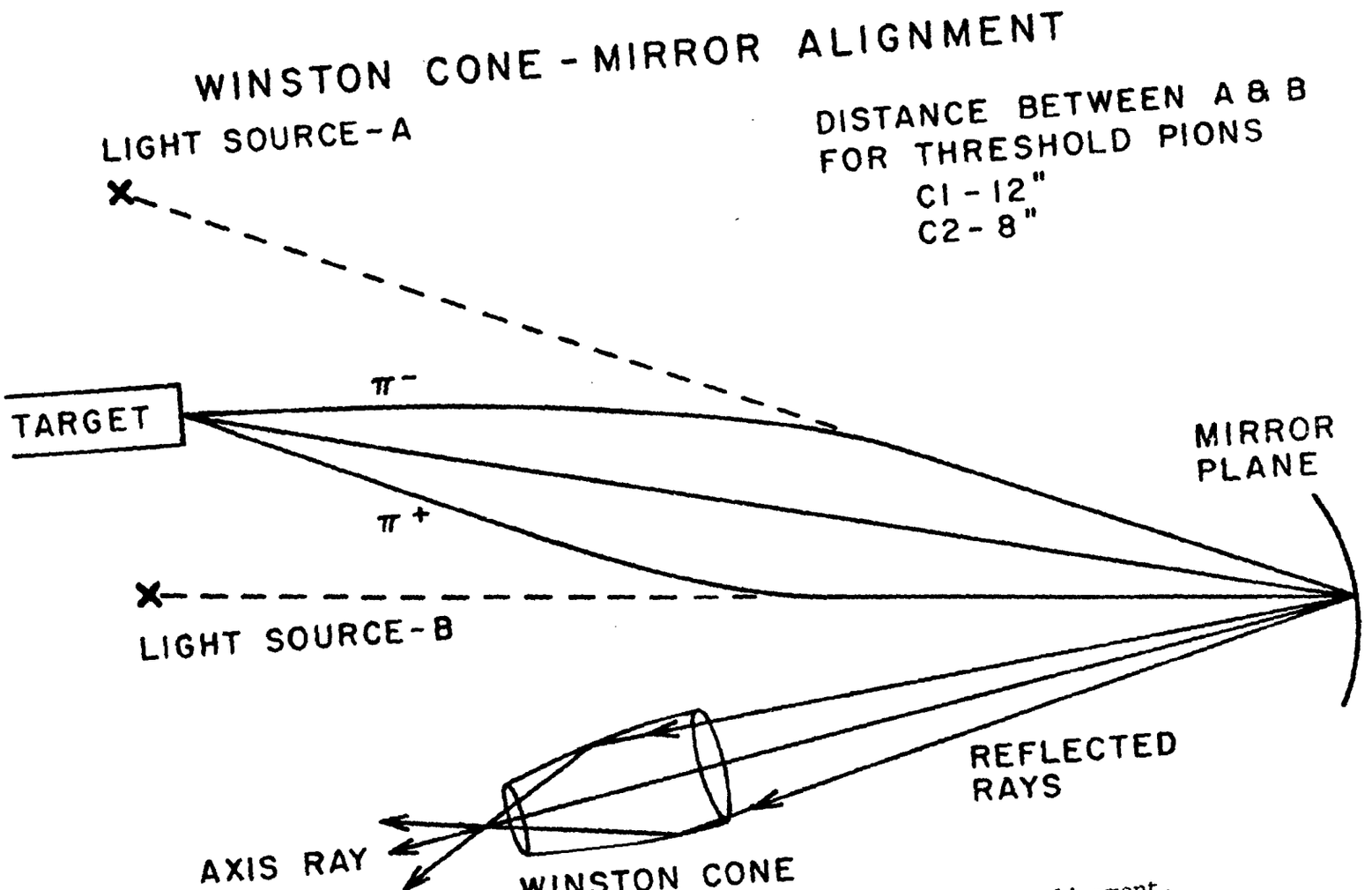

FIG. 27 Cerenkov counter mirror and Winston cone alignment.

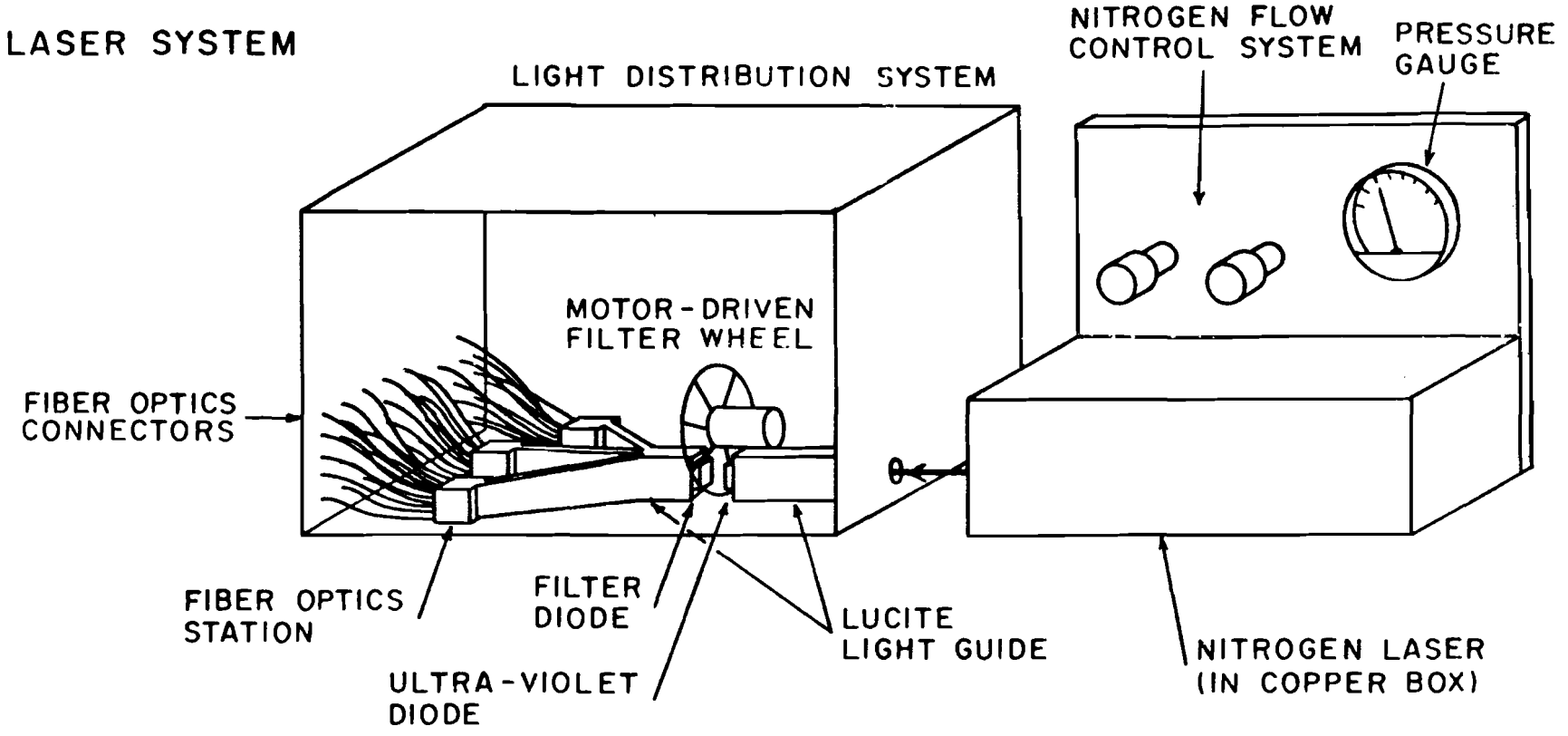

FIG. 28 Laser system used for maintaining phototube gains.

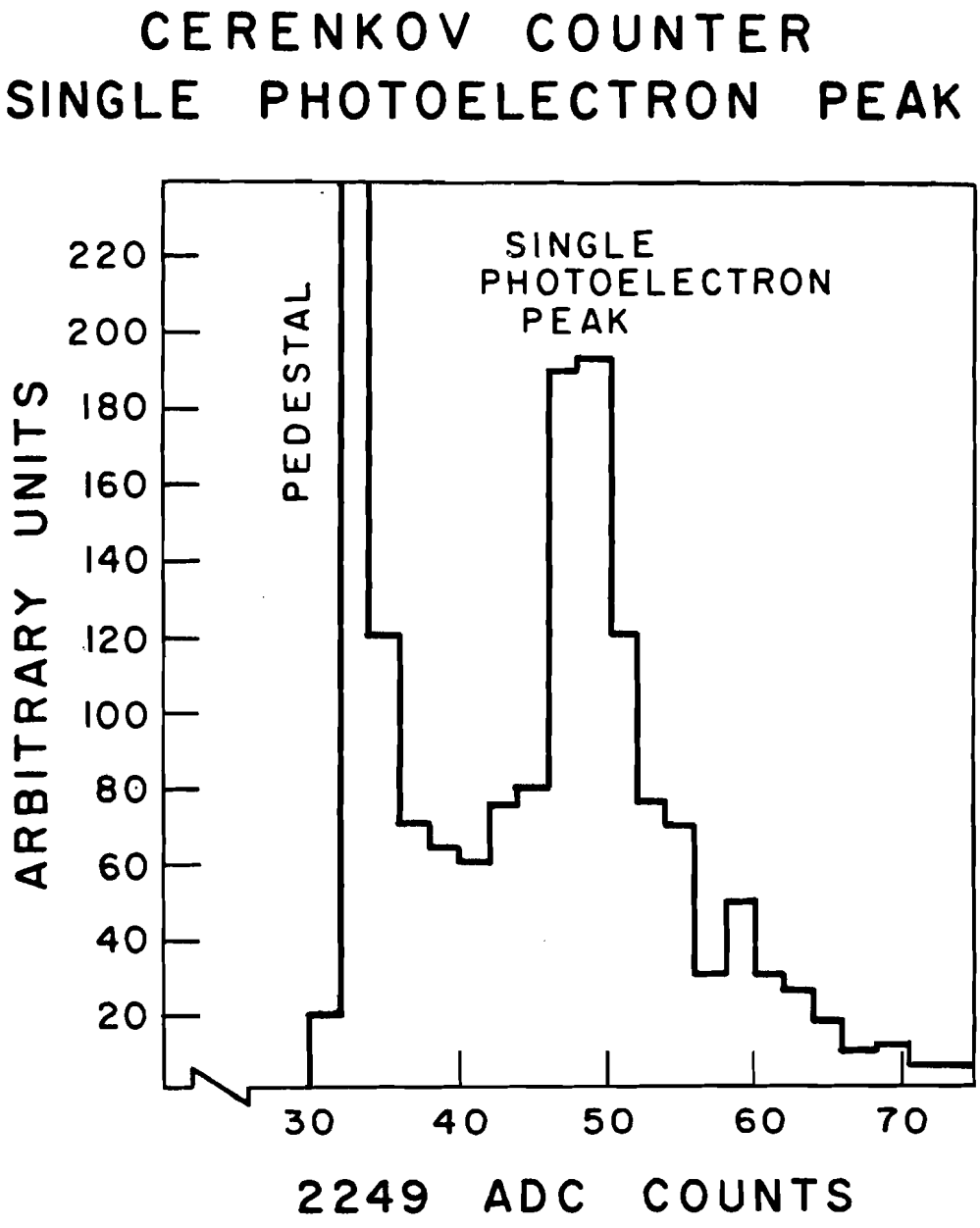

FIG. 29 Typical single photoelectron peak obtained using a low transmission filter with the laser system.

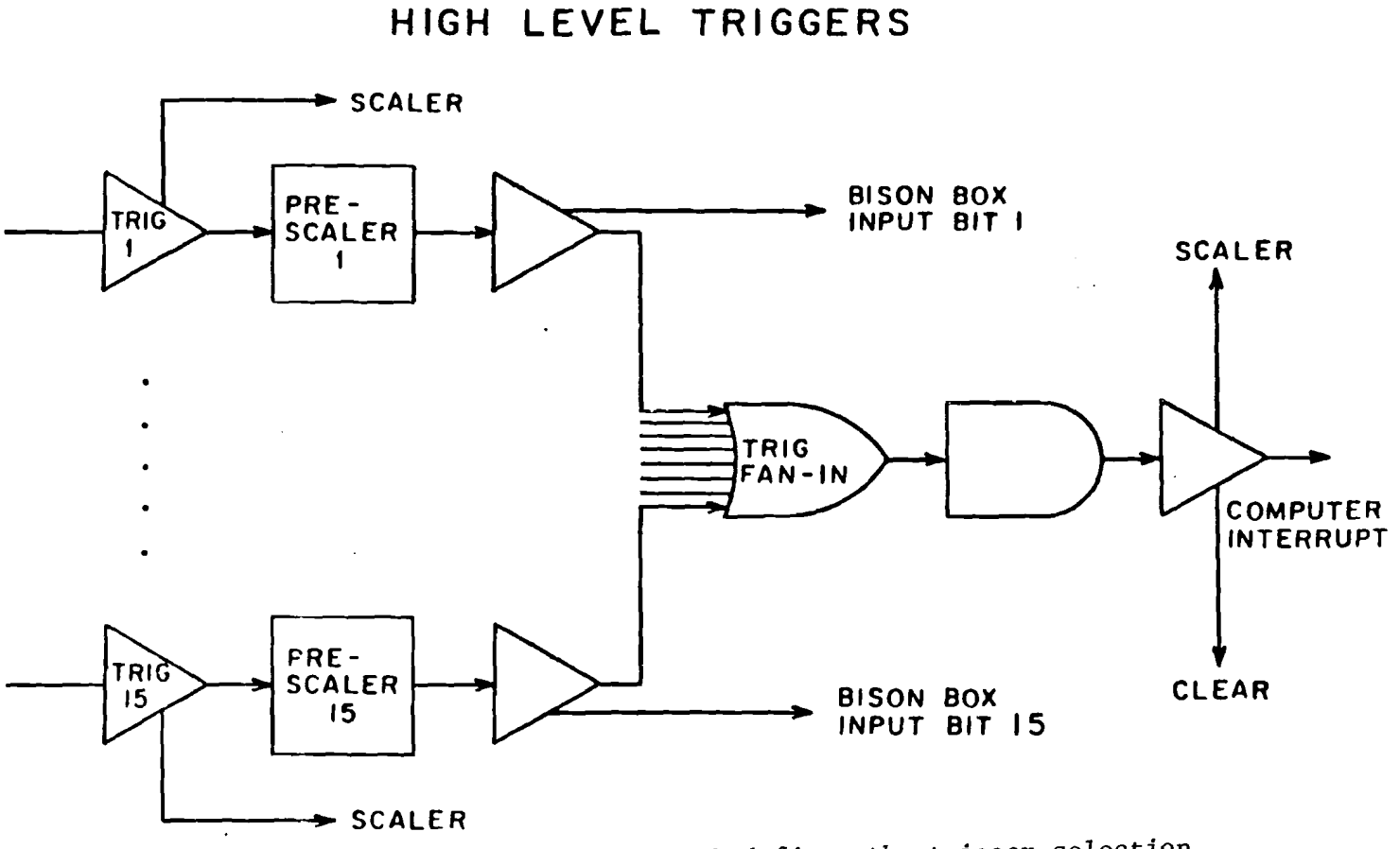

FIG. 30 High level trigger logic diagram which defines the trigger selection.

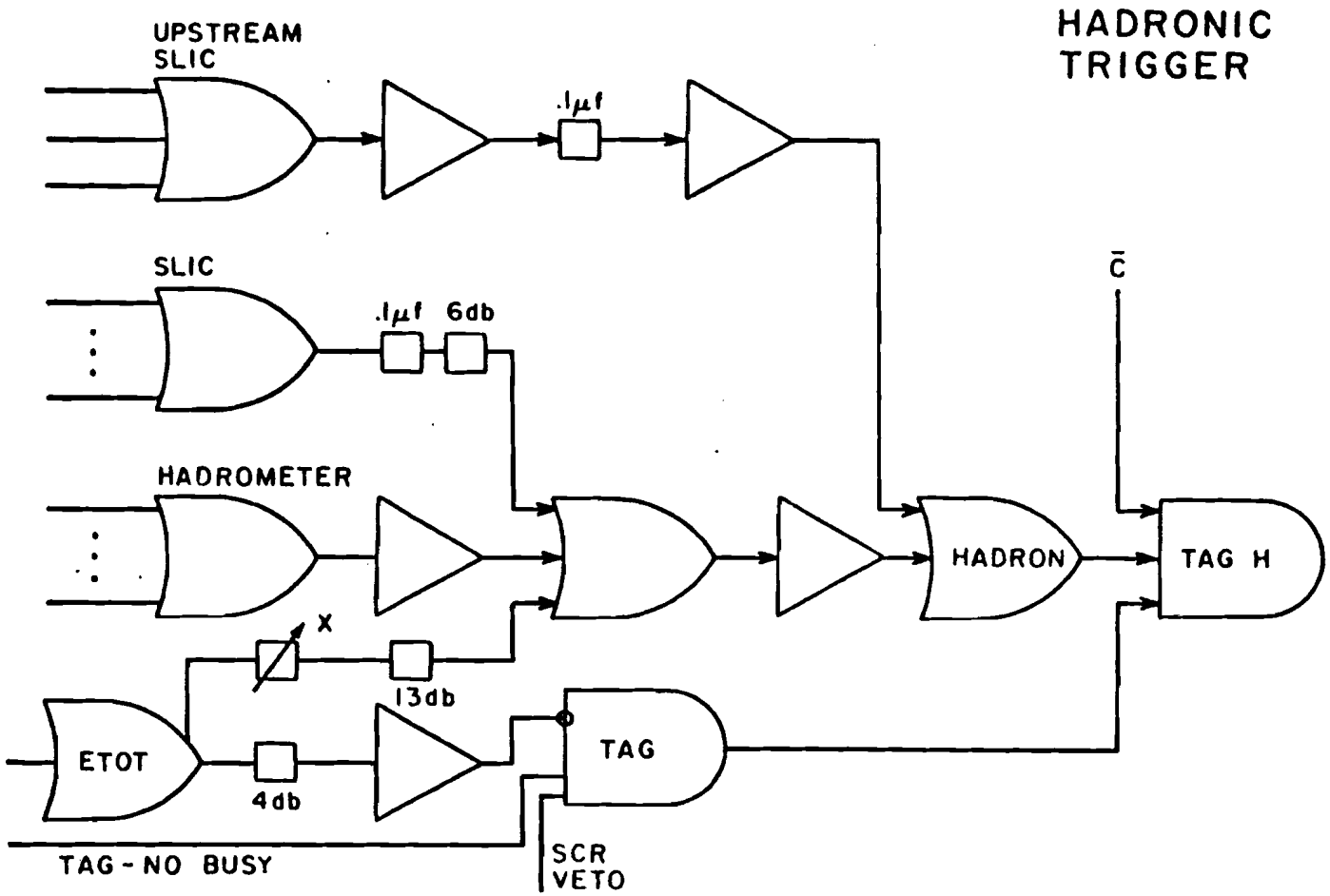

FIG. 31 TAGH trigger logic diagram which selects hadronic events.

RECOIL PROCESSOR
- BASIC FLOW CHART

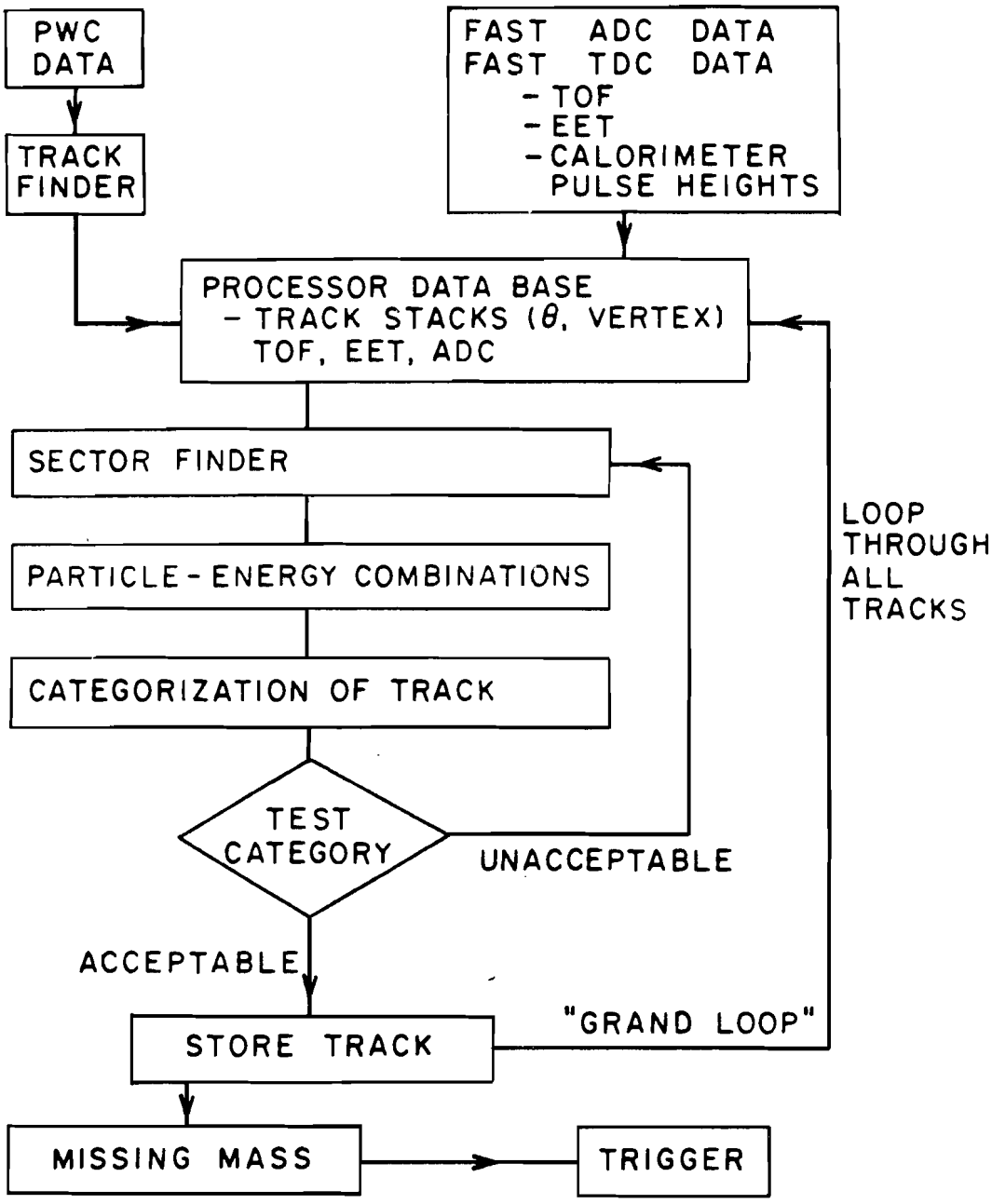

FIG. 32

ON-LINE COMPUTER CONFIGURATION

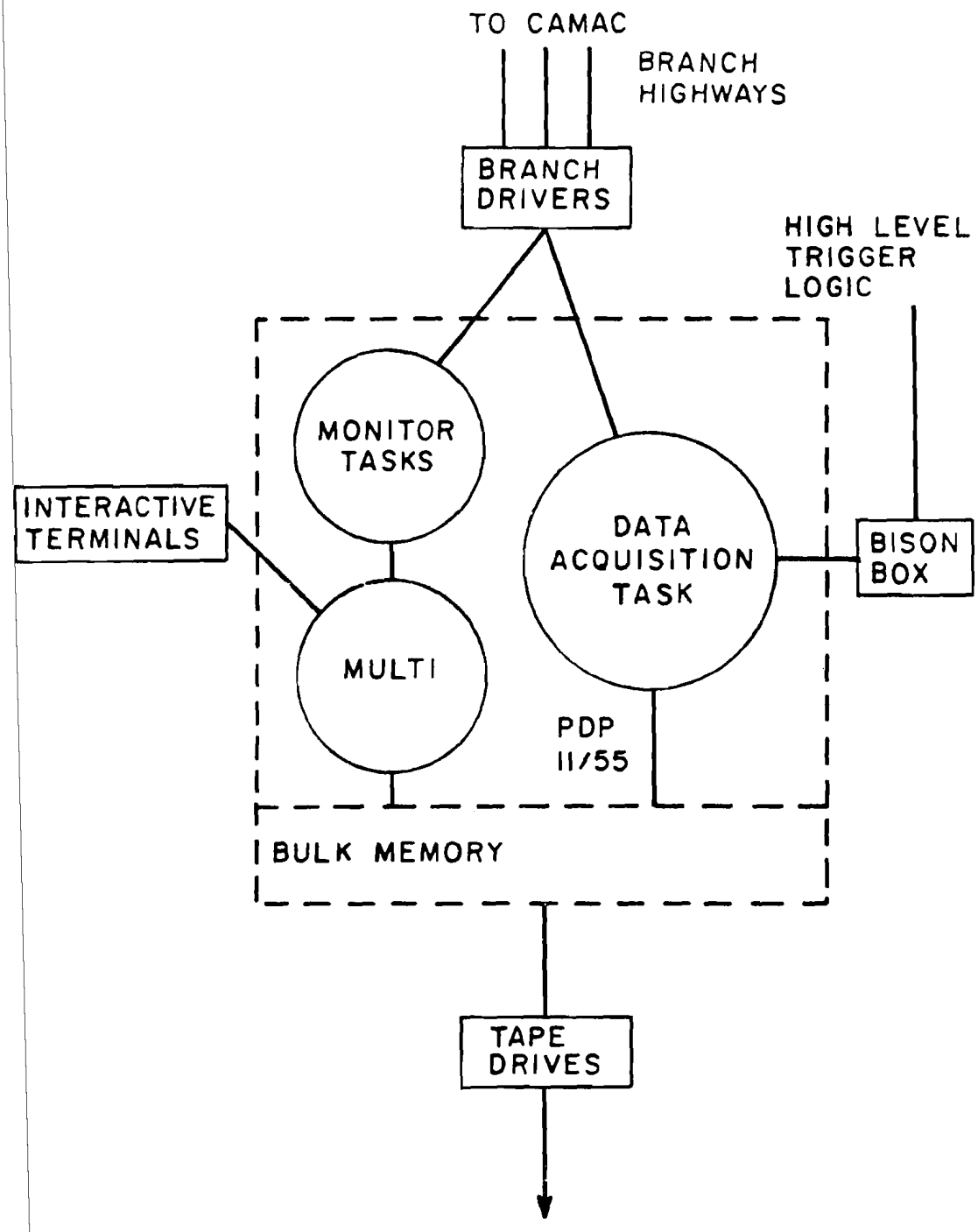

FIG. 33

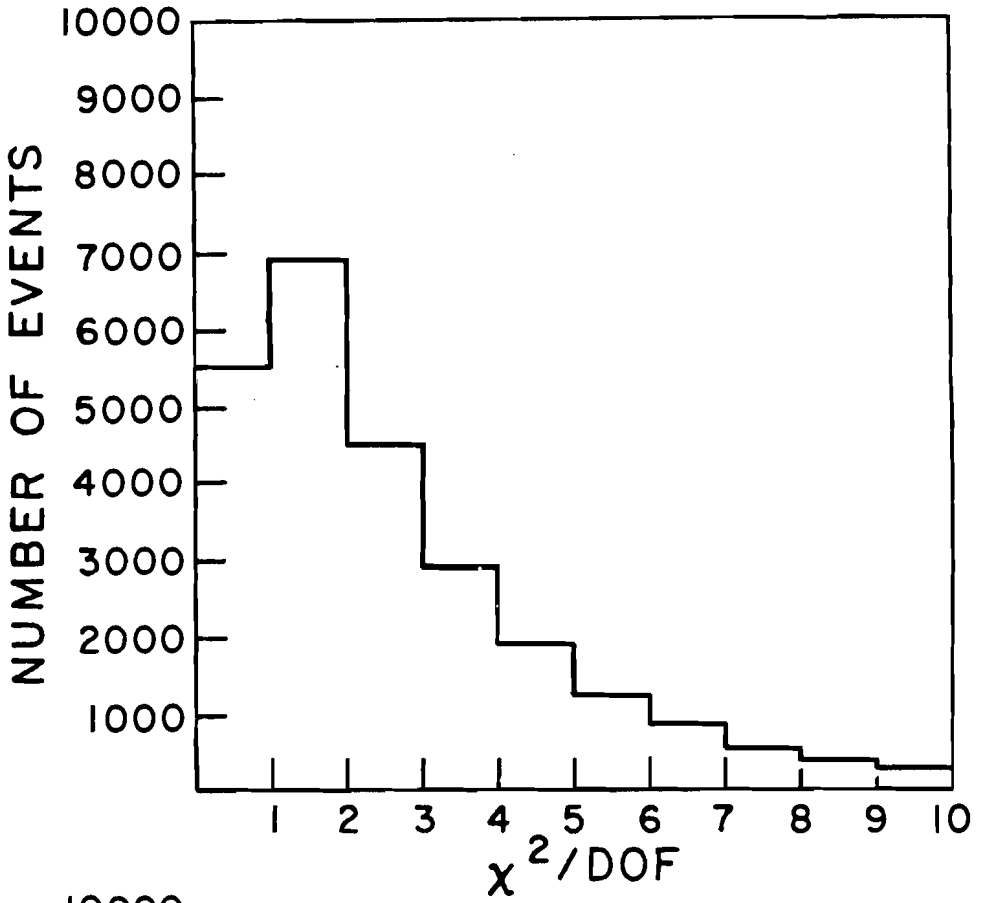

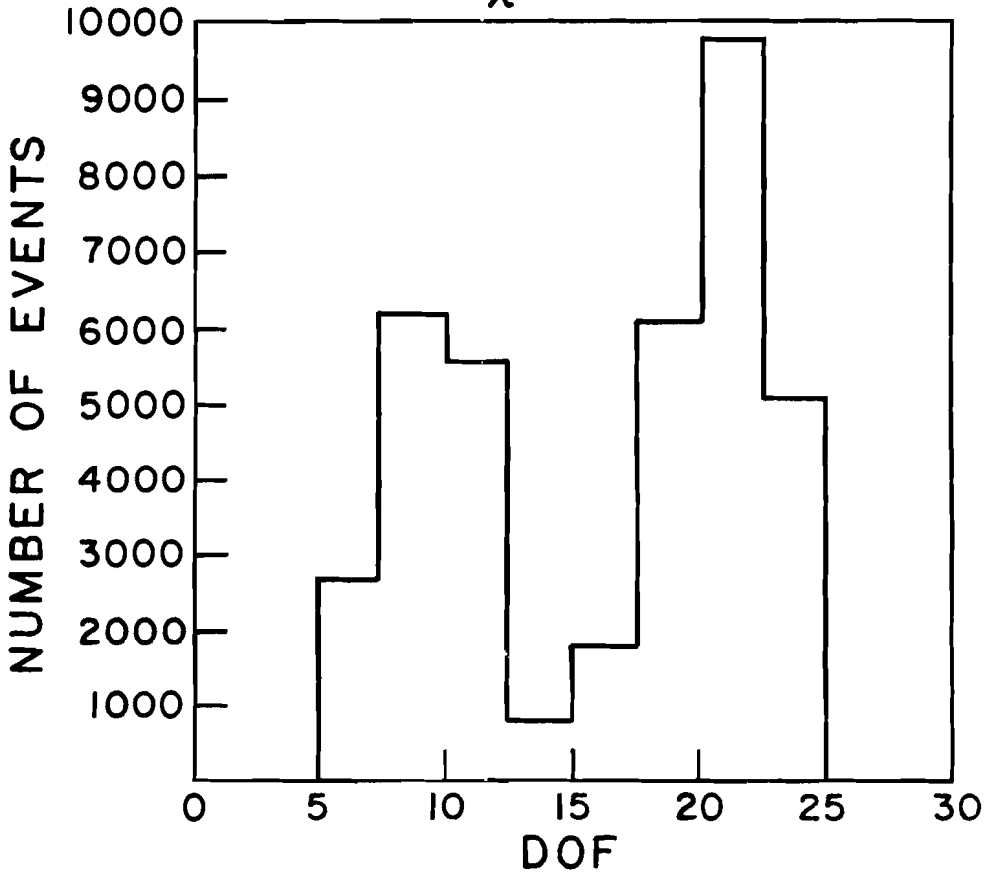

FIG. 34 Chi-square and degrees of freedom plots.

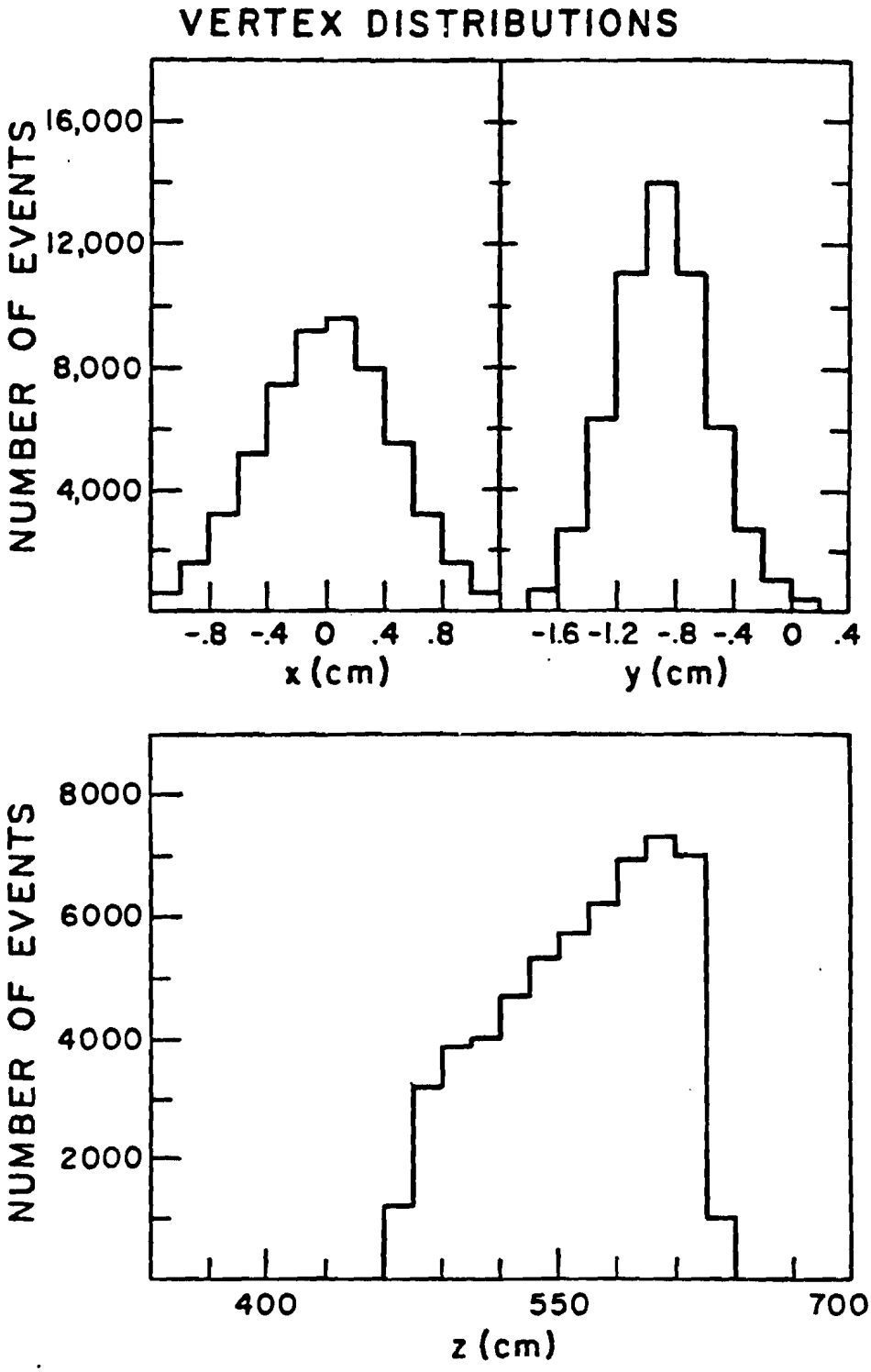
VERTEX DISTRIBUTIONS
NUMBER OF EVENTS
16,000
12,000
8,000
4,000
-.8 -.4 0 .4 .8
x (cm)
-1.6 -1.2 -.8 -.4 0 .4
y (cm)
NUMBER OF EVENTS
8000
6000
4000
2000
400
550
700
z (cm)

FIG. 35

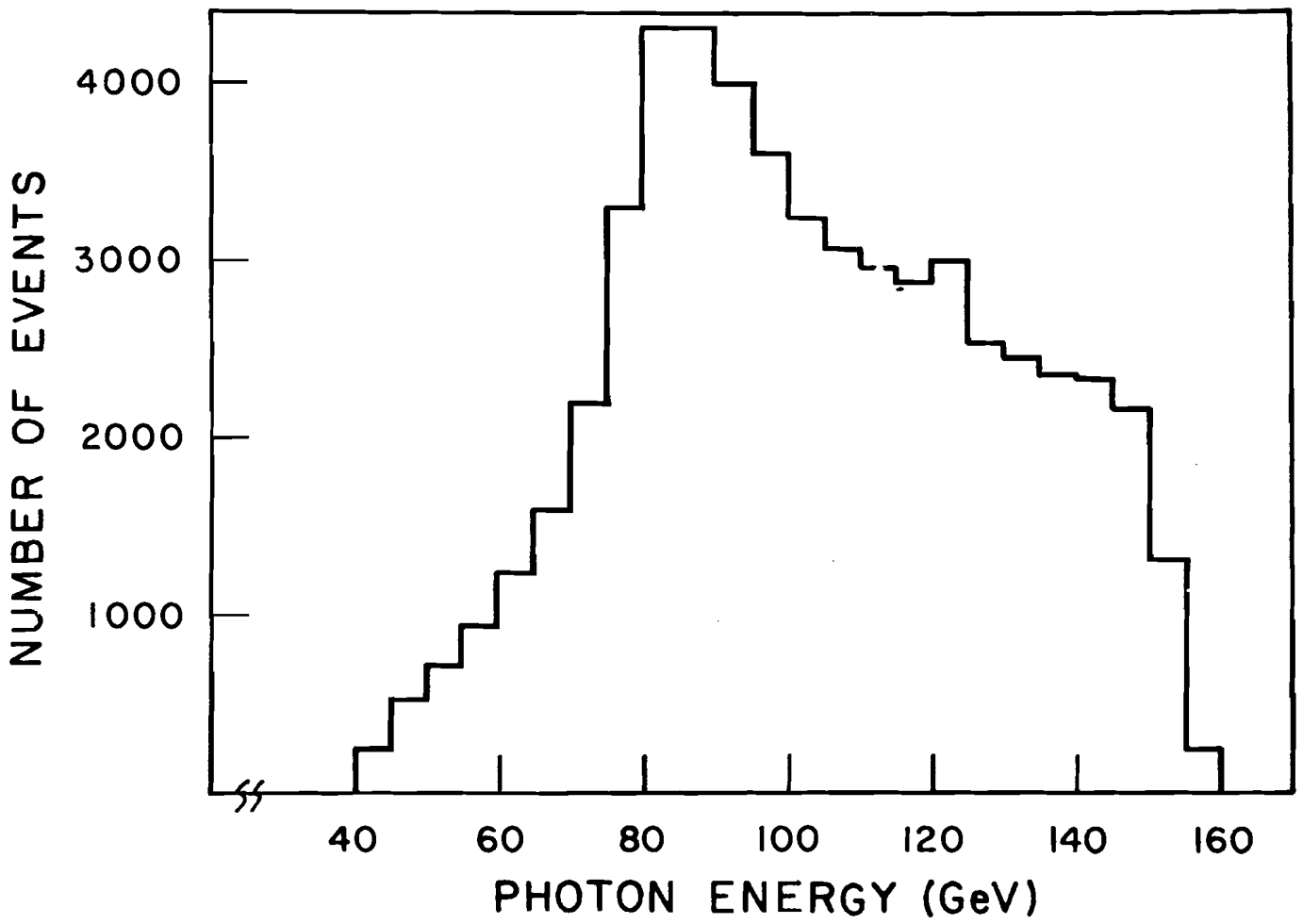

Fig. 36 Photon energy spectrum before corrections.

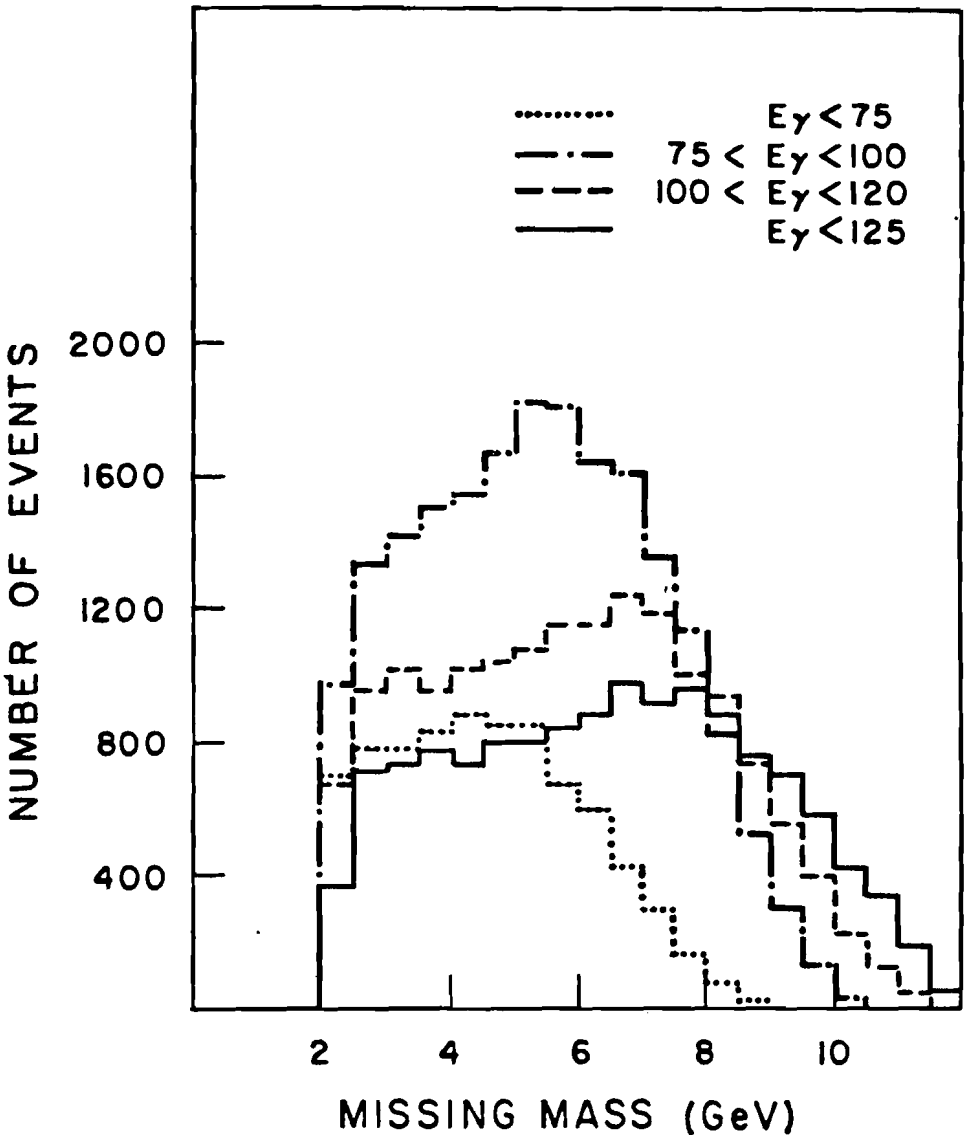

FIG. 37 Missing mass spectra before corrections for different photon energy bins.

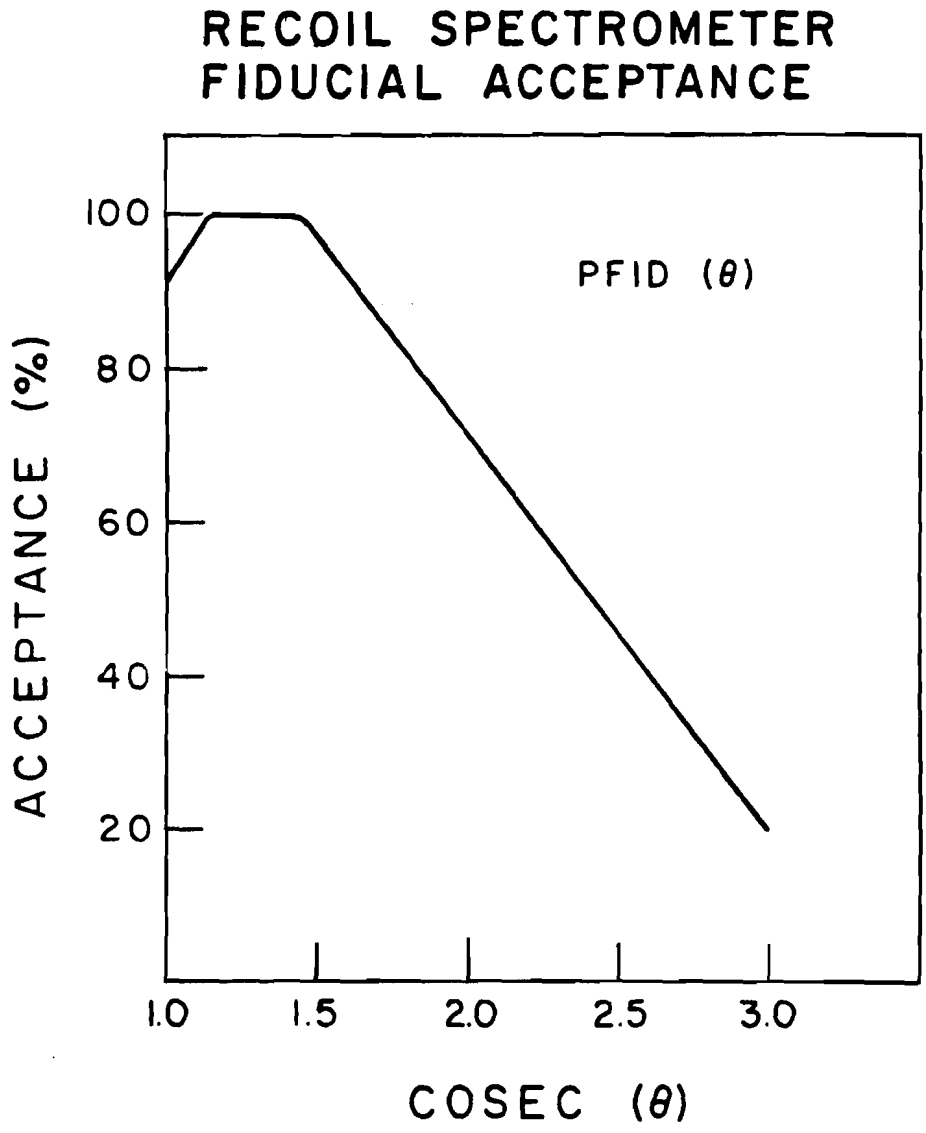

FIG. 38 Recoil spectrometer acceptance due to geometrical effects only as a function of the angle between the recoil proton and the photon projectile.

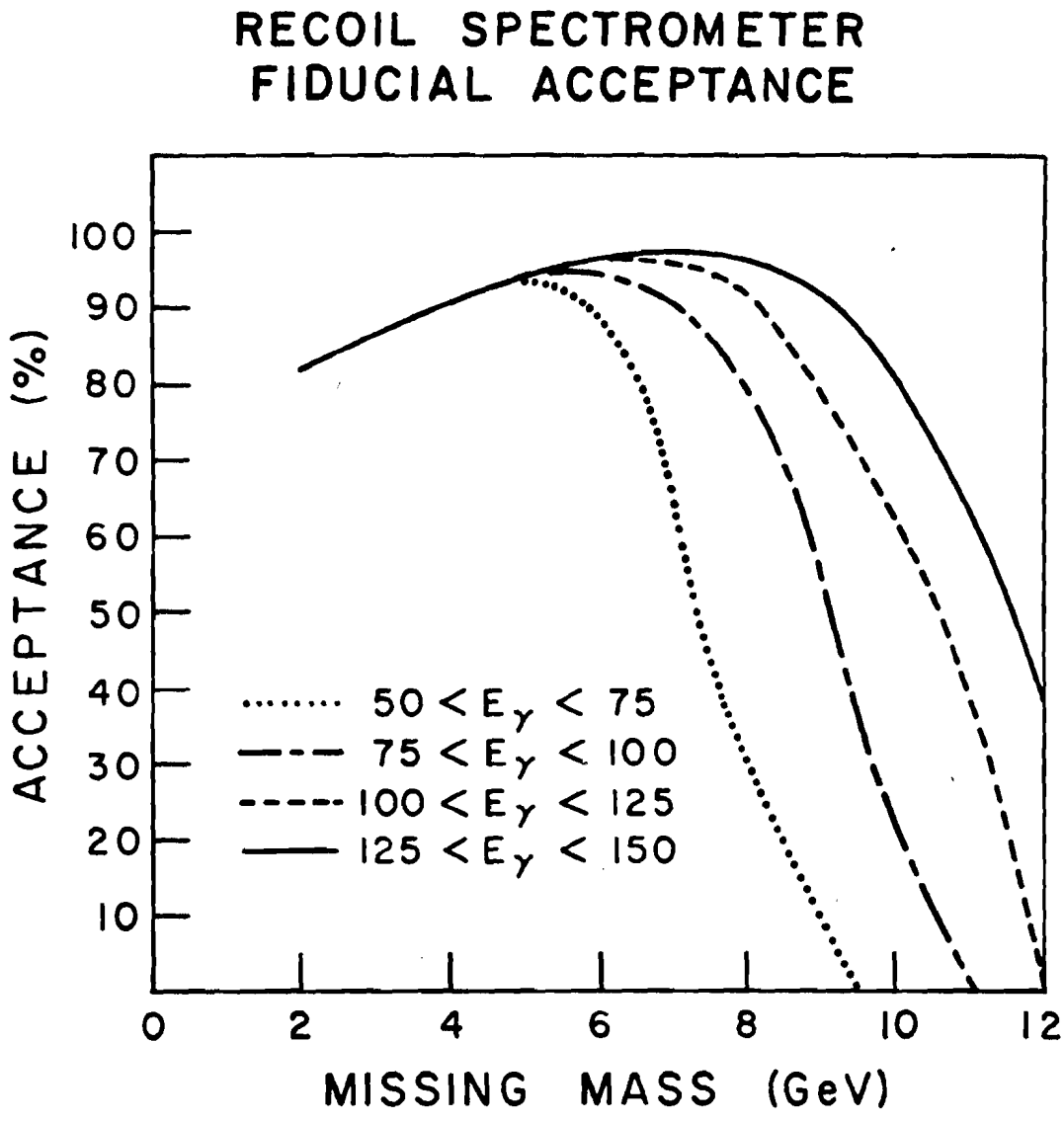

FIG. 39 Recoil spectrometer fiducial acceptance as a function of the missing mass for different photon energy bins.

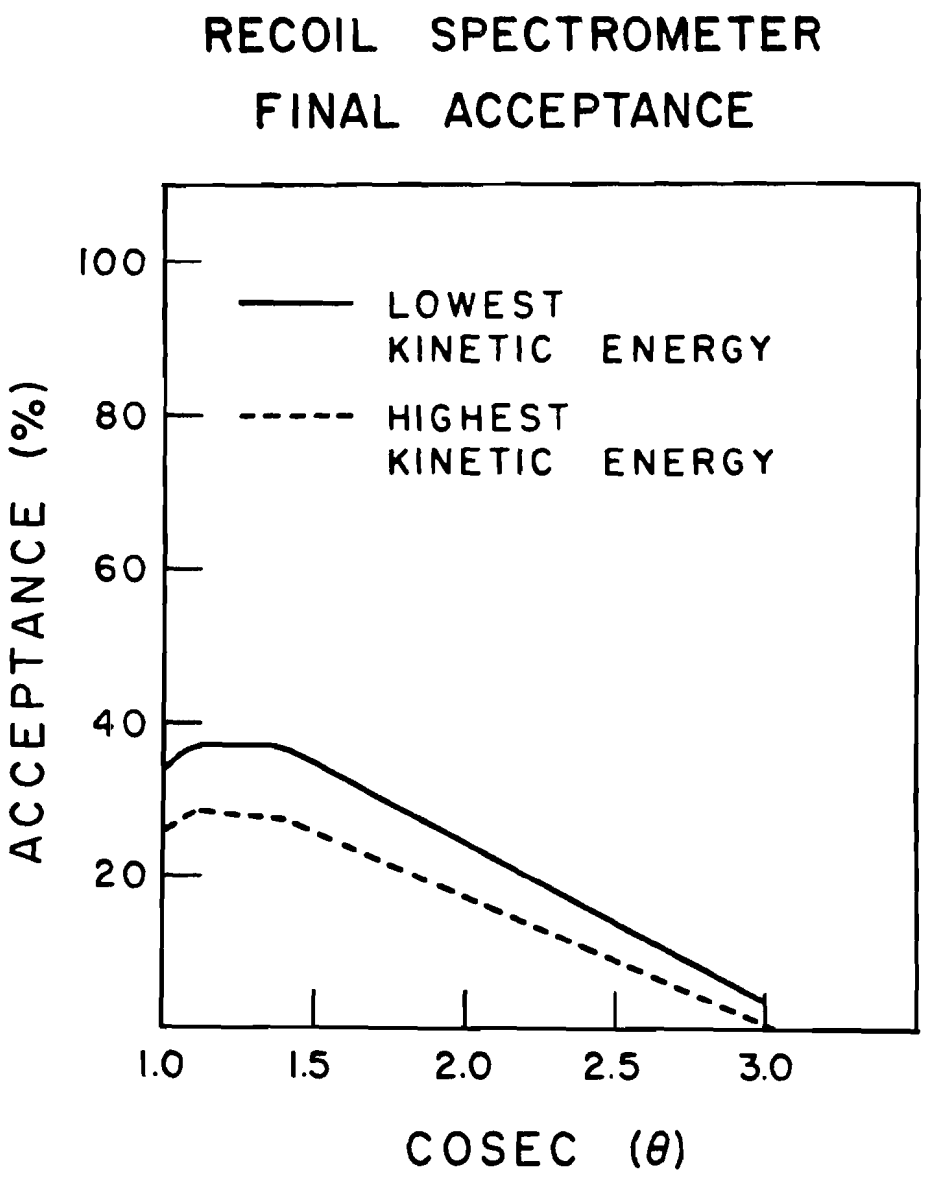

FIG. 40 Recoil spectrometer acceptance including detector efficiencies determined from the data.

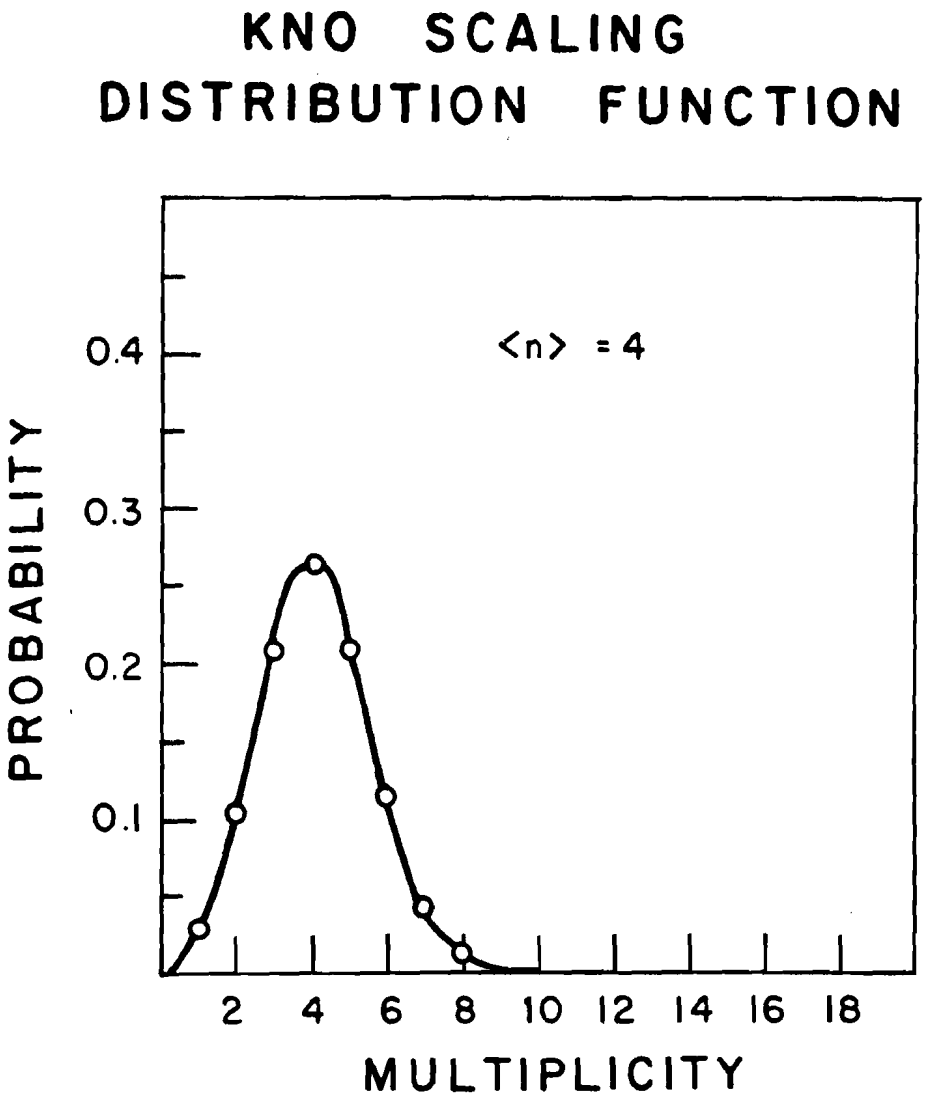

FIG. 41 Typical KNO scaling distribution function for an average multiplicity of 4.

MONTE CARLO EVENT GENERATION

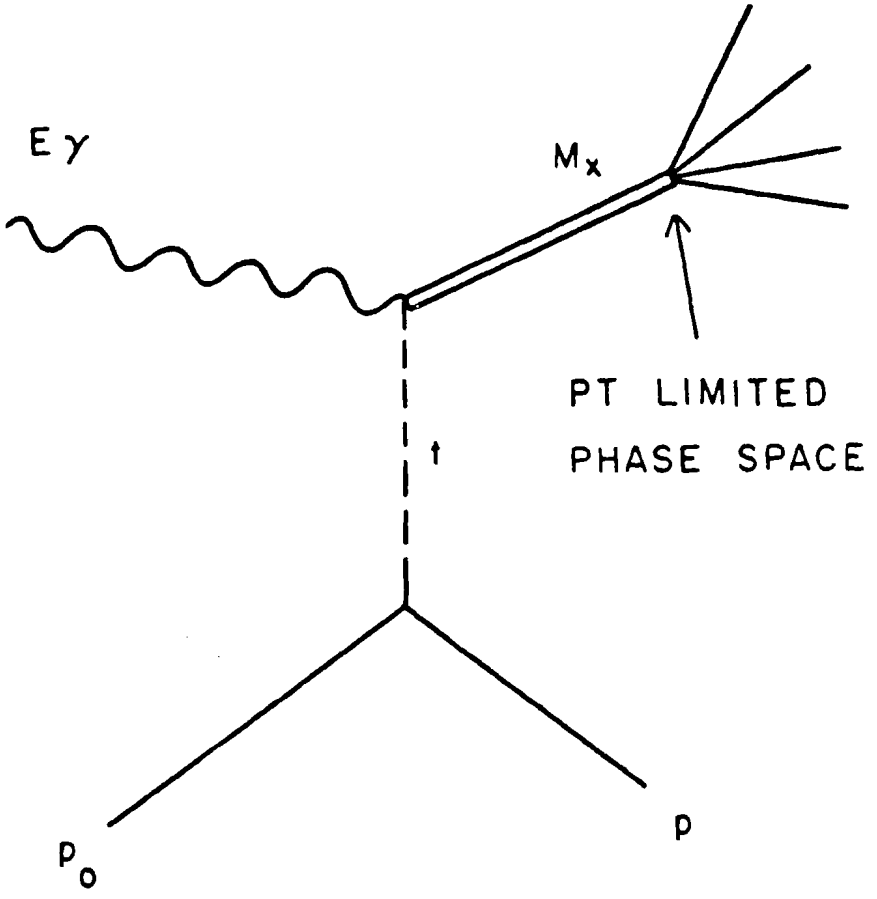

FIG. 42 Diagram defining kinematical variables used in the Monte Carlo event generation.

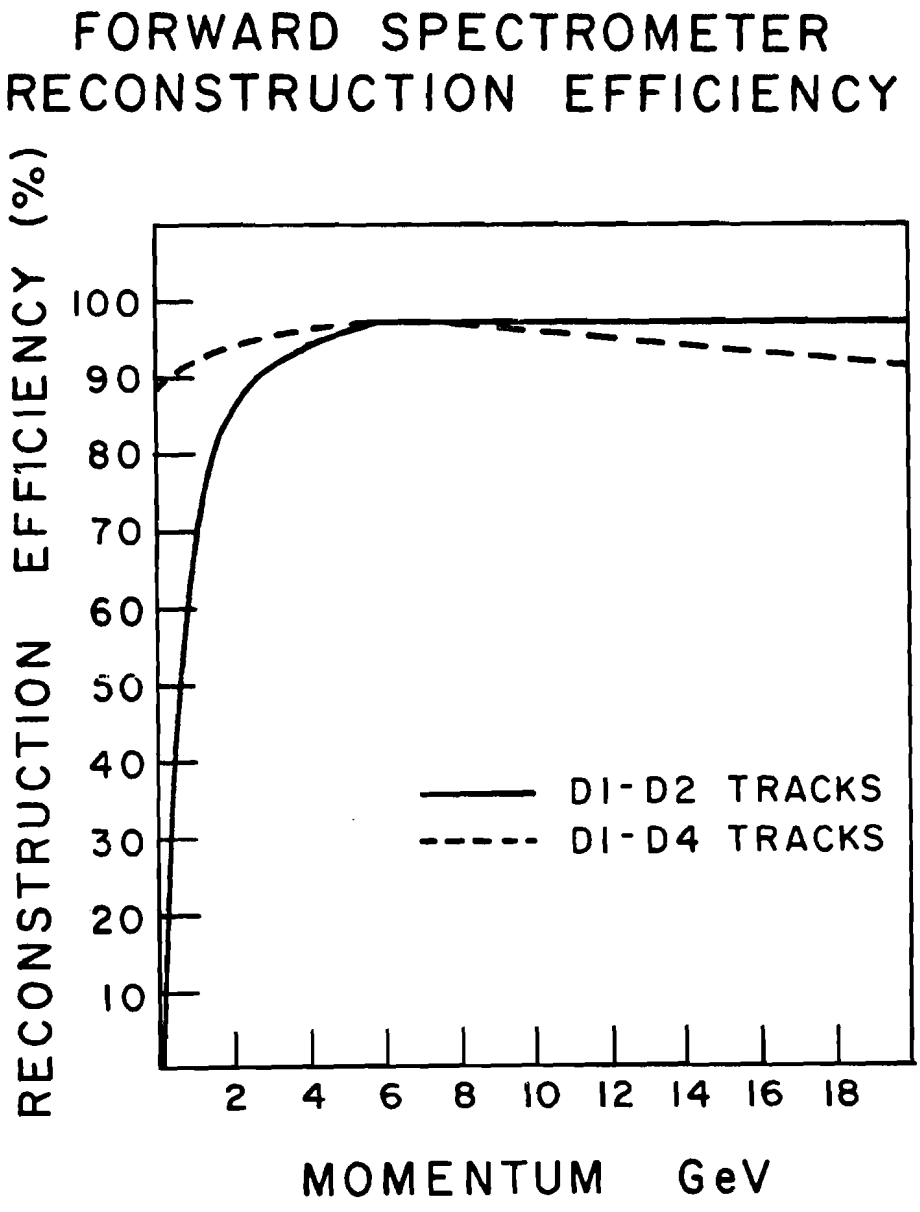

FIG. 43 Forward spectrometer reconstruction efficiency determined from the Monte Carlo for tracks reconstructed in D1-D2 only and for tracks which penetrated the entire drift chamber system (D1-D4).

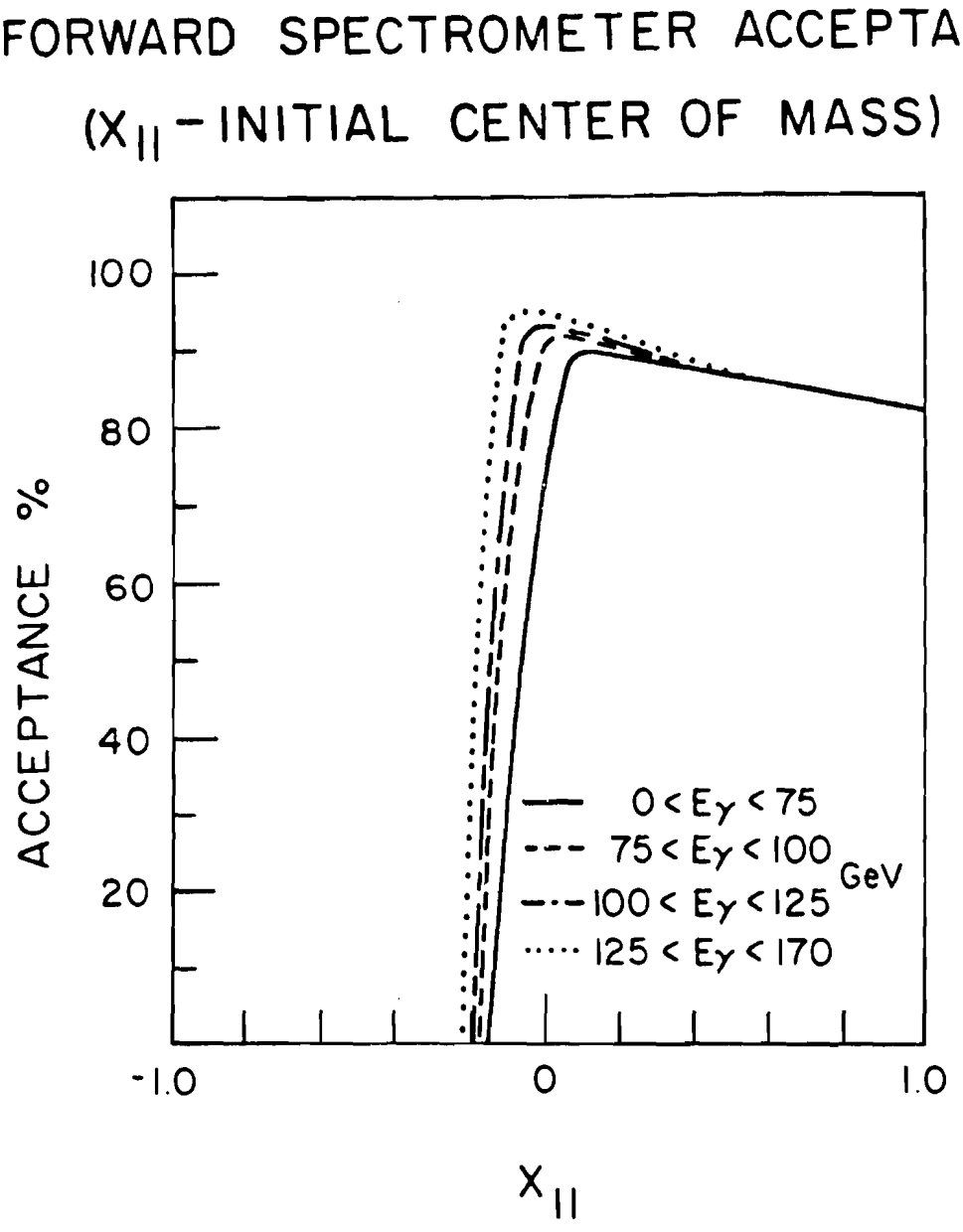

FIG. 44 Forward spectrometer acceptance plotted as a function of Feynman x in the initial center of mass for different photon energy bins.

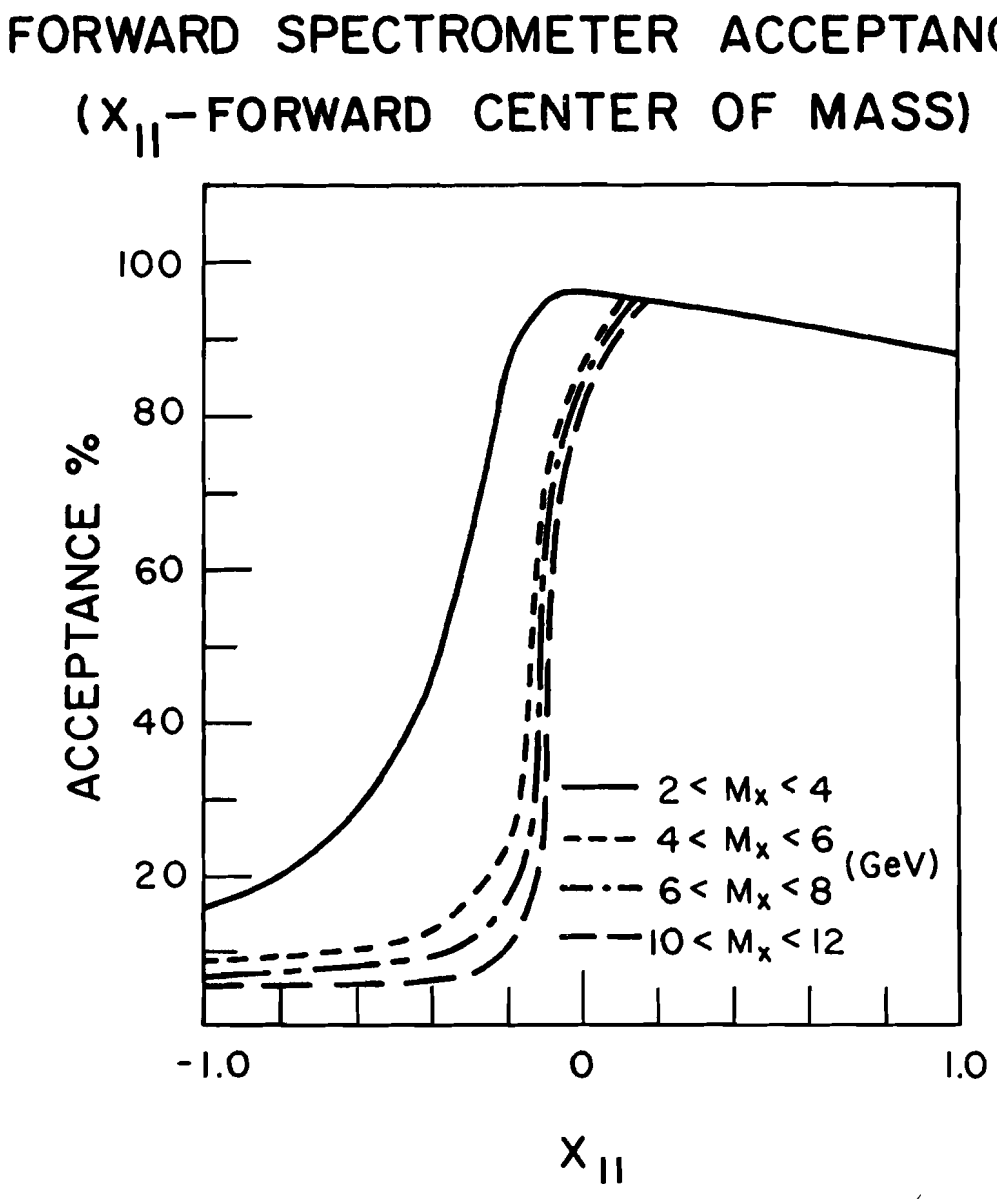

FIG. 45 Forward spectrometer acceptance plotted as a function of Feynman x in the forward center of mass for different missing mass bins.

NUCLEON RESONANCE DECAY MODES

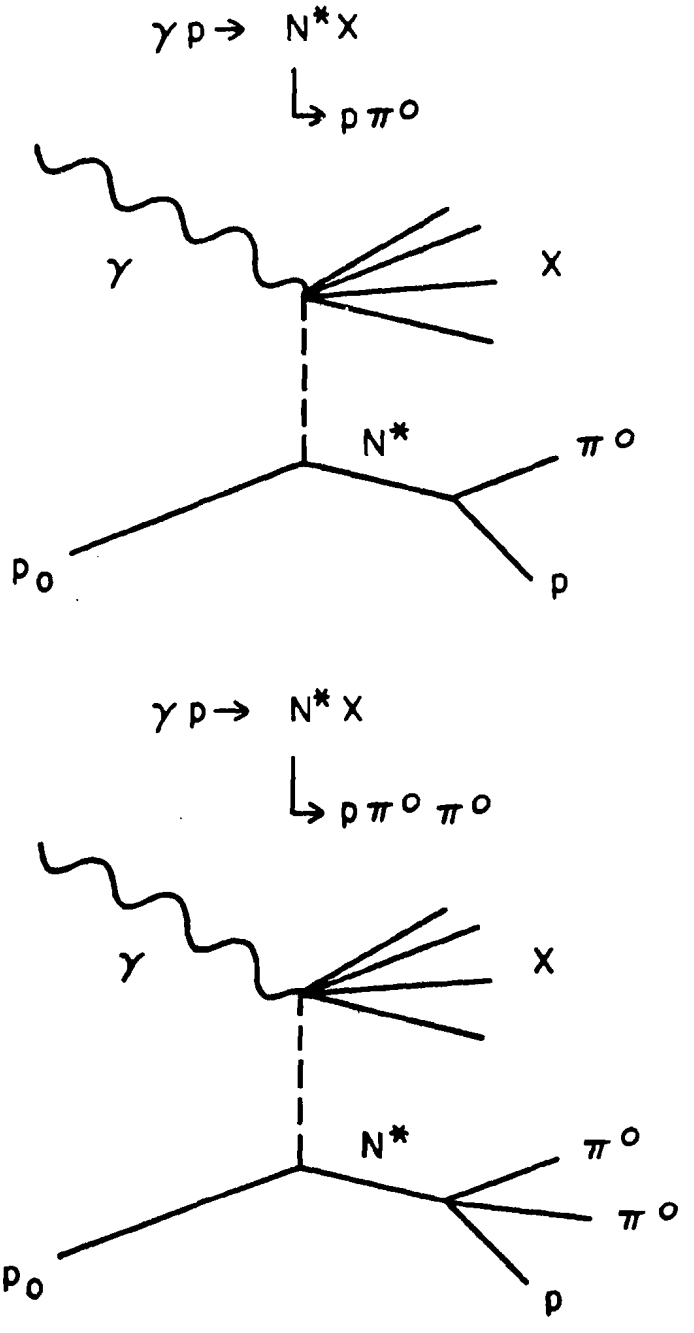

FIG. 46 N* decay modes involving neutral pions in the final state.

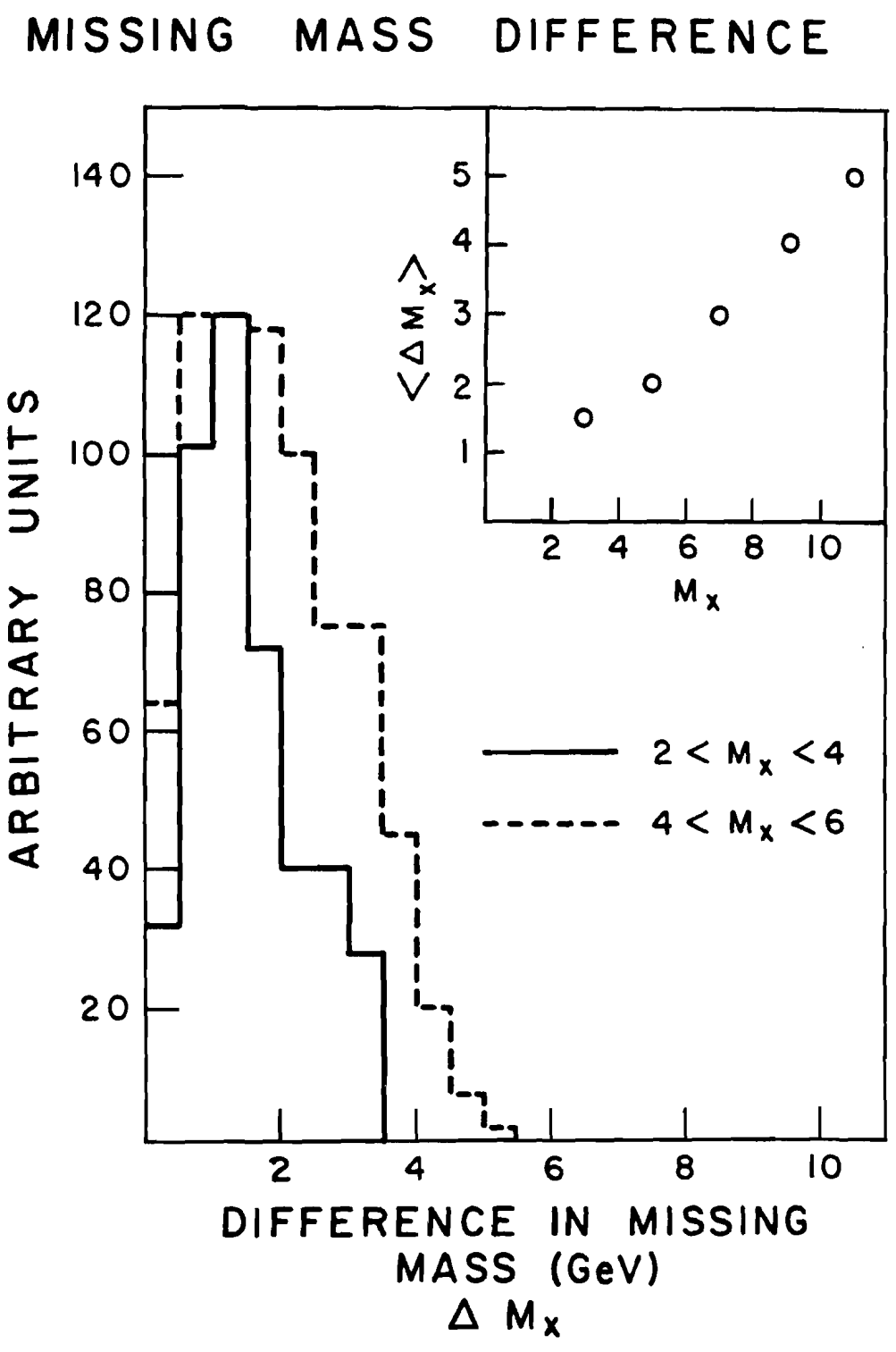

FIG. 47 Difference in the missing mass as measured by the N* and the proton which decays from the N*. The inset shows the average difference versus the missing mass of the proton.

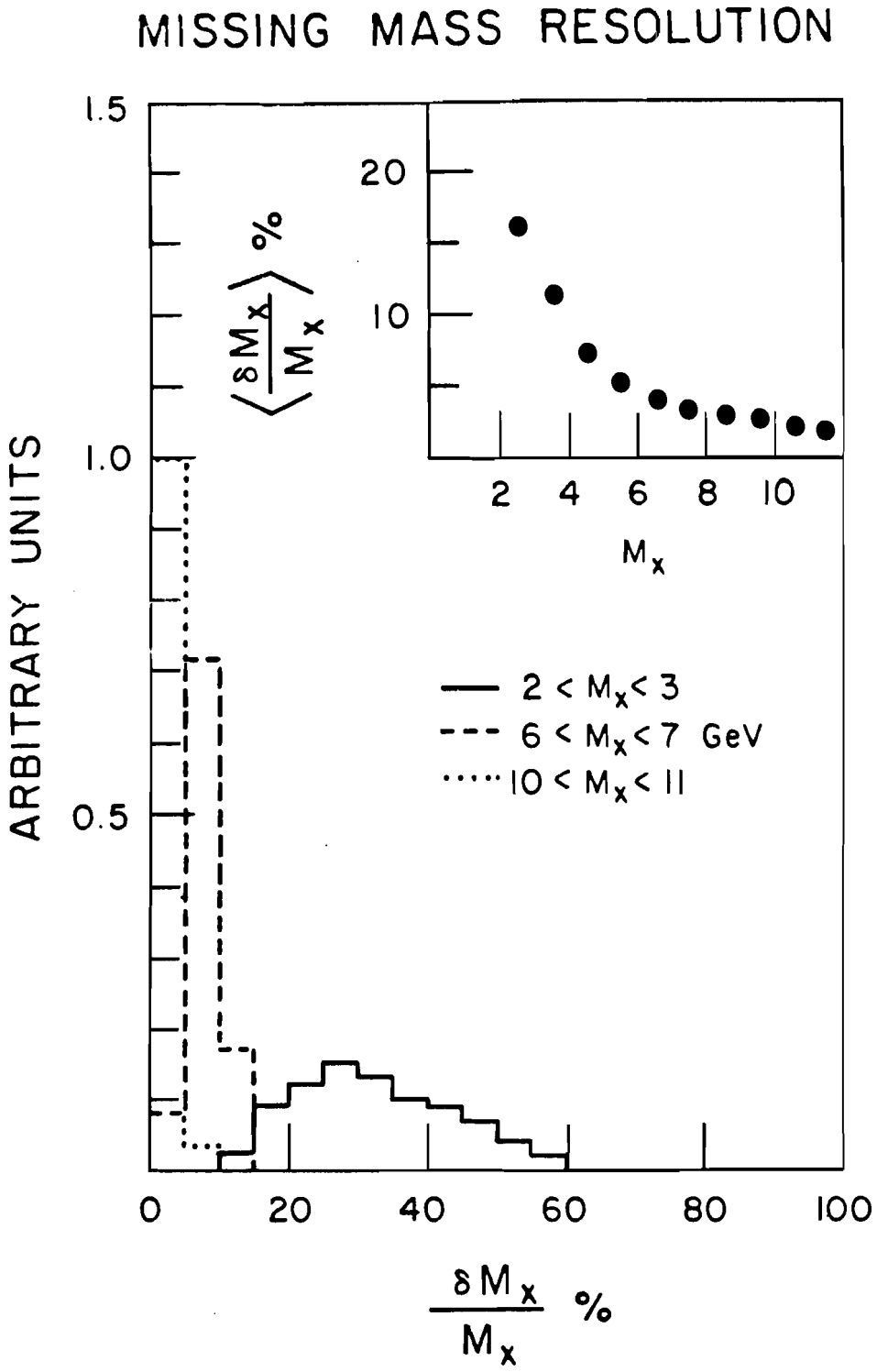
MISSING MASS RESOLUTION
ARBITRARY UNITS
1.5
1.0
0.5
0
20
40
60
80
100
$\frac{\delta M_x}{M_x}$ %
$\left\langle \frac{\delta M_x}{M_x} \right\rangle$ %
20
10
2
4
6
8
10
M_x
$2 < M_x < 3$
$6 < M_x < 7$ GeV
$10 < M_x < 11$

FIG. 48

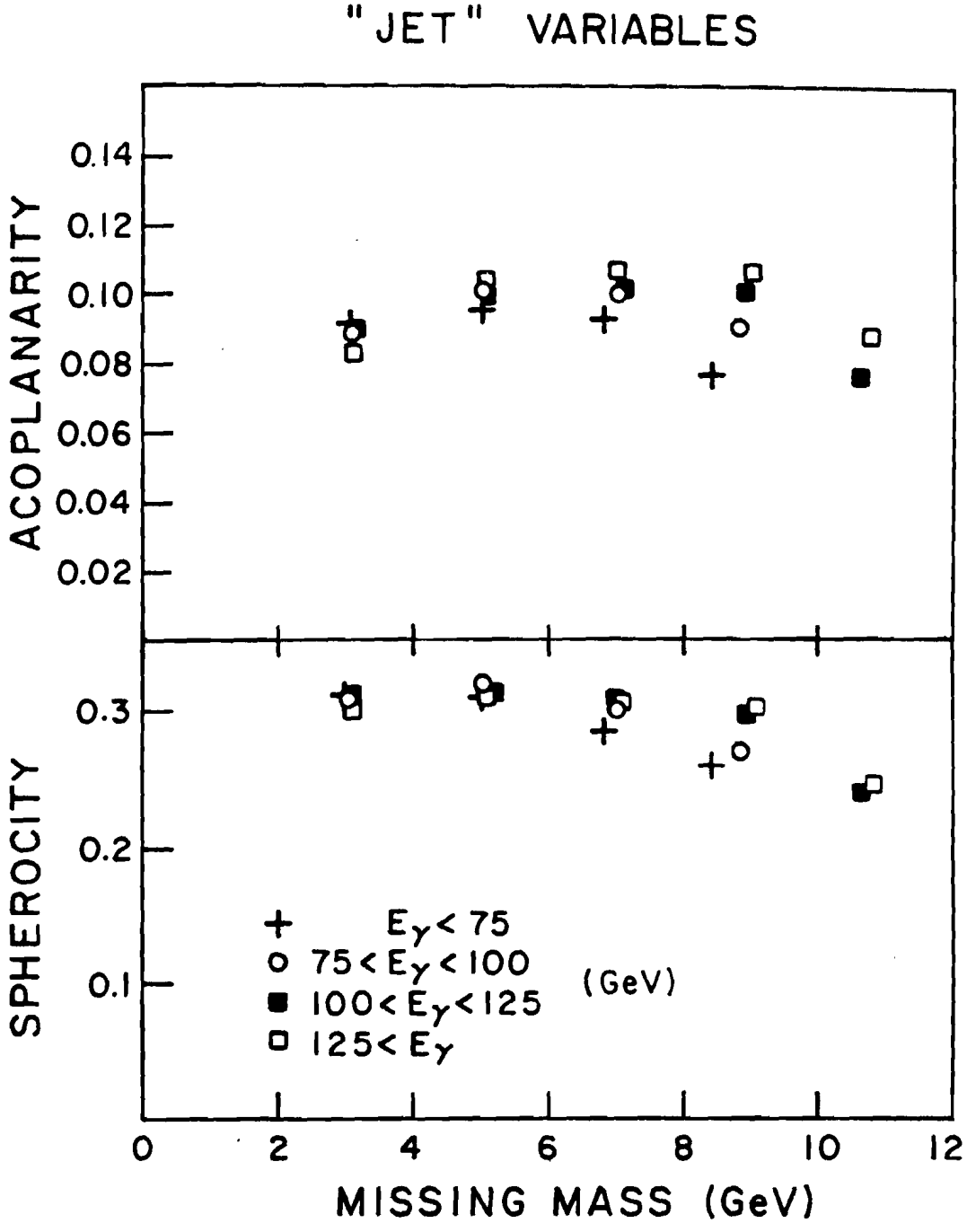

FIG. 49 Average spherocity and acoplanarity versus missing mass for different photon energy bins. The errors are statistical only.

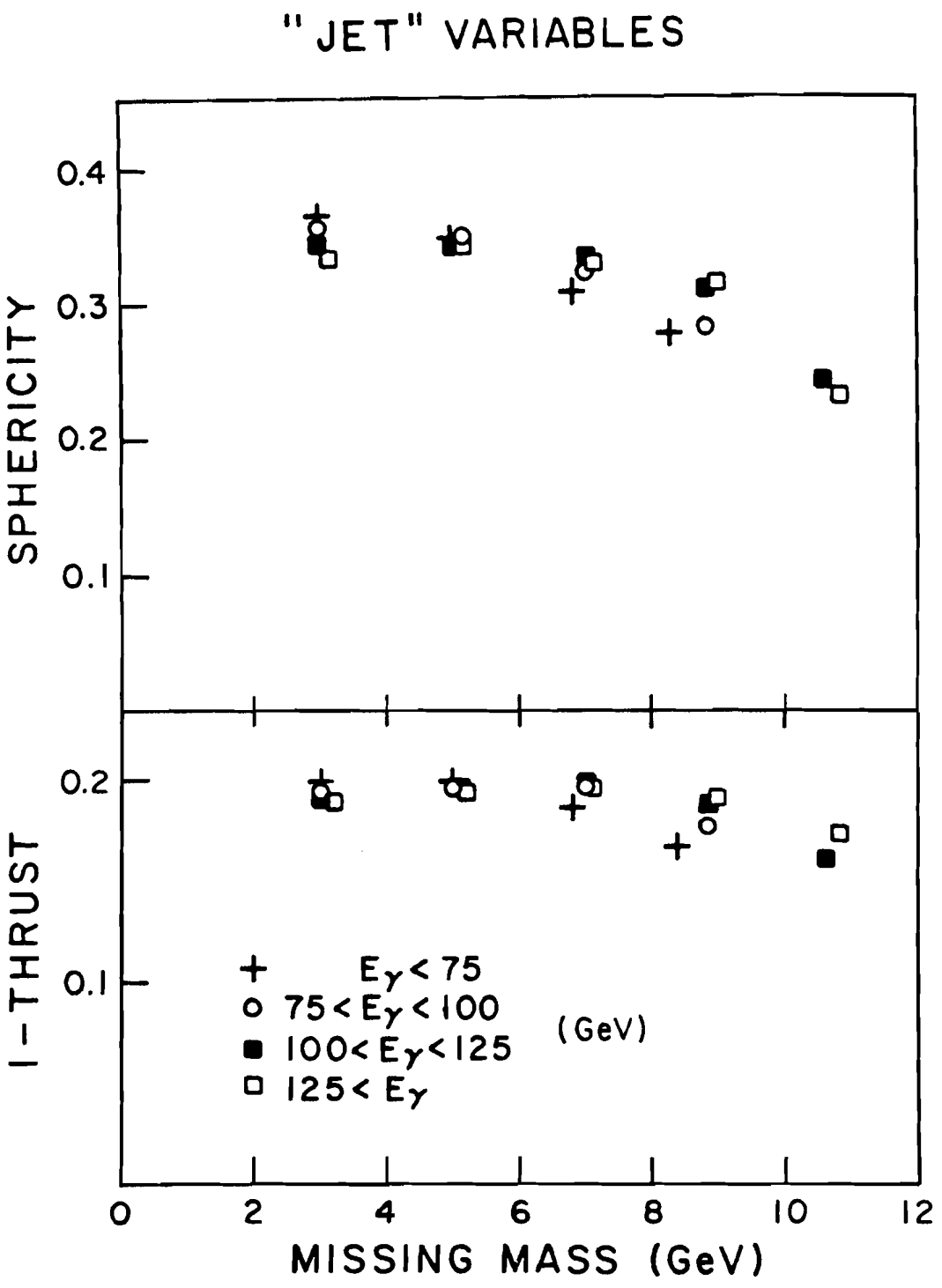

FIG. 50 Average thrust and sphericity versus missing mass for different photon energy bins. The errors are statistical only.

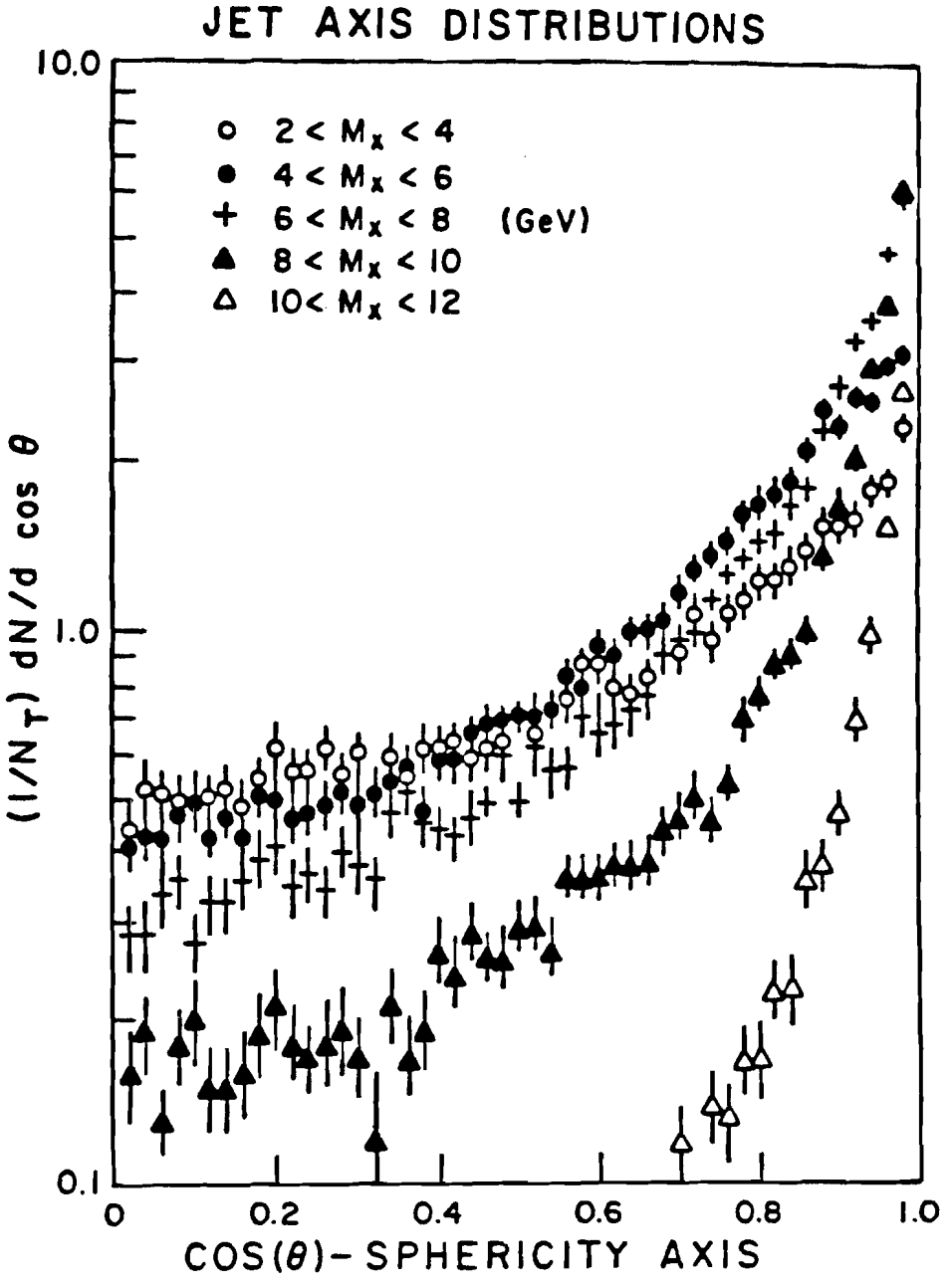

FIG. 51 Cos theta distributions for the sphericity axis relative to the initial photon direction for different missing mass bins.

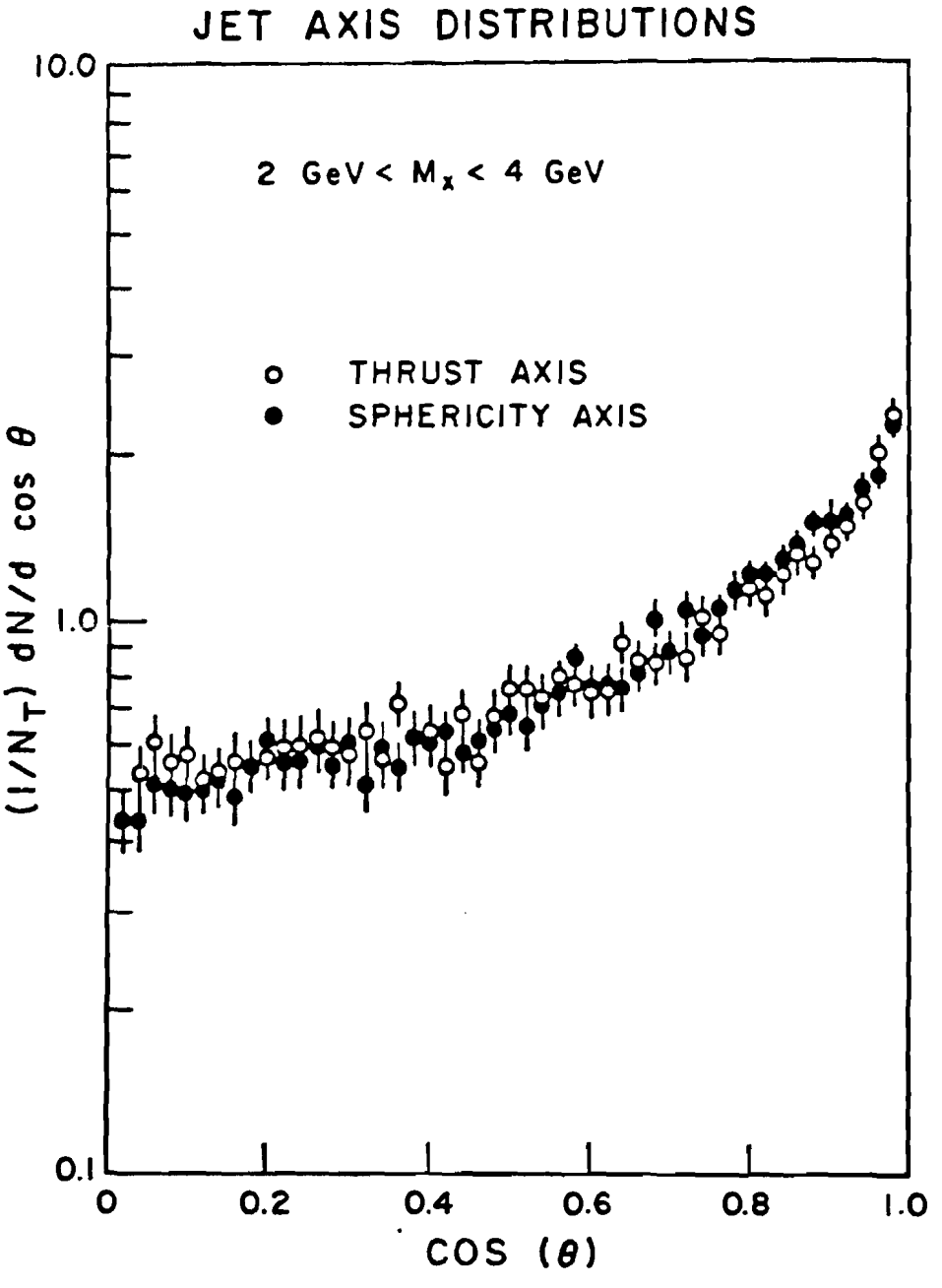

FIG. 52 Thrust and sphericity axis distributions relative to the initial photon direction.

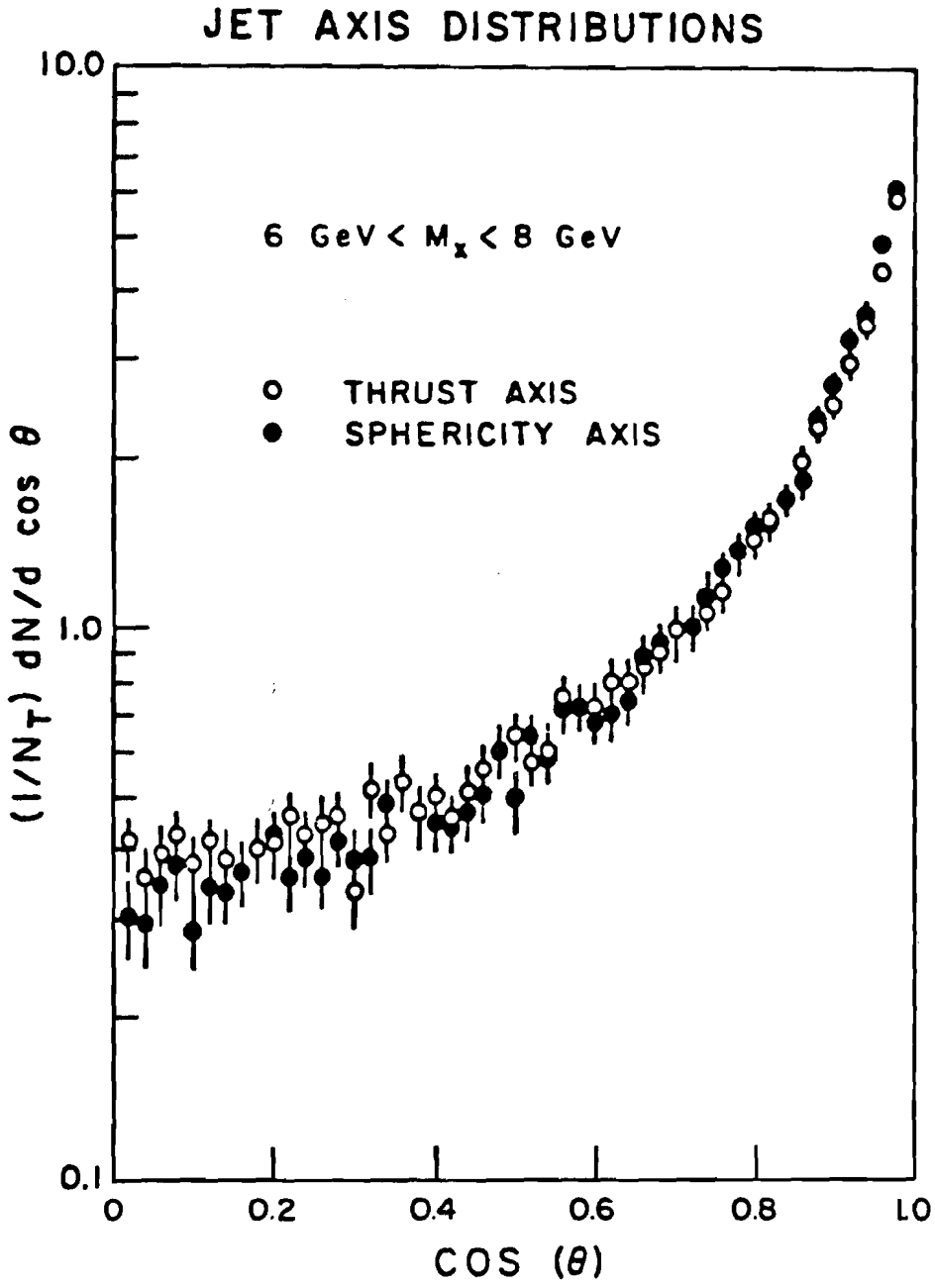

FIG. 53 Thrust and sphericity axis distributions relative to the initial photon direction.

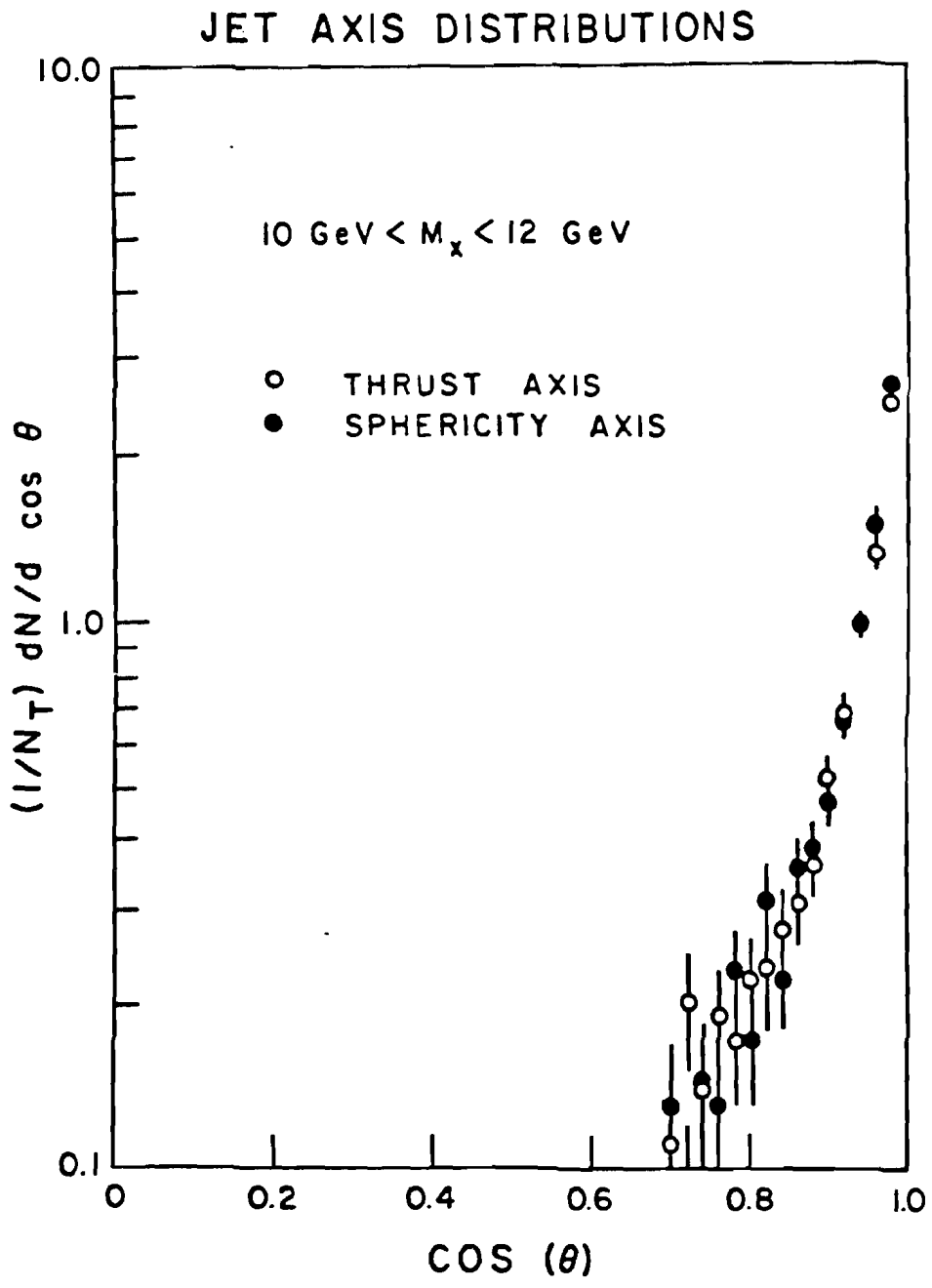

FIG. 54 Thrust and sphericity axis distributions relative to the initial photon direction.

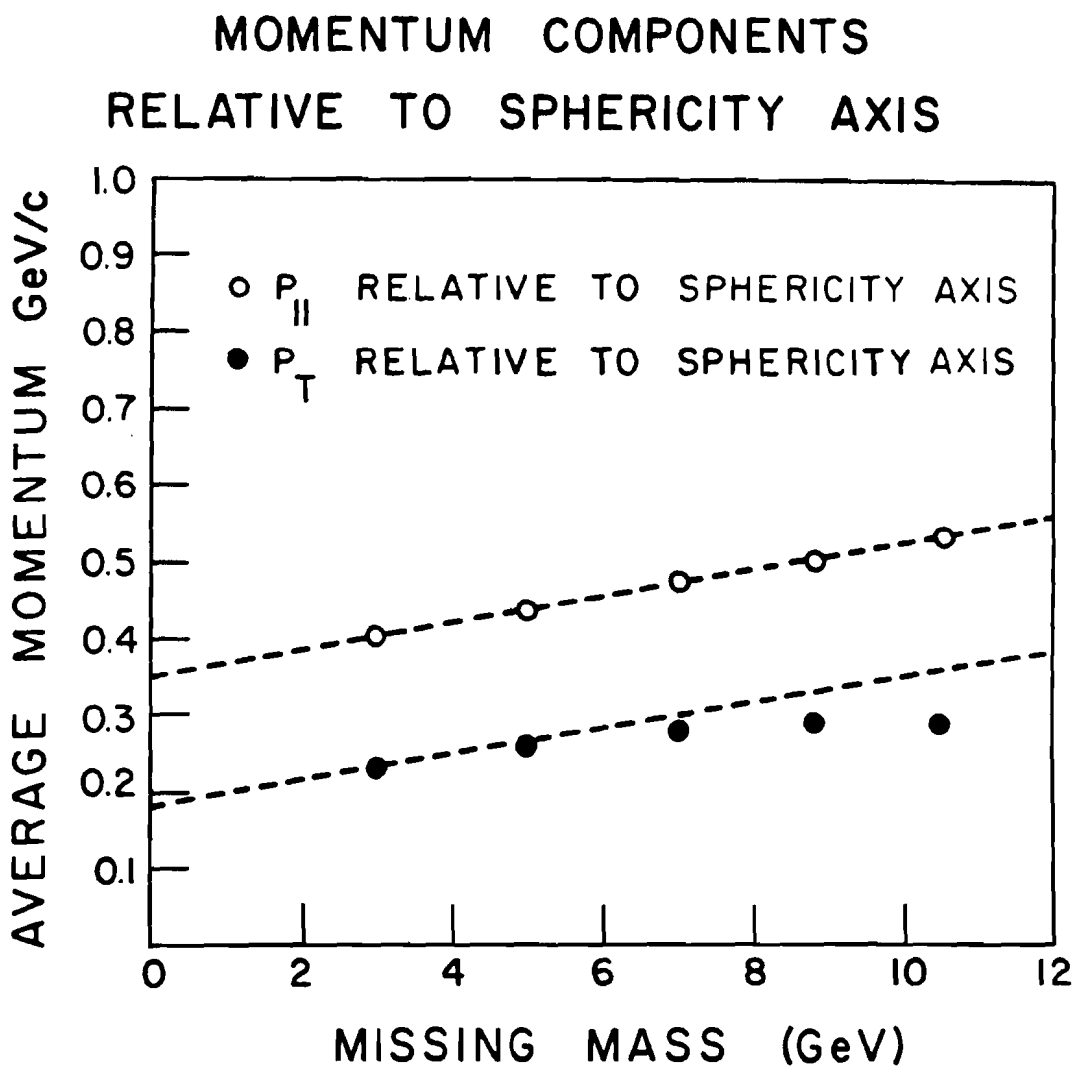

FIG. 55 Average transverse and longitudinal momentum components relative to the sphericity axis versus missing mass. The dashed line is not the result of any fit, merely a visual aid.

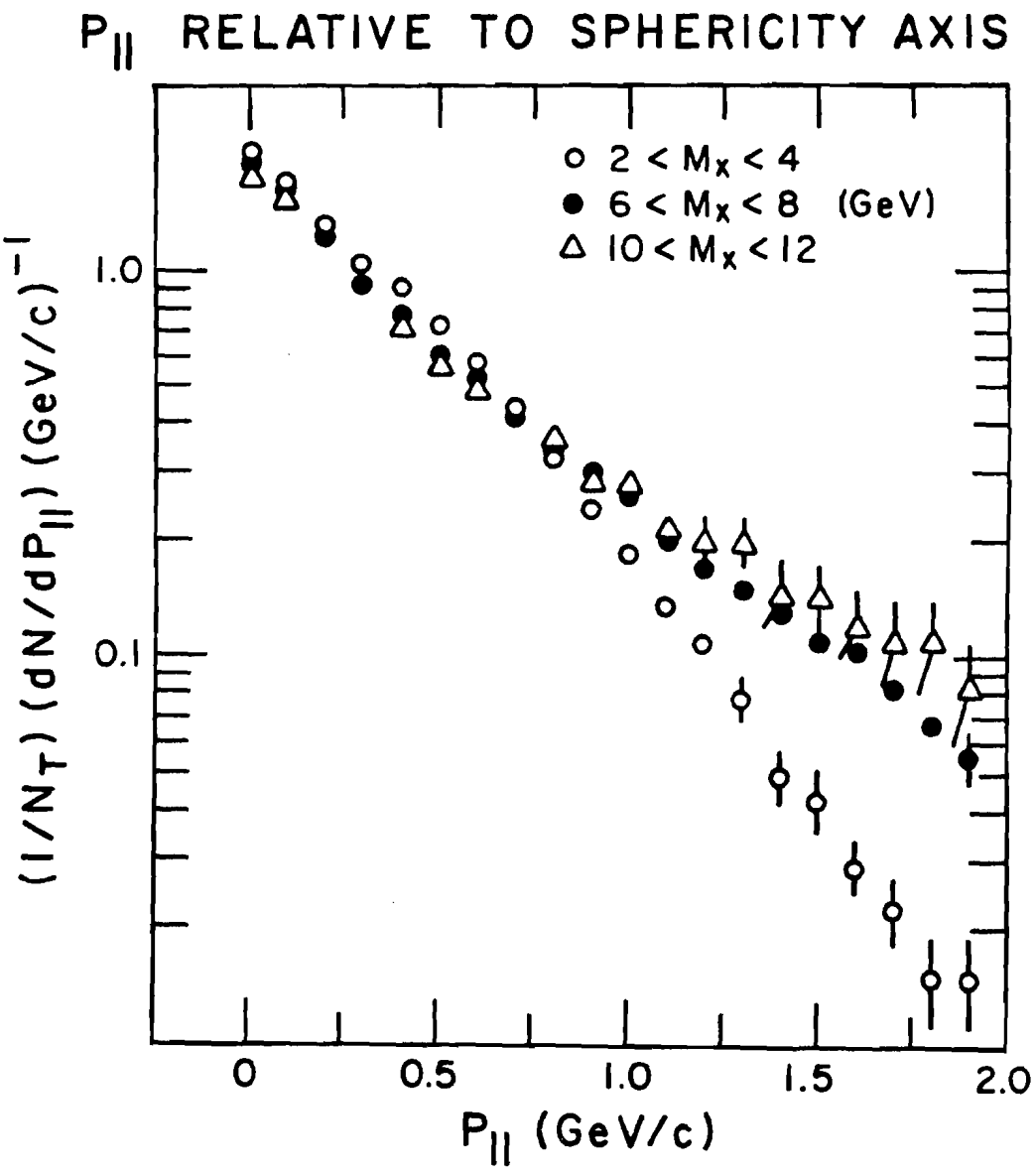

FIG. 56 Longitudinal momentum distributions relative to the sphericity axis.

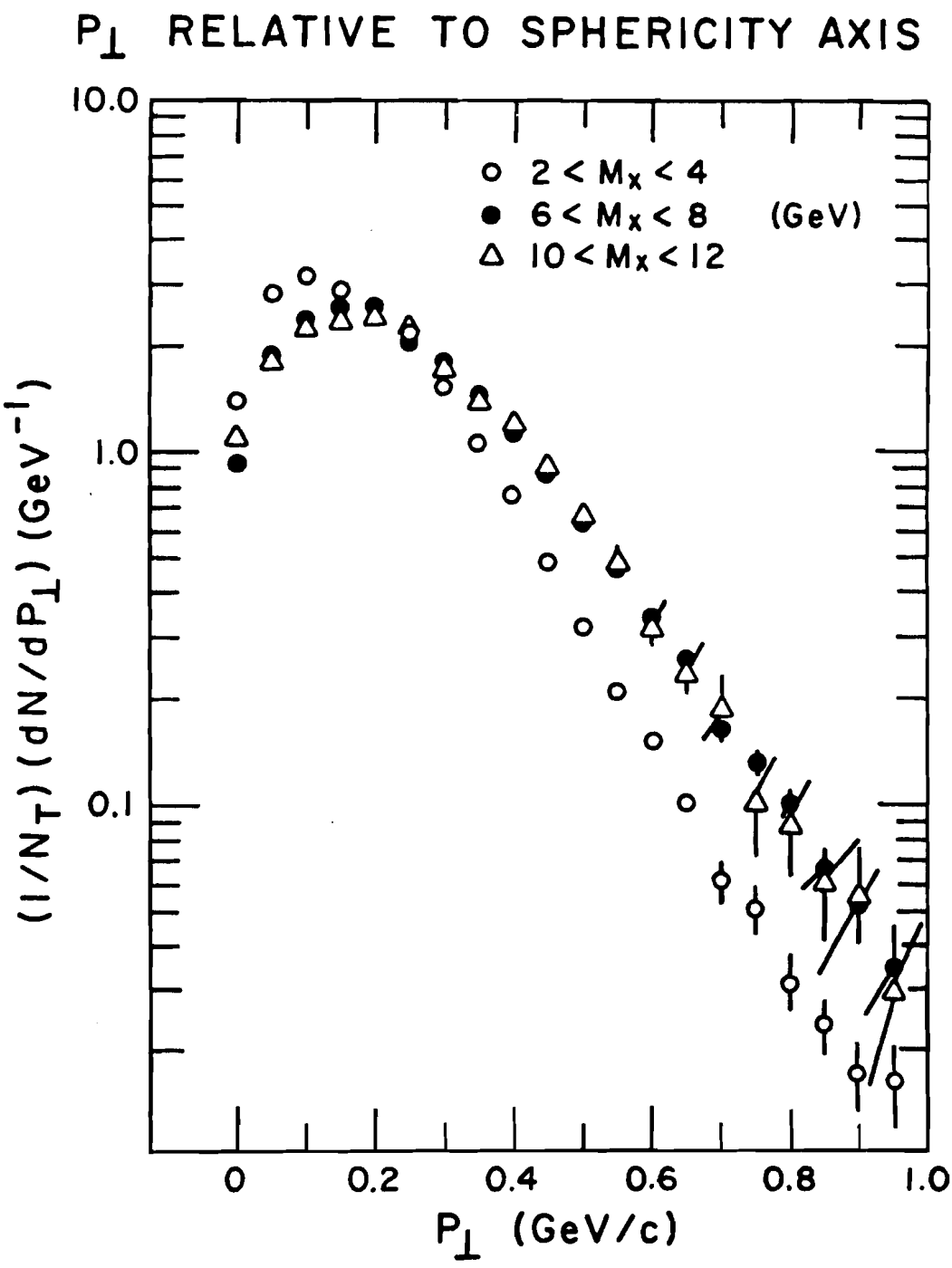

FIG. 57 Transverse momentum distributions relative to the sphericity axis.

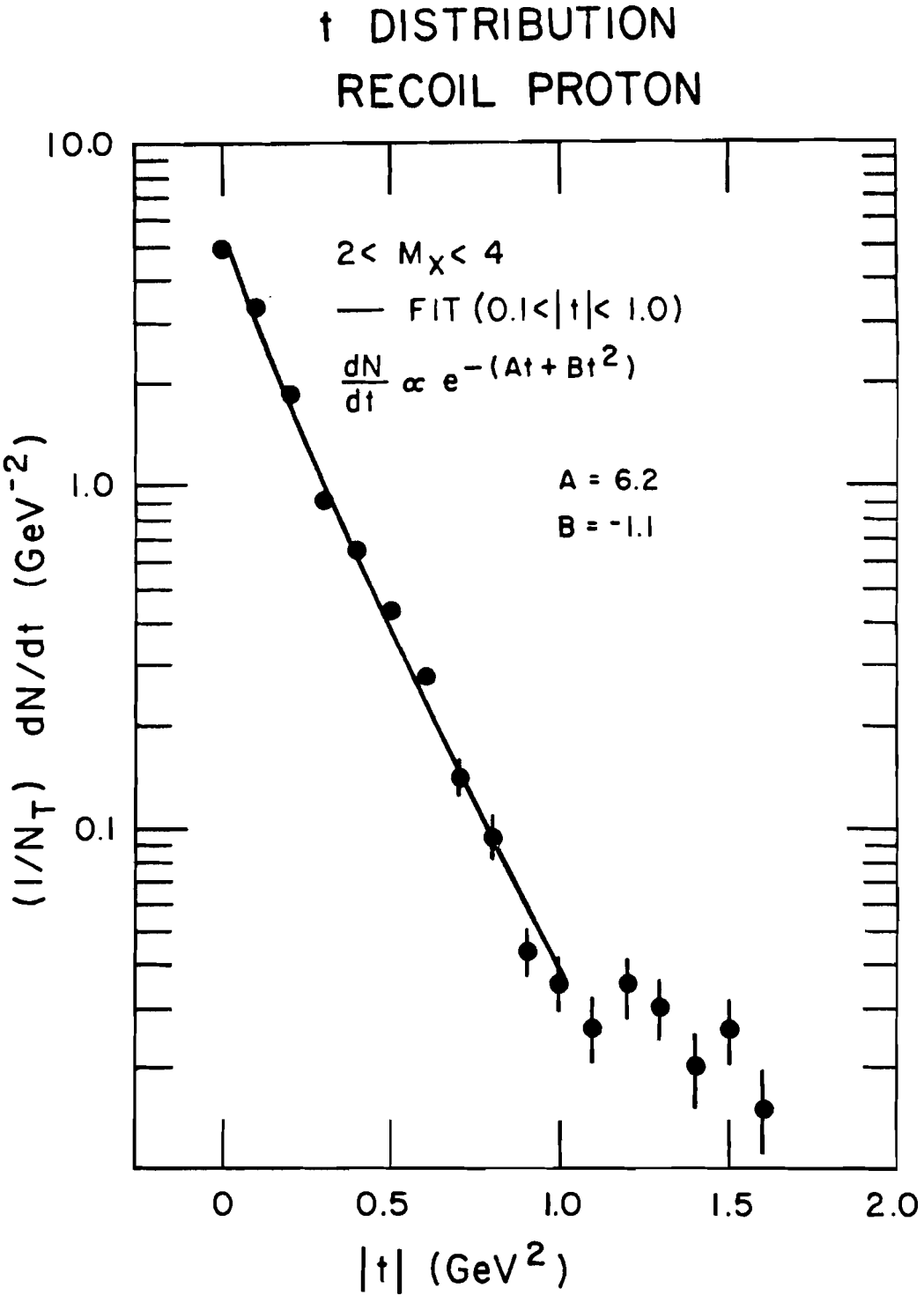
t DISTRIBUTION
RECOIL PROTON
10.0
1.0
0.1
2< M_X< 4
— FIT (0.1<|t|< 1.0)
dN/dt ∝ e^-(At + Bt^2)
A = 6.2
B = -1.1
(1/N_T) dN/dt (GeV^-2)
0
0.5
1.0
1.5
2.0
|t| (GeV^2)

FIG. 58

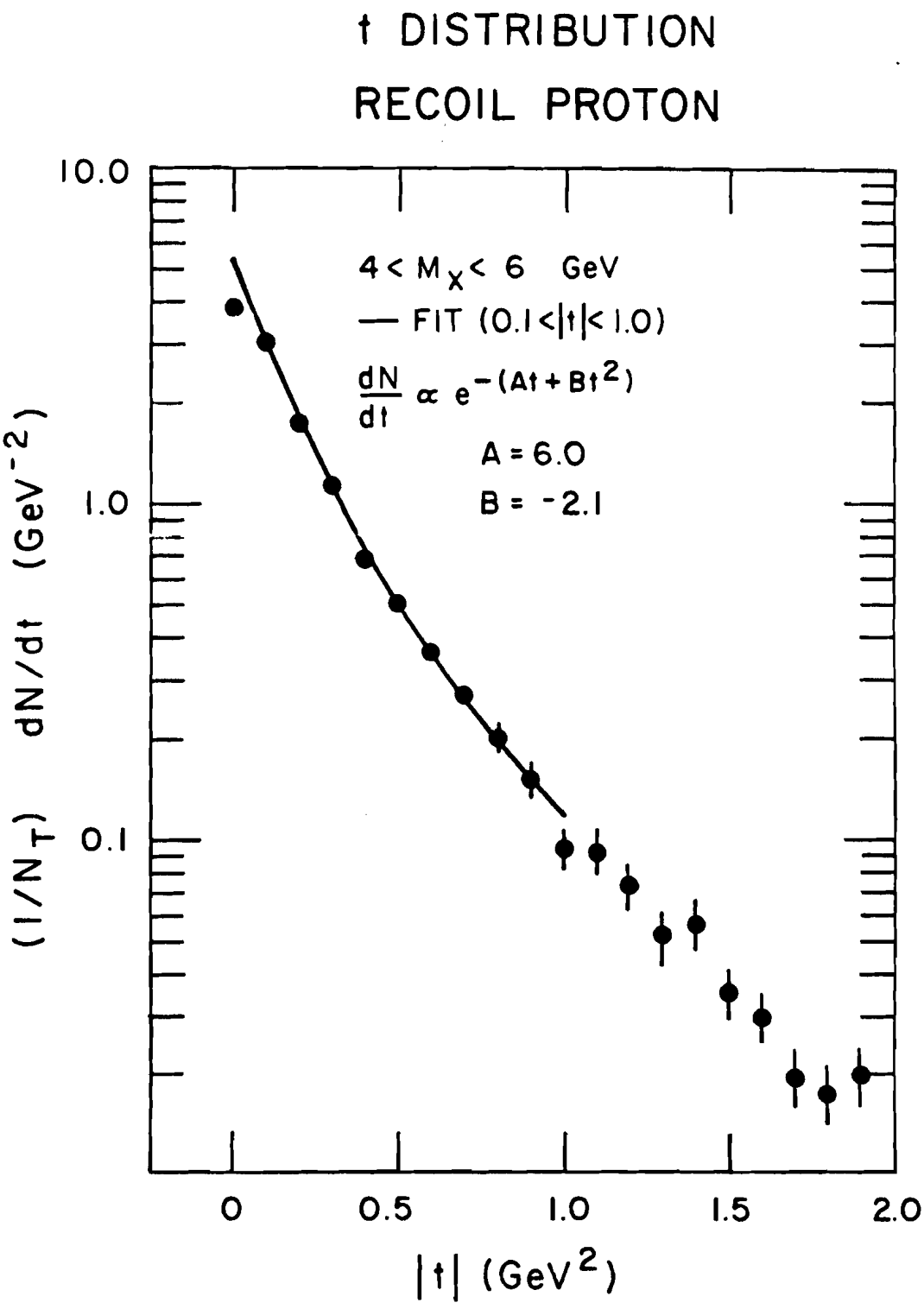
t DISTRIBUTION
RECOIL PROTON
10.0
1.0
0.1
(1/N_T) dN/dt (GeV^-2)
4 < M_X < 6 GeV
— FIT (0.1<|t|<1.0)
dN/dt ∝ e^-(At+Bt^2)
A = 6.0
B = -2.1
0
0.5
1.0
1.5
2.0
|t| (GeV^2)

FIG. 59

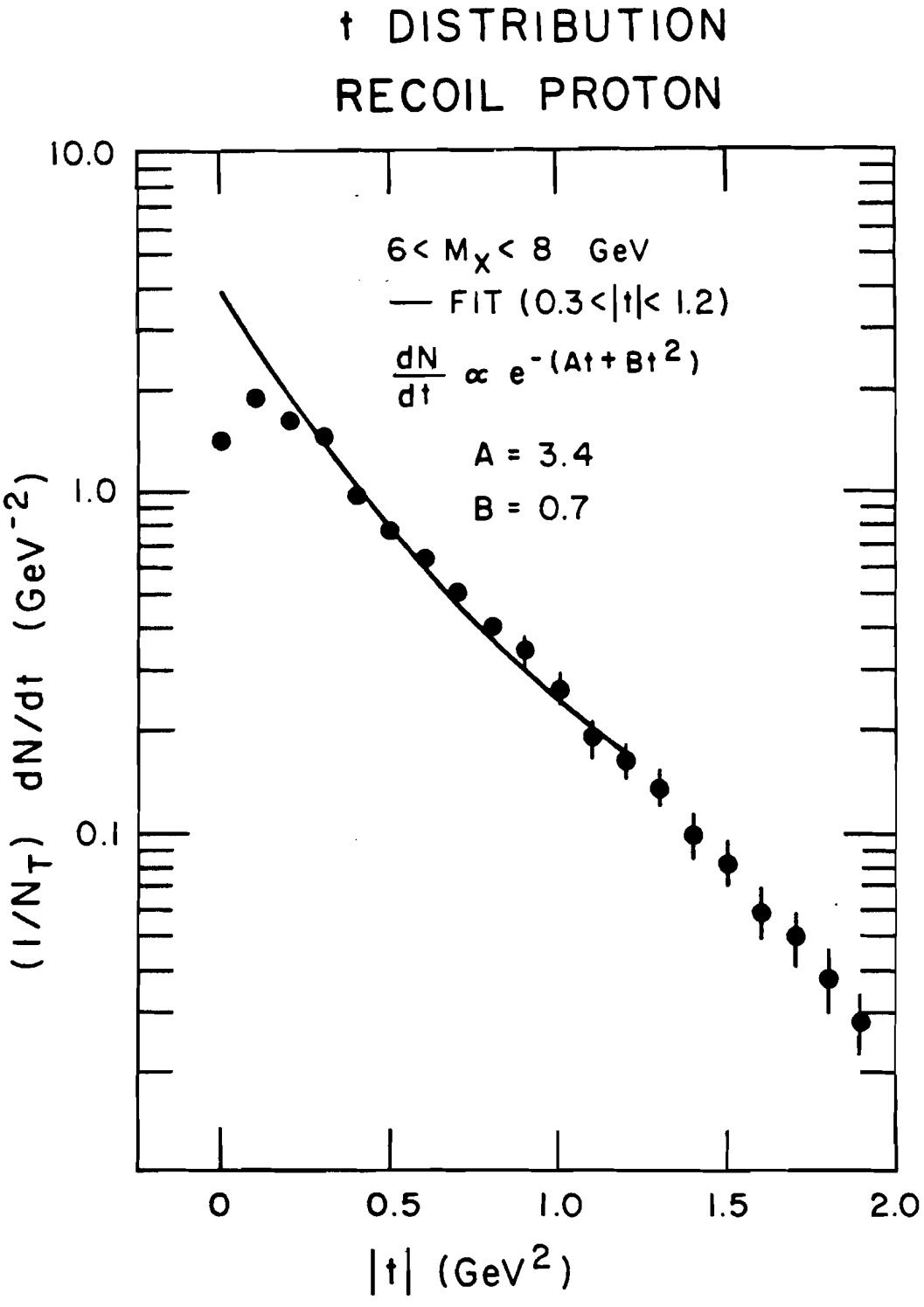
t DISTRIBUTION
RECOIL PROTON
10.0
1.0
0.1
$(1/N_T)$ dN/dt (GeV^{-2})
$6 < M_X < 8$ GeV
— FIT $(0.3 < |t| < 1.2)$
$\frac{dN}{dt} \propto e^{-(At+Bt^2)}$
A = 3.4
B = 0.7
0
0.5
1.0
1.5
2.0
$|t|$ (GeV^2)

FIG. 60

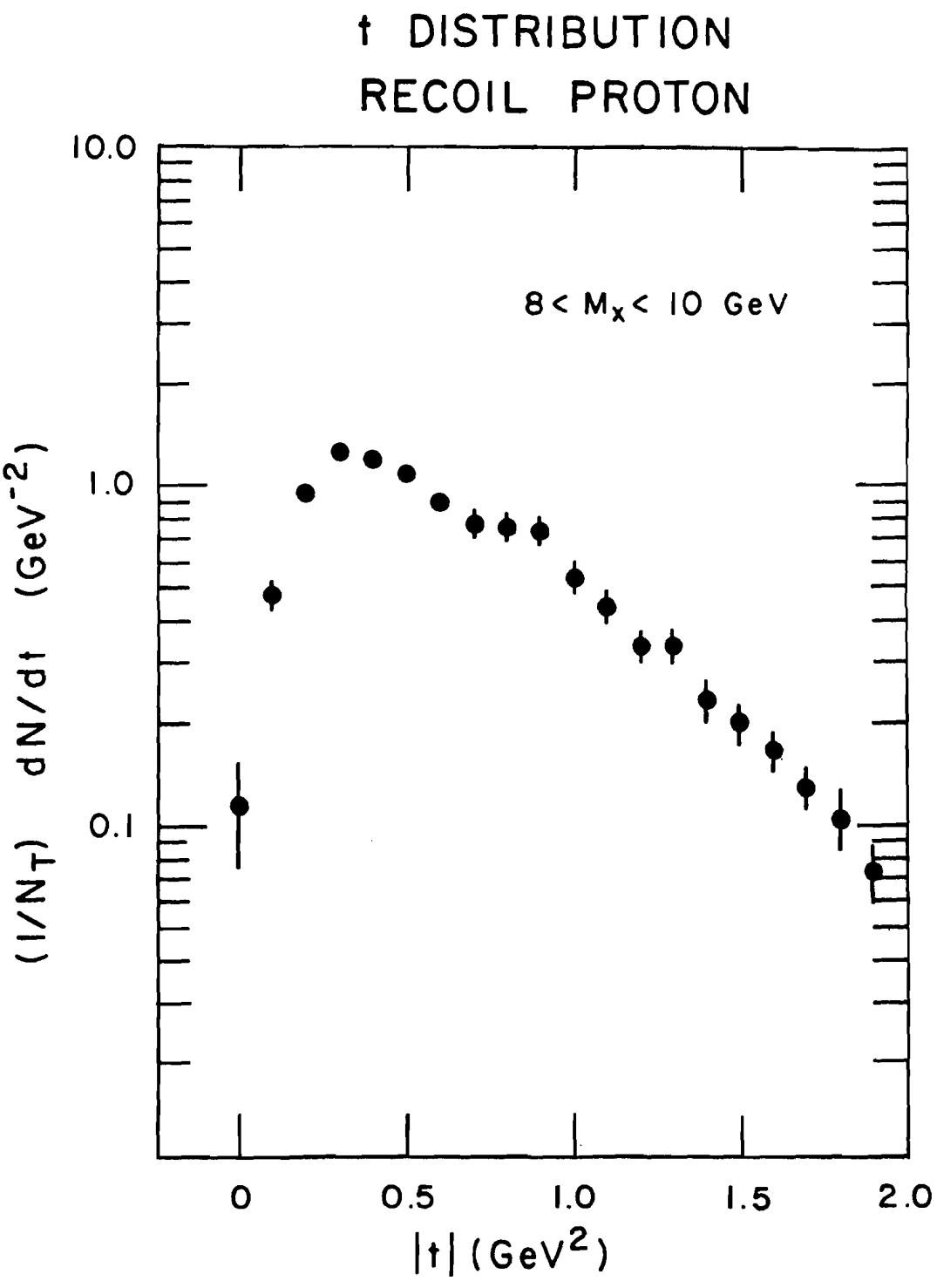
t DISTRIBUTION
RECOIL PROTON
8 < M_X < 10 GeV
10.0
1.0
0.1
(1/N_T) dN/dt (GeV^-2)
0
0.5
1.0
1.5
2.0
|t| (GeV^2)

FIG. 61

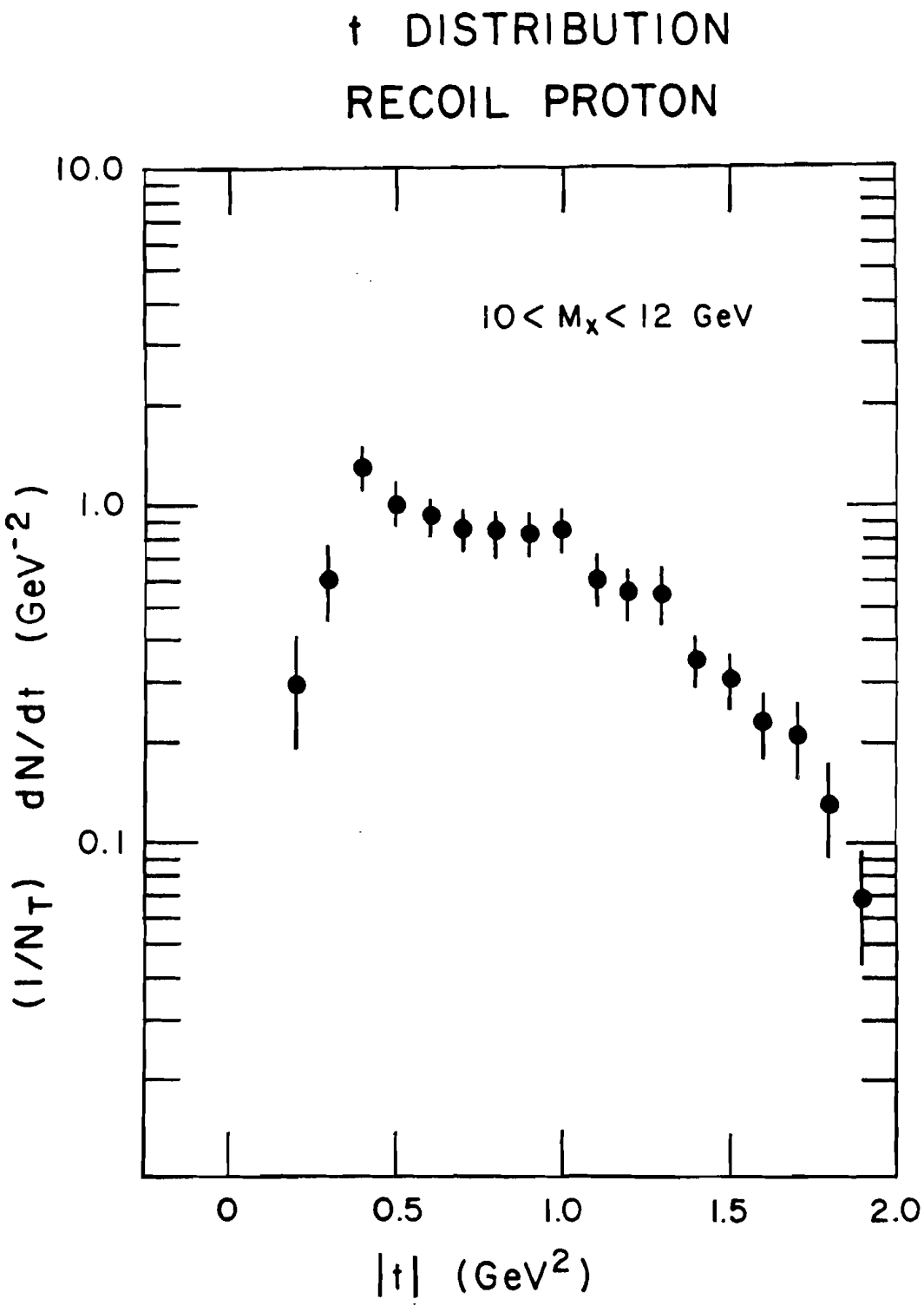
t DISTRIBUTION
RECOIL PROTON
10.0
1.0
0.1
10 < M_X < 12 GeV
(1/N_T) dN/dt (GeV^-2)
0
0.5
1.0
1.5
2.0
|t| (GeV^2)

FIG. 62

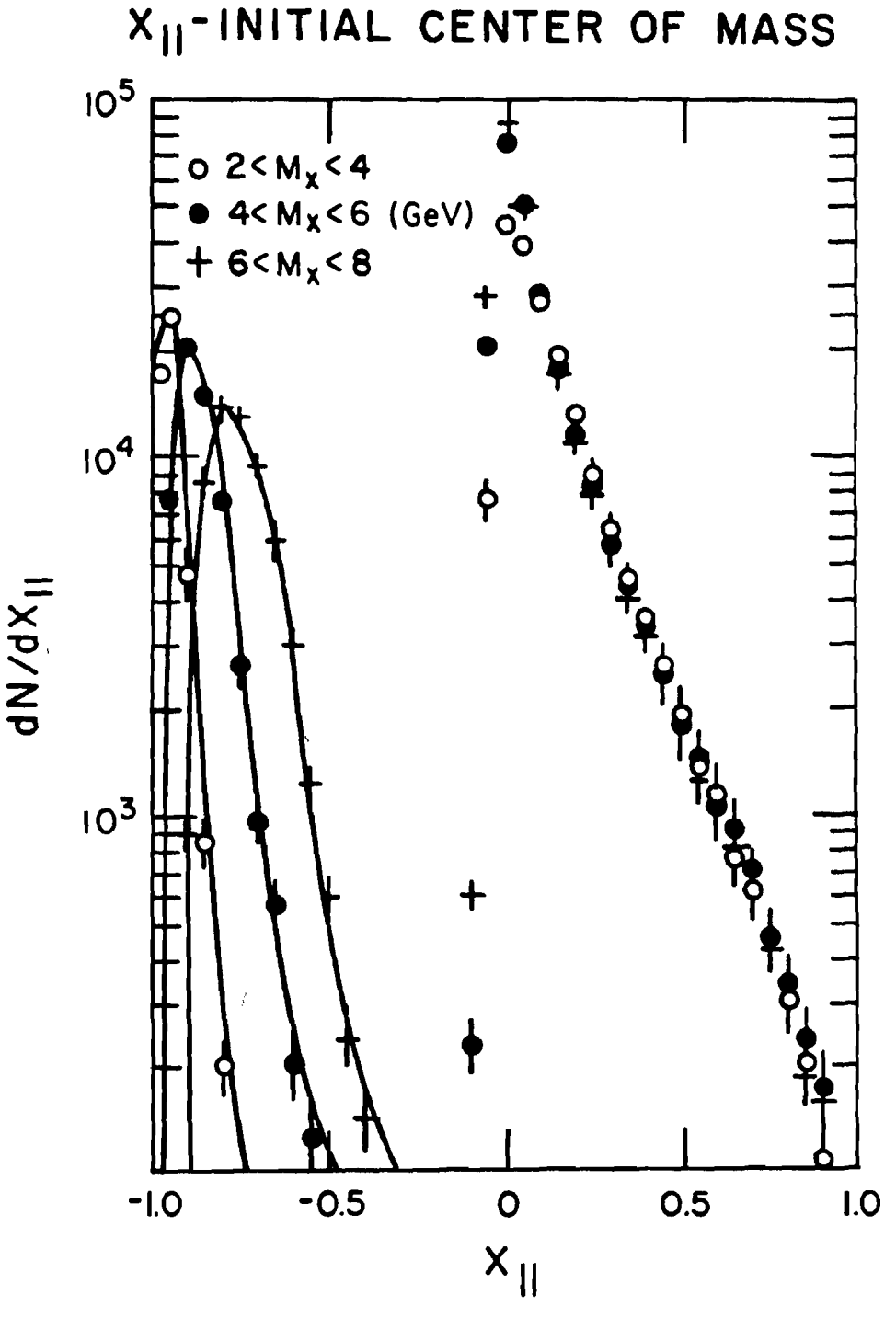

FIG. 63 Feynman x distributions including the recoil proton. The solid lines are visual aids not fits.

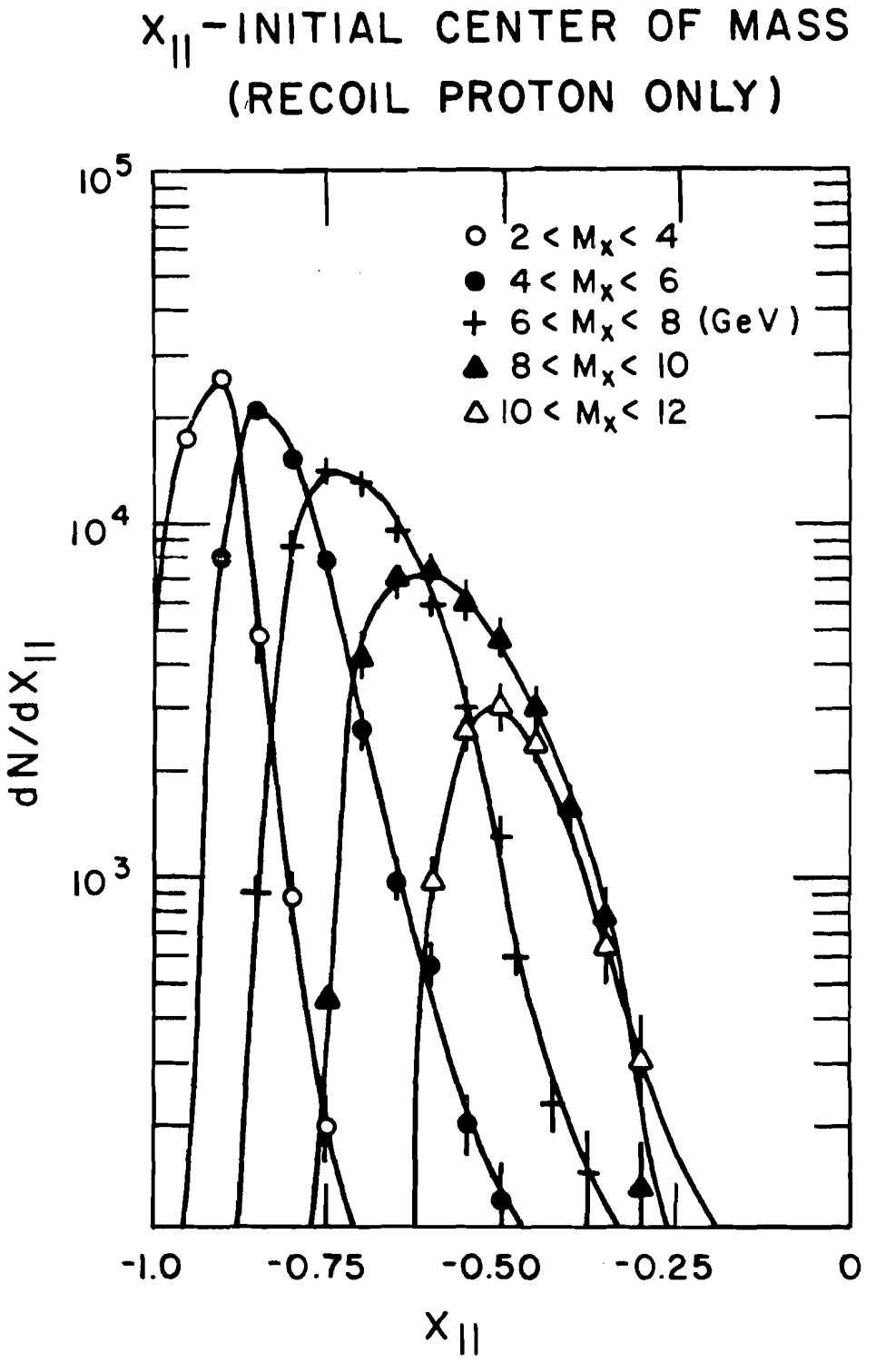

FIG. 64 Feynman x distributions for recoil protons only. The solid lines are visual aids not fits.

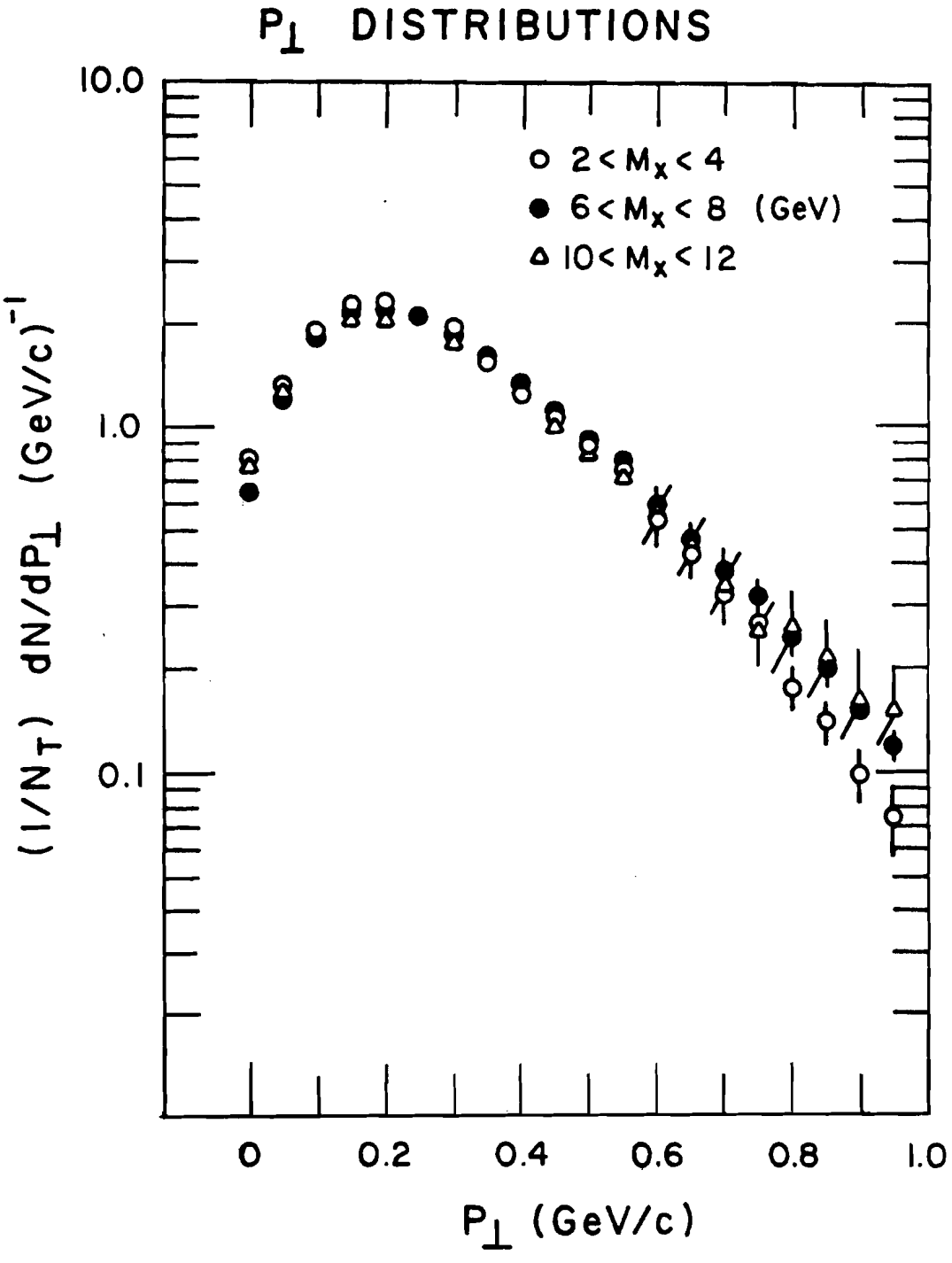

FIG. 65 Normalized single particle transverse momentum distributions (N_T is the total number of tracks).

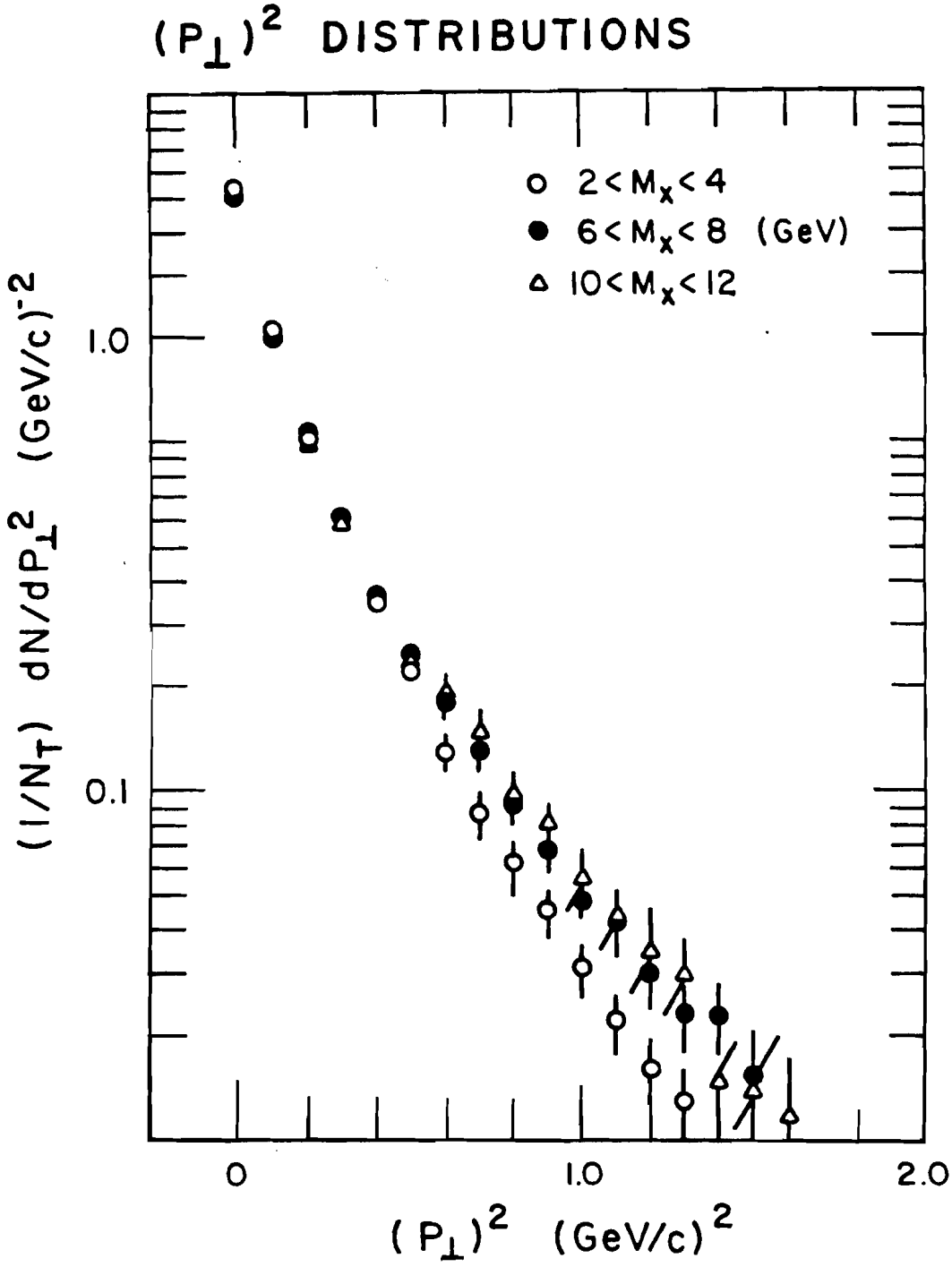
$(P_\perp)^2$ DISTRIBUTIONS
$2<M_x<4$
$6<M_x<8$ (GeV)
$10<M_x<12$
$(1/N_T)\ dN/dP_\perp^2\ (GeV/c)^{-2}$
1.0
0.1
0
1.0
2.0
$(P_\perp)^2\ (GeV/c)^2$

FIG. 66

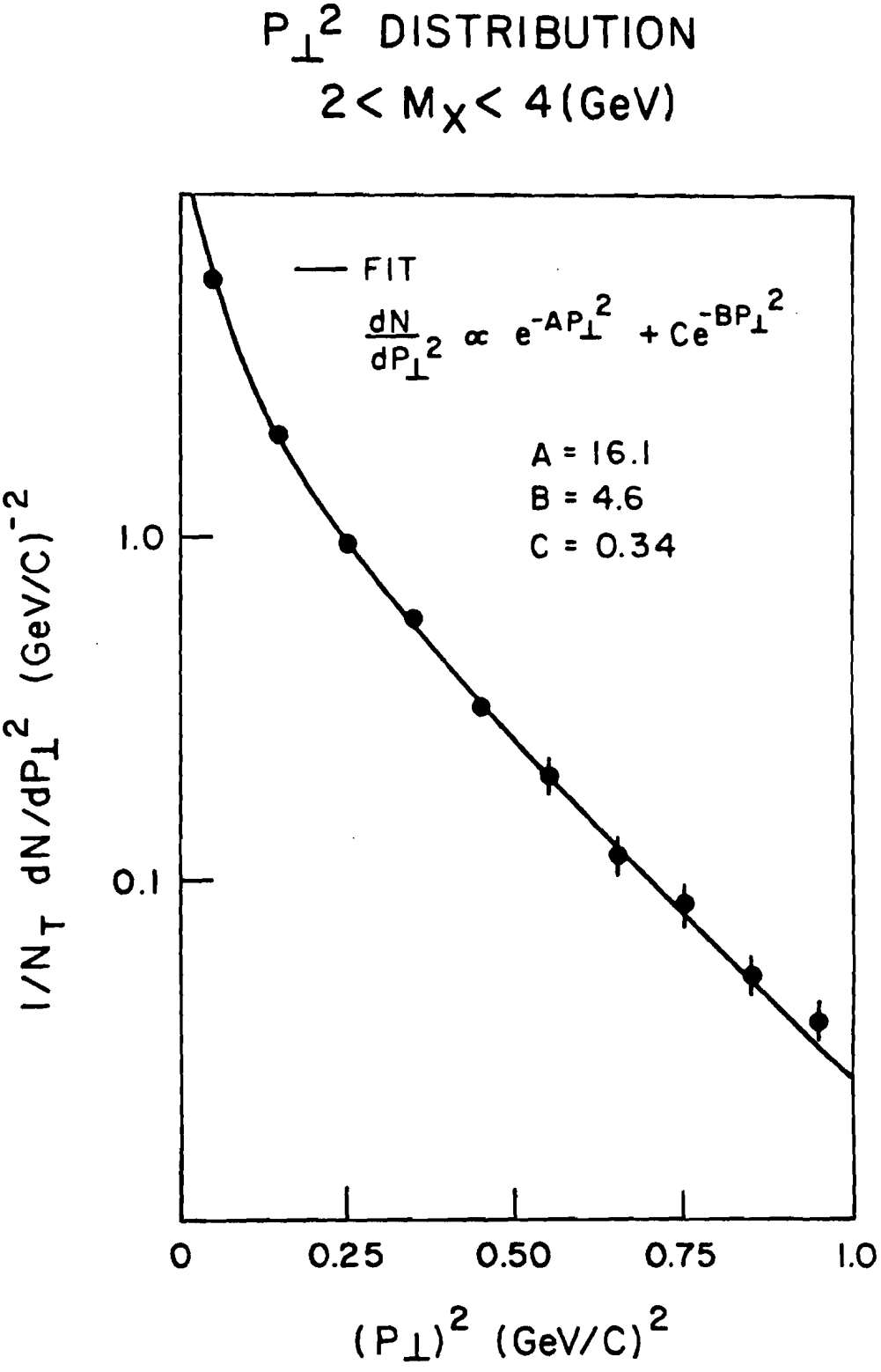
$P_\perp^2$ DISTRIBUTION
$2 < M_X < 4$ (GeV)
— FIT
$\frac{dN}{dP_\perp^2} \propto e^{-AP_\perp^2} + Ce^{-BP_\perp^2}$
A = 16.1
B = 4.6
C = 0.34
$1/N_T\ dN/dP_\perp^2\ (GeV/C)^{-2}$
1.0
0.1
0
0.25
0.50
0.75
1.0
$(P_\perp)^2\ (GeV/C)^2$

FIG. 67

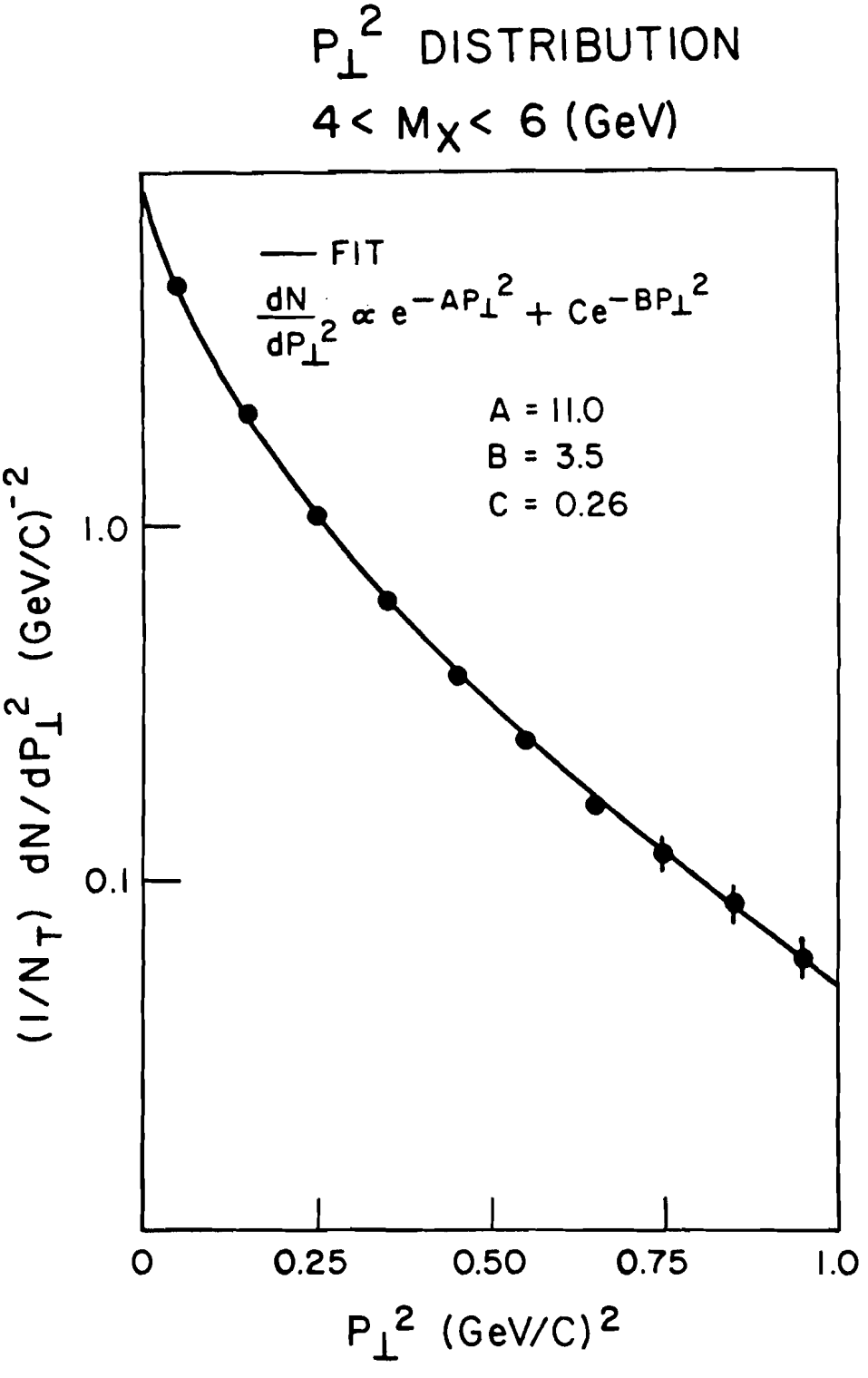
$P_\perp^2$ DISTRIBUTION
$4 < M_X < 6$ (GeV)
— FIT
$\frac{dN}{dP_\perp^2} \propto e^{-AP_\perp^2} + Ce^{-BP_\perp^2}$
A = 11.0
B = 3.5
C = 0.26
$(1/N_T)\ dN/dP_\perp^2\ (GeV/C)^{-2}$
1.0
0.1
0
0.25
0.50
0.75
1.0
$P_\perp^2\ (GeV/C)^2$

FIG. 68

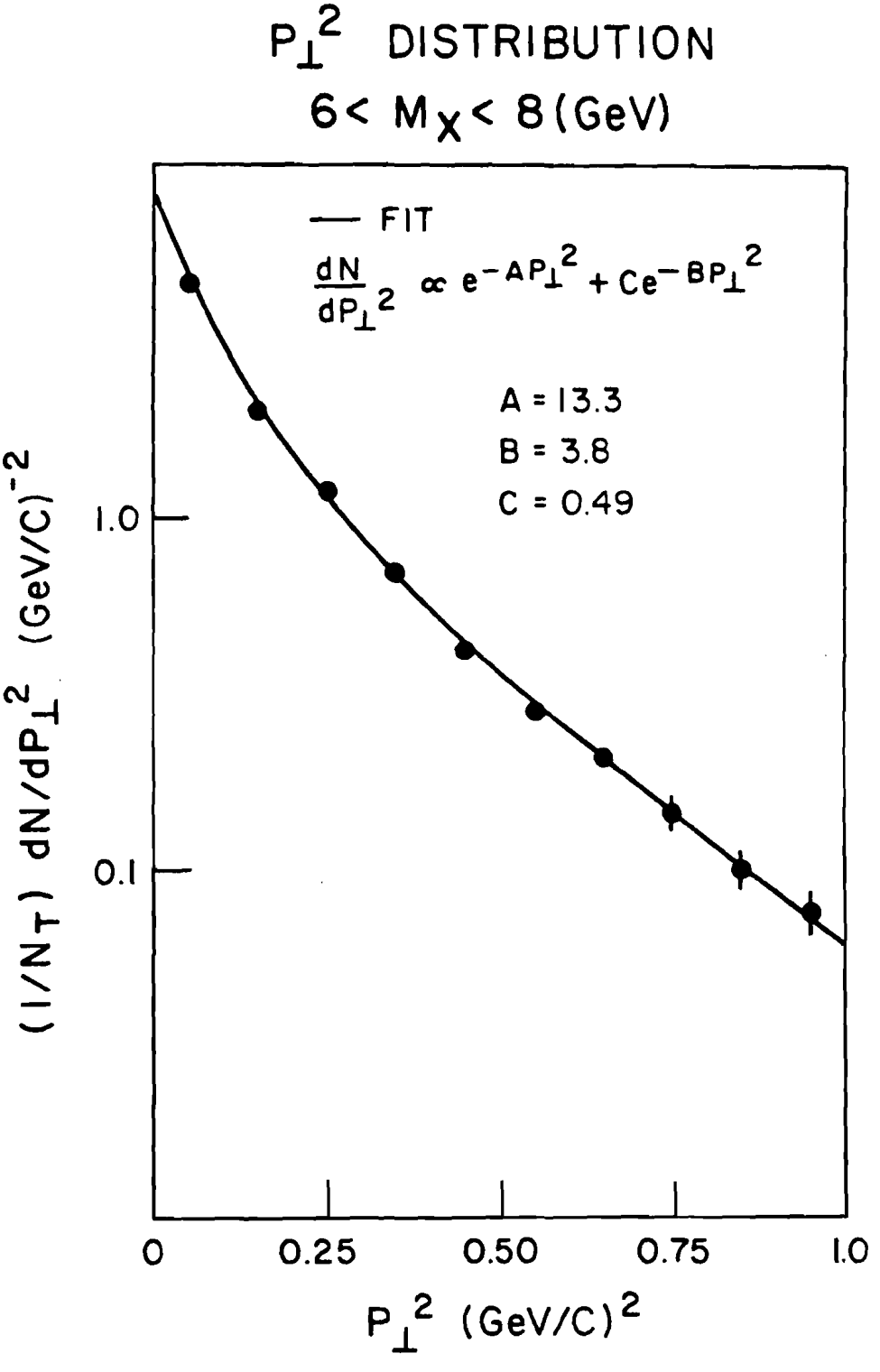
$P_\perp^2$ DISTRIBUTION
$6 < M_X < 8$ (GeV)
— FIT
$\frac{dN}{dP_\perp^2} \propto e^{-AP_\perp^2} + Ce^{-BP_\perp^2}$
A = 13.3
B = 3.8
C = 0.49
1.0
0.1
$(1/N_T)\ dN/dP_\perp^2$ $(GeV/C)^{-2}$
0
0.25
0.50
0.75
1.0
$P_\perp^2$ $(GeV/C)^2$

FIG. 69

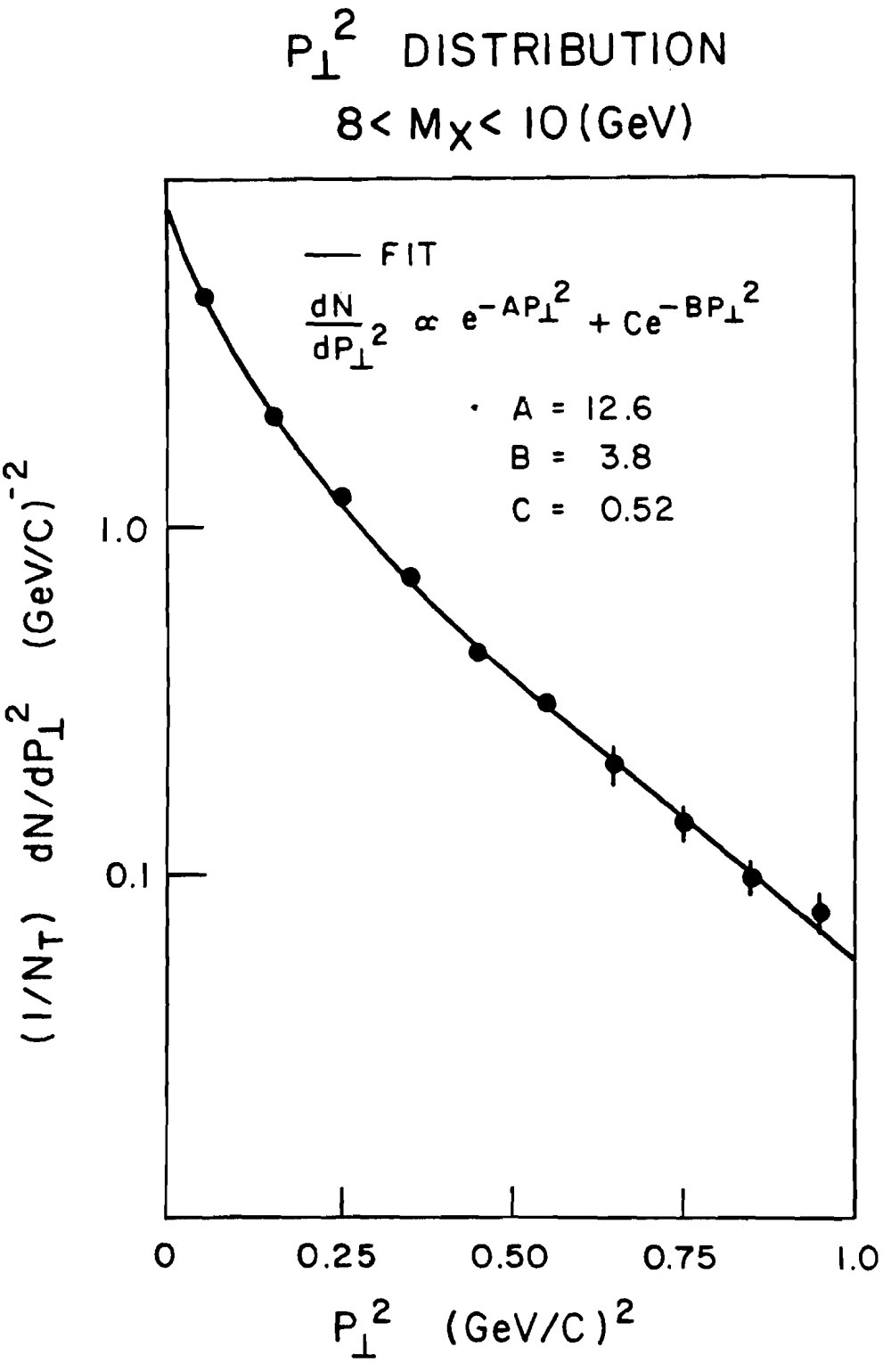
$P_\perp^2$ DISTRIBUTION
$8 < M_X < 10$ (GeV)
— FIT
$\frac{dN}{dP_\perp^2} \propto e^{-AP_\perp^2} + Ce^{-BP_\perp^2}$
A = 12.6
B = 3.8
C = 0.52
$(1/N_T)\ dN/dP_\perp^2$ $(GeV/C)^{-2}$
1.0
0.1
0
0.25
0.50
0.75
1.0
$P_\perp^2$ $(GeV/C)^2$

FIG. 70

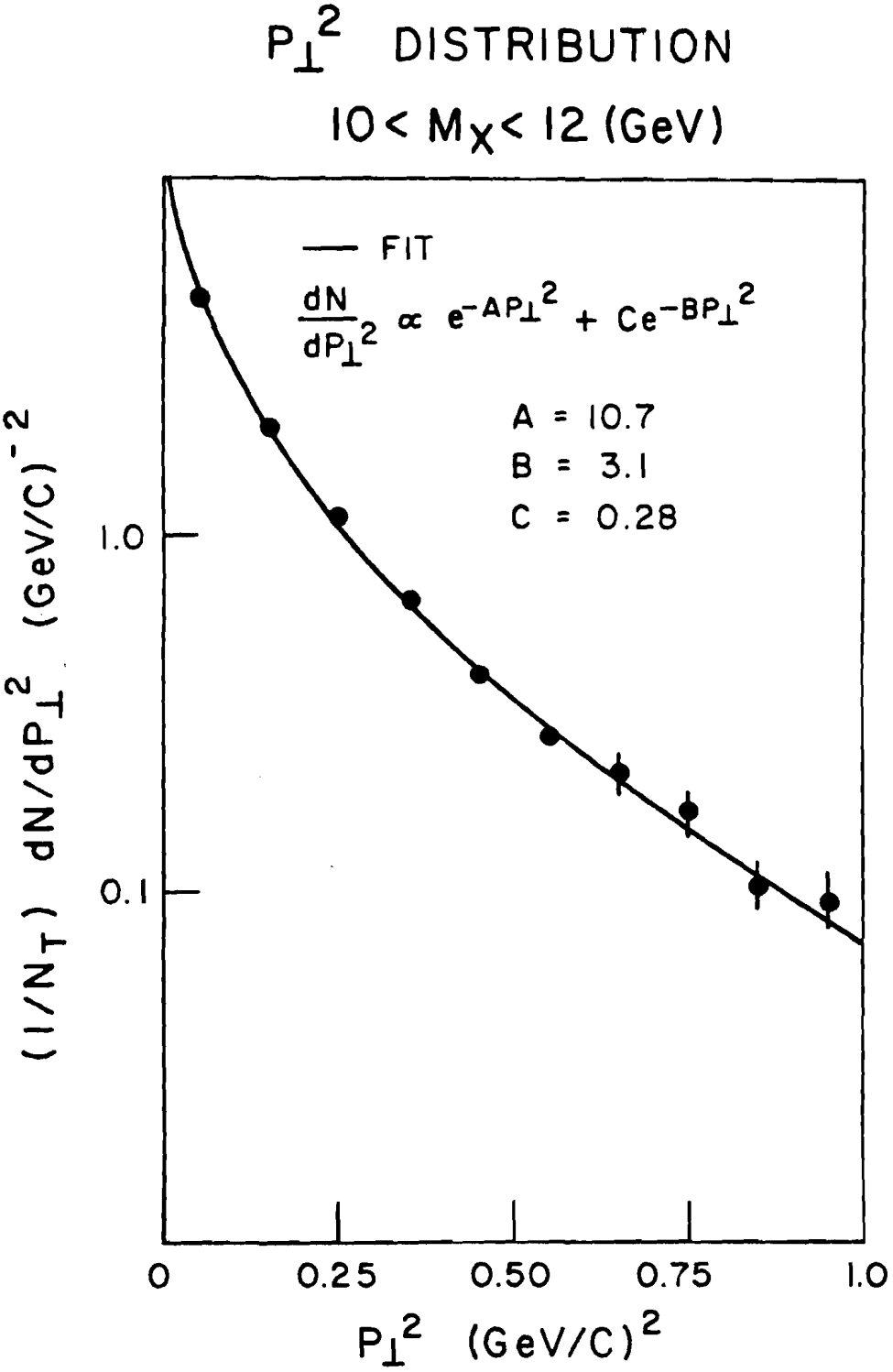
$P_\perp^2$ DISTRIBUTION
$10 < M_X < 12$ (GeV)
— FIT
$\frac{dN}{dP_\perp^2} \propto e^{-AP_\perp^2} + Ce^{-BP_\perp^2}$
A = 10.7
B = 3.1
C = 0.28
$(1/N_T)\ dN/dP_\perp^2\ (GeV/C)^{-2}$
1.0
0.1
0
0.25
0.50
0.75
1.0
$P_\perp^2\ (GeV/C)^2$

FIG. 71

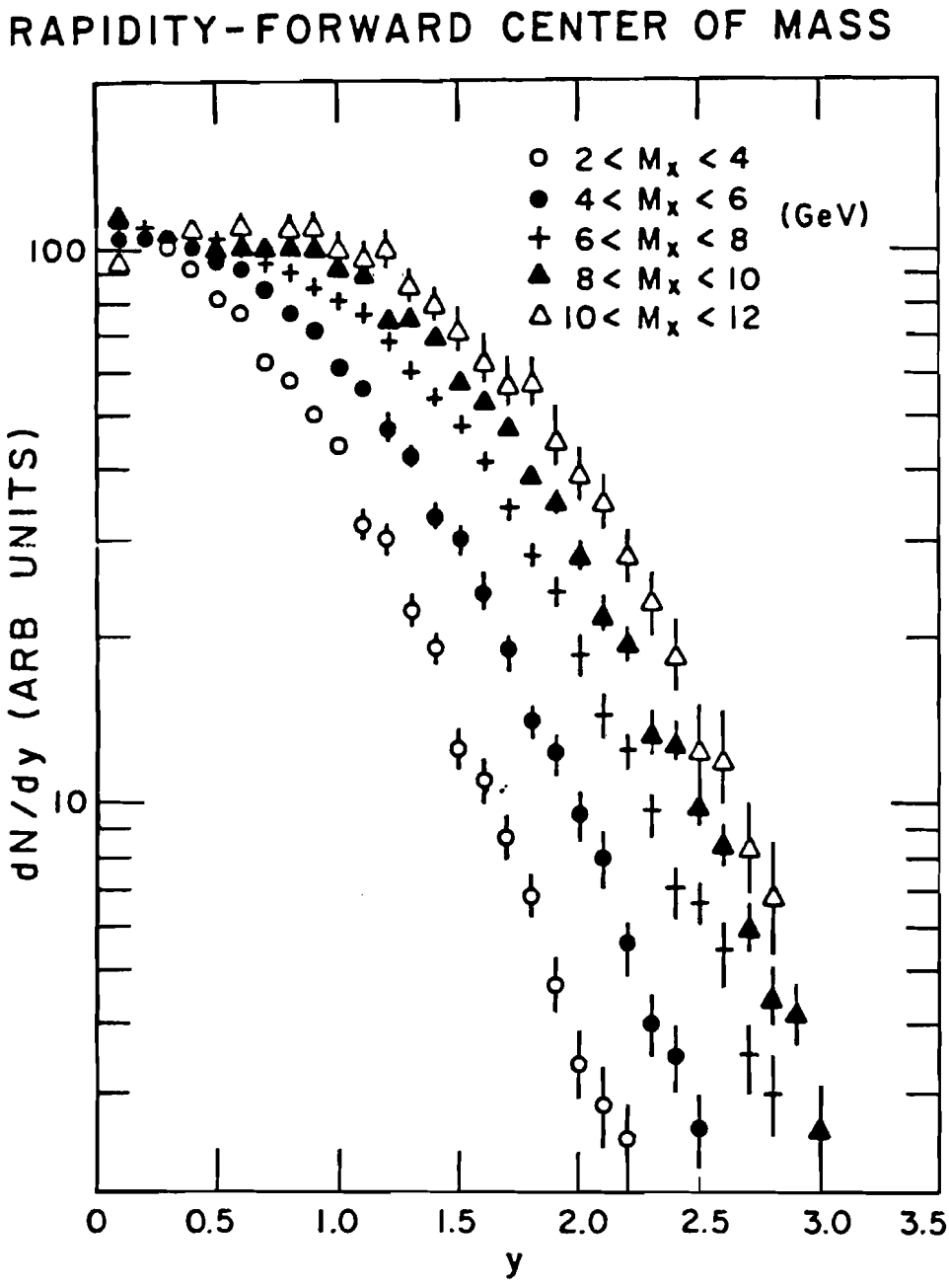

FIG. 72 Rapidity distributions for different missing mass bins normalized such that the plateau regions near y=0 coincide.

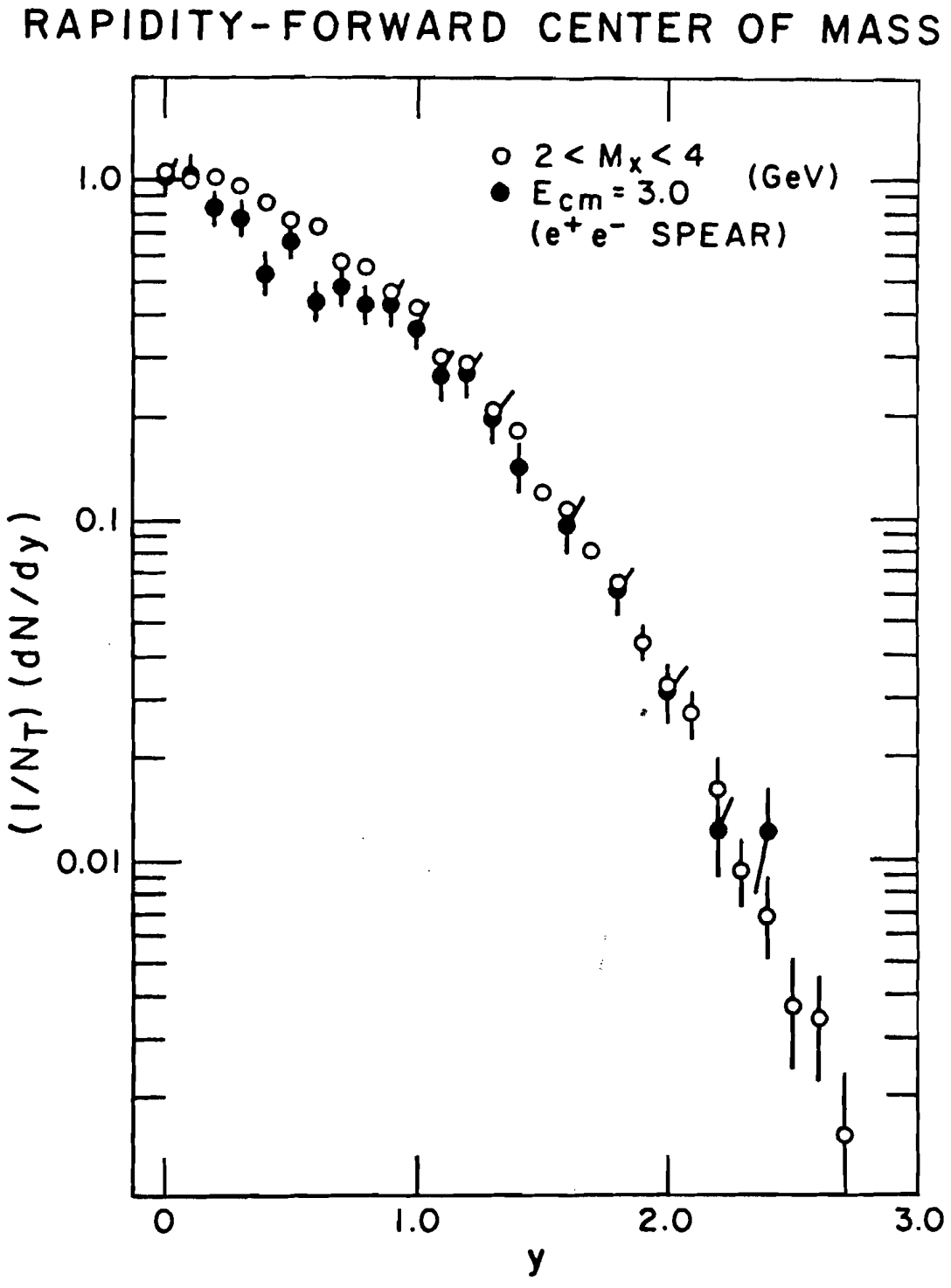

FIG. 73 Normalized rapidity distribution compared to Mark I data.

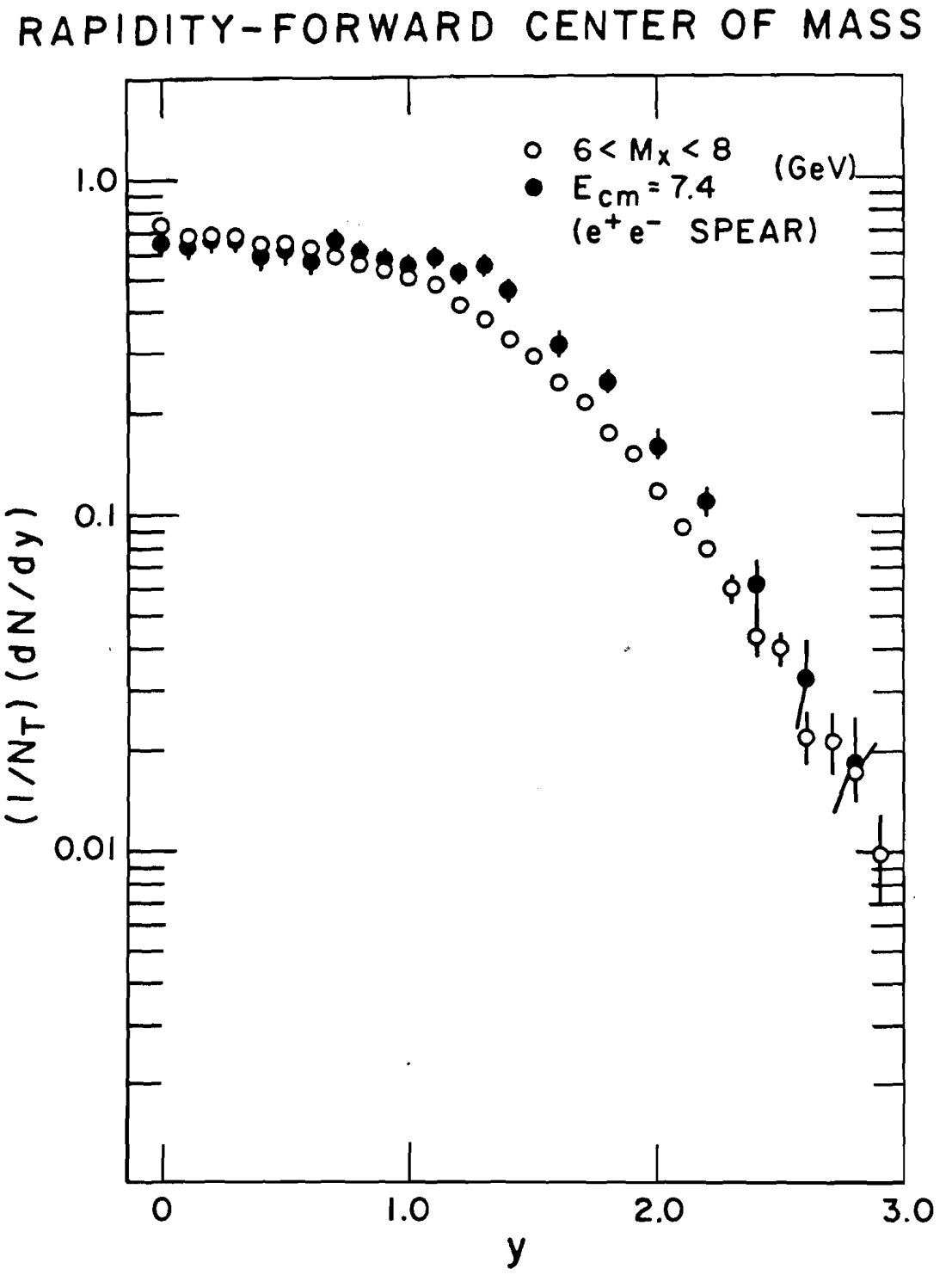

FIG. 74 Normalized rapidity distribution compared to Mark I data.

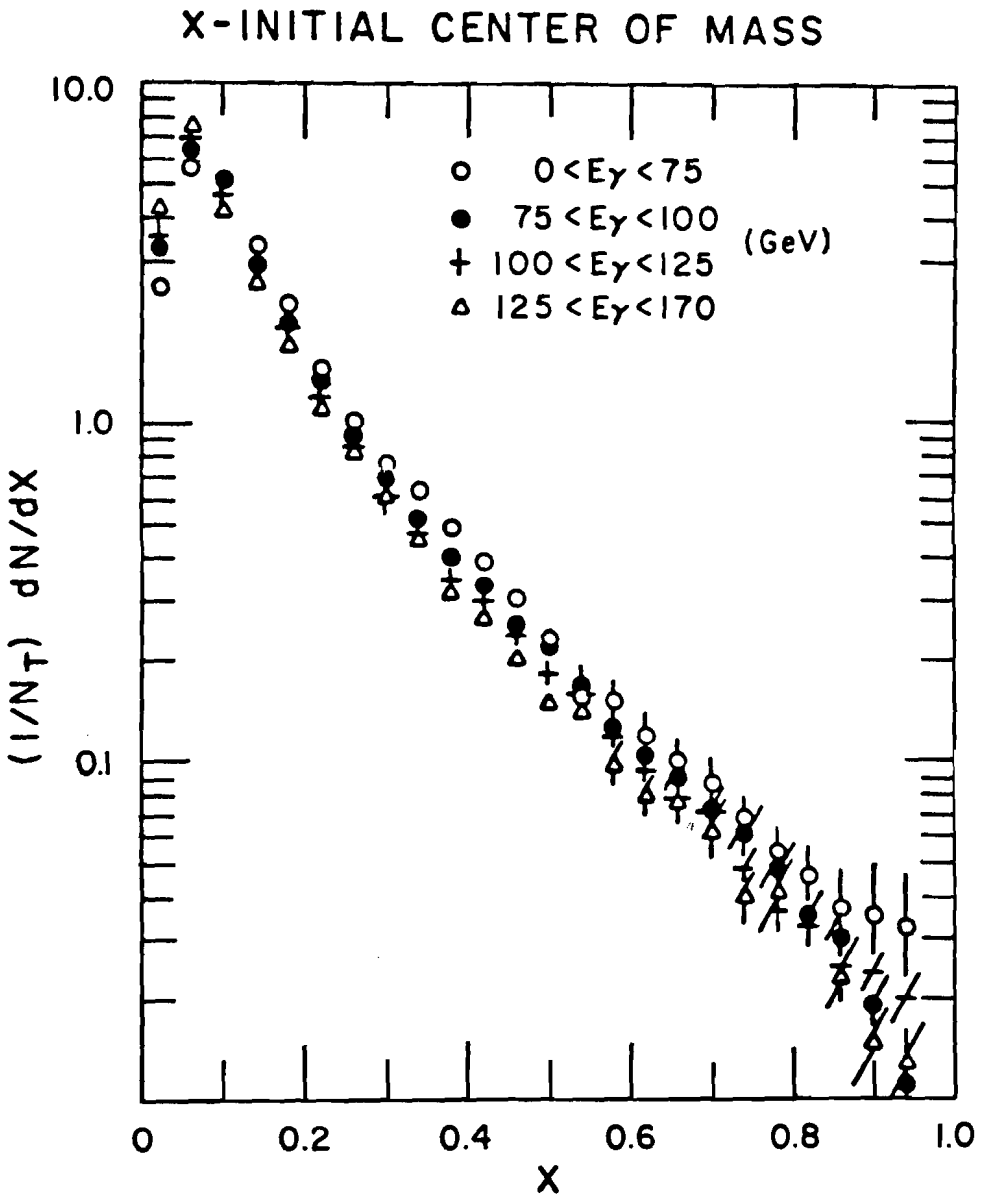

FIG. 75 x ($x=2p/\sqrt{s}$) distributions in the initial center of mass for different photon energy bins.

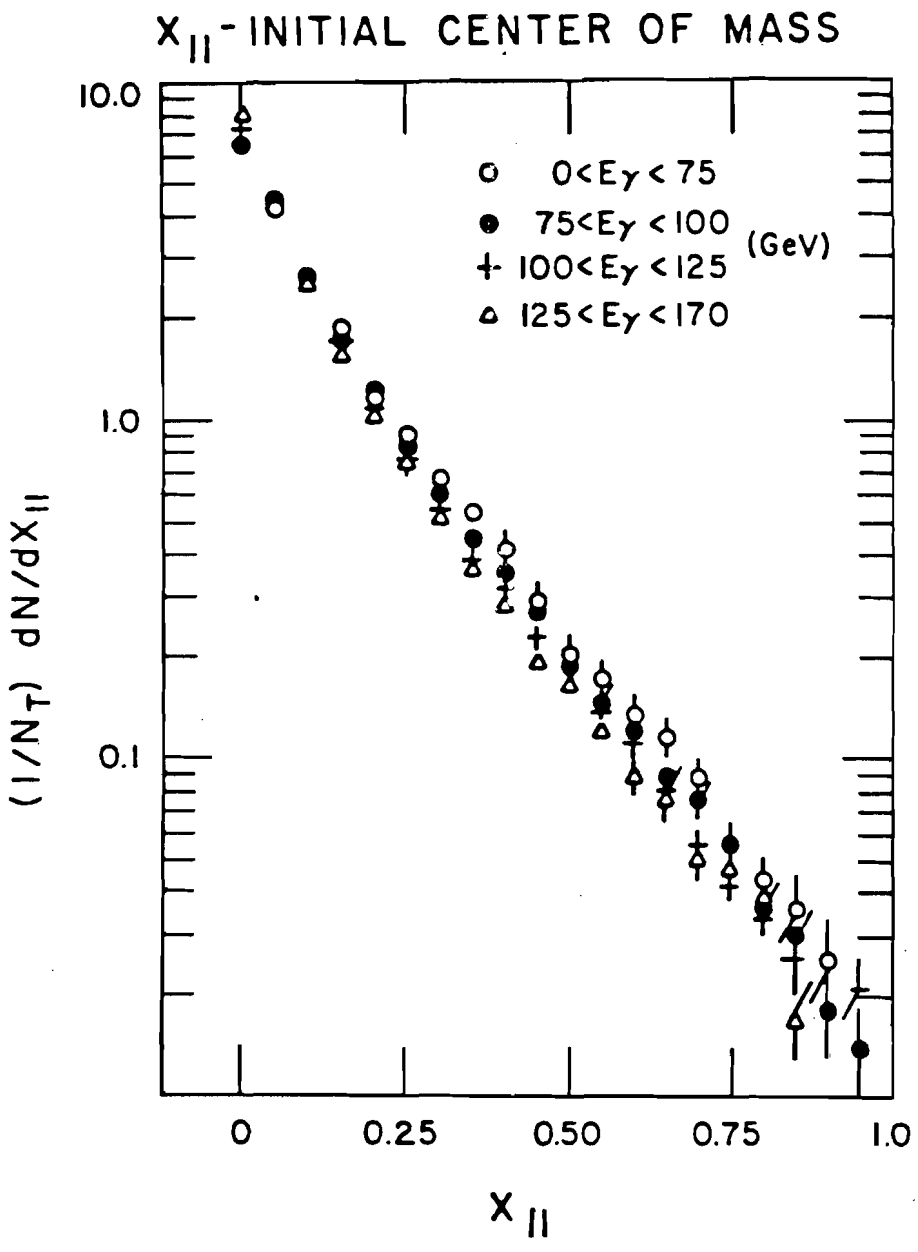

FIG. 76 Feynman x distributions in the initial center of mass for different photon energy bins.

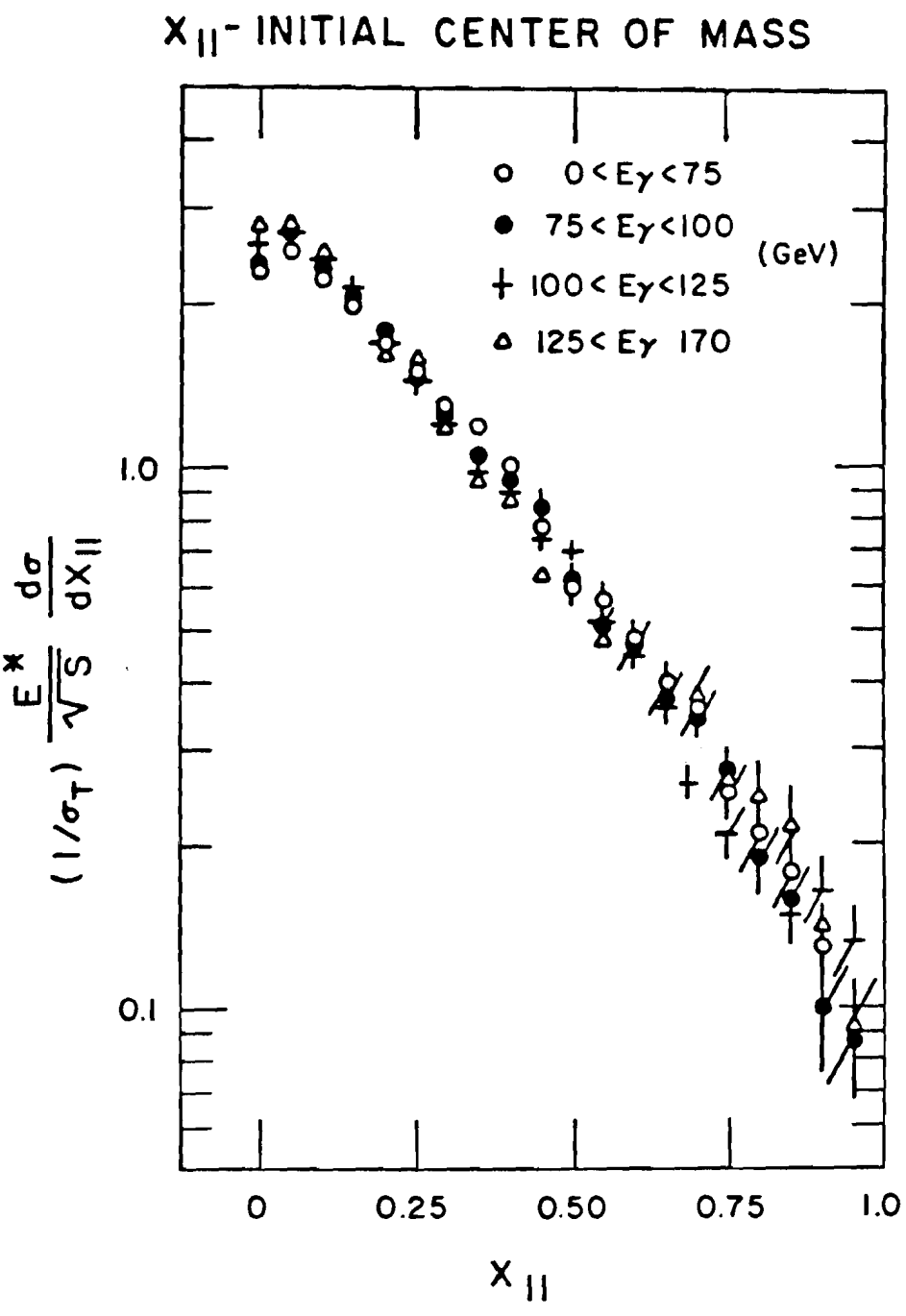

FIG. 77 Normalized invariant cross section distributions in the initial center of mass.

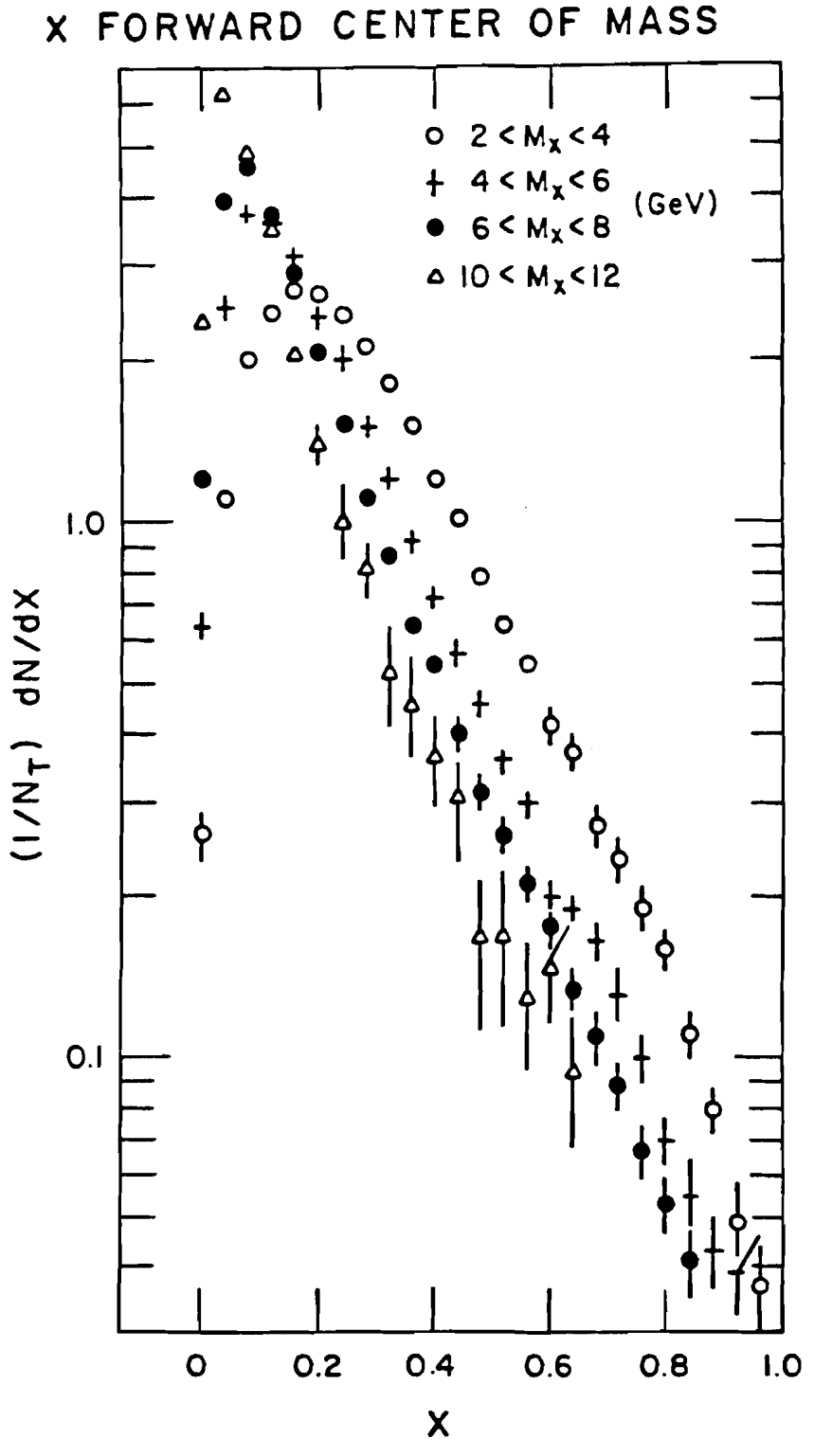

FIG. 78 x distributions in the forward center of mass for different missing mass bins.

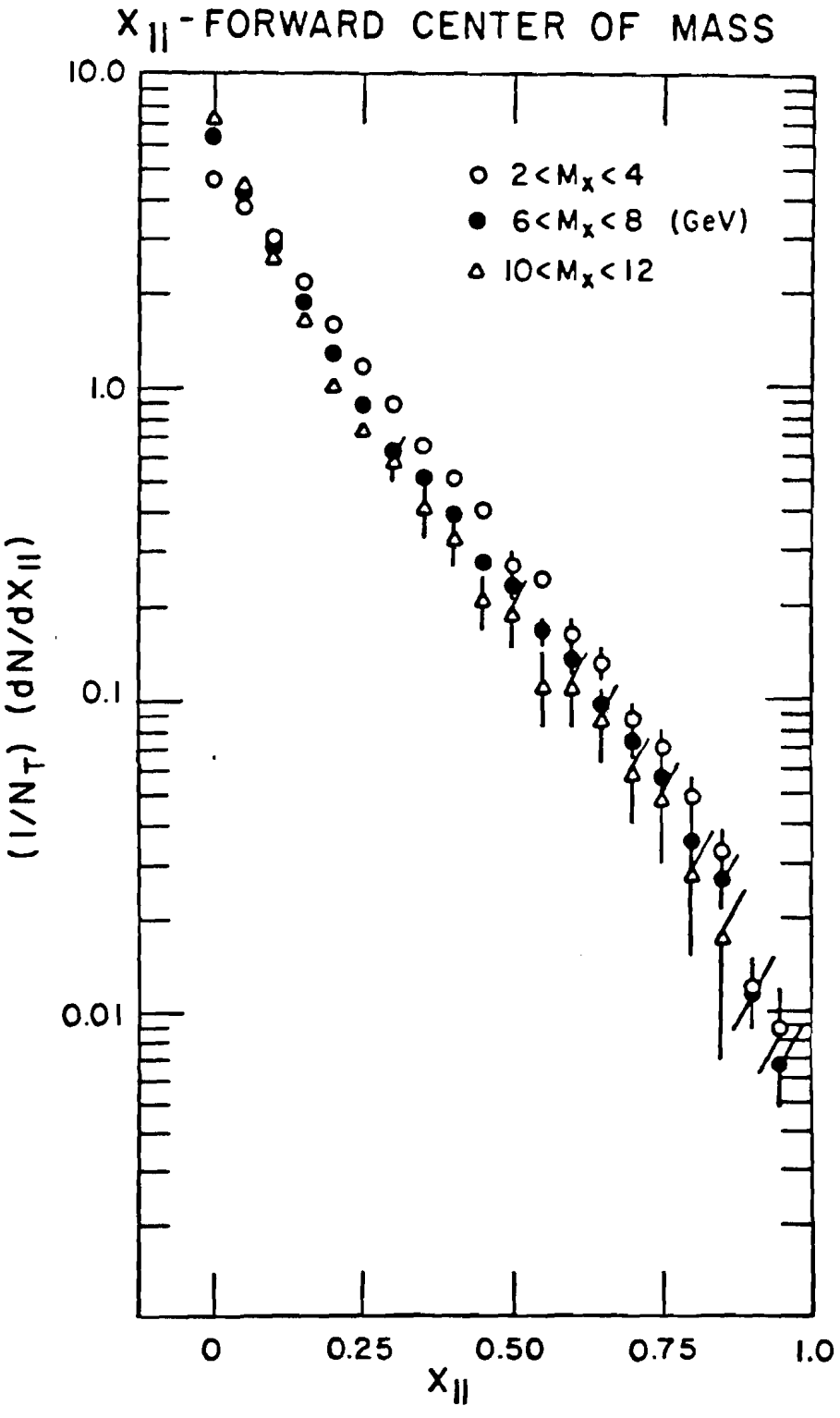

FIG. 79 Feynman x distributions in the forward center of mass for different missing mass bins.

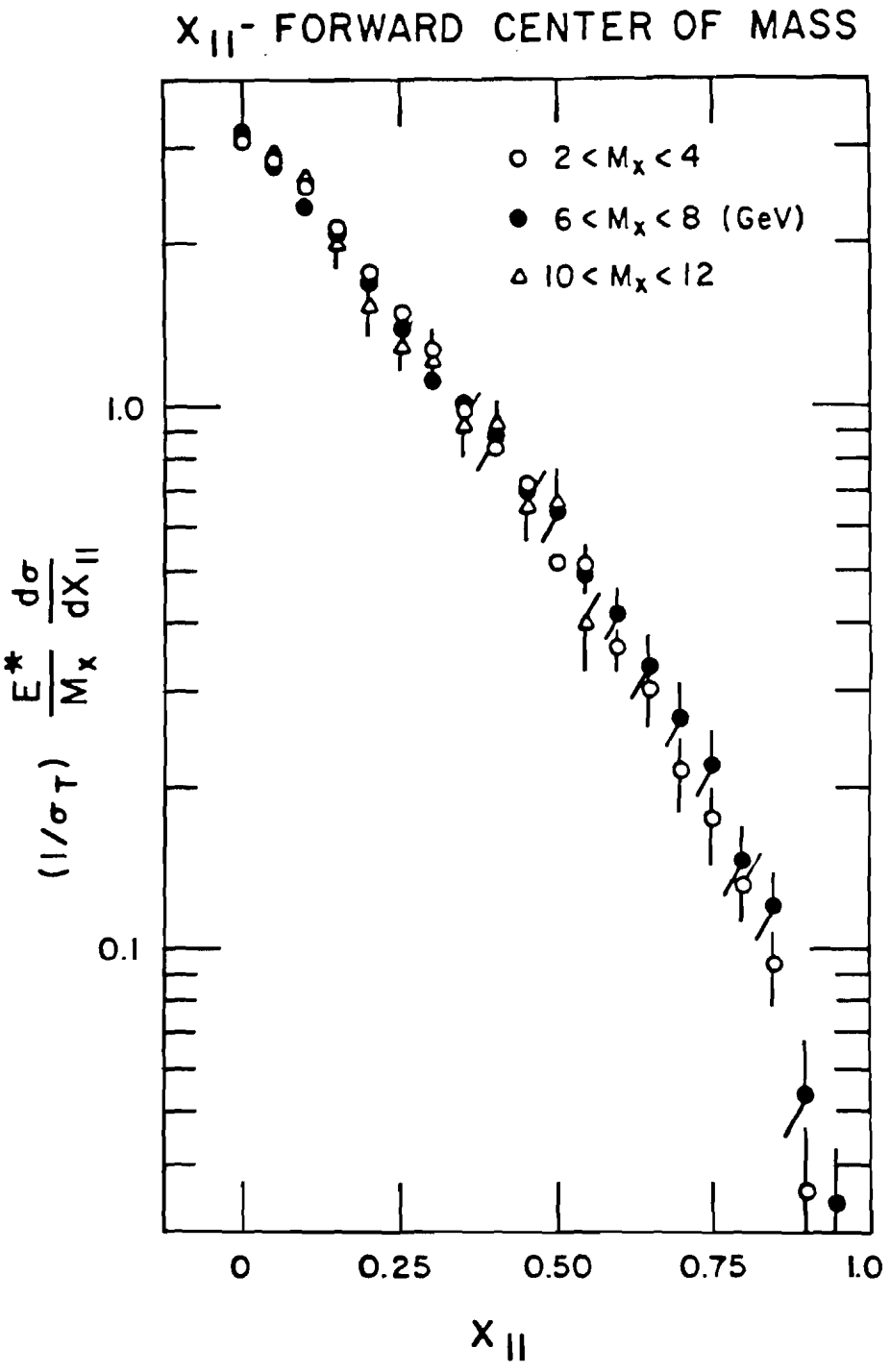

FIG. 80 Normalized invariant cross section distributions in the forward center of mass for different missing mass bins.

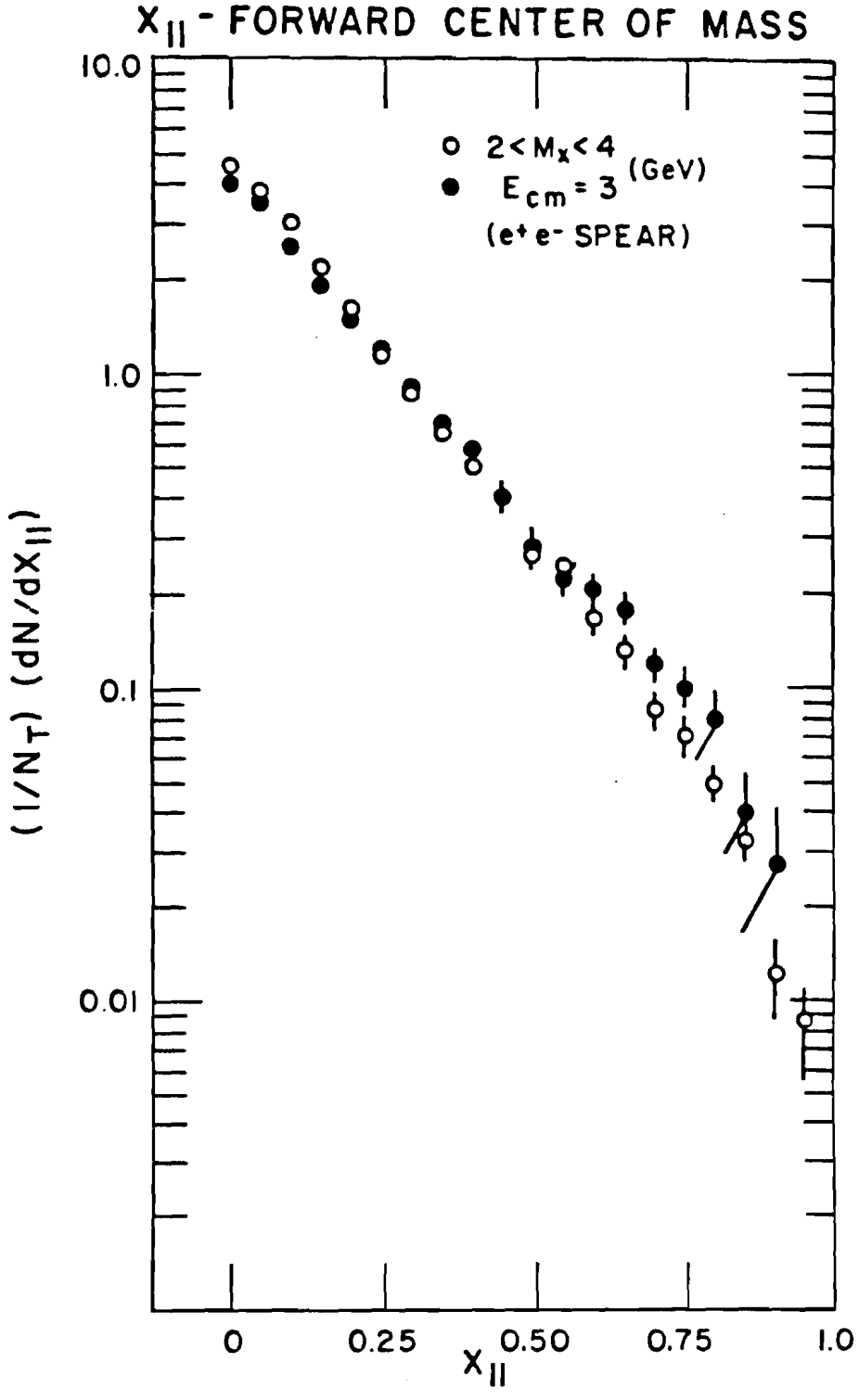

FIG. 81 Feynman x distribution compared to Mark I data.

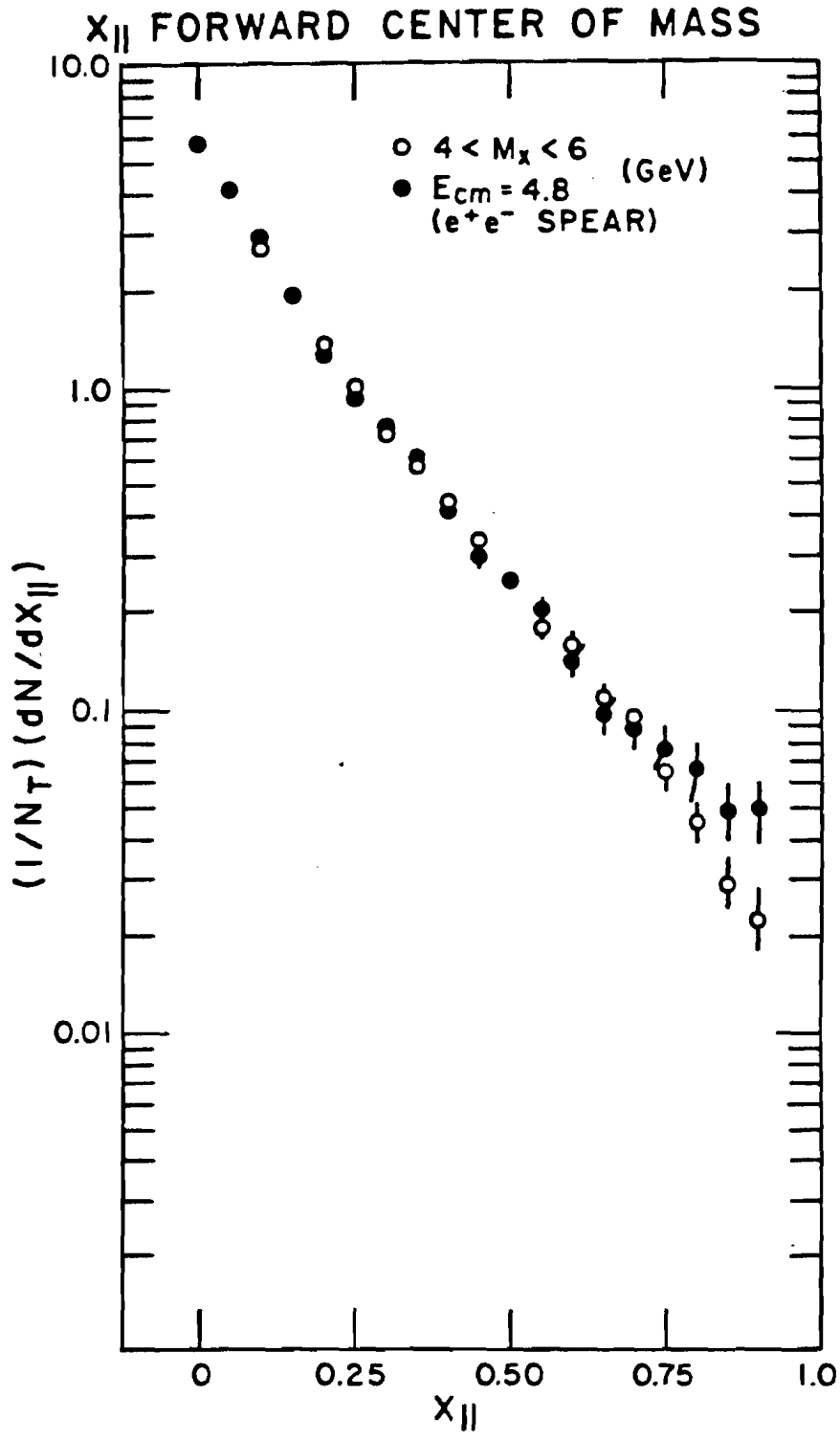

FIG. 82 Feynman x distribution compared to Mark I data.

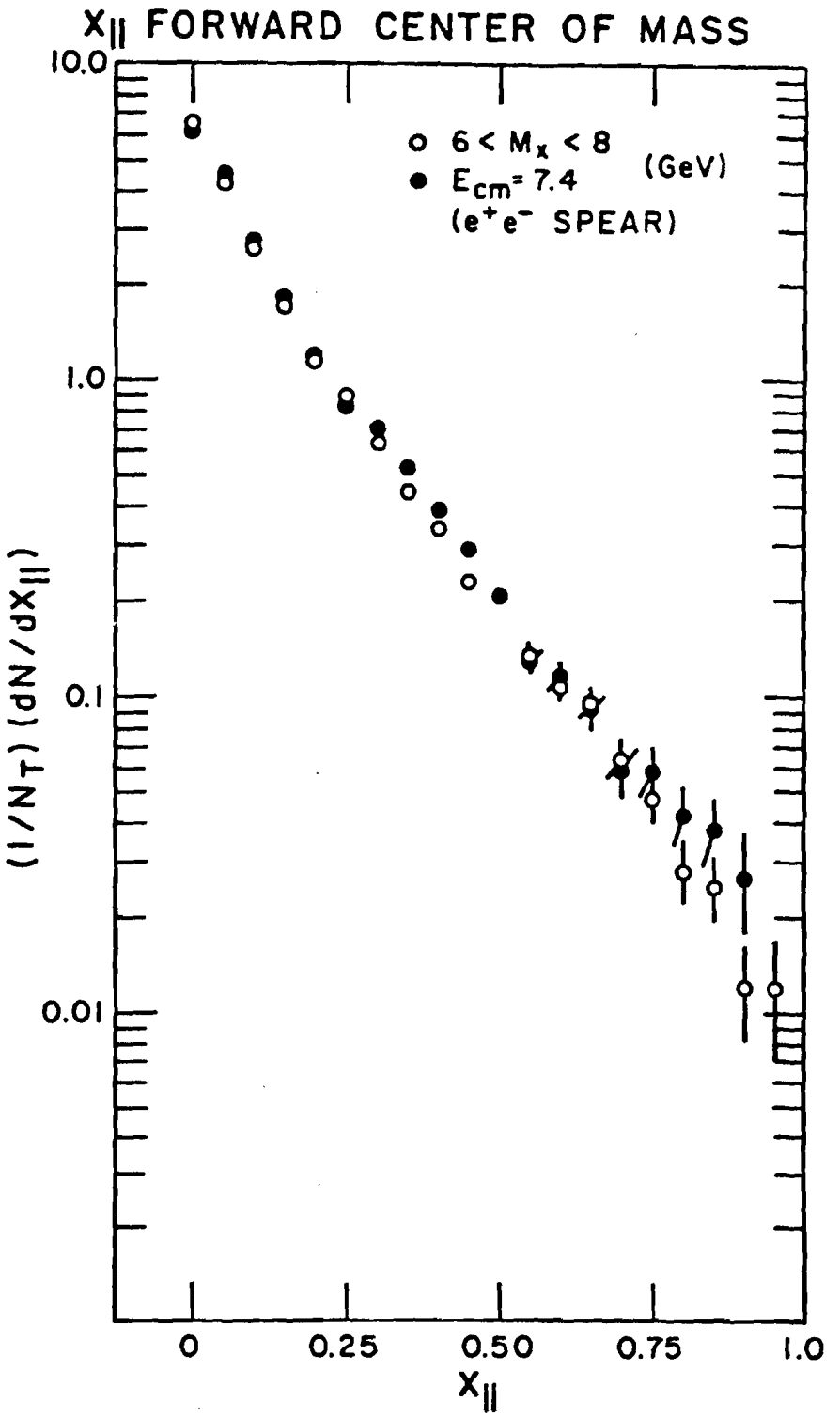

FIG. 83 Feynman x distribution compared to Mark I data.

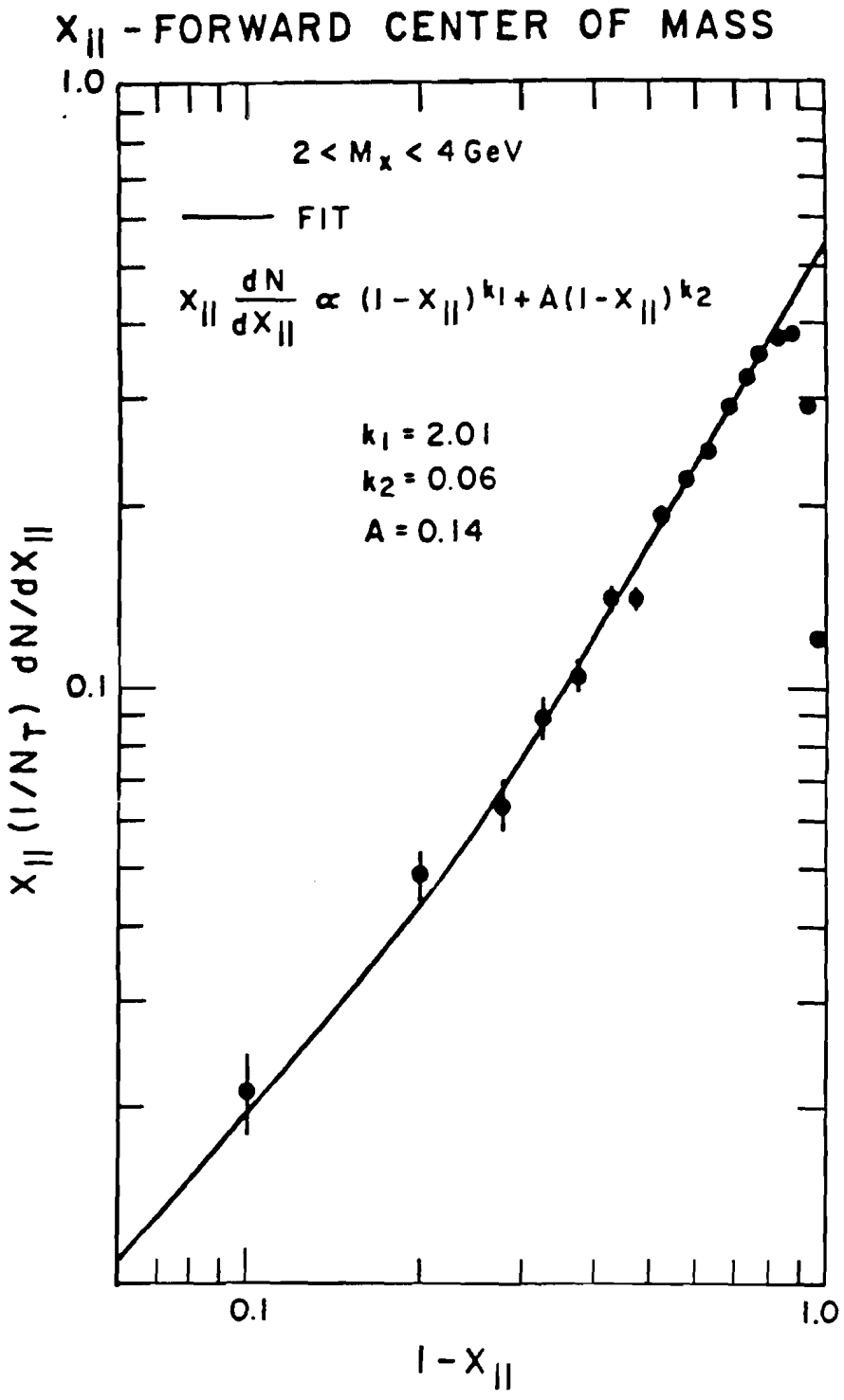
$X_{||}$ - FORWARD CENTER OF MASS
1.0
$2 < M_x < 4$ GeV
FIT
$X_{||} \frac{dN}{dX_{||}} \propto (1-X_{||})^{k_1} + A(1-X_{||})^{k_2}$
$k_1 = 2.01$
$k_2 = 0.06$
$A = 0.14$
0.1
$X_{||}(1/N_T)\ dN/dX_{||}$
0.1
1.0
$1-X_{||}$

FIG. 84

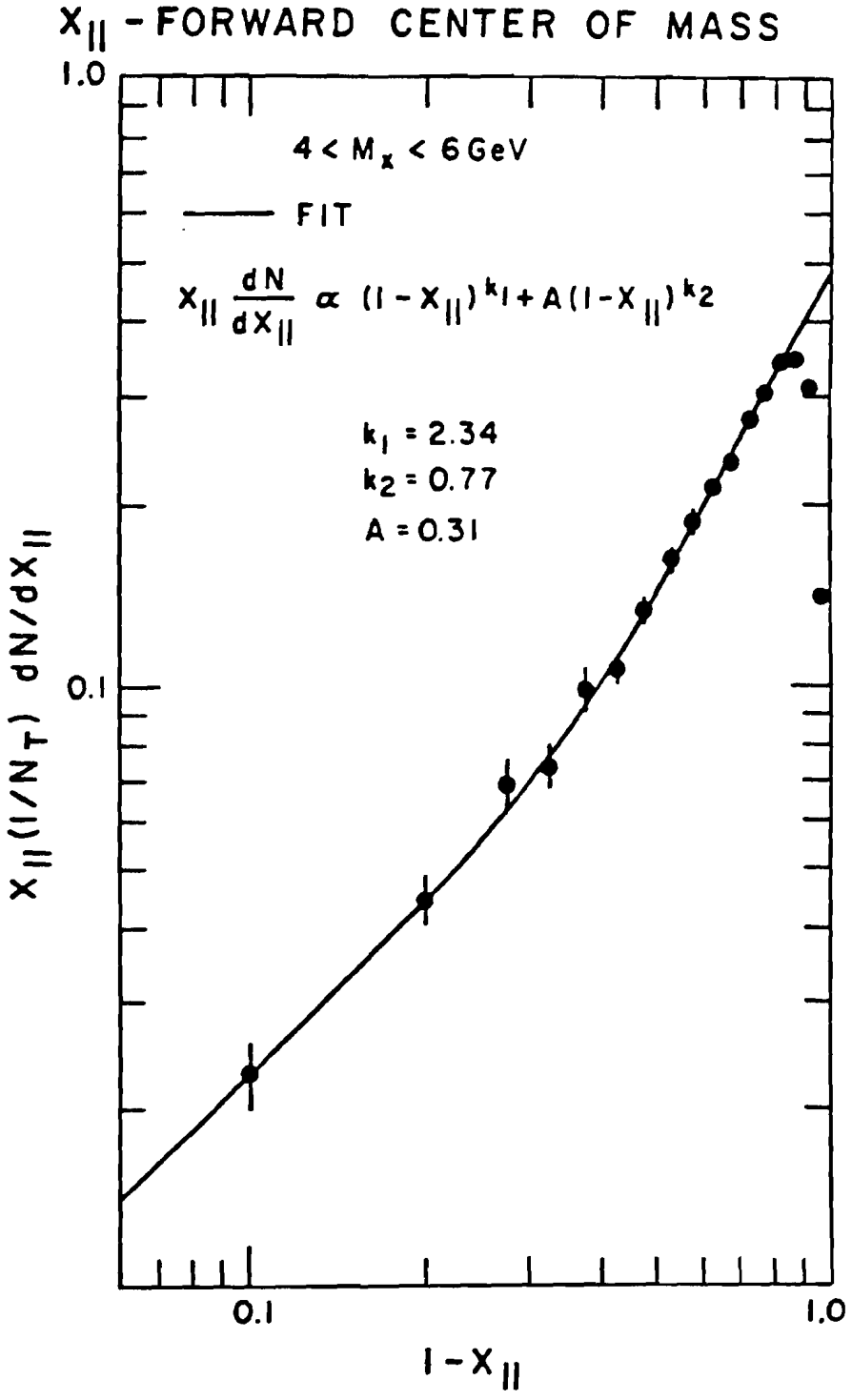
$X_{||}$ - FORWARD CENTER OF MASS
1.0
$4 < M_x < 6$ GeV
FIT
$X_{||} \frac{dN}{dX_{||}} \propto (1-X_{||})^{k_1} + A(1-X_{||})^{k_2}$
$k_1 = 2.34$
$k_2 = 0.77$
$A = 0.31$
0.1
$X_{||}(1/N_T)\ dN/dX_{||}$
0.1
1.0
$1-X_{||}$

FIG. 85

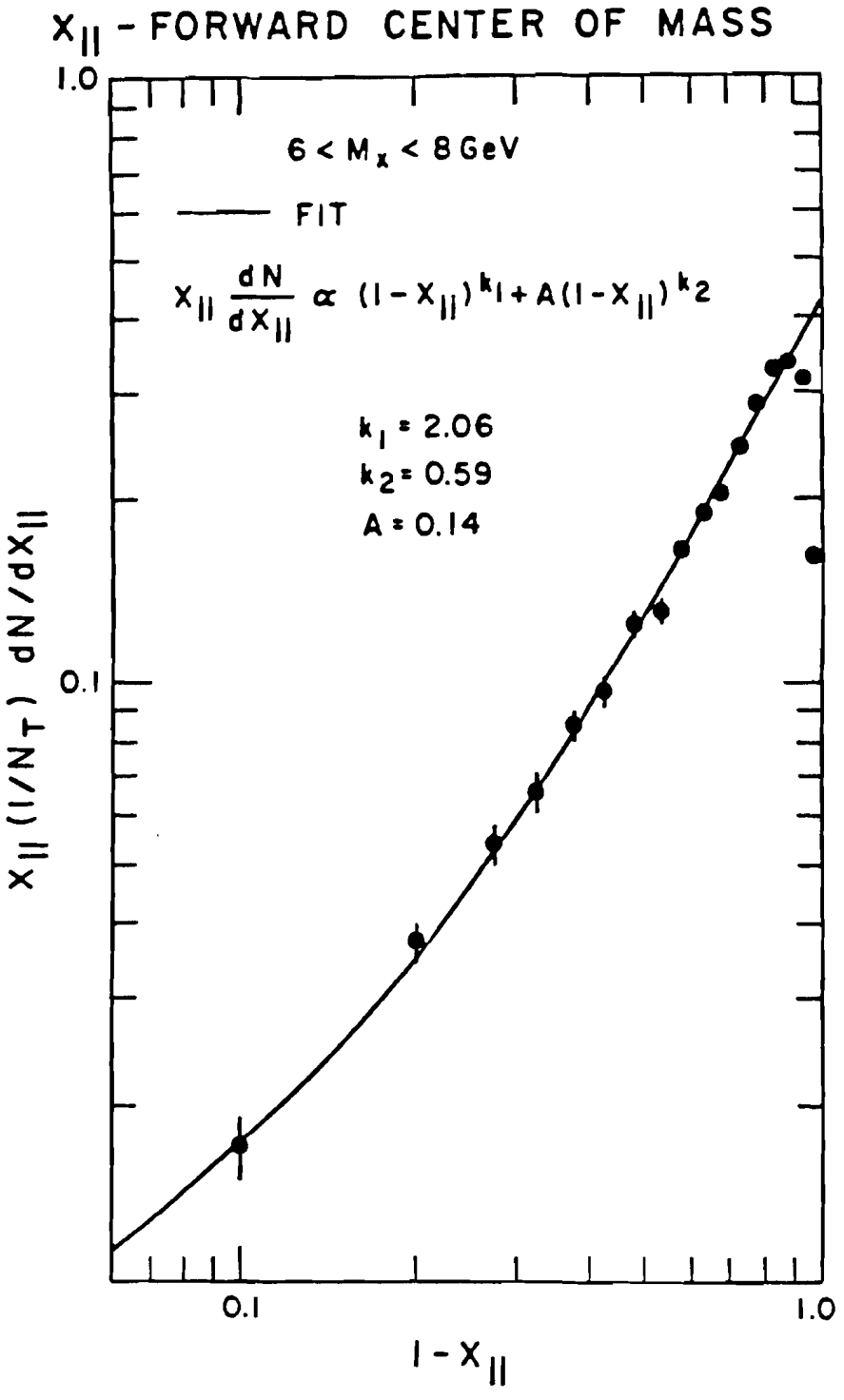
$X_{||}$ - FORWARD CENTER OF MASS
1.0
$6 < M_x < 8$ GeV
FIT
$X_{||} \frac{dN}{dX_{||}} \propto (1-X_{||})^{k_1} + A(1-X_{||})^{k_2}$
$k_1 = 2.06$
$k_2 = 0.59$
$A = 0.14$
$X_{||}(1/N_T)\ dN/dX_{||}$
0.1
0.1
1.0
$1-X_{||}$

FIG. 86

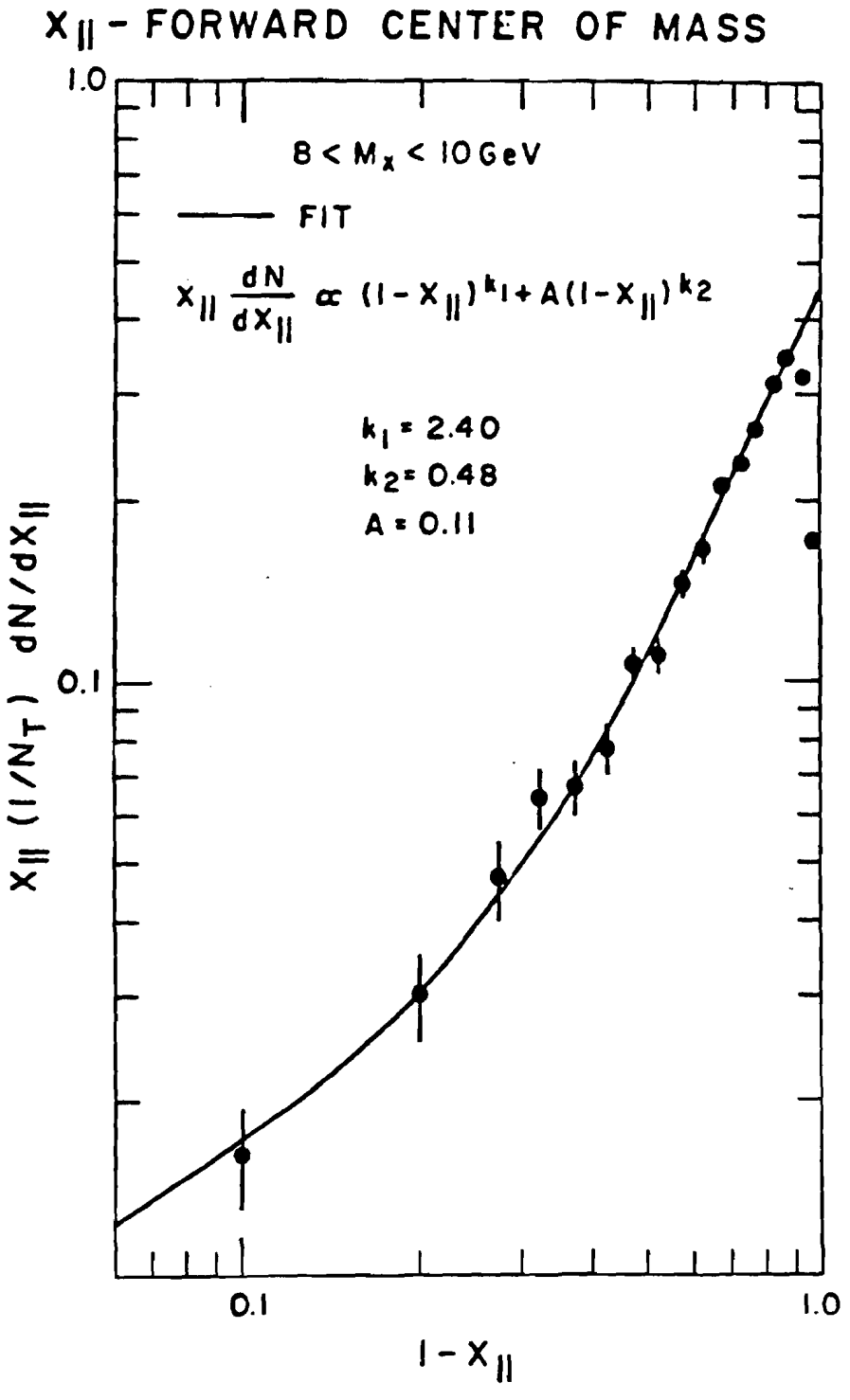
$X_{||}$ - FORWARD CENTER OF MASS
8 < M_x < 10 GeV
FIT
$X_{||} \frac{dN}{dX_{||}} \propto (1-X_{||})^{k_1} + A(1-X_{||})^{k_2}$
k_1 = 2.40
k_2 = 0.48
A = 0.11
1.0
0.1
$X_{||}$ (1/N_T) dN/d$X_{||}$
0.1
1.0
1 - $X_{||}$

FIG. 87

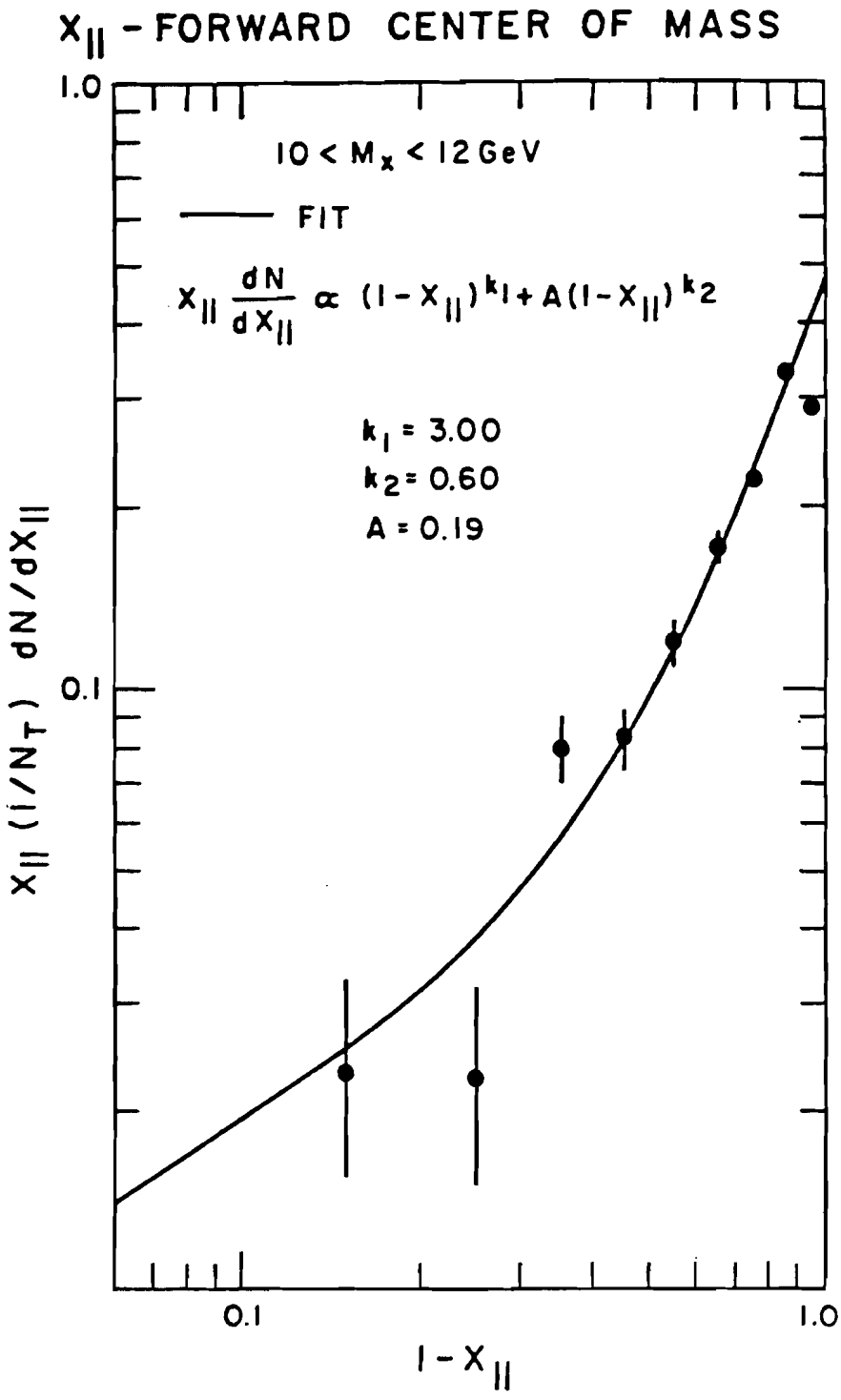
$X_{||}$ - FORWARD CENTER OF MASS
1.0
$10 < M_x < 12$ GeV
FIT
$X_{||} \frac{dN}{dX_{||}} \propto (1-X_{||})^{k_1} + A(1-X_{||})^{k_2}$
$k_1 = 3.00$
$k_2 = 0.60$
$A = 0.19$
$X_{||}\,(1/N_T)\,dN/dX_{||}$
0.1
0.1
1.0
$1-X_{||}$

FIG. 88

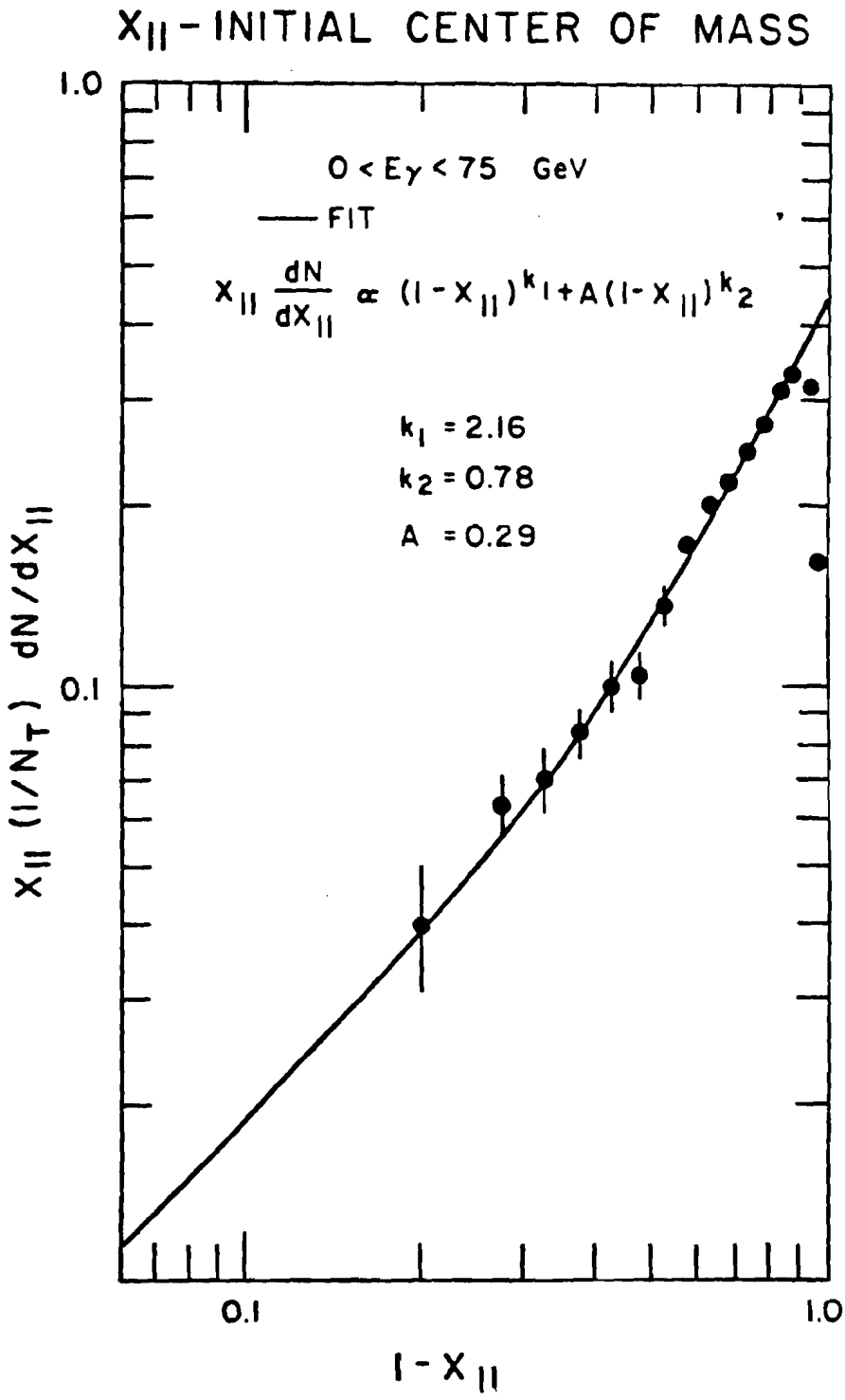
X_{11} - INITIAL CENTER OF MASS
1.0
$0 < E_\gamma < 75$ GeV
FIT
$X_{11} \frac{dN}{dX_{11}} \propto (1-X_{11})^{k_1} + A(1-X_{11})^{k_2}$
$k_1 = 2.16$
$k_2 = 0.78$
$A = 0.29$
$X_{11}\ (1/N_T)\ dN/dX_{11}$
0.1
0.1
1.0
$1 - X_{11}$

FIG. 89

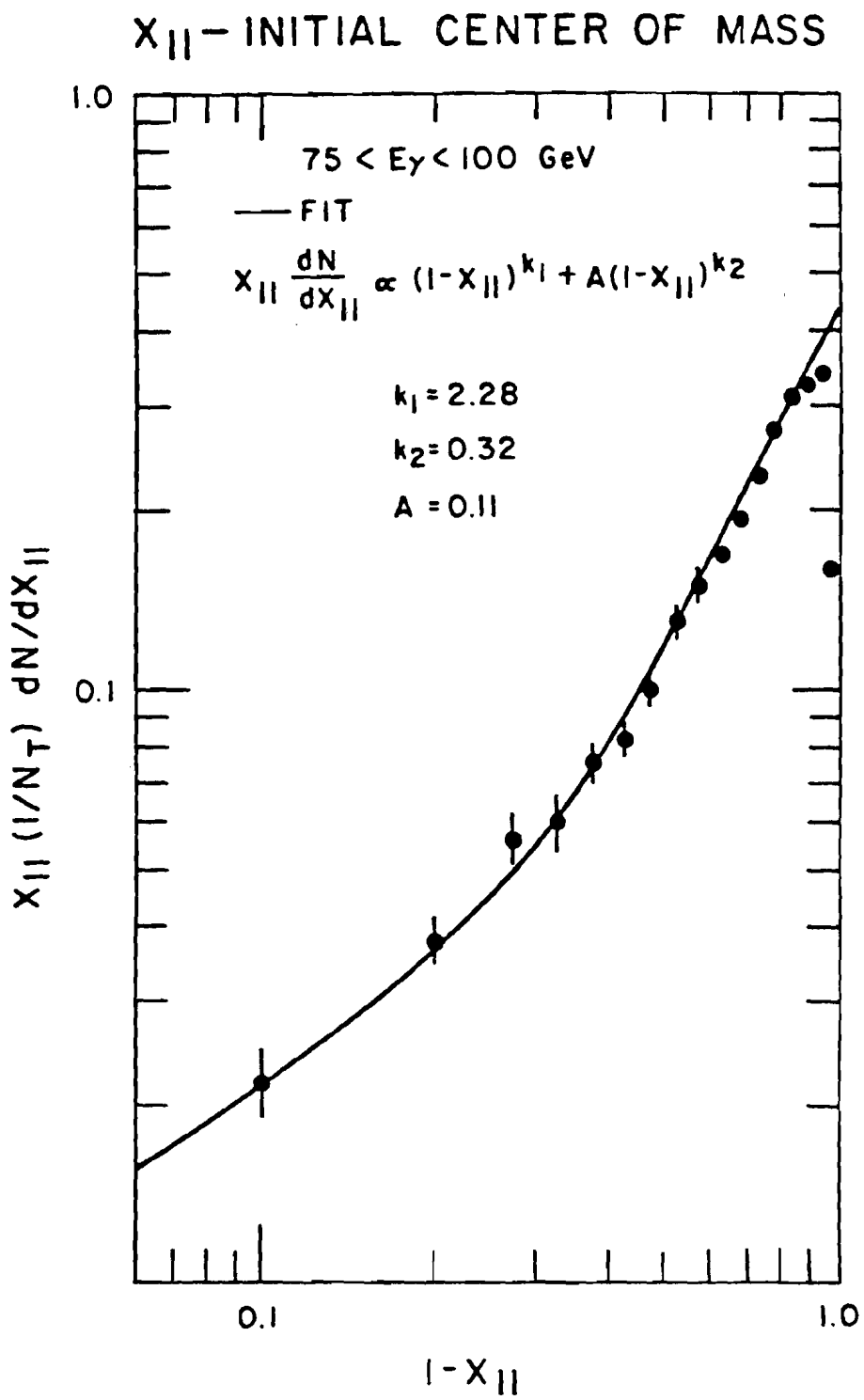
X_{11} – INITIAL CENTER OF MASS
1.0
0.1
75 < Ey < 100 GeV
— FIT
$X_{11}\frac{dN}{dX_{11}} \propto (1-X_{11})^{k_1} + A(1-X_{11})^{k_2}$
$k_1 = 2.28$
$k_2 = 0.32$
$A = 0.11$
$X_{11}\,(1/N_T)\,dN/dX_{11}$
0.1
1.0
$1-X_{11}$

FIG. 90

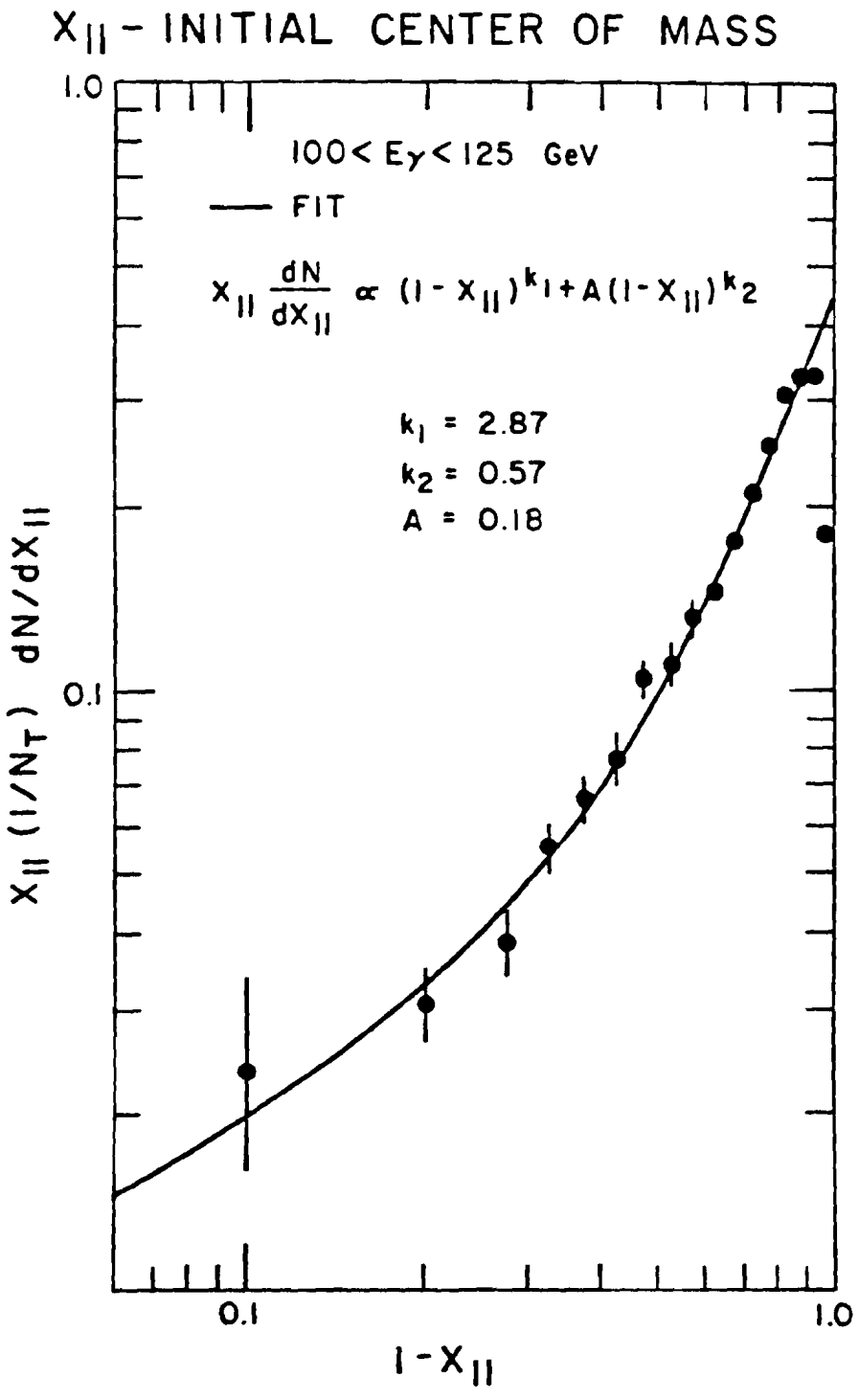
$X_{||}$ - INITIAL CENTER OF MASS
1.0
100< Eγ< 125 GeV
FIT
$X_{||} \frac{dN}{dX_{||}} \propto (1-X_{||})^{k_1} + A(1-X_{||})^{k_2}$
k_1 = 2.87
k_2 = 0.57
A = 0.18
0.1
$X_{||}$ (1/N_T) dN/d$X_{||}$
0.1
1.0
1-$X_{||}$

FIG. 91

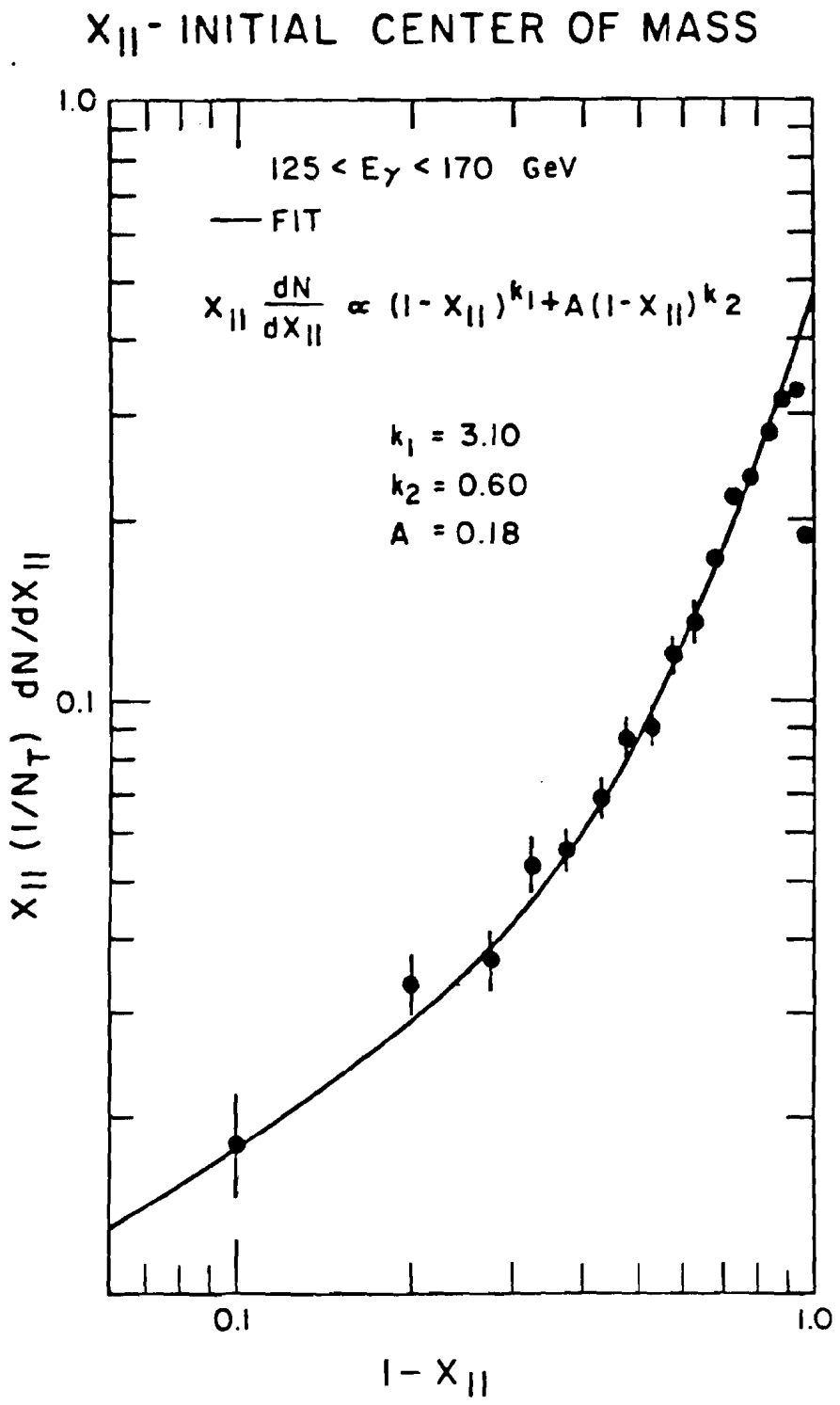
X_{11} - INITIAL CENTER OF MASS
1.0
$125 < E_\gamma < 170$ GeV
— FIT
$X_{11} \frac{dN}{dX_{11}} \propto (1-X_{11})^{k_1} + A(1-X_{11})^{k_2}$
$k_1 = 3.10$
$k_2 = 0.60$
$A = 0.18$
0.1
$X_{11}\,(1/N_T)\,dN/dX_{11}$
0.1
1.0
$1-X_{11}$

FIG. 92

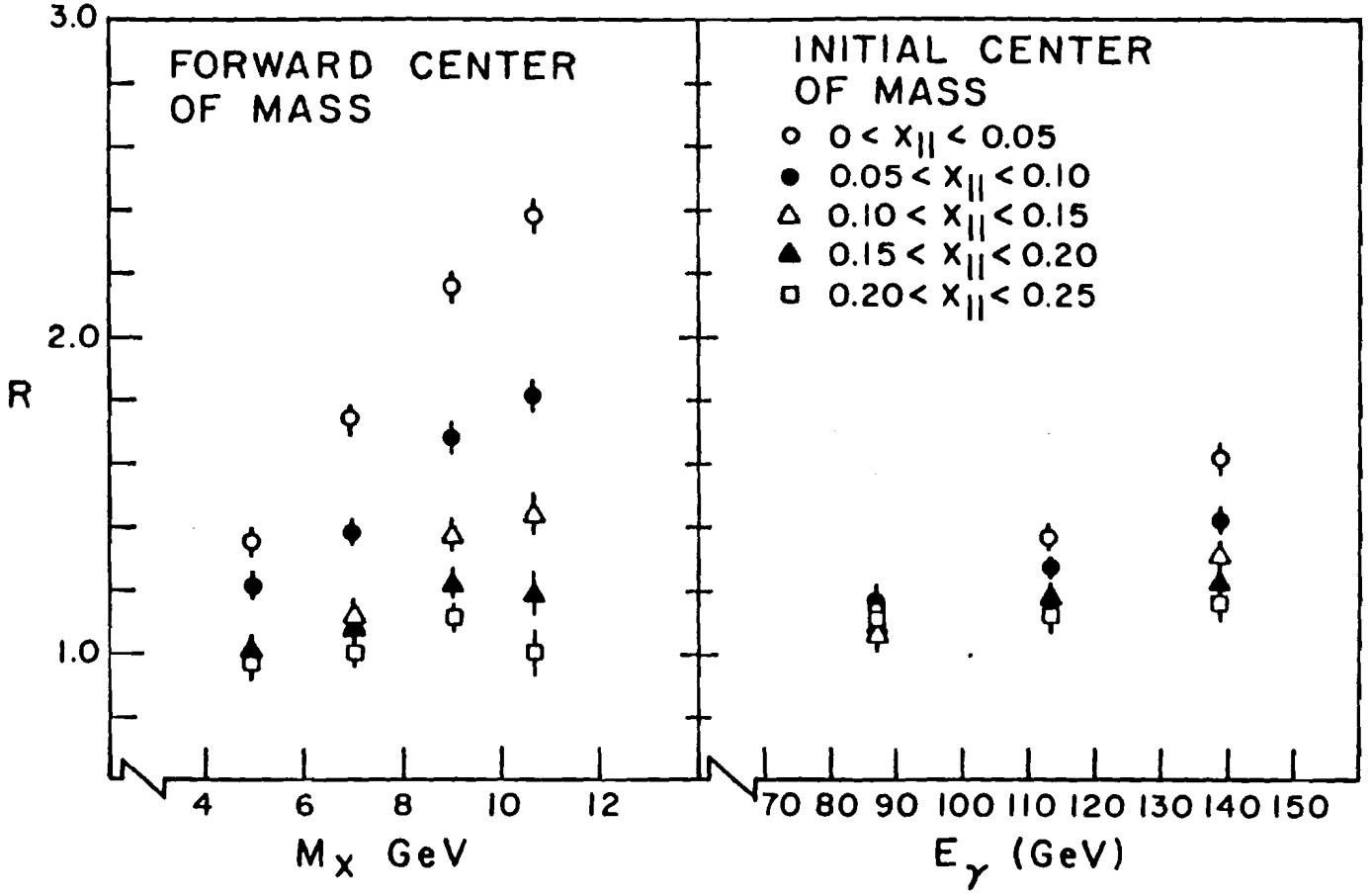

FIG. 93 Scaling violations in the central region. (R is defined in the text)